

University of Warwick institutional repository: <http://go.warwick.ac.uk/wrap>

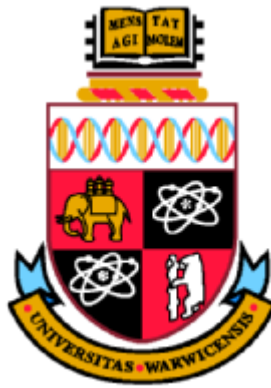
**A Thesis Submitted for the Degree of PhD at the University of Warwick**

<http://go.warwick.ac.uk/wrap/55977>

This thesis is made available online and is protected by original copyright.

Please scroll down to view the document itself.

Please refer to the repository record for this item for information to help you to cite it. Our policy information is available from the repository home page.



# **Flame Front Propagation Velocity Measurement and In-Cylinder Combustion Reconstruction using POET**

by

**Cheng Hua**

Thesis

Submitted to the University of Warwick

for the degree of

**Doctor of Philosophy**

School of Engineering

May 2012

THE UNIVERSITY OF  
**WARWICK**

# Acknowledgements

I would like to express my great appreciation to the people who have assisted me in finishing my PhD study. I thank them for helping me in both my academic study and daily life.

Firstly, I am very grateful to my supervisor, Peter Bryanston-Cross, who gave me intelligent advice to set up the POET project. Without his guide and financial support, this project could be not completed. I especially thank Dr. Brenda Timmerman who has assisted me with the format of my thesis, structure and content. I must thank my panel meeting supervisors and referees, Professor Derek Chetwynd and Dr. Daciana for helping me carry on my career life.

I would like to thank Dr. Andrew Skeen and Etalon Research lab for their contributions of building up the POET PC sets. I would also like to thank William Playford for assisting with the modification of the commercial engine. I am grateful to thank the previous OEL members for making the initial MART version.

Finally and most importantly, I would like to express my gratitude to my parents and my wife Jin Yingying for their encouragement, understanding and support in overcoming the obstacles during the past four years. I am thankful to Richard Dunton, Ivan Player and Dr. Fu Feng for proofreading my thesis. I am grateful to my friend Dr. Li Cong and Li Jia for helping me get through ups and downs.

# Declaration

I declare that the POET system has been patented. No person or organization has right to copy or imitate the system without permission of author and supervisor Peter Bryanston-Cross. We preserve the right to pursue legal actions against any person who use the system for commercial or personal purposes. The thesis is submitted to the University of Warwick for supporting my PhD degree. All the diagnostic approaches and experimental results have not been previously published or submitted for a degree at any other university or institution.



# Abstract

The objective of this thesis is to develop an intelligent diagnostic technique POET (Passive Optical Emission Tomography) for the investigation of in cylinder combustion chemiluminescence. As a non-intrusive optical system, the POET system employs 40 fibre optic cables connected to 40 PMTs (Photo Multiplier Tube) to monitor the combustion process and flame front propagation in a modified commercial OHV (Over Head Valve) Pro 206 IC engine.

The POET approach overcomes several limitations of present combustion research methods using a combination of fibre optic detection probes, photomultipliers and a tomographic diagnostics. The fibre optic probes are placed on a specially designed cylinder head gasket for non-invasively inserting cylinder. Each independent probe can measure the turbulent chemiluminescence of combustion flame front at up to 20 kHz. The resultant intensities can then be gathered tomographically using MART (Multiplicative Algebraic Reconstruction Technique) software to reconstruct an image of the complete flame-front. The approach is essentially a lensless imaging technique, which has the advantage of not requiring a specialized engine construction with conventional viewing ports to visualize the combustion image. The fibre optic system, through the use of 40, 2m long thermally isolated fibre optic cables can withstand combustion temperatures and is immune from electronic noise, typically generated by the spark plug.

The POET system uses a MART tomographic methodology to reconstruct the

turbulent combustion process. The data collected has been reconstructed to produce a temporal and spatial image of the combustion flame front. The variations of flame turbulence are monitored by sequences of reconstructed images. Therefore, the POET diagnostic technique reduces the complications of classic flame front propagation measurement systems and successfully demonstrates the in-cylinder combustion process.

In this thesis, a series of calibration exercises have been performed to ensure that the photomultipliers of the POET system have sufficient temporal and spatial resolution to quantitatively map the flow velocity turbulence and chemiluminescence of the flame front. In the results, the flame has been analyzed using UV filters and blue filters to monitor the modified natural gas fuel engine. The flame front propagation speed has been evaluated and it is, on average, 12 m/s at 2280 rpm. Sequences of images have been used to illustrate the combustion explosion process at different rpm.

# List of Acronyms

ART	Algebraic Reconstruction Technique
BDC	Bottom Dead Center
CA	Crank Angle
CT	Computerized Tomography
CH*	Methylidyne
CDF	Cumulative Distribution Function
CI	Compression Ignition
CNC	Computer Numerical Control
DAQ	Data Acquisition
DI	Direct Injection
EBF	Electron Beam Fluorescence
EM	Expectation Maximum
FS	Focusing Schlieren
FAR/AFR	Fuel-Air Ratio/Air-Fuel Ratio
FBP	Filtered Back Projection
FFT	Fast Fourier Transform
FFP	Flame Front Propagation
IC Engine	Internal Combustion Engine
ICCD	Intensified Charge Couple Device
MBT	Maximum Brake Torque

ML	Maximum Likelihood
MART	Multiplicative - ART
OAG	Optical Array Gasket
OHV	Over Head Valve
OHC	Over Head Camshaft
OPAL	Optical Access Layer
POET	Passive Optical Emission Tomography
PMT	Photo Multiplier Tube
PDE	Pulse Detonation Engine
PLIF	Plane Laser Induced Fluorescence
PMMA	Polymethyl-Methacrylate Resin
RTT	Radon Transform Technique
RGB	Red, Green and Blue
ROI	Region of Interest SHWF
SHWF	Shack-Hartmann Wavefront
SMA	Sub Miniature Version A
SI	Spark Ignition
TP	Thermographic Phosphor
TDC	Top Dead Center
UV	Ultraviolet

# Contents

Acknowledgements .....	i
Declaration .....	ii
Abstract .....	iii
List of Acronyms .....	v
Chapter 1. ....	1
Motivation .....	1
1.1 POET Approach Development.....	2
1.2 Thesis Structure.....	6
Chapter 2. ....	9
Literature Review .....	9
2.1 Reviews of In-Cylinder Combustion Measurement Techniques.....	10
2.1.1 Laser Induced Fluorescence .....	11
2.1.2 Particle Image Velocimetry .....	14
2.1.3 Laser Doppler Velocimetry .....	17
2.1.4 Thermographic Phosphors.....	22
2.2 Reviews of Tomography Techniques .....	24
2.3 Review of Other Optical Research Techniques.....	30
2.3.1 Shadowgraphy Method .....	30
2.3.2 Schlieren Method .....	32
2.3.3 Interferometry Method .....	34

2.4 Summary .....	41
Chapter 3. ....	43
Experimental Methodology.....	43
3.1 Introduction of the Otto Engine .....	45
3.1.1 Engine Operating System.....	47
3.1.2 Engine Performance Parameters .....	51
3.2 Optical Array Gasket Design and Engine Modification .....	54
3.2.1 Optical Array Gasket (OAG) .....	57
3.2.2 Engine Modification.....	65
3.3 PMT and Accessories Specification .....	73
3.3.1 Filter Selection .....	73
3.3.2 Optical Fibre.....	79
3.3.3 PMT Connecting Interface .....	81
3.3.4 Photo Multiplier Tube .....	82
3.4 Compact POET Computer System.....	86
3.4.1 Tomography Computer System Implementation .....	87
3.4.2 Hardware Components .....	90
3.5 Summary .....	91
Chapter 4. ....	93
Computational Methodology .....	93
4.1 Computed Tomography.....	95
4.1.1 Computed Tomography Concept .....	95

4.1.2 Tomography Mathematics .....	97
4.2 Parallel Projection and Fan Beam Projection.....	105
4.2.1 Parallel Beam Projection.....	106
4.2.2 Fan Beam Projection .....	111
4.3 Interactive Reconstruction Algorithm and Array MART Software Implementation .....	116
4.3.1 Transmission and Emission Tomography Technique .....	117
4.3.2 Iterative Reconstruction .....	119
4.3.3 Array MART Software .....	127
4.4 Summary .....	143
Chapter 5. ....	144
Experimental Results Analysis.....	144
5.1 Shack-Hartmann Camera Applied to the Study of Flame Turbulent Density .....	147
5.1.1 Flame Density Distribution Implementation using SHWF Technique .....	149
5.1.2 SH Experimental Results Analysis.....	150
5.2 Flame Front Analysis by Photogrammetric Technique .....	155
5.3 Simulated Model of Flame Propagation .....	162
5.4 Flame Propagation Analysis by POET Projections.....	168
5.4.1 Flame Turbulences Analysis .....	170
5.4.2 Flame Propagation Velocity Evaluation .....	180

5.5 Combustion Process Reconstruction and Flame Front Propagation Analysis .....	189
5.5.1 Combustion Visualization .....	193
5.5.2 UV Combustion Images Reconstruction.....	199
5.5.3 Blue Combustion Images Reconstruction.....	210
5.5.4 Combustion Reconstruction in Different RPMs .....	217
5.6 Summary .....	221
5.6.1 Optimized Combustion Images.....	221
Chapter 6. ....	223
Conclusion and Recommendations .....	223
6.1 Conclusion.....	223
6.2 Further Work .....	229
6.2.1 The Parallel Signal Collection Method and Radon Transform Algorithm in Application .....	231
6.2.2 Tomography System Update Using Shack-Hartmann Cameras.....	236
Reference.....	239
Appendix Figure List .....	248
Appendix A: Relevant Background Reviews.....	252
Laminar flame velocity .....	253
Turbulence flame velocity.....	257
Detonation flame.....	262
Fourier transform and Fourier slice transform theorem .....	269



Fourier transform .....	269
Fourier slice transform .....	272
Appendix B: Shack Hartmann .....	275
Shack-Hartmann sensor applications .....	275
Thorlabs Shack-Hartmann software application .....	279
House schematic diagrams for FS-105 lenslet array .....	282
Results .....	282
Appendix C: POET system .....	290
Mechanical .....	290
Compacted PC module.....	298
Overviews .....	298
Tomographic acquisition (TOMACK) software .....	300
File formats .....	304
Hardware components.....	307
Software applications .....	309
System calibration.....	309
Software user manual .....	312
Appendix D: Generals .....	323
Appendix E: POET Reconstruction Results.....	329
UV Filtered Combustion .....	329
Blue Filtered Combustion .....	332
Appendix Reference.....	335

## Table List

Table 1.1 Optical Sensor for combustion investigation .....	4
Table 2.1 Comparison between LIF, PIV and TP techniques.....	10
Table 3.1 Internal Combustion Engine Classifications [46] .....	46
Table 3.2 OHV Pro 206 Specifications .....	47
Table 3.3 OAG Array Plate Specifications.....	64
Table 3.4 Chemical composition of natural gas [49] .....	74
Table 3.5 Specification of Fibre Probe and PMMA Fibre.....	80
Table 3.6 Comparison of Photo sensors Performance.....	83
Table 3.7 PMTs Distribution of Embedded Module in Series Number .....	91
Table 4.1 List of Parallel-Beam Backprojection Algorithms [73] .....	111
Table 4.2 A Single Gaussian Flame Image Reconstruction by Numbers of Iterations.....	136
Table 4.3 Two Gaussian Function Flames Reconstruction by Numbers of Iterations.....	138
Table 4.4 MART Software Evaluations .....	140
Table 5.1 System Parameter Initialization of Velocity Measurement .....	170
Table 5.2 UV Propagation Velocity between Each Projection (Combustion Kernel passing the Number 2, 17 and 23 Projections).....	183
Table 5.3 Averaged Flame Speed (From the Central of Combustion to Chamber	

Boundary).....	184
Table 5.4 System Specifications.....	194
Table 5.5 Reconstructed Images of UV Combustion Process after One Iteration .....	201
Table 5. 6 UV Combustion Process Images after 1000 Iterations .....	204
Table 5.7 UV Combustion Process Hot Images after 1000 Iterations.....	206
Table 5.8 UV Combustion Images by Free Colourbars .....	209
Table 5.9 Blue Combustion Process Images after One Iteration.....	211
Table 5.10 Blue Combustion Process Images after 1000 Iterations.....	213
Table 5.11 Blue Combustion Process Hot Images after 1000 Iterations.....	215
Table 5.12 Reconstructed Images of Combustion Propagation by Different Engine Revolutions .....	218
Table 5.13 Optimized Reconstructed UV Images .....	222

## Figure List

Figure 1.1 Passive Optical Emission Tomography (POET) Layout Diagram (The POET system consists of a modified IC engine, a compact PMTs PC and an Array MART software) .....	6
Figure 2.1 OH LIF Set Up [20] .....	12
Figure 2.2 OH LIF images: Hydrogen (DI), SOI 220° & 280° CA AITDC, Spark Advance 15° CA& 40° (Intake Valves at the Top, Exhaust Valves at the Bottom). [20] .....	13
Figure 2.3 M.Reeves PIV system layout .....	14
Figure 2.4 PIV velocity mapping images .....	15
Figure 2.5 PLIF system layout [27] .....	16
Figure 2.6 A Finer Scale PIV Images of Turbulent Combustion [27] .....	17
Figure 2.7 Temperature measurement using phosphorescence in IC engine [28].....	22
Figure 2.8 Temperature displayed in 1D and 2D in IC engine [28] .....	23
Figure 2.9 Flame 3D Visualization Using Tomographic Cameras System [32] ...	25
Figure 2.10 Error and Correction Coefficient Comparison by Tomographic Methodologies [32] .....	26
Figure 2.11 Flame Reconstructed Images using FBP-ART tomography algorithm. [32] (a is a reconstructed image of cooled flame. b is time resolved flame reconstructed images).....	26

Figure 2.12 Manchester POAL system [33, 34].....	27
Figure 2.13 Tomographic Reconstructed Images by Paul Wright etc. [33] .....	28
Figure 2.14 Telescope Tomography System Layout by Karlsruhe University [35] .....	29
Figure 2.15 Simulated Images of Turbulent Burner Flame [35] .....	29
Figure 2.16 A Simple Shadow Experiment Measuring Displacement of Focus Light Rays .....	31
Figure 2.17 Shock Wave Visualization with High Speed Camera by Shadowgraphy [36] .....	31
Figure 2.18 Schlieren Photography Method System.....	33
Figure 2.19 Comparisons of Disturbance between Shadowgraphy and Schlieren Photography [36].....	33
Figure 2.20 A Michelson Interferometer System [38].....	34
Figure 2.21 Mach-Zehnder Sample [40] .....	36
Figure 2.22 High-Speed Interferograms Recorded by Differential Interferometry- Mach 0.4 [41] .....	36
Figure 2.23 Formation of a Hologram .....	37
Figure 2.24 A Transmission Holography System [41] .....	38
Figure 2.25 A Reflection Holography System [41].....	38
Figure 3.1 Set Up Process of The POET System .....	43
Figure 3.2 The Structure Diagram of a Reciprocating Engine.....	48
Figure 3.3 The Operation of a Four Stroke Reciprocating Engine .....	50

Figure 3.4 Crank Angles of Operation Engine versus Pressure .....	50
Figure 3.5 Diagram of Half Section of OHV Operation .....	55
Figure 3.6 Diagram of Valves Control System of OHV Engine .....	56
Figure 3.7 The OHV Pro Engine.....	57
Figure 3.8 Schematic of OAG Assembling with Chamber and Cylinder head.....	58
Figure 3.9 The Basic Schematic Diagram of OAG.....	60
Figure 3.10 Diagram of OAG Cover Plate.....	61
Figure 3.11 Schematic Diagram of Array Plate Interface .....	62
Figure 3.12 Acceptant Angle between Array and Cover Plates. ....	63
Figure 3.13 Optical Array Gasket Testing Diagram.....	65
Figure 3.14 The Modified Engine Test Cell in Laboratory .....	66
Figure 3.15 The Gas Intake System Modification .....	67
Figure 3.16 Reformed Carburetor Control System .....	68
Figure 3.17 The Ignition Coil Position Replacement.....	69
Figure 3.18 The Interface Function Gasket.....	70
Figure 3.19 The Sandwich Components including Cylinder head, Gaskets and Chamber. ....	71
Figure 3.20 Comparison of the Layout of the Original and Modified Engine.....	72
Figure 3.21 The Modified Engine Assembly .....	73
Figure 3.22 Typical Blue Flame Spectrum [49] .....	75
Figure 3.23 Blue, UV Filter, PMT and Fibre loss Specification Diagram (Appendix D) .....	77

Figure 3.24 Single-Shot PLIF Images of Flame: (a) CH and (b) OH [55] .....	78
Figure 3.25 Diagram of Fibre and Probe Structure .....	79
Figure 3.26 Signal Transmission Loss in Probe and Fibre.....	80
Figure 3.27 The Aperture of Optical Fibre in Vertical and Horizontal .....	81
Figure 3.28 Black Box Interface between Fibre and PMT .....	82
Figure 3.29 The PMT Chips and the Spectral Response of PMT Module [56] ....	84
Figure 3.30 PMT Intensity Units Principle .....	85
Figure 3.31 Intelligent POET Tomography Computer System .....	87
Figure 3.32 PMTs SMA Interface Schematic Diagram.....	88
Figure 3.33 The Gain Characteristics of PMT versus Supply Voltage [57] .....	88
Figure 3.34 Software Operation Interface.....	89
Figure 3.35 PMTs Tomography Computer System Hardware Components.....	91
Figure 4.1 Tomographic Reconstruction Technique in the Euclidean Plane.....	95
Figure 4.2 Tomography Reconstruction Technique Concept Diagram .....	96
Figure 4.3 Tomography Reconstruction Technique in Mathematics .....	97
Figure 4.4 The Projection of a Cylindrical Object to a Plane .....	98
Figure 4.5 Projection of Object in a Plane. ....	98
Figure 4.6 Projections of Multi Objects in Different View Angles .....	99
Figure 4.7 The projections in 2X2 matrix math module .....	100
Figure 4.8 Backprojection Evaluation Process .....	102
Figure 4.9 Image Reconstruction Process by a Gaussian Intensity Light Source .....	103

Figure 4.10 Projection Behaviors in $\theta \sim s$ Domain.....	105
Figure 4.11 Parallel Beam Projection and Fan Beam Projection .....	106
Figure 4.12 Fan Beam Projection and Parallel Beam Scanning Area.....	112
Figure 4.13 Geometric Transform between Parallel Beam and Fan Beam.....	113
Figure 4.14 Different Algorithm Methods for Fan Beam Projection.....	114
Figure 4.15 Fan Beam Ray Point (x, y) Transformed into Polar Coordinates ....	114
Figure 4.16 Iterative Method Algorithms Concept Diagram .....	120
Figure 4.17 Schematic Approximate Solutions Found by ART Algorithms .....	122
Figure 4.18 ART Algorithms Explanation Schematic Diagram.....	123
Figure 4.19 MART Algorithm Illustration Diagram .....	126
Figure 4.20 Flow Chart of Array MART Software Processing.....	127
Figure 4.21 The Schematic of Combustion Distribution Measurement by OAG Ring .....	129
Figure 4.22 The Projection and Radiation Distribution Diagram .....	130
Figure 4.23 Projection Coverage in One Pixel.....	130
Figure 4.24 Array MART Software Initialization Algorithm of OAG Design ...	133
Figure 4.25 Continuous Visualization Transformed by Intensity Interpolation Algorithm Diagram .....	134
Figure 4.26 Visualization of Object in Colour Map.....	134
Figure 4.27 A Linear Simulated Model Tested by Software .....	135
Figure 4.28 Error Characteristics of Single Gaussian Flame Model .....	137
Figure 4.29 Error Characteristics of Two Gaussian Function Flame .....	139



Figure 4.30 Visualization of Candle Flame and Laminar Flame .....	142
Figure 5.1 POET O-Ring Gasket Layout diagram (a) and an Example of 3D view of Projections Distribution (b) .....	146
Figure 5.2 Slope of Tilt Measurement by Single Microlens .....	149
Figure 5.3 Flame Density Gradients Reconstruction Process .....	149
Figure 5.4 Flow Density Measurement Set up .....	150
Figure 5.5 Comparison between uncrossed and crossed regions of candle .....	151
Figure 5.6 Varying of Turbulences. (Image a is the displacement between two instantaneous time; Image b is the contour map of small turbulences) .....	152
Figure 5.7 The Aberration Wavefront of Candle in 3D .....	153
Figure 5.8 Deformation Wavefront of Premixed Flame in Rich Fuels (Image a is the turbulent displacement between two instantaneous flames; Image b is the wavefront of flame turbulences) .....	154
Figure 5.9 Deformation Wavefront of Gasflow Turbulence (Image a is the turbulent displacement between two instaneouse flames; Image b is the wavefront of turbulent flame) .....	154
Figure 5.10 Photogrammetric Measurement System (In the experiment the filter is a 310 nm bandpass UV lens. The frequency of CCD camera is up to 2 kHz) .....	156
Figure 5.11 Photographic Images of Combustion Propagation without Filter (Top Views of Combustion Process using a sequence of different Crank Angles images taken by non-filter high speed camera) .....	157

Figure 5.12 Contour Images of Combustion Propagation without Filter (The black curve has been recognized as flame front which is with high intensities and also is an interface between burnt gas and unburt gas) .....	158
Figure 5.13 Photographic Images of Combustion Projections by UV Filter (Top Views of Combustion Process using a sequence of different Crank Angles images taken by the UV filtered high speed camera).....	160
Figure 5.14 Sum Intensities Comparison between UV and None-filter Combustion (Note: UV intensities are higher than non filter combustion but in different set up. In the PMT, it is shown that UV intensities are less than non filter intensities at same combustion temperature.).....	161
Figure 5.15 Vortex Modeling of Combustion in the IC Engine .....	163
Figure 5.16 No. 11 to 15 and 31 to 35 Projections Radiation Diagram and Intensity Plots in 2D, 3D .....	164
Figure 5.17 21 to 25 Projections Intensity Plot in Mesh 3D .....	165
Figure 5.18 Combustion Propagation Movements Diagram in the Test Engine.	166
Figure 5.19 The Three Orders of Summarized Intensities Peak Eruption Diagram .....	166
Figure 5.20 UV flame propagation behaviors in IC engine .....	167
Figure 5.21 3D and 2D Intensity Images of UV Combustion Projections.....	169
Figure 5.22 No. 3, 17, and 34 Projections Radiations Schematic Diagram .....	171
Figure 5.23 No. 17 Projection Intensity Plot of Four Engine Cycles .....	172
Figure 5.24 Intensity Plots of No. 3, 17 and 34 Projections in One Engine Cycle	

.....	173
Figure 5.25 Comparisons of Blue flame in Time Coordinate System .....	175
Figure 5.26 Crank Angle Delays between No. 3, 17 and 34 Projections in Blue Flame.....	175
Figure 5.27 UV Flames of Four Cycles Measurement by PMT Number 17 .....	177
Figure 5.28 UV Flames in One Cycle of the Number 3, 17 and 34 Projections..... .....	178
Figure 5.29 Comparisons of UV flame in Time Coordinate System .....	179
Figure 5.30 Crank Angle Delays between No. 3, 17 and 34 Projections in UV Flame.....	179
Figure 5.31 Flame Velocity Evaluation Method Schematic Diagram.....	181
Figure 5.32 Time Delays between No. 1 to No 5 Projections.....	182
Figure 5.33 Flame Speed Display in X, Y and CA Coordinates System .....	185
Figure 5.34 The Averaged Speed of Flame Propagation In-Cylinder .....	186
Figure 5.35 No. 17 Projection Intensity Plot at Different Engine Speeds .....	187
Figure 5.36 Flame Propagation Speeds at Different Engine Revolutions.....	187
Figure 5.37 MART Schematic Diagram .....	191
Figure 5.38 Fibre Distribution Panel and System Sensitivity Diagram ( a is the conceptual arrangement of fibre channels; b is the sensitivity diagram of reconstruction system and it is evaluated by the overlapped times of cross sectional region of interest.).....	193
Figure 5.39 Combustion Visualization Schematic Diagrams (On the image a,	

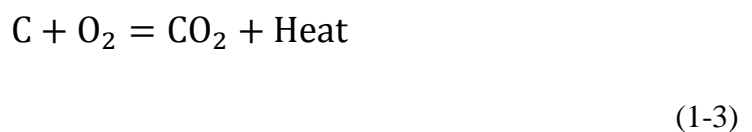
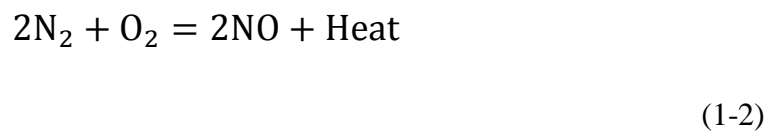
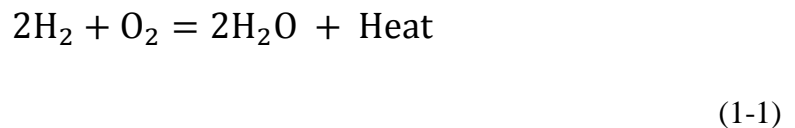
Spark Ignition locates at the central of chamber bottom. The intake valve is on the left and the exhaust valve is on the right. The chamber diameter is 68.3 mm. The b is a reconstruction image of combustion in $10 \times 10$ pixels and 1 pixel is equal to 7 mm. ....	195
Figure 5.40 Reconstructed Candle Images after One Iteration .....	196
Figure 5.41 Reconstructed Candle Images after 1000 Iterations .....	197
Figure 5.42 The Same Instant Combustion Images Visualized in Jet and Hot Colourmap Formats (Note: 1 pixel = 7 mm and the intensity unit is a.u. of all following images).....	198
Figure 5.43 The Intensity Response of PMTs of UV Flame by 1 MHz Sampling Frequency .....	199
Figure 5.44 UV Burner Flame Simulations by Karlsruhe University [32] .....	200
Figure 5.45 The Intensity Response of PMTs of Blue Flame by 1 MHz Sampling Frequency .....	210
Figure 6.1 POET System.....	223
Figure 6.2 Modified Engine Coupled with O-Ring Gasket .....	224
Figure 6.3 Flame Propagation Velocities by Crank Angles .....	226
Figure 6.4 Reconstructed Images of UV and Blue Combustion at the Same Time .....	227
Figure 6.5 A Comparison between Optimized POET UV Image and Karlsruhe University Simulation .....	228
Figure 6.6 3D Model Schematic for Combustion Simulation.....	233

Figure 6.7 O-Ring Filter OAG Plate Schematic Diagram .....	234
Figure 6.8 Parallel Beam Detection Schematic Diagram.....	235
Figure 6.9 Flame Front Study System by Employing Shack-Hartmann Camera .....	237
Figure 6.10 Tomography Schematic Diagram of Shack-Hartmann Method.....	238

# Chapter 1.

## Motivation

Combustion is a specialized and complicated research subject involving thermodynamics, chemical and mechanical kinetics disciplines. It can simply be explained as a complicated flame burning process accompanied by chemical reactions and heat transfer. During the combustion process, a series of chemical reactions occurs, for example:



Accompanying the chemical reactions, products are generated and energy is released. Products may be useful or harmful to the environment and engine. Thus, many studies of combustion are undertaken to understand characteristics of FFP (Flame Front Propagation) for improving the efficiency ratio of combustion. Because the flame is chemiluminescent, the optical diagnostic techniques are used to detect the burning process of combustion for the analysis of chemical reactions.

The objective of this thesis has been first to literature review of the current

optical methodologies and common diagnostic instrumentation used for combustion measurements. This is followed by an introduction of my PhD experimental approach and diagnostic system. The system named as, POET (Passive Optical Emission Tomography) has been presented both from an experimental and computational methodology. In the results chapter, two relevant methods of flame front measurements ‘Direct photometric and Shack Hartmann methods’ are evaluated for assisting in the understanding and evaluation of combustion wavefront and turbulence measurement approaches. Finally the results obtained using the POET system are presented and discussed.

My major PhD project is to develop the POET approach as an intelligent diagnostic technique for analyzing the turbulent characteristics of combustion. In POET project, the intensities and velocities of FFP are measured for the investigation of in-cylinder combustion in a modified commercial engine. Thus, this project aims to use the POET diagnostic approach to detect flame front propagation, analyze the property of the flame front and reconstruct the in-cylinder combustion in an IC (Internal Combustion) engine.

## **1.1 POET Approach Development**

Researchers have investigated flame front propagations for commercial and environment purposes for many years. Despite the rapid development of new technologies in the mechanical, microelectronic industry and intelligent diagnostics

optical methods, the study of combustion has been slowed by its complicated nature. The rapid flame propagation speed and the complex turbulent structure of the flame front make it difficult to either simulate or capture. This problem is compounded by the unstable characteristics of combustion. New measurement approaches have emerged in recent years, for example: intrusive, non-intrusive and tomographic system techniques. However these methods still have many limitations to understand the combustion process.

Historically measurements have been based on inserting measurement instrumentations into the flame. These techniques are significantly dependant on the specifications of the instrument. For example: flow velocity meters and pressure-tube anemometers. Since intrusive equipment often changes the nature of the process, such probes traditionally have been used to measure the bulk or average property of the flame. Alternatively they have been applied for specific point measurements.

Non-intrusive optical instruments can be used to measure the chemiluminescence phenomenon [1] without inserting instrumentation. Methods using non-intrusive techniques are more adapted in flame propagation research. Docquier and Candel [2] summarized the present popular sensors employed by non-intrusive techniques in 2002 (Table 1.1).

In this project, the UV-Vis emissions have been used to measure combustion chemiluminescence characteristics. Three typical sensors have been evaluated: CCD camera, PMT and PD. The CCD/CMOS camera sensor was subsequently abandoned



because of its limited frequency response and capability of being adapted to a tomographic set up. The photodiode sensor has been tested and evaluated in previous work by PhD student Paul Dunkley of Warwick OEL group [3]. The experimental results were only semi successful in measuring the in-cylinder combustion caused by the spark ignition noise and the electronic system noise. To overcome this problem, a new approach using PMT sensor and tomographic fibre probes has been developed in this thesis.

Table 1. 1 Optical Sensors for Combustion Investigation

Frequency	Technique	Detector	Parameter
Low	UV-Vis EM	CCD camera	OH*, CH*, C <sub>2</sub> *, CO <sub>2</sub> *, T <sup>0</sup> (soot)
		WB SPEC	
	IR EM	CCD camera	T <sup>0</sup>
High	UV-Vis EM	PMT and filter	OH*, CH*, C <sub>2</sub> *, CO <sub>2</sub> *, T <sup>0</sup> (soot)
		PD and filter	
	Vis-IR EM	PD and filter	T <sup>0</sup>
		NB SPEC	
	IR ABS	LD and PD	H <sub>2</sub> O*, CO <sub>2</sub> *, T <sup>0</sup> , ρ
EM – Emission, ABS – absorption, NB/WB SPEC – Narrow/Wide band spectrometer PMT – Photomultiplier tuber, PD – Photo diode, LD – Laser diode			

Tomography refers to cross sectional imaging of an object and reconstructing the image by gathering the projection data from multiple angles. Tomography diagnostic techniques have been successfully applied in many disciplines because of their accurate image reconstruction in several applications, for example, radiology, biology, geophysics and astrophysics. Generally, tomography diagnostics refer to iterative or FBP (Filter Back Projection) mathematical approaches of image reconstruction. The projection data is captured from a number of views; then the data is processed mathematically by iterative or FBP algorithms to complete a reconstruction image of the original objective. Hence, the region of an object of interest is recreated from image slices. Consequently, tomography as a modern diagnostic technique is frequently used for object visualization, especially in clinics, for example, Computerized Tomography (CT) [4]. In combustion research, tomography techniques have been applied in theoretical simulations and experiments [5-6]. In the POET system, the fibres are placed surrounding the cylinder chamber by a special O-Ring design gasket for collecting flame emission projections.

The POET approach is a passive emission diagnostic method combining non-intrusive and tomographic techniques to investigate the combustion process within engines (Fig 1.1). In the experiment, 40 Photo Multiplier Tubes (PMTs) are employed to set up a detecting system for recording combustion chemiluminescence which has fast response (20 kHz) and a gain of ( $1 \times 10^5$ ). An overhead Briggs and Stratton IC engine has been modified to couple with the detecting system. A computer system

including ArrayMART software and Data Acquisition card (DAQ) hardware is used to record tomographic FFP projections and reconstruct the combustion process using MART methods. The measurements of in-cylinder combustion suffer a series of requirements: temperature (1200°C), pressure (50 bar in practice), turbulence (up to 4 kHz).

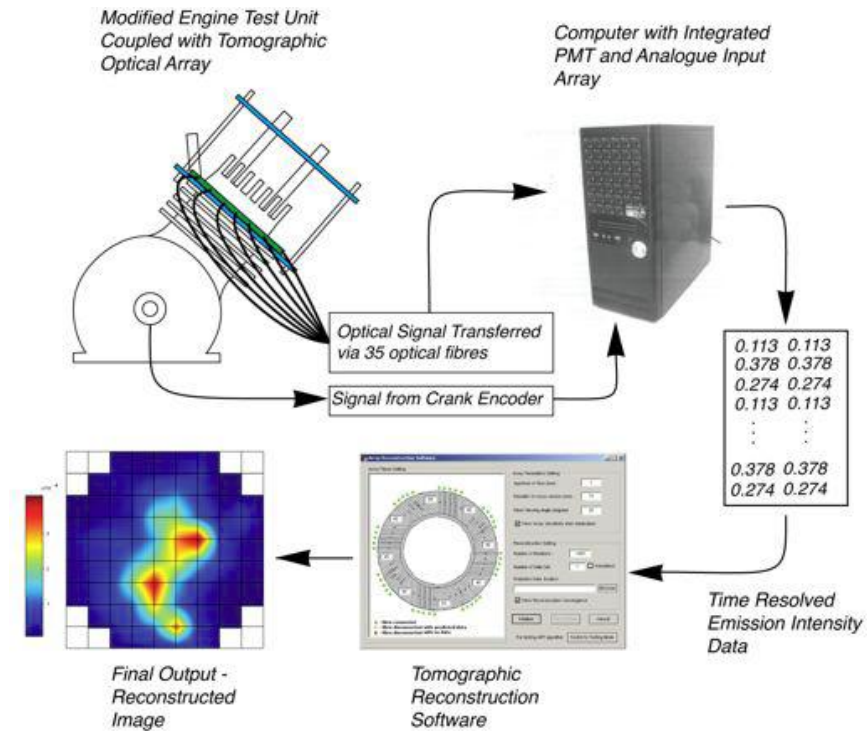


Figure 1. 1 Passive Optical Emission Tomography (POET) Layout Diagram (The POET system consists of a modified IC engine, a compact PMTs PC and an Array MART software)

## 1.2 Thesis Structure

In the dissertation, 6 chapters are written to review recent optical diagnostic approaches, describe the modified engine and POET system, explain the POET computational methodologies and discuss the POET measurement results.

- 1 Chapter 1 explains the motivations of this project. In this chapter, the development of POET approach has been explained. The content structure of dissertation has been listed. Moreover, the POET system layout diagram has been illustrated.
- 2 Chapter 2 reviews the combustion measurement techniques. In this chapter, LIF (Laser Induced Fluorescence), PIV (Particle Image Velocimetry), LDV (Laser Doppler Velocimetry) and TP (Thermographic Phosphors) techniques are discussed. Then the present tomography experiments are surveyed. Moreover, other relevant techniques are reviewed.
- 3 Chapter 3 demonstrates the POET system of this project. This chapter specifies the engine modifications according to the requirements of measurement system. The PMTs PC suit has been illustrated.
- 4 Chapter 4 discusses the methodologies of POET system design and tomographic reconstruction of combustion. In this chapter, the computational tomography system model has been designed using Radon transform theory. The method of combustion process reconstruction has been specified by Multiplicative Algebraic Reconstruction Technique (MART) algorithm. In following, several simulated models have been reconstructed to verify the performance of MART.
- 5 Chapter 5 analyzes experimental results. The flame front propagation velocities are evaluated using projections data from PMTs. The combustion process has been reconstructed by MART technique. In comparison, UV and Blue flames images are demonstrated by different engine revolutions.

- 6 Chapter 6 summarizes the contributions of this project. In this chapter, the conclusion is present. The recommendations of further works have been proposed.
- 7 Appendix A reviews the nature of laminar flame, turbulence flame and detonation flame by theory. Furthermore, the Fourier transform which is relative to Radon transform has been explained.
- 8 Appendix B demonstrates the Shack-Hartmann system set ups and experimental results. The specifications of the Shack-Hartmann camera and the computational method for wavefront reconstruction are displayed.
- 9 Appendix C gives the details of test engine specifications, POET PC module introduction and software operation manual.
- 10 Appendix D explains filters and photomultiplier specifications.
- 11 Appendix E demonstrates UV and Blue reconstructed combustion images by sampling at 2.5 degree Crank Angles.

# Chapter 2.

## Literature Review

Combustion has been recognized as a major energy release mechanism since its application to both industry and daily human life. Despite the rapid development of new energy systems to replace the combustion system, for example electric vehicles; combustion will still play an important role in the future. With increasing energy utilization and decreasing availability of crude oil, improvements to the combustion process become increasingly important. The challenge now is to increase the efficiency of the combustion explosion and study the combustion performance of new fuels like biomass and other renewable fuels. The combustion process produces large amounts of pollutants such as incompletely burnt hydrocarbons and nitrogen oxides that are hazardous to the environment. For these reasons new combustion diagnostic techniques have been developed in recent decades. Firstly, four popular techniques have been firstly reviewed: LIF (Laser Induced Fluorescence), PIV (Particle Image Velocimetry), LDV (Laser Doppler Velocimetry) and TP (Thermographic Phosphors). Secondly, three tomographic experiments are discussed and compared. Apart from comparison, other methods for flame measurement are illustrated.

## 2.1 Reviews of In-Cylinder Combustion Measurement Techniques

In the historic flame study, most experiments are based on a Burner flame or flame simulation model because the conventional techniques are difficult to measure the combustion in IC engines can prove difficult. With the rapid development of new techniques, more and more experiments have been taken to study the combustion characteristics within engines in last few years. The popular methods are LIF (Laser Induced Fluorescence), PIV (Particle Image Velocimetry), LDV (Laser Doppler Velocimetry) and TP (Thermographic Phosphors). Soid and Zainal have summarized these optical techniques in 2011 [7].

Table 2.1 The Comparisons between LIF, PIV, TP and LDV techniques

Technique	Application and parameters	Disadvantages and limitations
LIF	Fuel concentration Liquid and vapor fuel	Quenching at high pressures and difficult to calibrate
PIV	Fuel sprays flow Instantaneous whole field velocities	Difficult to implement on dense sprays
LDV	Accuracy, great temporal and spatial resolution	Detection arear dependent on cross section region
TP	Precise temperature and density measurement	Difficult to calibrate.

## 2.1.1 Laser Induced Fluorescence

LIF has commonly been used in research of flame concentrations since the fluorescence has great sensitivity to turbulence and has very low background noise [8-11]. In the basic instrumentation, a dye laser was used. The laser beam frequency is typically doubled or tripled in order to excite the relevant combustion chemical species of interest. Then the beam is crossing combustion to excite the OH or CH fluorescence. LIF offers accurate visualizations to measure the flame turbulences density and it has been popularly applied to study chemical reactions. One of the limitations is that the experiment results rely on the system performance. The measured result is fluorescent intensity, and this is difficult to calibrate and convert to emission intensity.

Aleiferis and Rosati have used the LIF technique to image the OH chemiluminescence images in a hydrogen-fuelled SI engine in 2011 [12]. In the experiment, a Nd:YAG pump laser was used to generate 532 nm wavelength light. Then the light beam is directed into a dye laser that emits a 566 nm wavelength beam. Through a frequency doubler, the wavelength of output light became 283 nm which is adaptive to excite the OH fluorescence. The camera for OH LIF measurement is an Intensified Charge Couple Device (ICCD) with a UV lens to collect light emissions (Fig 2.1).

The engine of this practice was special designed for the experimental purpose. A hollow 'Bowditch' piston allowed for a 45 degree stationary mirror to be fitted inside the block to gain optical access to the combustion chamber through a quartz



piston crown. The engine was also modified with a pent roof window and side full stroke window for optical access through the liner.

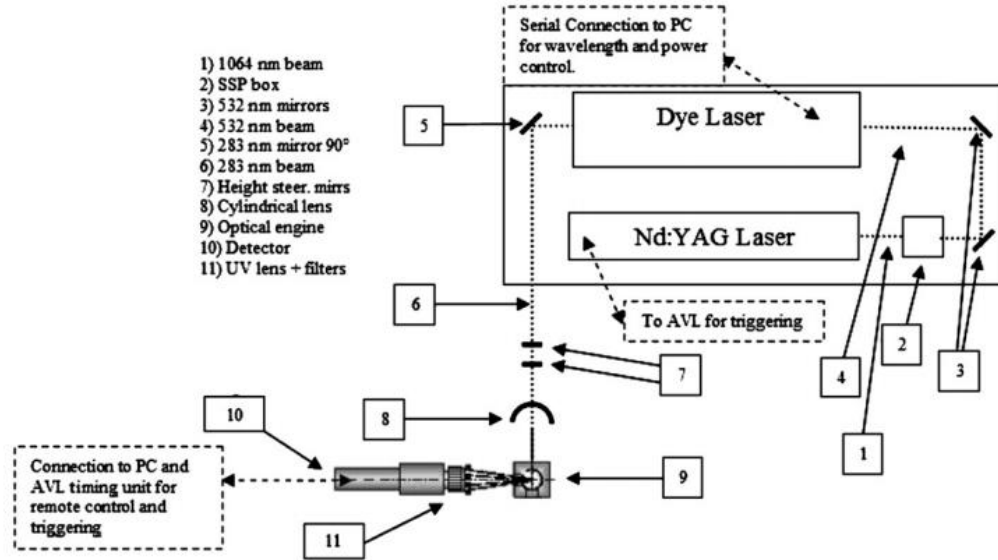


Figure 2. 1 The Implementation of OH Trace System by LIF Technique (Nd:YAG laser: 532 nm, Dye Laser: 566 nm and output beam: 283 nm in wavelength) [12]

In the results, characteristics of OH have been illustrated using several images (Fig 2.2). The instant OH LIF presents a good image of OH density. The paper has found although flames have symmetric expansion in the typical cycles, some cycles exhibit distorted shapes on a macro-scale along with presence of small-scale wrinkling. The hydrogen flame speed for DI (Direct Injection) engine is up to 35 m/s in the equivalent ratio  $\phi = 0.67 - 0.83$  and in the range 25-30 m/s for the ratio  $\phi = 0.50 - 0.59$ .

According to the review of LIF, it has clearly been shown that LIF can visualize the flame density structure in accuracy. However, several limitations exist. The system needs a special design of engine for introducing the laser beam

and for the capture of the photogrammetric images. This designed optical engine has some control and fuel injection difficulties which restrict measurement results. Further the low light level image intensified CCD camera performance limits the capture frequency of the data.

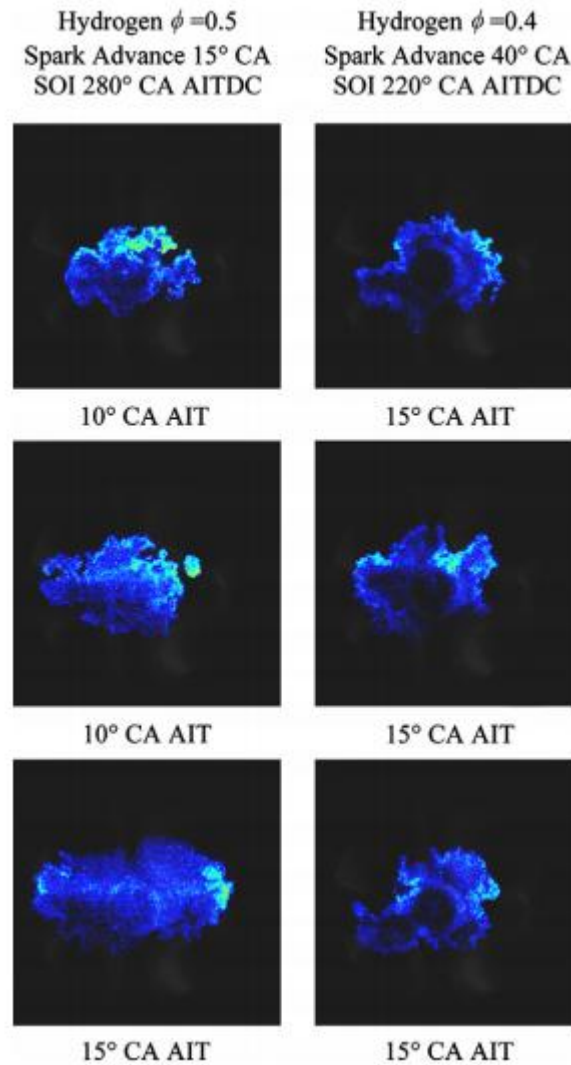


Figure 2. 2 OH LIF images of Direct Injection Engine Combustion) (SOI 220° & 280° CA AITDC, Spark Advance 15° CA & 40°, Intake Valves at the Top, Exhaust Valves at the Bottom). [12]

## 2.1.2 Particle Image Velocimetry

In the PIV experiment, particles are seeded into fuel and sprayed into flame. Because these particles are following the flow dynamics in both direction and speed, the image of flow dynamics can be mapped using motions of particles. Using a large volume of particles, the turbulent velocities are visualized in finer scale images. The disadvantage is the particles have to be added into fuels and it has some effects on the engine performance. Moreover, if the spray fuel is dense, it is difficult to apply [13-17].

Reeves et.al [18] set up a PIV system to measure the combustion within SI engine cylinders in 1998. In their experiment, a Kodak 4540 digital camera was employed to record frame propagations images. The camera frame frequency was up to 1.3 kHz with a  $128 \times 128$  pixel map. An Oxford Lasers LS20 Copper Vapour Laser and sheeting optics were applied to assist capturing combustion images.

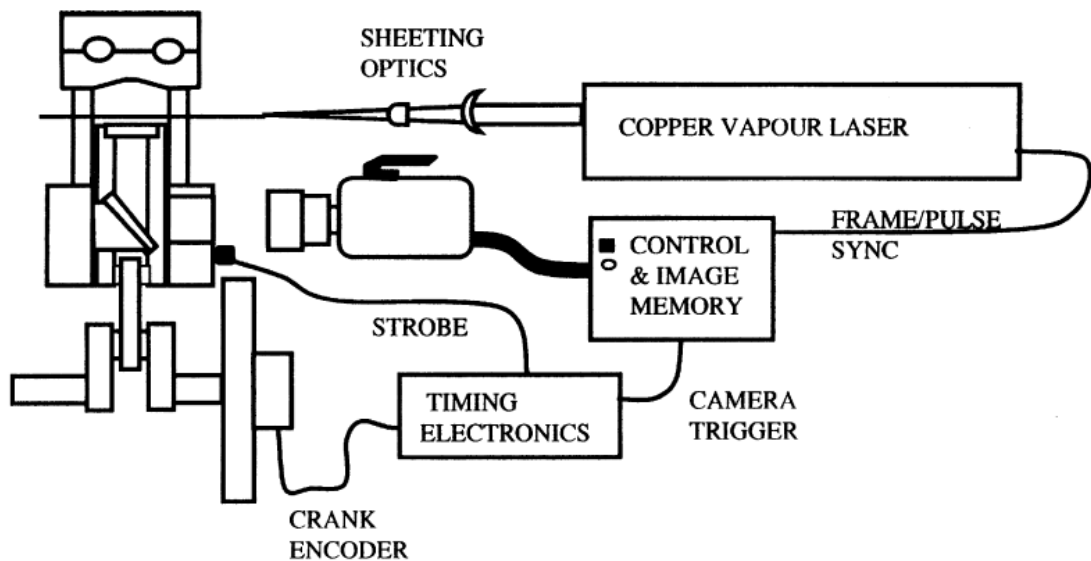


Figure 2. 3 The Layout Diagram of Reeves' PIV system [18]

The test engine is a single cylinder four stroke engine with optical access. The optical engine is modified with a piston crown, fused silica cylinder and side window for camera taking images (Fig 2.3).

In the result, the visualization images spatial revolutions are limited to  $16 \times 16$  speed vectors for improving the accuracy. The sequences of images are reformed using FFT based cross-correlations technique. The result images present a finer mapping of velocity vector of combustion process (Fig. 2.4). Volumes of images within one engine cycle are up to  $1^\circ$  CA angles per frame.

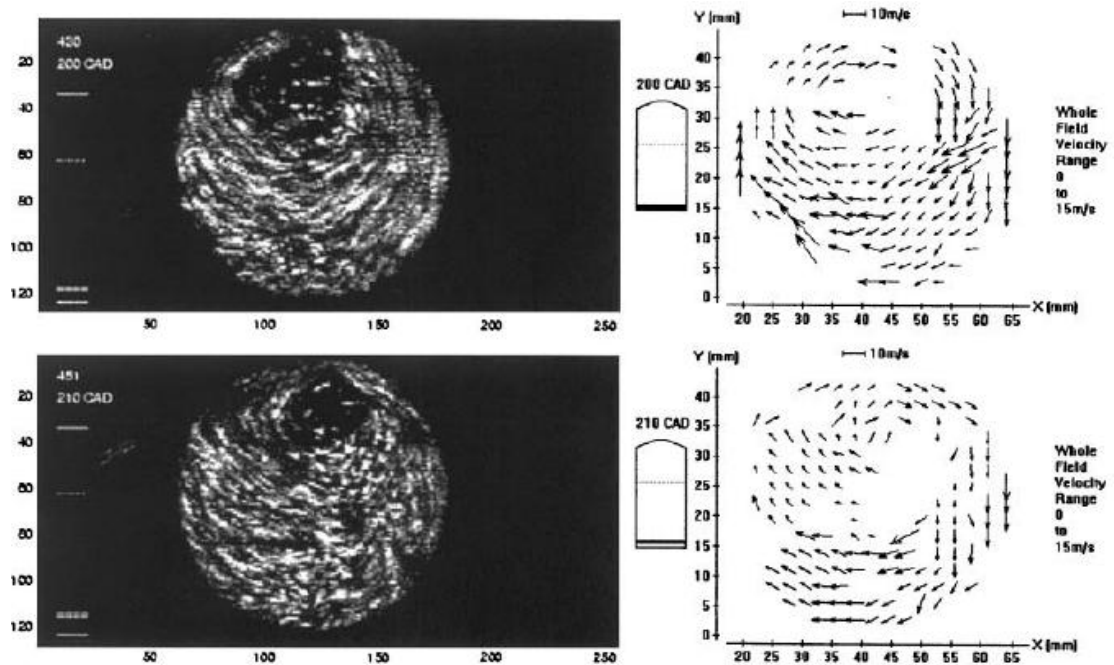


Figure 2. 4 The PIV velocity mapping images of Reeves' Experiment (200° CAD images at the top and 210° CAD images at the bottom) [18]

Peterson et.al [19] built a system using PIV and PLIF techniques to measure flame propagations in a spray spark ignition direct-injection optical engine. They use a doubled frequency Nd:YLF 527 nm laser for PIV and a frequency tripled Nd:YAG

laser at 355 nm for fluorescence measurements. A CMOS camera was employed to map velocity vectors (Fig 2.5).

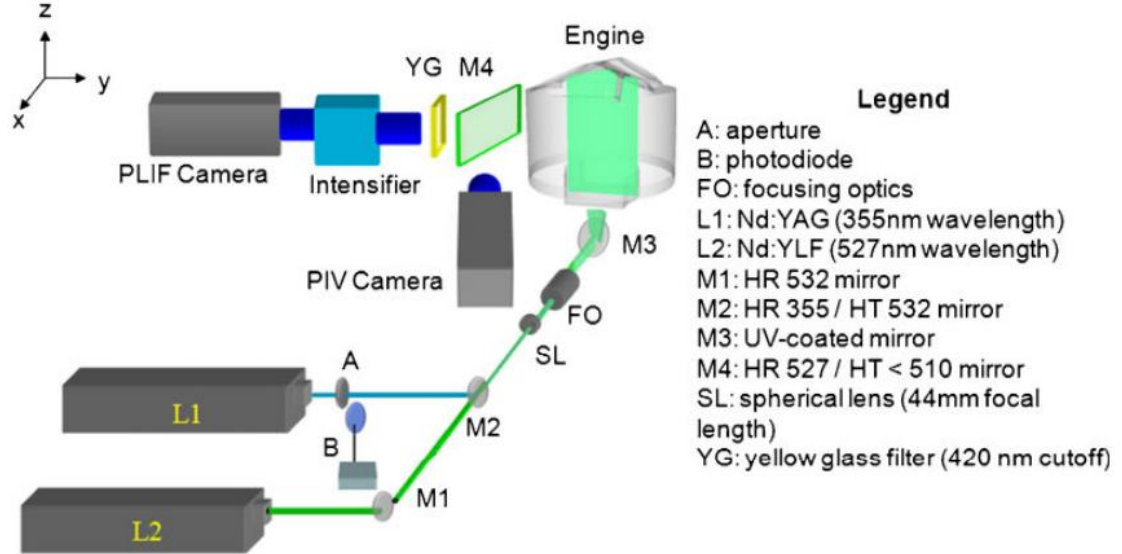


Figure 2. 5 The PLIF System layout of Peterson's Implementation [19]

In their results (Fig. 2.6), the finer scale mappings of velocity vectors are visualized by well-burned, misfire and partial burn. In their conclusion, the combustion produced rare and random partial burns and misfires in an engine operated under idle condition with one degree of spark delay off optimum. Only 9 misfires and five partial burns occurred within 1392 cycles. Moreover, velocities of PIV and PLIF images are very similar surrounding the spark plug no matter the combustion is misfired, partial burned or well burned.

After reviews, PIV techniques offer a finer scale mapping of flame front propagation velocity vectors. However, its experiment setup is complex as LIF system. It needs an optical engine design for implementation. The time resolved combustion process is difficult to visualize for the limitation of camera specifications.

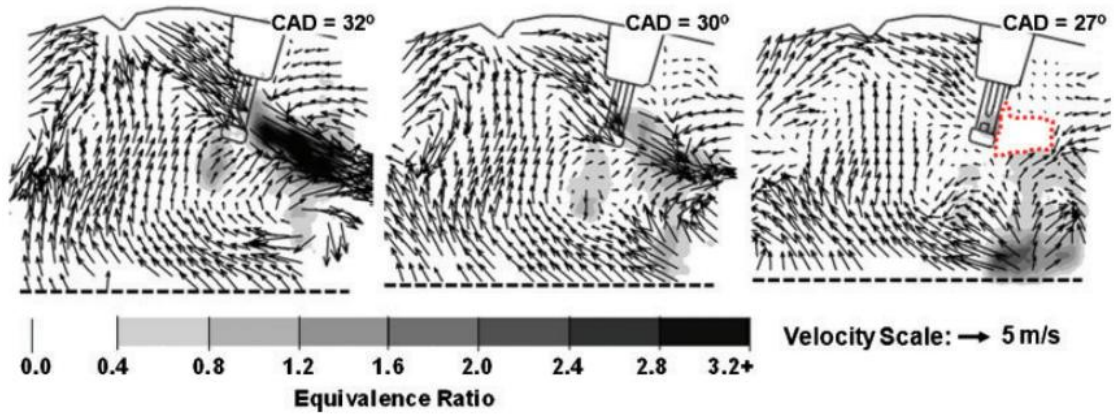


Figure 2. 6 Finer Scale PIV Images of Turbulent Combustion (32°, 30° and 27° CAD, Velocity Scale is 5 m/s) [19]

### 2.1.3 Laser Doppler Velocimetry

Doppler Velocimetry is another popular approach for the measurement of flow velocity. Typically in the LDV experiment, two coherent laser beams are intersected by each other and generate a set of fringes by interference. The induced particles flow through the fringes area. Then the particles are reflecting and scattering laser light which results in light intensity varying. This phenomenon is able to capture by photodetectors (Cameras or Photodiodes). Thus, the frequency of intensity fluctuations can be recorded which is equivalent to the Doppler shift between incident and scattered light. Therefore, the particles flow velocity can be determined by Doppler shifts by frequencies. In velocity measurements, PIV and LDV results generally agree with each other for the mean velocity. The LDV, however, has advantages in both spatial and temporal resolutions for quantitative researches [20-21]. Nevertheless, the detection area of LDV commonly is limited by laser intersection area. Furthermore, during

experimental, the LDV requires higher quality set ups to ensure obtain accuracy results. So in the large scale volume measurement, the PIV is more popular than LDV for the mean velocity measurements [22].

The Charrett and Tatam have invented a novel two frequency PDV system for the measurements of flow velocity [23]. The conventional PDV techniques require a three laser-cameras system for three dimensions velocity measurements. In this system, they designed an imaging fibre bundles to receive signals from multiple views to simplify the laser-cameras system (Fig. 2.7). In the fibre bundles system, a coherent array of fibres is spilt into four channels for detecting laser sheeting from four directions. A single CCD camera and temperature stabilized iodine cell is used to receive signals which are transformed by fibre bundles.

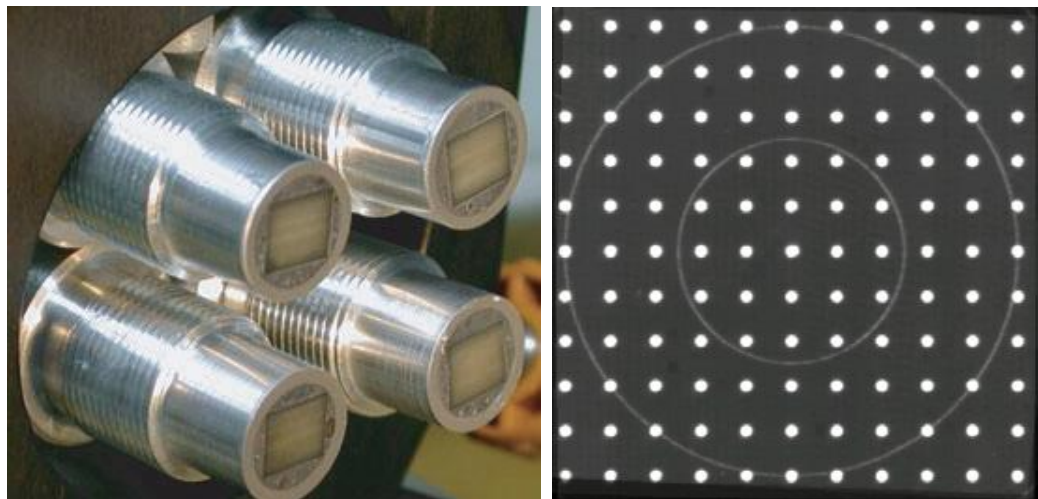


Figure 2. 7 The Image of Fibre Bundles System of Charrett and Tatam' s Experiment (Each channel is 4 meter long and has  $600 \times 500$  fibres that are  $8 \mu m$  in diameter. The image at the right is an example of the 'de-warped' view in field of  $100 \text{ mm} \times 100 \text{ mm}$  and the white dots are  $2.5 \text{ mm}$  in diameter) [23]

In practice, the system was applied in measurements of an axis-symmetric air jet. A smoke generator produced 0.2-0.3  $\mu\text{m}$  diameters particles which had been seeded by a 20 mm diameter smooth contraction nozzle. In the 3D results, dual frequencies PDV in-plane velocities were measured and mapped at 60, 80, 100 and 120 mm distances from the jet nozzle exit. (Fig. 2.8).

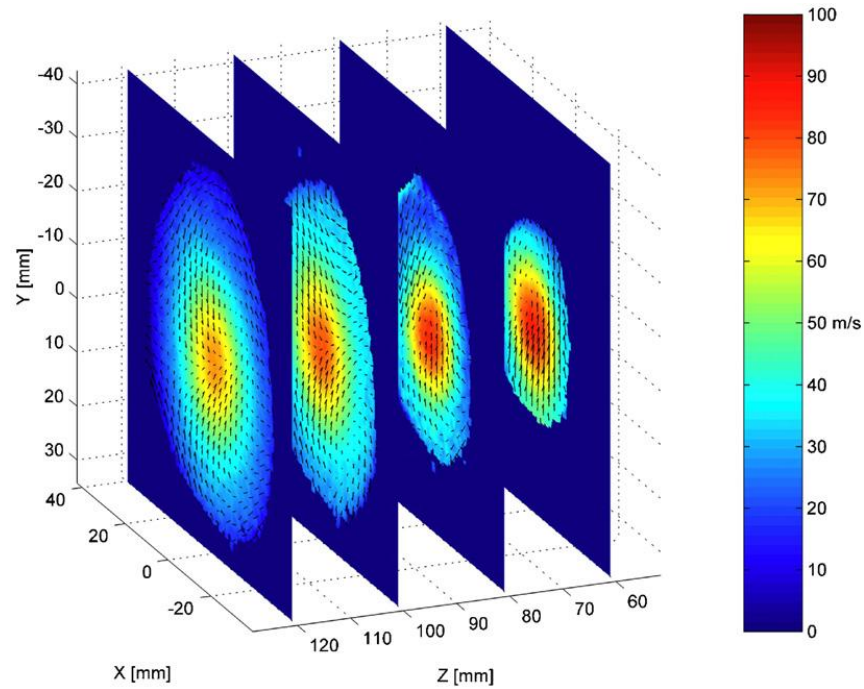
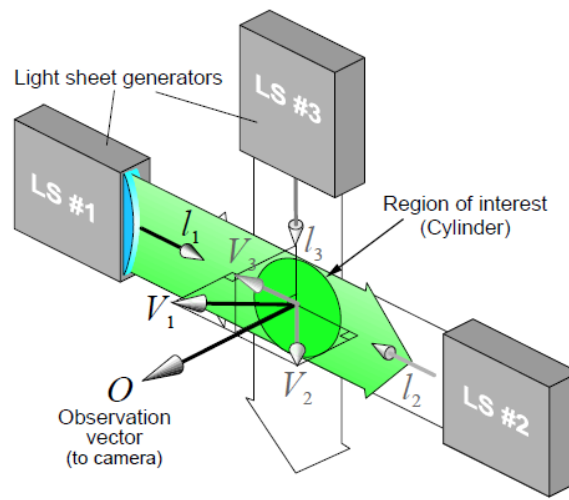


Figure 2. 8 3D 2ν-PDV Volumetric Velocity Map of a Air Seeded Jet. (Cross sections are measured at 60, 80, 100, 120 distances from the jet nozzle exit) [23]

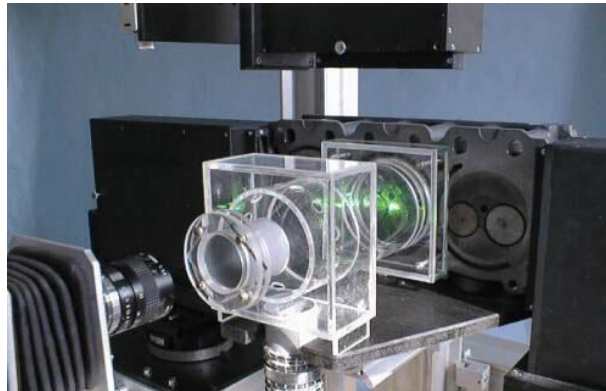
For the engine flow velocity measurement, Willert has developed a Plane Doppler Velocimetry (PDV) system for combustion flow investigation within piston engine cylinders [24]. They employ three continuous-wave laser (Argon-ion laser) instead of classic pulsed laser to generate intersected beams within a designed optical engine. Then they use one camera to record the Doppler shifts for the measurement of time-averaged velocity maps (Fig. 2.9). This system has several advantages compared



with traditional LDV method. The continuous-wave laser system is more stabilized than pulsed laser system. Only a single camera system are required to record PDV data and normally the pulsed PDV needs three cameras for observing the light sheet from different directions. Furthermore, the system is more adaptive for the in-cylinder combustion flow measurements.



( a )



( b )

Figure 2. 9 Laser Sheet Arrangement (a) for in-cylinder flow measurements and the camera and optical engine system (b). [24]

In a sample result, they proved the cylinder (40 mm Diameters) can be imaged at approximately 250 pixel diameter in spatial resolution. The speed resolution is better

than 0.5 m/s. The maximum velocity is up to 60 m/s can be measured near the inlet valves (Fig. 2.10). 8 to 11 measurement planes per volume data set (5 min per volume date set) can be recorded.

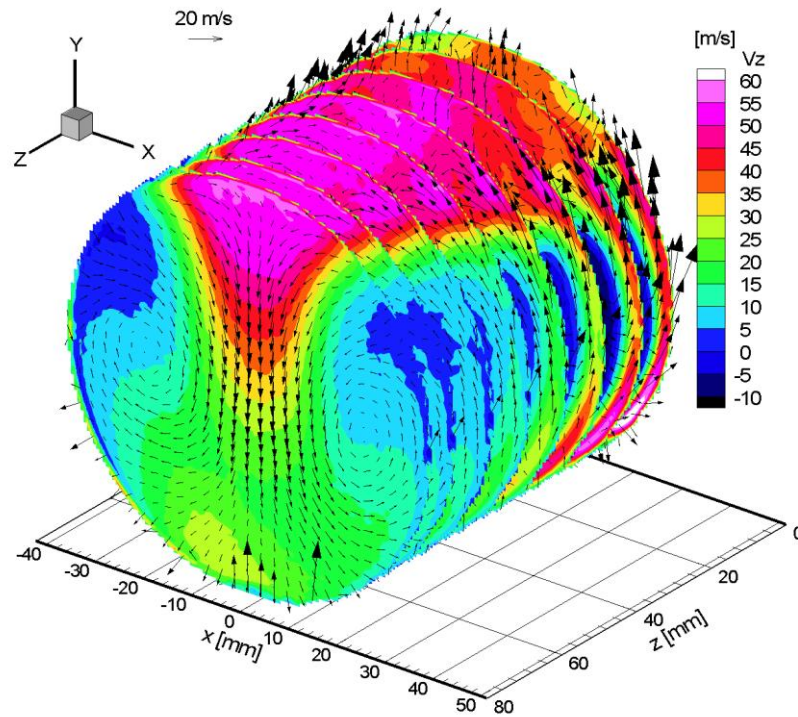


Figure 2. 10 Volumetric Velocity Map of Stead-Cylinder Charge Flow Consisting of 8 Separate Measurement Planes [24]

The LDV demonstrates excellent performance of flow velocity vector mapping. Compared to PIV, LDV has advantages in temporal and spatial resolution. Two previous LDV reviews have simplified the implemental system using novel methods. However, this simplified system still needs laser-camera system so it is still difficult to apply in reality to obtain engine measurements. Nevertheless, in Charrett and Tatam experiment, fibre bundles are very interesting development and it could be employed for in-cylinder combustion research in further study.

## 2.1.4 Thermographic Phosphors

Combustion temperature is most frequently studied in respect of energy transition using diagnostic techniques. Many methods have been developed to research the flame temperature. In recent research, an element tracing measurement technique based on emission methods using thermographic phosphors (TP) has been used to measure the temperature of combustion phenomena.

The development of phosphorescence methods enabled TP to be investigated to measure temperature in an IC engine. Figure 2.11 illustrates a thermometry method using TP method to investigate the temperature performance of a gasoline engine (Volvo 4-value cylinder head). Omrane et.al [25] set up a system to measure the combustion temperature of an AVL 528 engine using TP. The system provided a horizontal view through a quartz window and a vertical view through a modified piston. The detection region of the cylinder was coated in the TP element. Phosphor particles  $\text{Mg}_4\text{FGeO}_4:\text{Mn}$  were excited by a 266 nm Nd:YAG laser and emissions were guided to sensors.

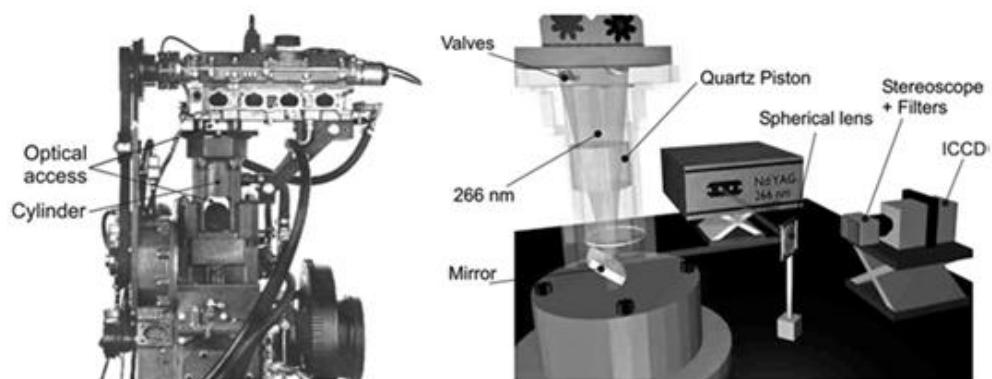


Figure 2. 11 Temperature measurement using phosphorescence in IC engine [25]

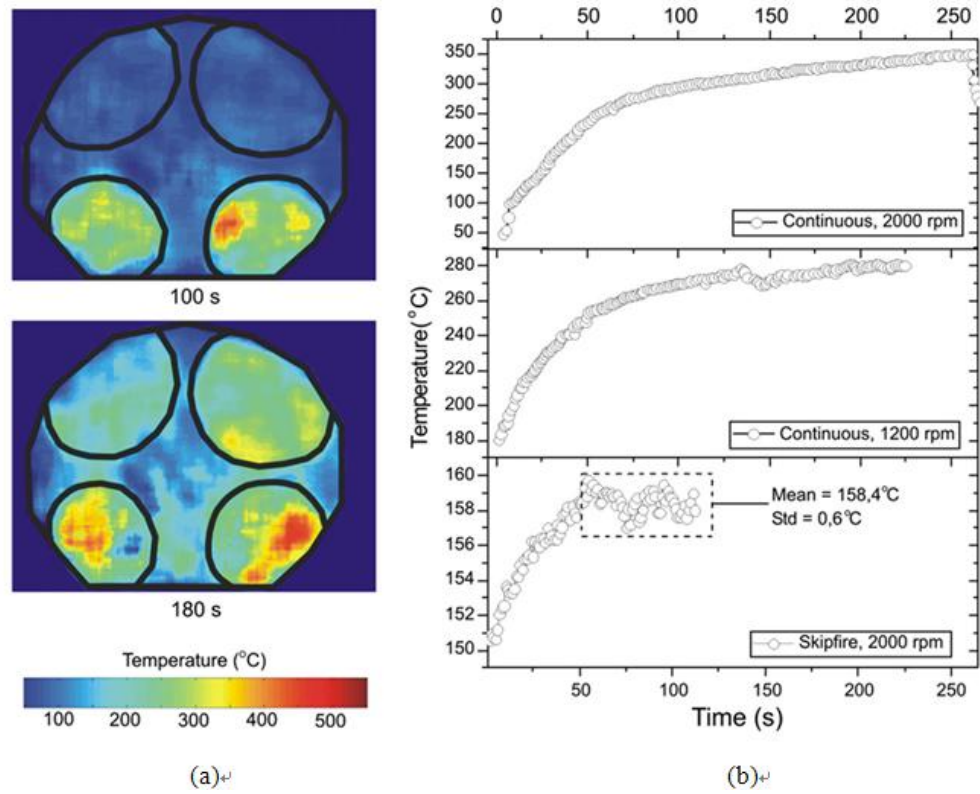


Figure 2. 12 Temperature displayed in 1D and 2D in IC engine [25]

Figure 2.12 (a) displays the temperature investigation for 1D and 2D formations. The Figure 2.12 (b) shows results of experiment which was taken under two conditions: continuous and skipfire combustion was measured every 5 cycles. The experiment showed that under continuous conditions at 2000 rpm the temperature increased to a maximum of 350 °C; at 1200 rpm the temperature maximum was 280 °C. Under skipfire conditions at 2000 rpm, some turbulence was observed and a mean peak temperature of 158.4°C was obtained. In the experiment, an Intensified Charge-Couple Device (ICCD) Camera with a stereoscopic filter was used to capture temperatures in two different spectrums: 631 nm and 657 nm. In Figure 2.12 a), a 2D image shows the temperature distribution of reactants in the exhaust and intake valves.

The top picture shows an exhaust valve step; in this step, the engine chamber is about to go through the exhaust cycle because of lean fuel the temperature decreases as the exhaust gas exits. The bottom picture shows the temperature during the intake valve. Because of the high pressure and sufficient fuel, the combustion spreads quickly and the explosion occurs throughout the chamber.

The Omrane experiment performed an adaptive measurement of flame temperature. However, some limitations exist. The frequency of ICCD camera affects its performance to capture the variations of combustion turbulences within one complete engine cycle. In the POET analysis, the frequency of turbulences varying is over 4000 Hz. Most camera response frequency is lower than 4000 Hz. Moreover, the engine system has to be modified lots to match the requirements of experimental system. The POET approach has overcome these limitations. Nevertheless, the results have not been evaluated in terms of temperature. In further works, it suggests to calibrate the intensity and temperature relationships for heat releasing measurements.

## **2.2 Reviews of Tomography Techniques**

Tomography techniques are comprehensively employed in medical diagnostics [26-28]. With the development of combustion diagnostic techniques, several approaches have been developed to investigate in-cylinder combustion. There are several difficulties in creating a tomographic diagnostic for in cylinder combustion measurement. Firstly, the cost in providing a multi-sensor system with sufficient

sensitivity for meeting the frequency and intensity measurement of the flame front is high. Secondly, great care is required in coupling the system to a modified IC engine without altering the performance of engine. Finally, the combustion process is inevitably turbulent and random. It demands a suitable data processing methodology for reconstructions. Currently, many present experiments are based on a combination of simulation and experimental data. Several tomography combustion investigation techniques are reviewed as follows.

Gilabert and et.al have set up an experiment to reconstruct the gaseous flame [29]. The system employed three RGB CCD cameras surrounding the flame at  $30^\circ$  angles to capture the flame projections (Fig. 2.13). Then they use the Logical Filter Back Projection (LFBP) and ART technique to reconstruct the flame based on inverse Radon transform algorithms.

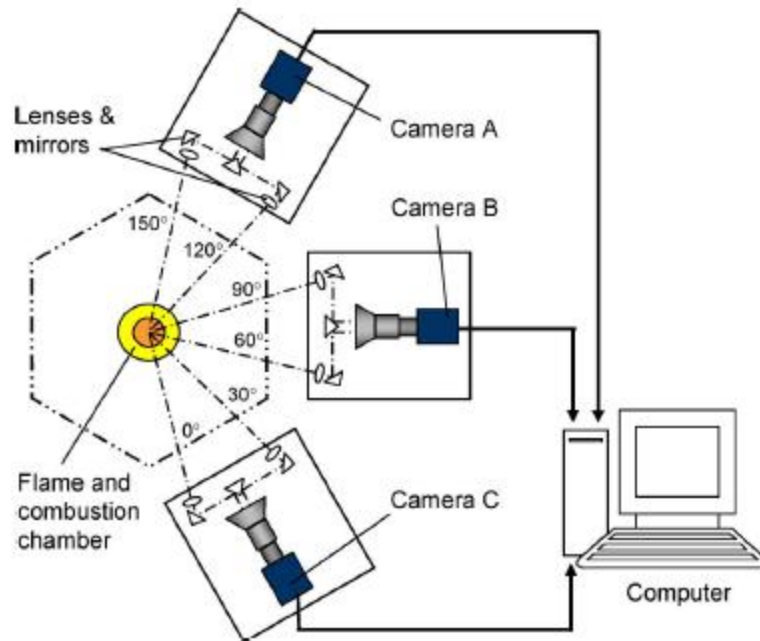
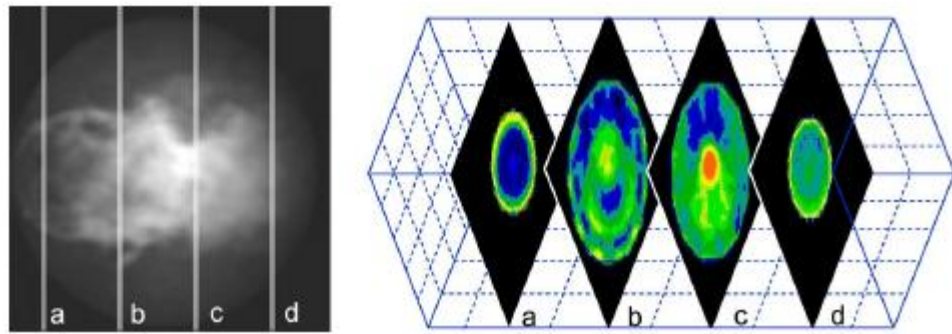


Figure 2. 13 Flame 3D Visualization Using Tomographic Cameras System [29]

To prepare reconstructions of flame, they evaluated several tomography reconstruction methodologies (Table 2.2). After the simulation and evaluation, they suggest the LFBP-ART methodology gives the smallest mean absolute error and highest correlation coefficient in square, cross and head phantom simulations.

Table 2.2 Error and Correction Coefficient Comparison by Tomographic Methodologies [29]

Template	FBP		LFBP		ART		LFBP-ART	
	Error	CC	Error	CC	Error	CC	Error	CC
Square	0.38	0.75	0.09	0.99	0.19	0.93	0.02	0.99
Cross	0.56	0.74	0.30	0.93	0.29	0.94	0.11	0.99
Head phantom	0.53	0.76	0.35	0.90	0.28	0.94	0.15	0.98



( a )

( b )

Figure 2. 14 Flame Reconstructed Images using FBP-ART tomography algorithm. [29] (a is a reconstructed image of cooled flame. b is time resolved flame reconstructed images)

In the results, they reconstruct the Burner flame using LFBP – ART technique (Fig. 2.14). The reconstructed images demonstrate good visualizations of turbulent

flame. In their conclusion, they demonstrate that with a limited number of projections (up to six), the LFBP- ART gives a good solution to reduce the mean absolute error and gives a highest correlation coefficient. Nevertheless, this system has not been applied to investigate the in-cylinder combustion. Since the in-cylinder combustion is much more turbulent and swirl, it is difficult to obtain a good correlation coefficient using FBP technique. In the POET system, a MART methodology is employed for finding the best coefficient to match the initial combustion model.

Wright and et.al developed an absorption tomography system to reconstruct the combustion of a production engine in 2005 [30, 31]. This system uses two diode lasers to generate a laser beam. The two beams are subdivided into 32 channels by optical fibre splitter. Thus 32 sub laser beams cross the combustion. Then the sub beams are received by 32 photodiodes after crossing the combustion (Fig 2.15).

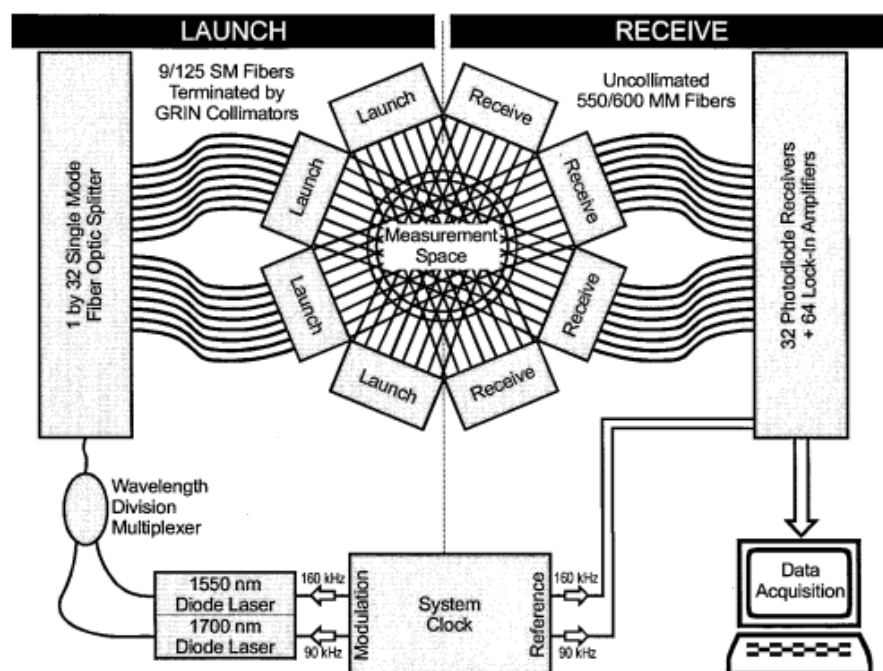


Figure 2. 15 Manchester University OPAL (Optical Access Layer) System [30, 31]



This approach uses an absorption technique to obtain the Near IR chemiluminescence. They expected 5% absorption of targets to be detected at 1700 nm. The results however reconstructed the combustion process at 1700 nm [Fig. 2.16]. There are two apparent limitations: The tracing elements are limited by the characteristics of limited absorption spectrum of combustion. The SNR ratio significantly affects the results since the experiment using a laser generator and photodiode receiver. This also has been proved by Paul Dunkley of Warwick OEL in 2002 [3].

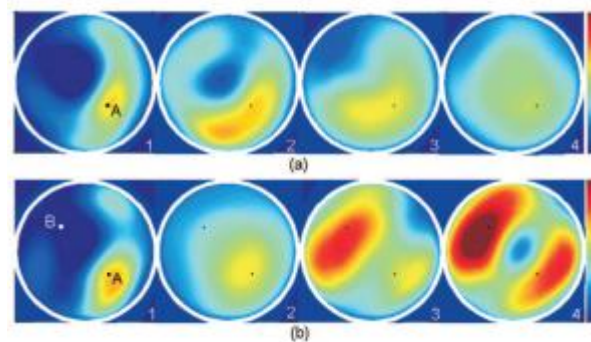


Figure 2. 16 Tomographic Reconstructed Images by OPAL [30]

Karlsruhe University attempted to build up a tomographic system to reconstruct the flame [32]. In their experiment, Ten Kepler-telescopes are equally surrounding the flame in a semi-circle. A total of 90 fibres have been employed to transmit the flame emission placed in groups of 10 at intervals of  $18^\circ$  (Fig. 2.17). Two anti-reflection lenses are used to optimize the fibre probe detection apertures. An ICCD camera is coupled with the fibres to capture the flame projections. In the reconstruction, they use a Radon-transform technique to simulate a Burner flame (Fig. 2.18). The images

illustrate ideal images of diffusion flame burning.

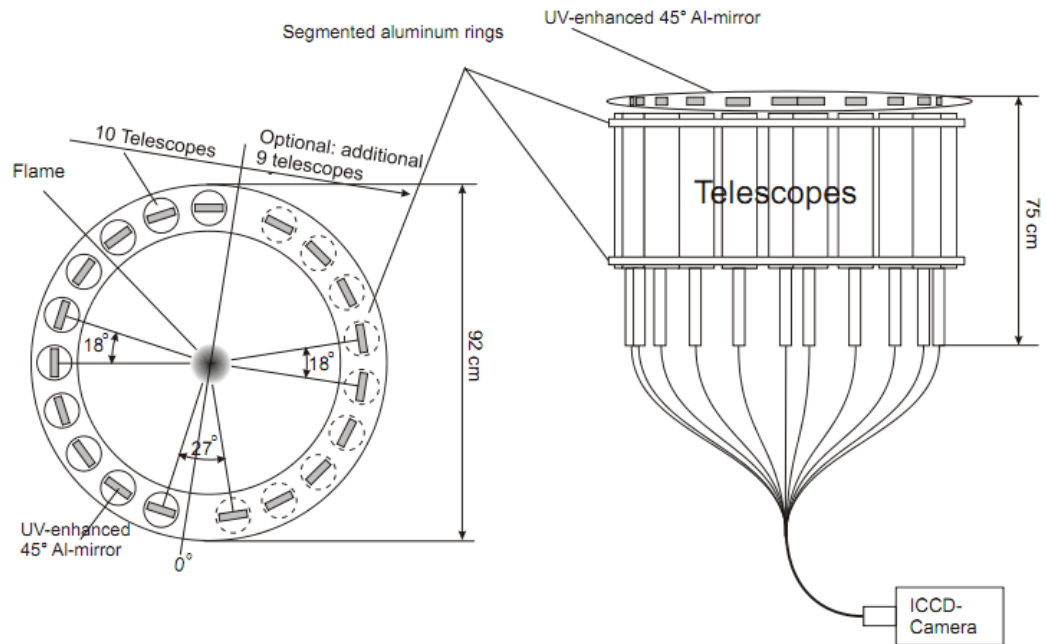


Figure 2. 17 Telescope Tomography System Layout by Karlsruhe University [32]

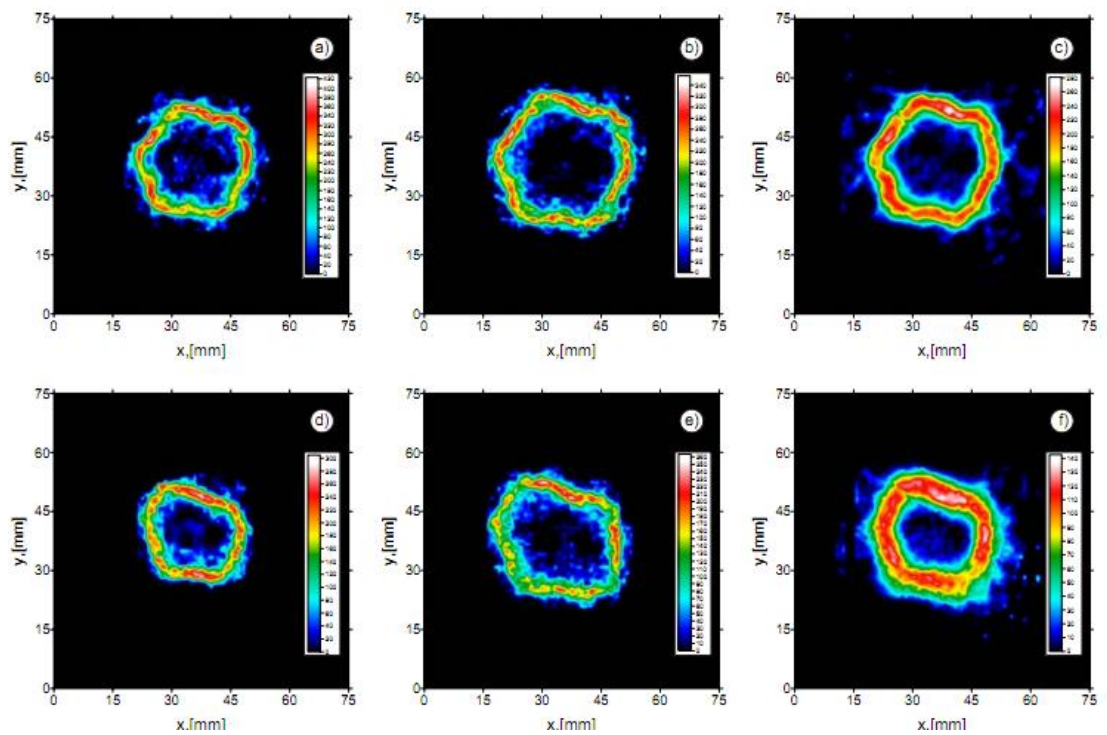


Figure 2. 18 Simulated Images of Turbulent Burner Flame [32]

The tomographic system shows a good performance and it is more simplified

comparing with other tomographic systems because of its emission applications. However, the initial design of this system is based on Radon Transform. Thus it has an inverse Radon Transform problem in the result of its probably non-cross-section system.

## **2.3 Review of Other Optical Research Techniques**

### **2.3.1 Shadowgraphy Method**

In turbulence flow, the variable intensity gradient causes changes of refractive indexes. Different refractive indexes cause deviations to the uniform bundle light ray after crossing the flow region. Methods which record the behaviors of turbulent fields using a camera or displacement screen are called Shadowgraphy methods or Schlieren photography methods. Shadowgraphy uses photographic methods to measure the gas intensity gradient of invisible gas. Consider a displacement screen illuminated by a parallel light ray: there is no deviation of illumination on screen after passing an ideal uniform gradient density. If an object such as a prism, is placed between the collimated light source and the screen and it is in a constant gradient intensity; a constant spatial displacement of parallel light rays will be caused by the refraction. Then, the displacement is adopted on the screen and can be measured (Fig 2.19). However, the turbulence gas commonly has variable refractive indexes due to its variable density gradients. Thus, the focuses of the light beam are scattered on the screen; because of

the different orders of focus. The illumination level of each focus is different and displaced in darkness and brightness on the screen. The brightness level and displacements of the refocus record the gradients distribution of turbulence.

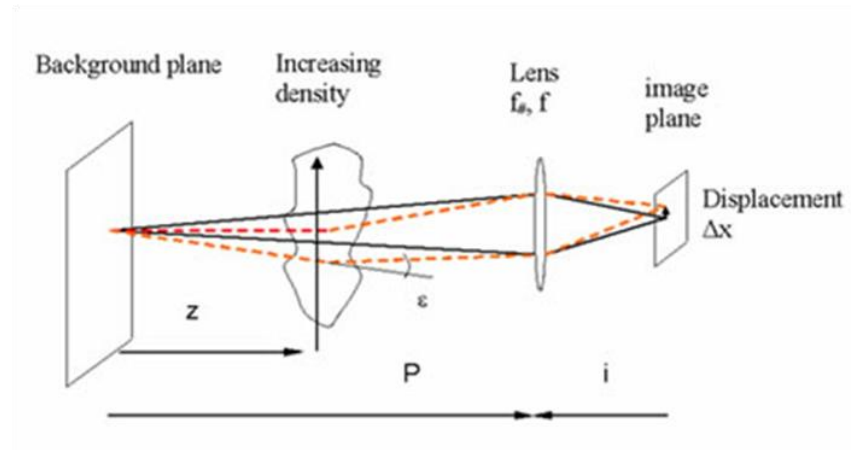


Figure 2. 19 A Simple Shadow Experiment Measuring Displacement of Focus Light Rays

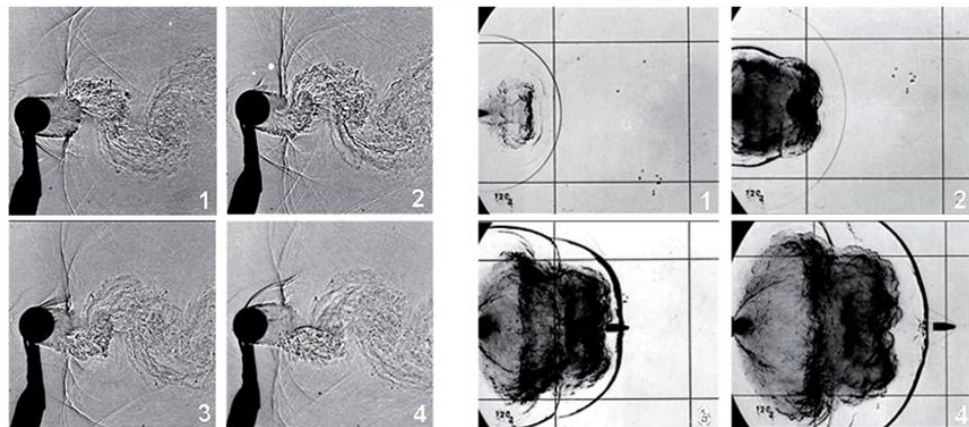


Figure 2. 20 Shock Wave Visualization with High Speed Camera by Shadowgraphy [33]

The visualization of the shock wave gives particularly good results (Fig 2.20). Nevertheless, the shadow method is a qualitative method which is useful to record the outline of the flame. But it is insensitive to high frequency turbulence

and it is hard to record precise profiles of density gradients. As seen in Figure 2.20, it is only displace the general outline of the flame even though the turbulence is an intensive shock wave. Another drawback of Shadowgraphy is the shadow images always record the real time size of the disturbance, comparing to the Schlieren methods, it is difficult to record large volume disturbance.

### 2.3.2 Schlieren Method

Toepler [34] devised the Schlieren method to analyze fluid flow and shock waves in 1864. Schlieren photography passes a collimated light source over a disturbance object. The light rays are bent at a subtended angle similarly to Shadowgraphy. The light rays are refocused on the straight edge of a knife. Since illumination is partly blocked by the knife the disturbance object is displayed in half darkness and half brightness. If the illumination of irradiance of light source is  $I$ , corresponding to the passing irradiance of light  $dI$  cut by the knife edge; and the passing light height is  $h_s$ ; the distance between the knife and the disturbance is  $d$ ; the subtended angle is  $\theta$  caused by the refractive index of the intensity gradient of the disturbance. The Schlieren formula is:

$$\frac{dI}{I} = \frac{dA}{A} = \theta \times \frac{h_s}{d} \quad (2-1)$$

Where  $dA$  is the uncut area by knife and  $A$  is the disturbance area.

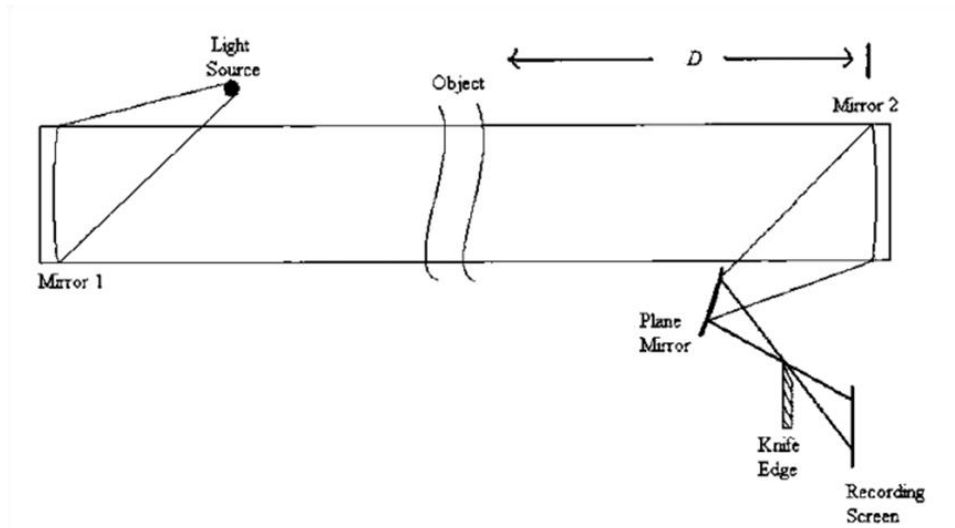


Figure 2. 21 Schlieren Photography Method System

The Schlieren method is extraordinary sensitive and accurate in the measurement of small changes of density caused by the disturbance (Fig. 2.22). The Schlieren images show more detail of the disturbance than Shadowgraphy methods.

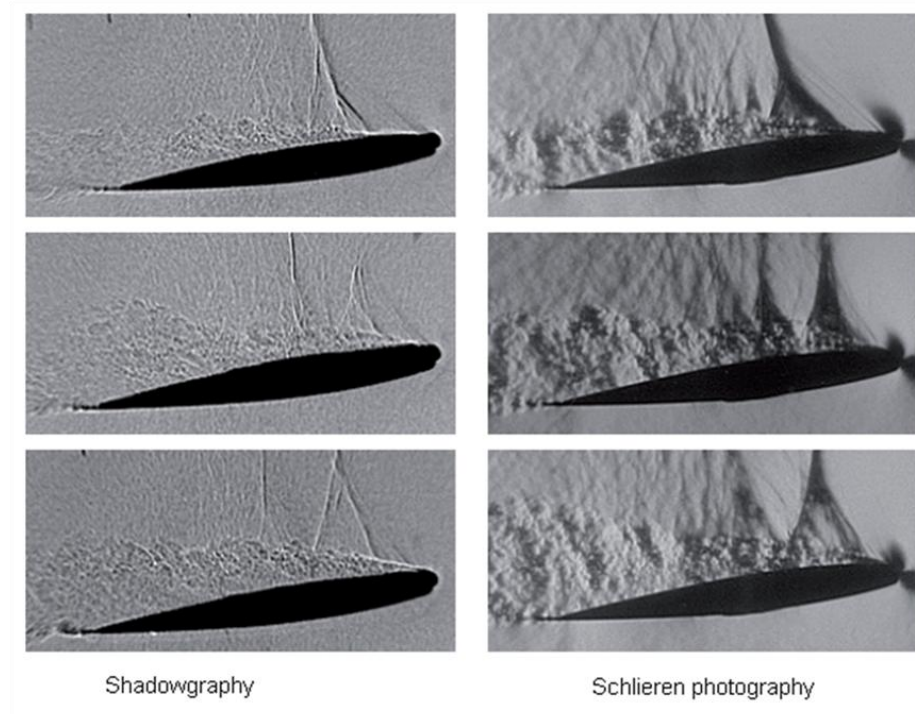


Figure 2. 22 Comparisons of Disturbance between Shadowgraphy and Schlieren Photography [33]

Schlieren methods are better able to record turbulent eddies, shock waves and density gradient for qualitative analysis but are at a disadvantage in quantitative measurement. Recent research makes use of new optical components, like phase, multicolour and polarization filters to replace the knife edge to visualize disturbance in different situations.

### 2.3.3 Interferometry Method

Interferometry unlike shadow photography is a qualitative method suited to measuring changes in the refractive index of the disturbance gradient density. Interferometry is a quantitative method suitable for investigating the density gradient. These methods are very sensitive to visualizing the patterns of mixing processes in high speed disturbance fields.

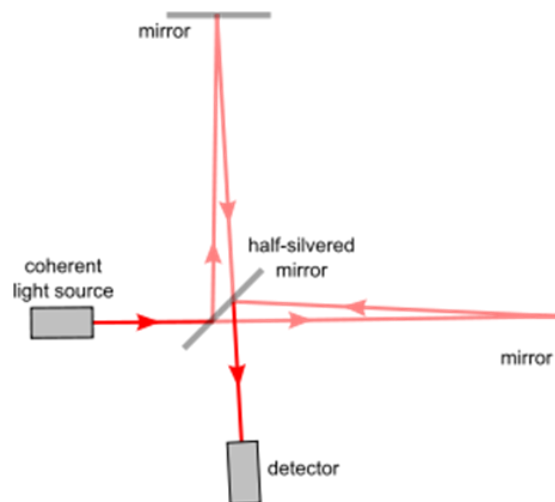


Figure 2. 23 A Michelson Interferometer System [35]

Michelson and Morley 1887 [35] used optical Interferometry to measure disturbance distribution (Fig. 2.23). A coherent light beam is split into two parts with

different phases by a half-silvered mirror. The two parts of the beam are reflected by two mirrors and recombined into one beam by the half-silvered mirror. The resulting interference fringes are photographed.

Many researchers make use of Interferometry method to study wave propagation properties. These methods are employed to measure refractive index, phase shifting and frequency shifting. A Diffraction grating is a common interferometer who combines diffraction and Interferogram. A light beam is split by a grating into several beams traveling at different diffraction angles. Then it generates fringes surface on a plate by intereferogrametry in darkness and brightness or chromatic colour in an alternating pattern. According to the Huygens-Fresnel [36] principle, each beam from the grating slits can be considered as a new point source. The diffraction equation is:

$$d_g (\sin \theta_i + \sin \theta_m) = m\lambda \quad (2-2)$$

Where  $d_g$  is the slit spacing of grating is;  $\theta_i$  is the incident angle of incoming beams;  $\theta_m$  is the maximum angle of diffraction beam where  $m$  is an integer;  $\lambda$  is the wavelength of light beam;  $m = 0, \pm 1, \pm 2, \dots$

Interferometry methods are commonly used to measure the phase shift in the wave front propagation or density gradient. The Mach-Zehnder interferometer is a typical system used to measure the phase shift of a wave front. In a simple configuration a collimated light beam is split in two using a half-silvered mirror. The



two beams are reflected by mirrors to pass another half-silvered mirror and into the detector. If one beam crosses a disturbance field there is a phase shift. The phase shifted beam is compared with the other reference beam and the disturbance measured.

Figure 2.24 is a mathematics module of Mach-Zehnder interferometry system.

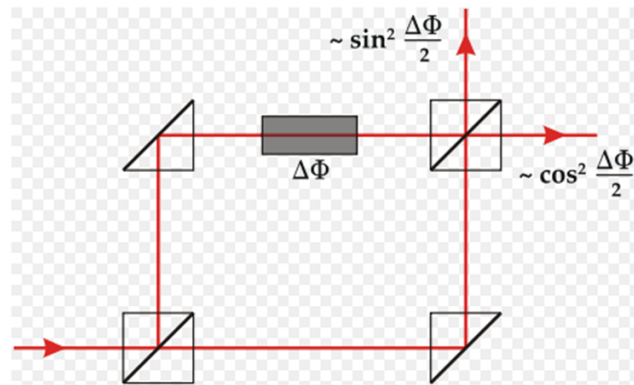


Figure 2. 24 A Sample of Mach-Zehnder Interferometry [37]

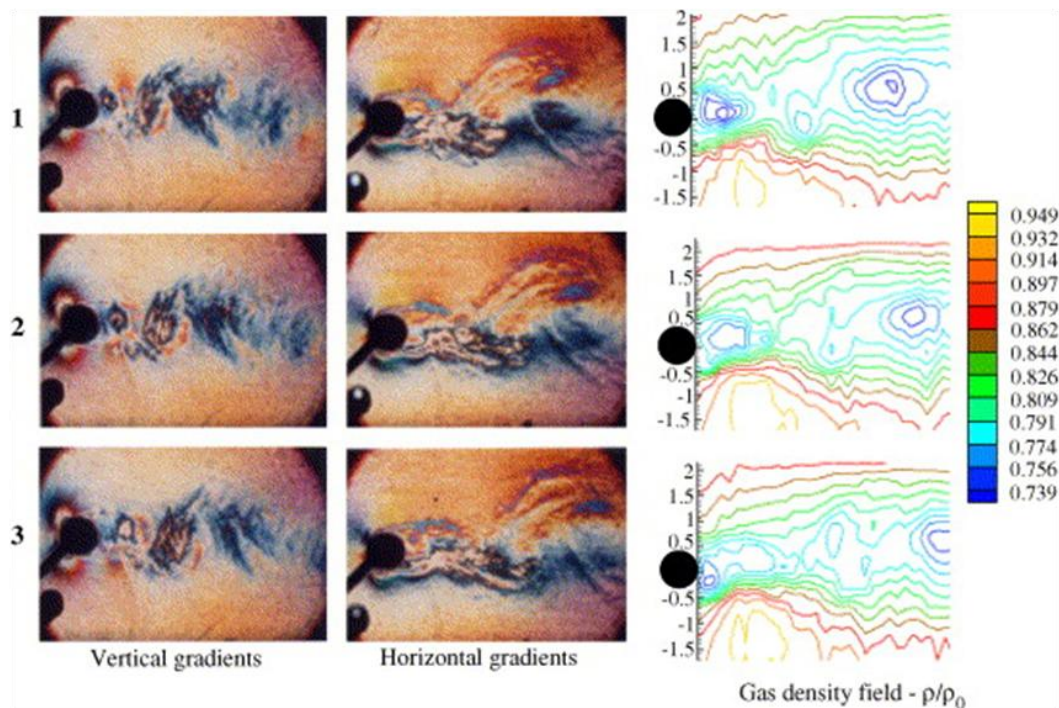


Figure 2. 25 High-Speed Interferograms Recorded by Differential Interferometry-  
Mach 0.4 [38]

Interferometry is well adapted to obtaining quantitative information about gas

density. Due its high sensitivity, Interferometry is well suited to measuring weak vortex gas gradients in polarized light. Figure 2.25 shows a recording of gas density by Interferometry methods [38]. The Figure illustrates the reconstruction images of gas density and indicates the size of gas vortexes in different directions.

### 2.3.4 Holography Methods

Holography was invented by Dennis Gabor who developed the theory in 1947 [39, 40]. This technique is primarily used in electron microscopy also known as electron holography. Optical holography methods were first used to record 3D objects by Yuri Denisyuk in 1962 [41]. The usefulness of holography in many fields including research has ensured its rapid development.

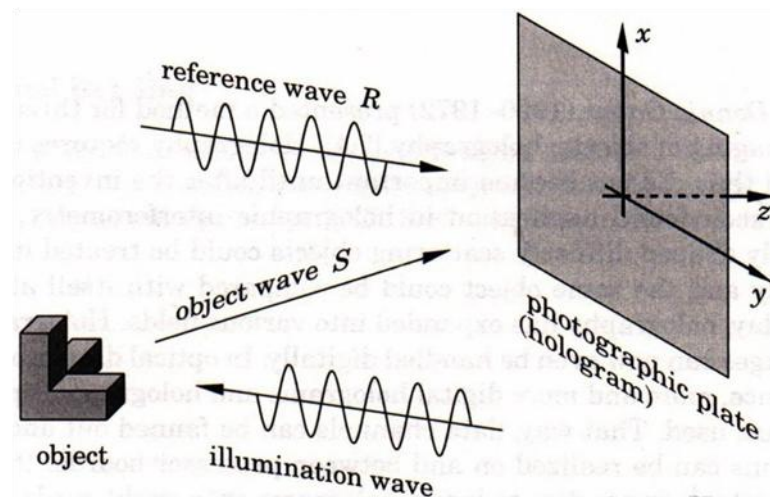


Figure 2. 26 Formation of a Hologram

Holography is an interference method of recording light waves diffracted by a subject illuminated with coherent light [42]. The diffraction waves are interfered with reference waves and distributed in intensity patterns onto a recording medium. The

diffraction wave information including amplitude and phase shifting are photographed to model the subject. Hence, illuminating the photograph by white light or laser light, a hologram of wave front is vividly visualized. The system is shown in Figure 2.26. A photography only records object intensity information in a spatial distribution. Holography records both amplitude and phase information of light intensity of an unfocused subject.

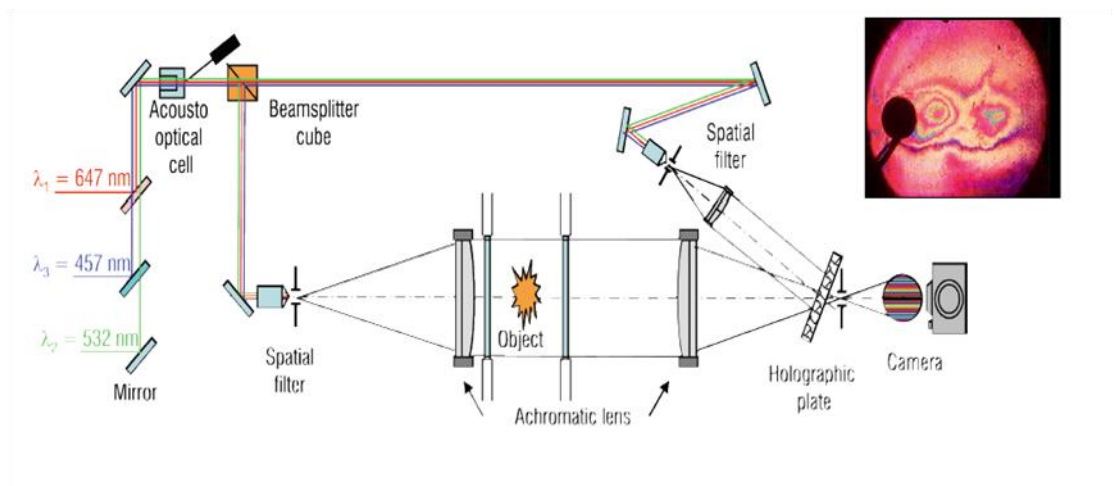


Figure 2. 27 A Transmission Holography System [38]

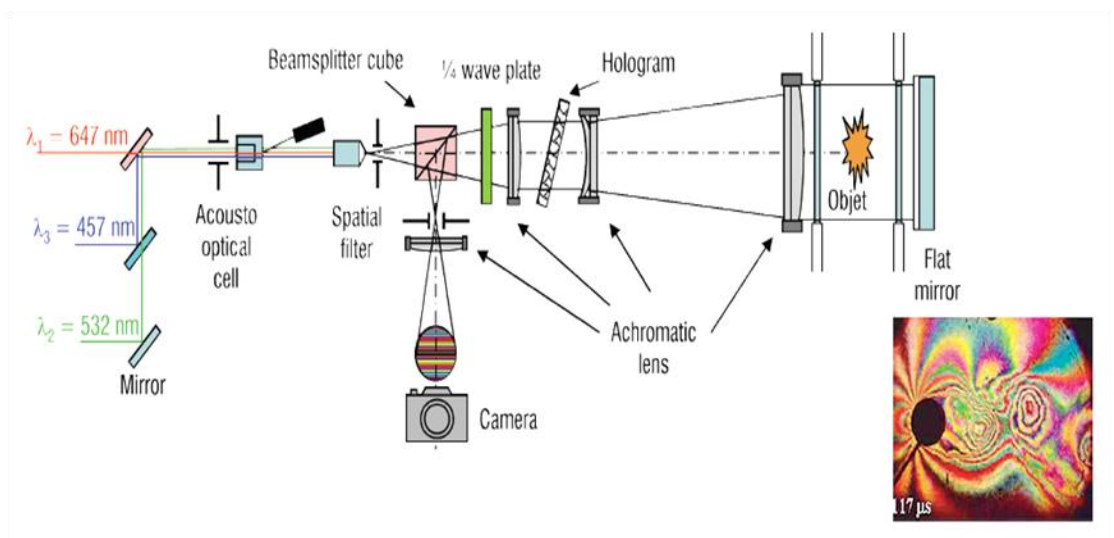


Figure 2. 28 A Reflection Holography System [38]

Two types of holography can be identified: transmission holography and reflection holography. In transmission holography, a light beam is split into two. One beam is passed over the disturbance object and the other beam is a reference beam. The beams are interfering on a hologram medium and the holographic image is transmitted to the observer side by interferometric lighting. A sharp virtual image of the object is obtained (Fig 2.27). In a reflection system, a hologram image is recorded in the same way as the transmission system. The difference is that the light beam is reflected by the object and the hologram is received on the observer's side of the holography medium (Fig 2.28)

Reflection holography exhibits greater interference than transmission holography because the higher sensitivity of reflection holography to variations. The drawback of reflection holography is that parts of the beam are reflected by the object affecting the results. For example, the holographic image of a diamond shows sparkles. Many types of holography have been investigated [43]:

- Embossed holography commonly used in identification cards records the object information on a photo resist material.
- Integral holography records the target object as a series of holographic images using transmission or reflection holography. The images are combined to give a stereoscopic image. The sensitivity to small changes of disturbance parameters makes holographic Interferometry or real time holographic Interferometry useful with invisible and disturbance objects; gas turbulence, shock waves, etc

- Multichannel holograms use viewers to obtain holographic images from various angles.
- Computer-generated holography uses mathematic methods to model objects. This technique is developing rapidly and popularly used in clinical medicine and movie applications.

The analysis of wave front holograms is based on temporal and spatial modulations [42]. The complex amplitude of the wave front is relative to the Fourier transform; it is present in temporal –frequency domains and spatial- frequency domains. It assumes that in a spatial domain the point source light amplitude is  $a(x,y)$ ; the  $a(x,y)$  represents light propagation in the spatial coordinates  $x,y$  of an observation plane. The complex amplitude distribution corresponds to the frequencies  $\gamma$  and  $\delta$ . Hence, the amplitude in a spatial domain  $(x,y)$  can be represented as  $A(\gamma, \delta)$  in frequency domain. The equation for point source holograms can be expressed as:

$$\begin{aligned} F[a(x,y)] &= \int_{-\infty}^{\infty} \int_{-\infty}^{\infty} a(x,y) \exp(2\pi i \gamma x) \exp(2\pi i \delta y) dx dy \\ &= A(\gamma, \delta) \end{aligned} \quad (2-3)$$

Where,  $a(x,y)$  is the inverse Fourier transform of  $A(\gamma, \delta)$ :

$$\begin{aligned} F^{-1}[A(\gamma, \delta)] &= \int_{-\infty}^{\infty} \int_{-\infty}^{\infty} A(\gamma, \delta) \exp(-2\pi i \gamma x) \exp(-2\pi i \delta y) d\gamma d\delta \\ &= a(x,y) \end{aligned} \quad (2-4)$$

The Shadowgraphy, Schlieren, Interferometry and holography methods are present good results of flame density measurements. However, there are some distinct limitations on these methods. Shadowgraphy and Schlieren methods are adapted to

measure the invisible density. The Interferometry and Holography methods are too complex to detect in cylinder flame.

## 2.4 Summary

This chapter reviews the present in-cylinder combustion investigation techniques by LIF, PIV, LDV and TP. Most of these techniques are based on a laser – camera system. They demonstrate great performances for visualizations of instantaneous combustion or flame. In Special the LIF is good for measuring flame density; the PIV and LDV illustrates the finer scale map of velocity vector; the TP demonstrates the precise temperature distributions. Nevertheless, there are several distinct limitations of these techniques for applying in research of in-cylinder combustion.

- Both of these methods employ a complex laser and camera system. Therefore, they are not adaptive to measure the combustion within engines.
- The frame frequency specification of camera system limits the capability of sampling numbers in a complete engine cycles. Thus, the time resolved problem has not been overcome.
- The test engine has to be particularly designed to match the requirements of optical measurement system. The optical engine has a more or less different performance to the original engine and it is less adaptive to modifications.

Secondly this chapter reviews the tomographic measurements of combustion and

several experiments are illustrated for comparison. After reviews, it found that few tomographic experiments are successfully to reconstruct the combustion process in IC engine. The major reasons are from two aspects:

- The system design is difficult and the way of tomographic placements of sensors is significant.
- The algorithm solution to find a best correlation coefficient is important and has to pay more attention.

After reviews and comparisons of these techniques, it suggests the passive emission system is better than absorption system for tomography measurement because it great reduce the system complications. The image reconstruction methodology has been suggested to use ART with other algorithms. In the POET instrumentation, the passive emission approach using PMT sensors has been adopted. In the image reconstruction, the MART methodology has been applied for approaching the initial combustion, even it may increase some errors during iterations.

# Chapter 3.

## Experimental Methodology

After above reviews of the complex features of combustion, a new optical intelligent diagnostic technique system to investigate the flame front is introduced in this chapter. The system is called Passive Optical Emission Tomography (POET) and is a non intrusive optical method. The POET system instruments and modified engine are explained and the methodology of implementation setup is illustrated. Figure 3.1 presents the experimental process: the IC spark-ignition engine was modified to meet tomographic requirements; the integrated PMTs computer with DAQ card to obtain flame signals; and the designed software using MART algorithm to reconstruct 2D images of combustion.

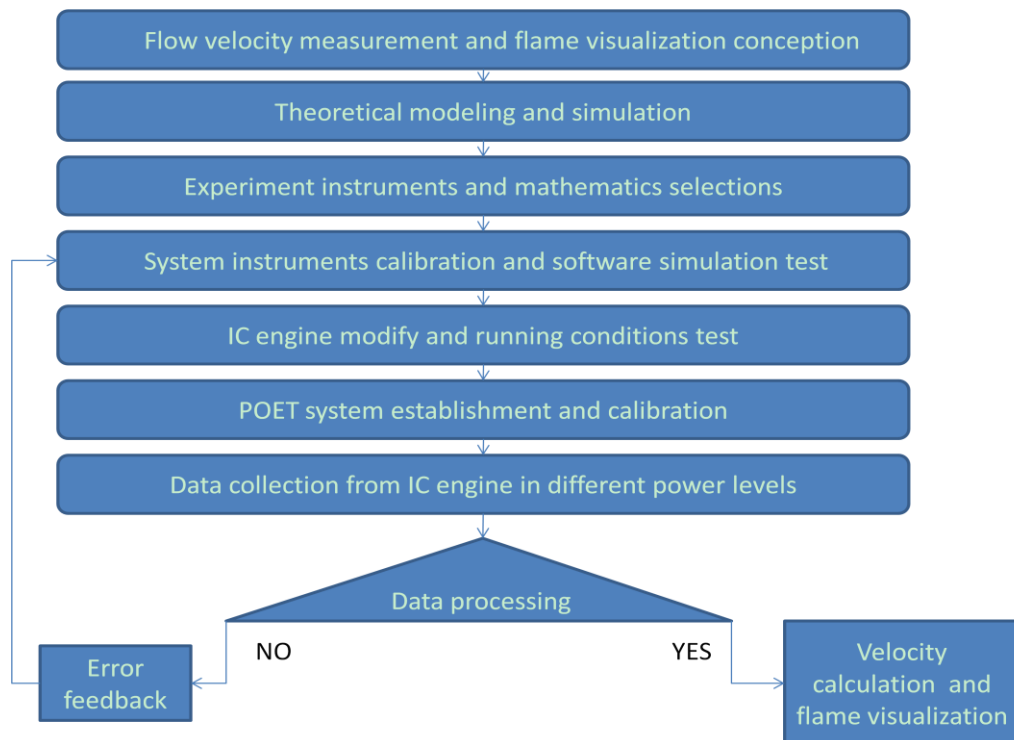


Figure 3. 1 Set Up Process of The POET System



This chapter describes the engine modifications and O-Ring Gasket (OAG) design for satisfying the experimental demands. There are two major purposes of engine reformation: one is to ensure that the modified engine could be safely operated by natural gas fuel. Another purpose is to couple the engine with PMT detectors. Furthermore, the OAG is the fundamental of the POET system. Thus, the design of the OAG is very important and the idea of OAG design is from project analysis and previous experiments by Professor Peter Bryanston-Cross and his students [44]. The challenges of OAG design are the placement of the fibre probes which receive the intensity signals and reconstruction of information from just the intensity. Thus, the OAG has 8 groups of 5 channels and  $45^\circ$  between each group for tomographically placing the probes around  $360^\circ$  of the cylinder. This design enables the probes to receive the fan beam projections of in-cylinder combustion (using the Radon Transform Algorithm) and to collect the cross-sectional signals from special angles (using the MART algorithm). Therefore, the in-cylinder combustion can be reconstructed according to the information of the special arrangement of probes. Nevertheless, this  $360^\circ$  placement of 40 fibres limits the reconstruction image resolution and the resolution is roughly equal to  $5\text{ mm} \times 5\text{ mm}$ . So the limitation of combustion turbulence is  $5\text{ mm} \times 5\text{ mm}$ . However, the limitation size of turbulence meets the experimental requirements because Bryanston-Cross and Chana state that the recognized size of turbulence is  $5\text{ mm} \times 5\text{ mm}$  for our research requirements [44]. The conceptual design of the OAG used 40 channels but only 35 were used in practice due

to the engine push rods.

## **3.1 Introduction of the Otto Engine**

The POET system is suitable for analyzing combustion in IC gas engines as well as gasoline, diesel, gas turbine and jet engines. A modified spark-ignition internal combustion engine was employed to analyze FFP during combustion. The engine characteristics and engine modifications are detailed in this section.

In internal combustion engines combustion is an energy releasing and transmitting process. The process of burning the fuel-air mixture is a series of complex chemical reactions in a sealed vessel. The first commercial engine which had no compression before combustion was developed in the 1860s. Then Lenoir [45] developed a type of engine where a gas and air mixture enters the cylinder during the first half stroke at atmospheric pressure and ignited. The burnt gas forces the piston down in the second half stroke. At atmospheric pressure, the efficiency of this type of engine was only 5 percent. In 1867, Nicolaus A. Otto and Eugen Langen added a stroke to precompress the fuel-air mixture in the cylinder. The use of a precompression stroke improved the thermal efficiency by 11 percent and had a profound influence on engine development in the following years. In 1884, Alphones Beau de Rochas described the principles of the four-stroke cycle engine which would perfect the Otto engine in theory. The development of engine proceeded rapidly. In 1892, Rudolf Diesel invented the diesel engine. The diesel engine is a compression ignition type engine

with high expansion ratios without detonation or knock. Since signification use of engines in commercial applications, more and more new type engines are developed such as rotary engine, bio-engine in recently. A deep understanding of combustion is helpful to improve the efficiency and reduce the pollution of engine exhaust.

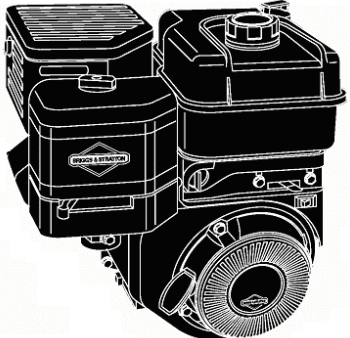
Table 3. 1 Internal Combustion Engine Classifications [46]

Classifications	Types
Fuels	Gasoline; Diesel; Natural gas; Alcohols fuels; Liquid petroleum gas; Dual fuel; Bio fuel.
Ignition manner	Electrically ignition; Spark ignition (SI); Compression ignition (CI);
Strokes	Two stroke engine; Four stroke engine;
Pistons	Reciprocating engine Rotary engine
Cooling system	Water cooling engine Air cooling engine
Chambers	One cylinder engine Multi cylinder engine
Speed	Low speed (< 300 r/min) Medium speed (300 ~ 1000 r/min) High speed (> 1000 r/ min)
Intake valve	Natural aspirated engine Supercharged engine

A single cylinder natural gas reciprocating spark-ignition combustion Briggs and Stratton Over Head Valve (OHV) Pro 206 engine was modified for the experiment

and it is suitable to set up in laboratory environment. The reasons for using this type of engine are set out in the engine modification section.

Table 3. 2 OHV Pro 206 Specifications

Manufacturer	Briggs and Stratton	OHV Pro 206
Valve Type	Overhead Valve	
Model no.	123432-1401	
Horse Power (HP) Rating	6.5	
Compression Ratio	6 to 1	
Ignition Timing Degrees BTDC	22.5	
Stated Maximum Pressure	500	
Running Pressure [GAS] (PSI)	200 (est.)	
Temperature at flame front [Petrol] (°C)	1650	
Nominal Established Oil Temperature (°C)	106	
Rev. Range [GAS] (rev/min)	1090-2280	
Displacement(cc)	206	
Bore (mm)	65	
Stroke (mm)	55.8	

### 3.1.1 Engine Operating System

The Briggs and Stratton engine is a four stroke reciprocating engine. The piston moves up and down in a single cylinder transmitting power through a crank to drive the shaft rotating at the variable  $\theta$  angles known as crank angles (Fig. 3.2).

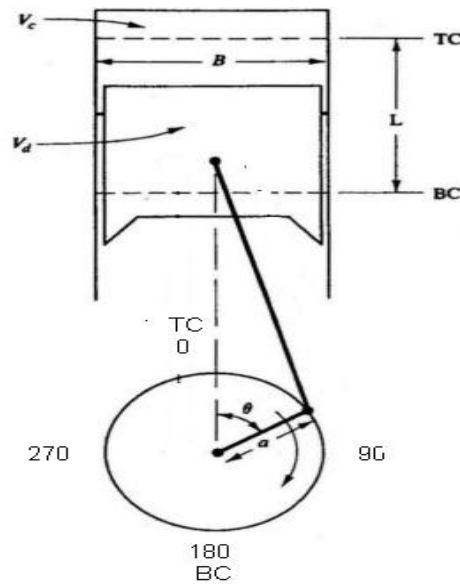


Figure 3. 2 The Structure Diagram of a Reciprocating Engine.

When the piston is at top dead center (TDC) the corresponded crank angle is zero. The volume of the cylinder is at a minimum. When the piston reaches bottom dead center (BDC) the crank angle is 180 degrees and the volume of the cylinder is at a maximum. The minimum volume is the clearance volume  $V_c$  and the volume which is swept out by the piston is called the swept volume  $V_d$ . The motion of the piston from top to bottom is one stroke.

The reciprocating engine has a four-stroke cycle: intake, compression, expansion and exhaust strokes. The performance of these strokes process is corresponded to two complete revolution cycles as a critical indicator of engine characteristics.

1. Intake stroke: the piston motion starts at TDC and moves downward to BDC of the cylinder. During this process, the intake valve opens sucking in the fuel-air mixture l., The intake valve opens just before the start of the intake stroke and closes just after improving the efficiency of drawing in the mixture.

Numerically from Figure 3.3, the crank angle is  $0^\circ - \Delta\theta < \theta < 180^\circ + \Delta\theta$ , where  $\Delta\theta$  is variable and critical to engine performance.

2. Compression Stroke: the piston returns to TDC. The intake valve is closed and the fuel-air mixture is compressed.
3. Expansion stroke: This is the combustion stroke moving the piston from TDC to BDC. The fuel air mixture is ignited moving the piston down rotating the crank and supplying the energy for the next three strokes process.
4. Exhaust stroke: the exhaust valve is opened and the burned gas is forced out by the piston. As the piston approaches TDC, the intake valve opens. As the piston passes TDC, the exhaust valve is closed. The next four-stroke cycle starts.

Numerically the crank angle is  $180^\circ - \Delta\theta < \theta < 0^\circ + \Delta\theta$ .

Furthermore, the crank angle is a significant parameter of engine performance.

In a four stroke engine, temperature, pressure and velocity parameter measurements are relative to crank angles. The analysis of crank angle and other parameters is useful to modify engine to improve its performance. For example, adjusting the opening time of the intake valve and the spark ignition time will both affect performance. Figure 3.4 shows that in four-stroke engine, the spark ignition is between  $-40^\circ < \theta < -10^\circ$  crank angles and starts the combustion process. The optimum sparking time occurs when the burned gas is exhausted at a minimum level known as maximum brake-torque (MBT). Early or late ignition will affect engine performance.

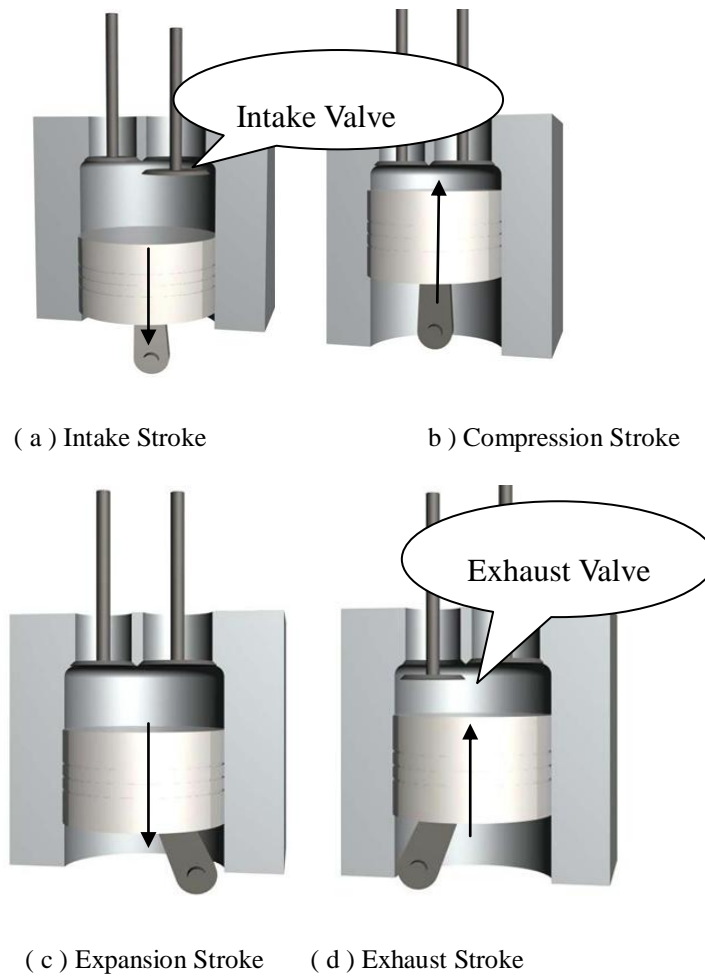


Figure 3. 3 The Operation of a Four Stroke Reciprocating Engine

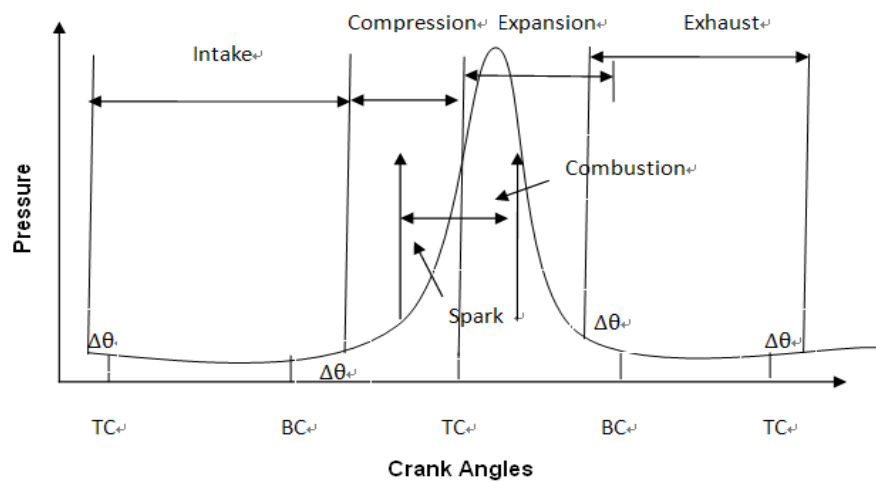


Figure 3. 4 Crank Angles of Operation Engine versus Pressure

### 3.1.2 Engine Performance Parameters

Many factors influence engine performance, efficiency and chemical reactions.

Some important factors affecting performance are discussed in the following [46].

- Compression ratio

The compression ratio for a reciprocating engine is given by:

$$r_c = \frac{\text{Maximum Cylinder Volume}}{\text{Minimum Cylinder Volume}} = \frac{V_d + V_c}{V_c} \quad (3-1)$$

Where  $V_d + V_c$  is the initial volume of fuel-air mixture in the cylinder and  $V_c$  is the maximum compressed volume of fuel-air mixture (Fig 3.3). Typically the value of the compression ratio is  $r_c = 8$  to 12 for a SI engine and  $r_c = 12$  to 24 for a CI engine.

- Mean speed velocity of the piston

The mean speed of piston  $\overline{S_p}$  is given by :

$$\overline{S_p} = 2LN \quad (3-2)$$

Where  $N$  is the rotational speed of the crankshaft,  $L$  is the distance between TDC and BDC of the cylinder. The mean speed of the piston is important in analyzing engine behavior. The instantaneous piston velocity  $S_p$  is obtained in the formula:

$$\frac{S_p}{\overline{S_p}} = \frac{\pi}{2} \sin \theta \left[ 1 + \frac{\cos \theta}{(R^2 - \sin^2 \theta)^{1/2}} \right] \quad (3-3)$$

Where  $R$  is the ratio of the connecting rod length to crank radius, typically  $R=3$  to 4 for small and medium engines, and  $R= 5$  to 9 for CI engines.



- Torque of engine

Engine torque is as an indicator of power output. It is measured using a dynamometer [47]. The torque of an engine can be measured by connecting a dynamometer as a load which indicates the torque in terms of voltage output or force. The torque expression is:

$$P = 2\pi NT \quad (3-4)$$

Where  $N$  is rotational speed;  $T = F \times b$ ,  $F$  is force,  $b$  is the distance from the pivot.

- Fuel-air ratio and equivalence ratio

The fuel-air ratio is critical in engine combustion. Changes in the fuel-air ratio influence the chemical reactions in combustion and the power output of the engine. Under high ratio fuel-air ratio, a detonation referred in the detonation section occurs by generating great pressure and temperature that damages the engine cylinder:

$$\begin{aligned} \text{Air/Fuel ratio (AFR)} &= \frac{\text{Air Mass}}{\text{Fuel Mass}} \\ \text{Fuel/Air ratio (FAR)} &= \frac{\text{Fuel Mass}}{\text{Air Mass}} \end{aligned} \quad (3-5)$$

The  $AFR$  ratios are able to be measured in both mass and moles, but they are different from each other under the same condition. Thus, to adopt more accuracy results, the equivalence ratio is induced and its expression is:

$$\phi = \frac{AFR}{AFR_{stoich}}$$

(3-6)

- Volumetric efficiency

Volumetric efficiency is usually presented as induction efficiency of engine which is only used in four-cycle engines. The intake stroke process is forcing the air and fuel to the cylinder by intake valve; thus the mass of incoming fuel-air mixture is another parameters to affect the engine behaviors which is similar to fuel-air ratio. For the air density, the volumetric efficiency is expressed as:

$$\eta = \frac{2m}{\rho V N}$$
(3-7)

where  $m$  is the mass of air,  $\rho$  is the density of air,  $V$  is the volume of the cylinder and  $N$  is the rotational speed of the piston.

- Combustion efficiency

In combustion process, the equivalence of fuel-air ratio is an important factor for flame burning. Under lean burning conditions numerous small incomplete burnings occur and the chemical reactions produce a few harmful products like CO. Lean burning of fuel results in reduced power output. Under rich fuel burning conditions, insufficient oxygen results in incomplete burning. Combustion efficiency is a measure of the percentage of chemical energy released by the combustion process.

$$\eta_c = \frac{H_R(T_A) - H_p(T_A)}{mQ_{HV}}$$
(3-8)

Where the combustion process is in the adiabatic condition;  $H_R$  is the Enthalpy of

reactant;  $H_p$  is the Enthalpy of product;  $T_A$  is an ambient temperature;  $m$  is average mass of flow rates and  $Q_{HV}$  is the heating value or calorific value of fuels.

These characteristics affect the results of the experiment. Testing accuracy was improved by adding some accessories to the system to control the equivalence ratio and modifying the engine. Characteristics such as engine torque are intrinsic properties of the engine and were not considered for modification.

## **3.2 Optical Array Gasket Design and Engine Modification**

The Briggs and Stratton Overhead Valve 206 pro engine, a single cylinder spark-ignition reciprocating IC engine that uses natural gas was chosen. This type of engine has been used frequently in experiments, motor vehicles and industry machines by its high compression ratio and simpler drive system. The simple layout of the OHV pro engine and its combustion performance make modification simpler. Engine performance details are given in table 3.2. The engine is capable of 6.5 Hp and has a speed range of 1000-2500 rpm using natural gas. In OHV operation (Fig 3.5) the intake and exhaust valves are ordinarily parallel with the piston moving direction permitting modification without serious alteration to cylinder structure. The difference between OHV and OHC (overhead camshaft) is generally in the valve control system. The OHV control system directly connects the crankshaft with valves to control the opening and closing by mechanical transmission power from piston inertia (Fig 3.6).

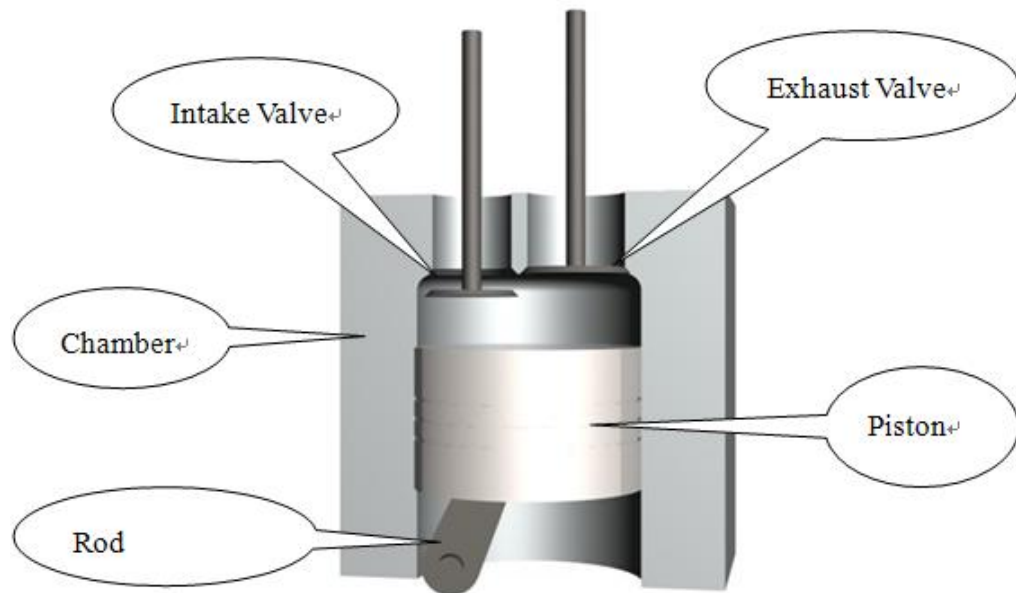


Figure 3. 5 Diagram of Half Section of OHV Operation

The OHC valve control system is a more complex independent system. The control valve is located separately on the side of the cylinder and is operated by the engine belt. This complexity increases the cost and reduces the torque. The disadvantage of the OHV engine is that it is difficult to accurately control the valve opening and closing because of the great inertia of piston movement. For this reason, the drawback of OHV is apparent at high speed revolutions. Even the direct valve control system makes the maximum engine torque output; this type of engine is commonly lower speed in average than OHC engine especially in multi cylinder modes. Nevertheless, the OHV design is perfect for experiments in a laboratory environment, especially with natural gas fuel for its well flow ratio.

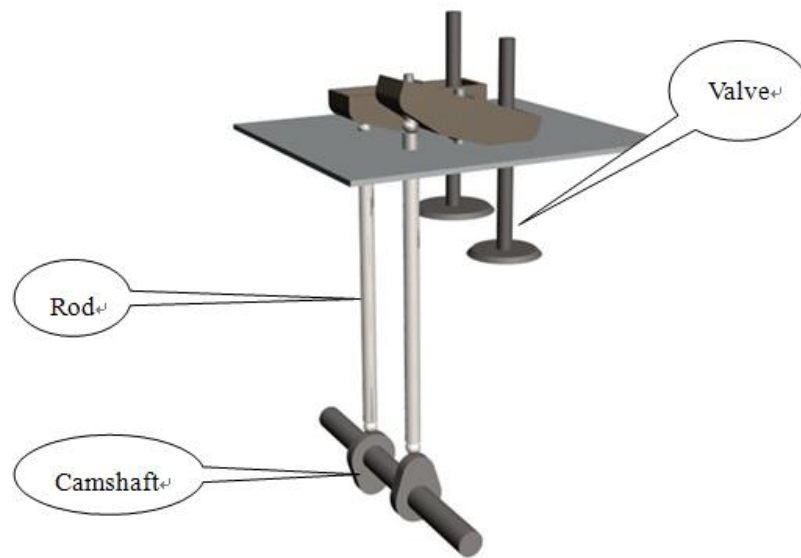


Figure 3. 6 Diagram of Valves Control System of OHV Engine

The modified engine was coupled with the POET system to detect combustion behavior (Fig. 3.7). Many factors had to be considered since the complex engine structure. The engine modification objectives were:

1. A low cost small, single cylinder, OHV engine with a simple layout.
2. Simple structures so that experiments can be easily repeated.
3. Consideration of the safety factors while working with high pressure, high temperatures and exhaust gas.
4. Changes to engine geometry do not affect engine performance.
5. The modified engine can be coupled to the Optical Array Gasket (OAG) of the POET system.

During modification of the OHV engine, the fuel tank was replaced by a methane gas inducing system. A spark ignition control system was coupled to the engine. The chamber was modified to connect to the OAG. A safety 'body guard' block was fitted

to the modified engine. The modifications were mainly to couple the engine to the POET system. The design of the OAG is discussed below.

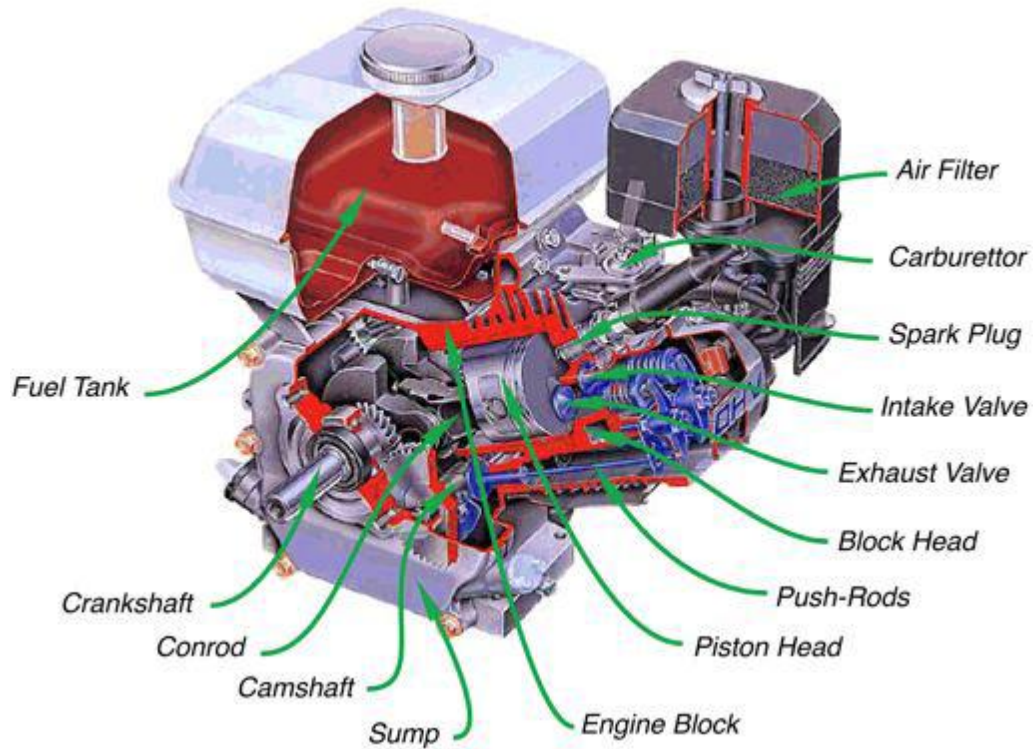


Figure 3. 7 The OHV Pro Engine

### 3.2.1 Optical Array Gasket (OAG)

#### Introduction of Optical Array Gasket

The design of the Optical Array Gasket was the critical element in the POET system in respect of engine modifications and the computational methodology of data analysis. The fundamental algorithm of OAG design is based on Algebraic Reconstruction Technique (ART). The conception of engine modification is considering how to place the OAG in right position coupled with engine. To find a solution of the placement alters the engine performance slightly. In the OHV pro

engine, the cylinder is divided into three parts: the cylinder head, spark plugs and valves; the chamber in which the piston moves; and the gaskets used to seal the cylinder head and chambers. Placing the OAG with the gaskets between the cylinder head and chamber creates a 'sandwich' system. Ideally this system only minimally alters the layout of the engine (Fig. 3.8). Two neoprene type gaskets are coupled with the OAG on both front and back sides to prevent the leakage of fuel-air mixture under compression to avoid the uneven metal surface of the OAG. The thickness of OAG is slight changed the compression ratio of fuel-air, the performance of engine does not alter too much. The thickness of the OAG is minimal (only 3 mm) compared to the height of cylinder chamber.

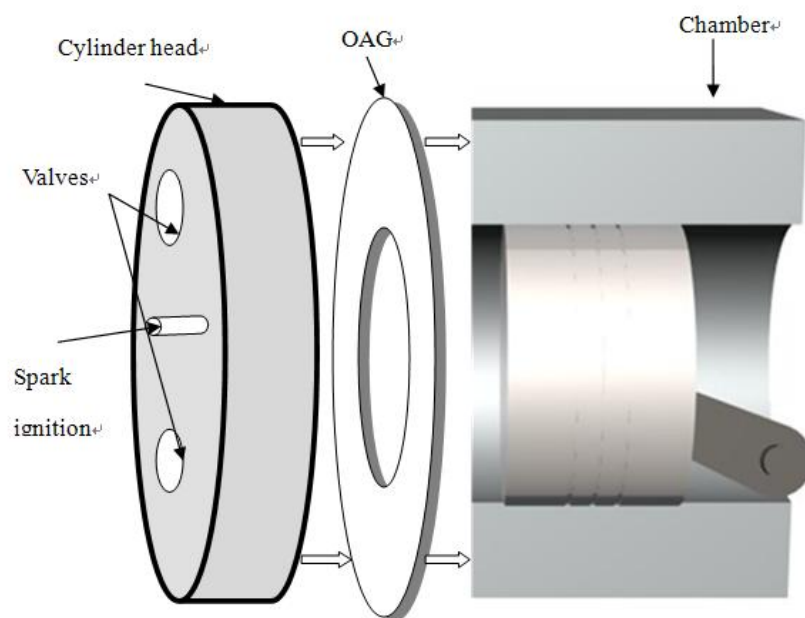


Figure 3. 8 Schematic of OAG Assembling with Chamber and Cylinder head

The requirements of OAG design are:

1. The placement of the OAG using the 'sandwich' method does not alter the

engine structure and slightly influences the behaviour of engine operation.

2. The layout of the OAG permits its insertion between the chamber and cylinder head. That requires the correct position to fit in to the structure of engine operation accessories.
3. The design of the OAG must allow 35 fibres plugging into chamber in 55 mm length span and 3 mm thickness.
4. The arrangement of fibres is in parallel and placed on the OAG plate in 7 groups of 5 fibres with an angle between each group of 45 degrees to match the tomographic reconstruction algorithm.
5. The fibres have to be place at a constant distance from each other, and must be in the X-Y plane.

The combination of fibres and OAG must operate safely in great pressure condition where the pressure in the engine is up to 41 bars, practical: 12-14 bars in gas condition. In the experiment, the solution is using super blue glue adhesives which can afford more over than 20N of fibre ejection force.

The OAG plate and fibres must survive high temperatures, a maximum of 1650°C and in a standard operation range it is : 1200°C – 1350°C. The OAG is made of aluminum and is not affected by temperature or high pressure.

The OAG fits tightly between the gaskets preventing gas leakage and the fibre from being pulled out.



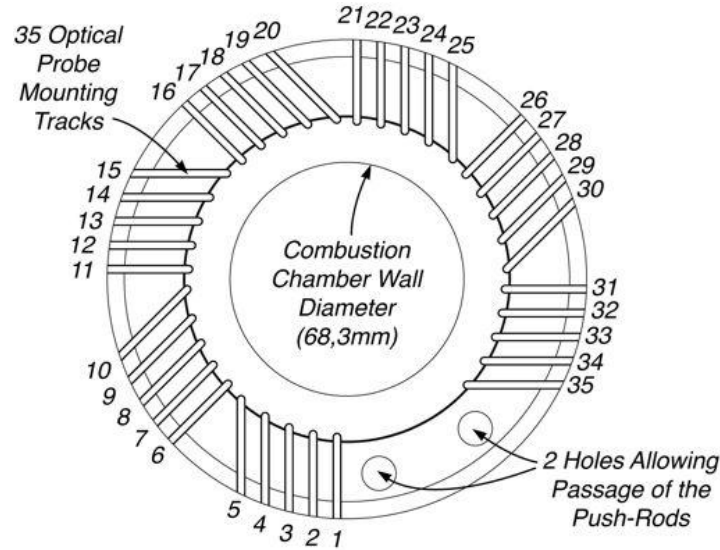


Figure 3. 9 The Basic Schematic Diagram of OAG

## Design of the OAG

The design of the OAG has to meet the requirements of engine operation and fitting of the optical fibre array. Under the precision to a millimeter level, the layout design needs to be very accurate. Auto-CAD and Solidworks software were used to minimize error,

The Auto-CAD software was used to create a 3D model of the OAG. The 3D design is considered for analyzing the detail of the mechanical problem, to evaluate its capable of combining with engine modification and highlight the problems in 3D mode in case of ignoring minor details. The Auto-CAD is using for engine modification problems analysis in further.

The solidworks software was used to create a 2D design of the OAG from which the specifications could be detailed. The OAG drawing produced by solidworks

was used by the university engineering department technicians to produce the OAG on a Computer Numerical Control (CNC) machine.

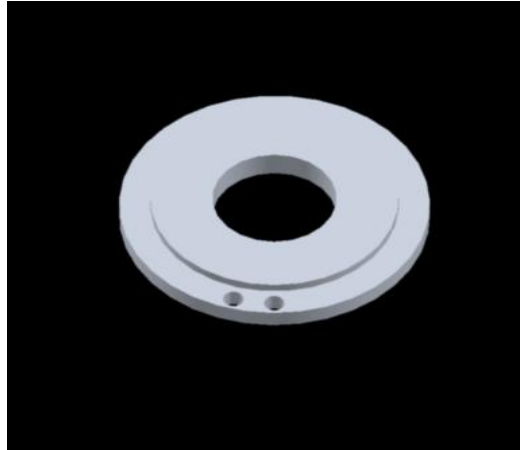


Figure 3. 10 Diagram of OAG Cover Plate.

The OAG consists of two parts: the cover plate and the array channel plate. The cover plate (Fig. 3.10) is 2 mm thick and 130 mm in diameter and has two holes in 10 diameters for the pushrods. The internal bore of 68 mm diameter is the same as the combustion chamber and array plate bores. The cover plate comprises two layers; the upper layer has a 90 mm diameter from center to the fibre edges and depth of 2 mm thickness. The outer layer starts from the step back boundary of 95 mm diameter to the cover plate edge of 130 mm diameter. The function of the cover plate is to form a vessel with the array plate to insert the fibre optic cable and to seal the chamber. In that form, the fibres are firmly placed between cover and plate using super glue to withstand 20N thrust forces of combustion energy.

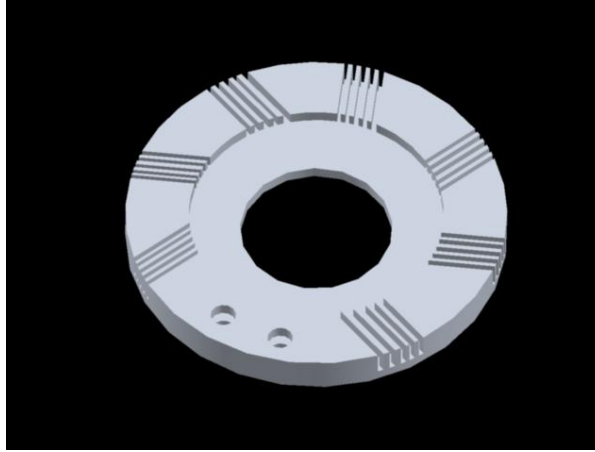


Figure 3. 11 Schematic Diagram of Array Plate Interface

The array plate design (Fig. 3.11) was complicated by the requirements of withstanding high temperature and great pressure from internal combustion in case of ejections of the fibres and the setting of the slit detection angles between the cover and array plate. The array plate is a ring plate with an internal bore diameter of 68 mm, 35 tunnels of 2 mm diameter take the fibre optic cables and two 10 mm diameter holes for engine pushrods. For the pressure design, it is a boundary of 5 mm width and 3 mm thickness in the outer region array plate to combat the force transmission from cover plate. To reinforce fibres, a 35 mm width and 2 mm step back ring for fibres insertion and 1mm thickness ring from the boundary of internal bore. The 2D design layout in details is in the appendix C.

The layout of OAG significantly influenced the experimental results in 2 ways. In the POET system, optical fibres are used to measure internal combustion behavior. The information from combustion reactions is transmitted along the optical fibres by photons to PMT detectors. The scale of the photons received by the optical fibres is

critical to experiments.

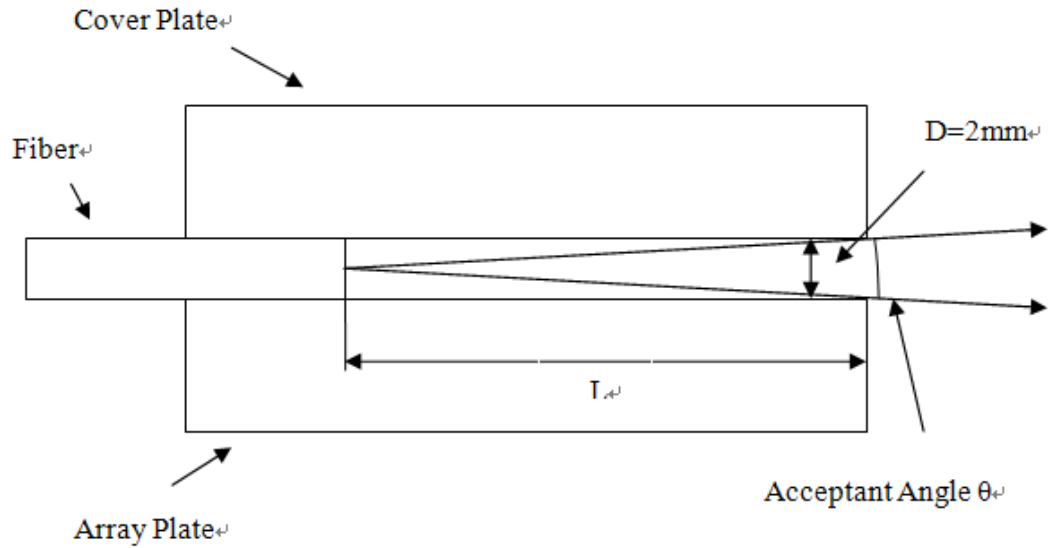


Figure 3. 12 Acceptant Angle between Array and Cover Plates.

Hence, the acceptance angle of the fibre has to be considered in the vertical plane (Fig 3.12). The acceptant angle is expressed by:

$$\theta_a = \arctan\left(\frac{D}{2L}\right) \quad (3-9)$$

Where  $\theta_a$  is the acceptance angle of the fibre, typically in the range from 4 degrees to 11 degrees; D is the gap distance of the slits between the two plates; L is the distance from the bore boundary to the fibre.

Photons lose intensity during transmission. The main loss of signal occurs within the fibre and during transmission between different surfaces of the optical instruments. Changes of acceptance angle affect the loss of signal from combustion which affects the results data. In theory the information loss is small in the thinness of

the plates. In comparison with the losses during transmission, information loss is inconsequential, only 0.01 dB and under ideal conditions. Transmission loss is discussed under the detection system section. The protection engine block is opposites the engine combustion pressure in the experiment. The various distributions of pressure on the surfaces of the OAG plates cause changes to the acceptance angles of each fibre. In the experiment some losses of information were significant because for example, some acceptance angles were reduced to less than 1 degree while others remained at 10 degrees. To overcome this problem, a small polysilicon ring was placed between the Cover and Array plates. This caused additional transmission loss. A new sSMART OAG assembly design is set out in chapter 6 Further Works.

Table 3. 3 OAG Array Plate Specifications

Body	Width: 140 mm in Diameter Thickness: 5 mm
Internal Bore	Width: 68.3 mm in Diameter Thickness: 1 mm
Inner ring	Width: 20 mm Thickness: 2 mm
Pushrod Hole	Width: 10 mm in diameter
Fibre Tunnel	Width: 2.4 mm in diameter Length: 55 mm.
Materials	Aluminum
Acceptance angle	4°~11°

A further specification was the 35 fibre array layout on the array plate separated into 7 groups of 5 fibres. 35 tunnels, 2.4 mm wide were engraved on the plate and arranged at an angle of 45 degrees between each group. The reason for the step back design is to make sure that the view of the fibres in the horizontal surface plane of the array plate is open enough and the view is only restricted by its aperture limitation. Then the good viewing performance is much more appropriated to the computation and correlation in the tomographic algorithm.

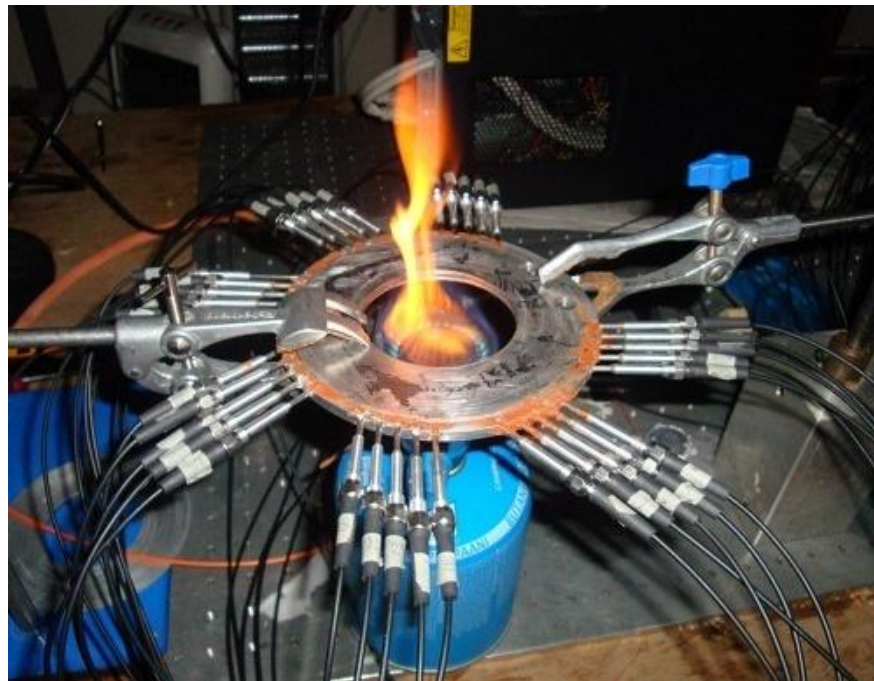


Figure 3. 13 Optical Array Gasket Testing Diagram

### 3.2.2 Engine Modification

The OHV pro engine was modified to investigate the natural gas FFP behaviors. To consider the alteration affects on engine performance, the engine undergoes some main aspect modifications and it consists of a fuel supply system reformation, a spark

ignition system creation, an OAG insertion part and a safety engine plate. The engine head is placed at 30 degrees to the horizontal desktop as in the original design of this engine exactly corresponding to the modification requirement.

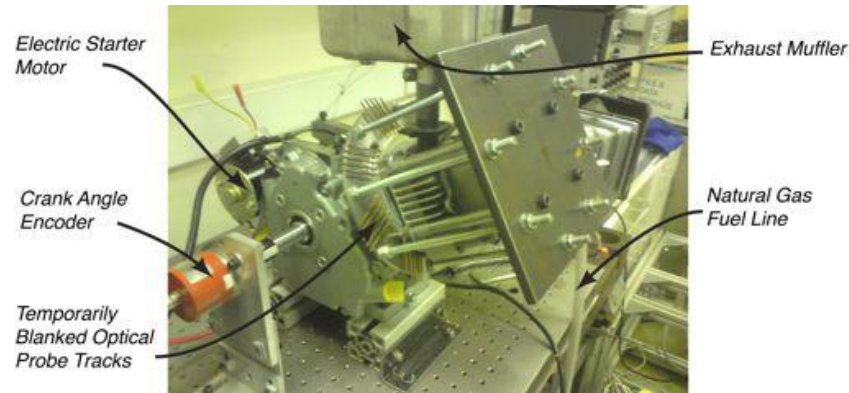


Figure 3. 14 The Modified Engine Test Cell in Laboratory

## Fuel supply components

The advantage of the OHV pro engine is that the supply system of the model engine is simple to modify to burn other fuels. Natural gas was used to investigate internal combustion behavior. In the laboratory, since the natural gas is clear burning, thus it is more ideal for observing combustion than the petrol fuels. Natural gas is more suitable than other fuels for analyzing methane, oxides and chemical reactions. Despite some relevant experiments that are developed to investigate gasoline or diesel engines for commercial purposes; the use of natural gas is the first choice to consider its pure burning phenomena and the new development of biomass fuels.

To convert the fuel supply system the fuel tank and assembly were replaced by the connection of a gas intake ring (Fig 3.15). From the a) photo, a ring gas tap was connected to the central gas supply pipe on one side. A gas intake volume controller on

the other side controls the flow ratio of natural gas. The gas supply tap is installed between the air filter and the carburetor.

The throttle and choke were modified. The choke remains the original control level, but there was greater modification to the throttle. In Figure 3.16, a carburetor is placed near throttle butterfly valve. After the modification, the throttle is controlled by a bolt and choke is controlled by a spring.

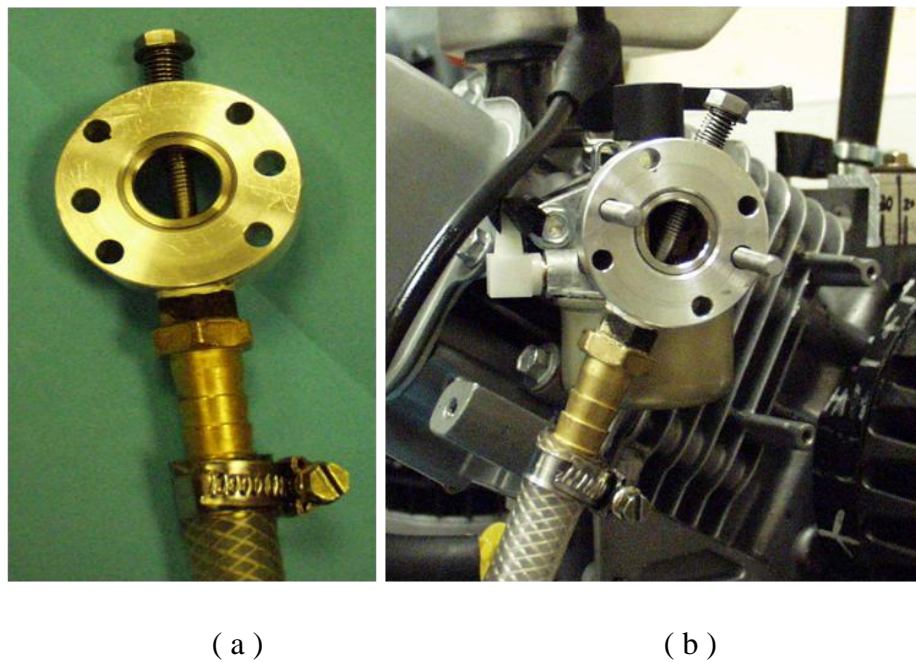


Figure 3. 15 The Gas Intake System Modification

Testing the alteration of supply system, the speed range is from 1500 to 2280 rpm with the engine governor removed. The various speeds are of research interest and the results suggest that the engine is running better in lean oxide condition than rich oxide condition.



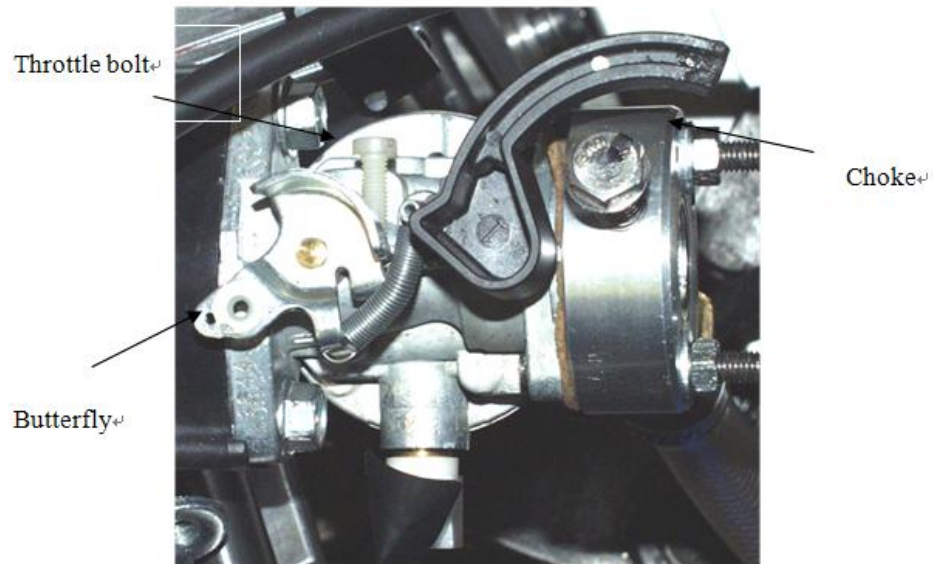


Figure 3. 16 Reformed Carburetor Control System

## Spark ignition components

The OHV pro engine is a spark ignition engine. The spark is controlled by an ignition circuit (spark coil). The ignition circuit (spark coil) delivers a high voltage charge to control the spark time. The ignition of combustion explosion on efficiency time was specified in section 3.2. The ignition coil is an auto ignition system which transforms the low battery voltage (commonly 12 volts) to the thousands of volts needed by the spark plugs. The ignition coil consists of a magnet transformer, a contact breaker and a capacitor (condenser). When the contact breaker closes, a low input voltage current flows from the battery into the primary winding of the ignition. Then the breaker opens; the much higher output voltages are generated by galvanomagnetic effect by the capacitor in the secondary coil. The output voltages are enough for supplying the spark igniting.

The OHV 206 pro is a single cylinder engine with a simple ignition system. The timing of spark ignition is only dependent on the process of transforming the voltage from low voltage to high voltage caused by flywheel rotations. However, the location of the ignition coil is not ideal for engine modification. The ignition coil is originally located between the flywheel and cylinder head. The magnet effect of ignition coil generates noises to detection system. Thus, the ignition coil has been rotated and placed in the bottom of engine. To consider the different ignition time between petrol and gas, the ignition coils placement around the flywheel was designed to be flexible. Approximately 15 degrees rotation movement space is applied by comparing with ignition time 22.5 degrees of the initial engine design. In the experiment, the engine ignition time is set to 27 degrees of Crank Angles.

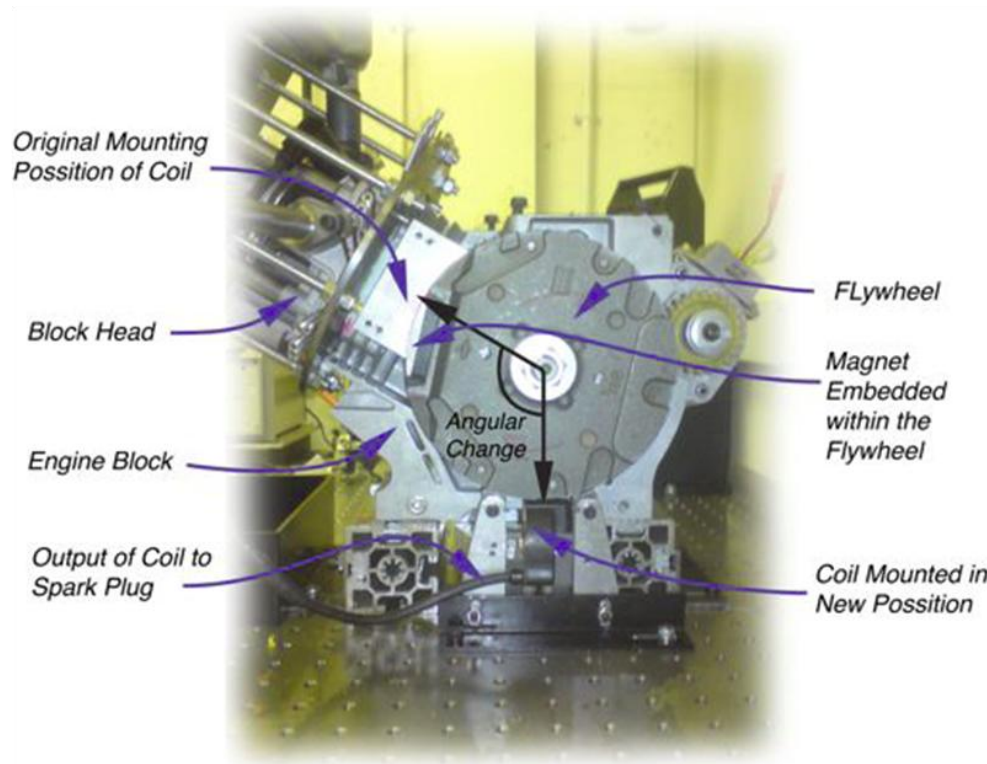


Figure 3. 17 The Ignition Coil Position Replacement

## OAG insertion components

The OAG is a critical component which allows the optical fibres access to the chamber to obtain combustion propagation information. A sandwich OAG was developed to meet the requirements. Two problems arose after the engine was modified. The interface surfaces between the OAG plates, chamber and cylinder head allowed natural gas leakages. To prevent leakages two pieces of the original gaskets were introduced as interfaces to both sides of the OAG plate (Fig 3.18).



Figure 3. 18 The Interface Function Gasket

During testing the engine was run at full power and under maximum pressure there was no gas leakage after the double gasket modification. Although the gaskets overcame the sealing problem the increased thickness of the OAG (6mm) thickness altered the compression ratio of the intake gas flow. The original compression ratio was 6:1 but after modification, the ratio was approximately 6.3:1. The high pressure from the anti-pressure engine plate, distorts the OAG and gaskets reducing them to less

than 5 mm. The modification of the gas intake system slightly altered the flow ratio and the combustion behaviors.

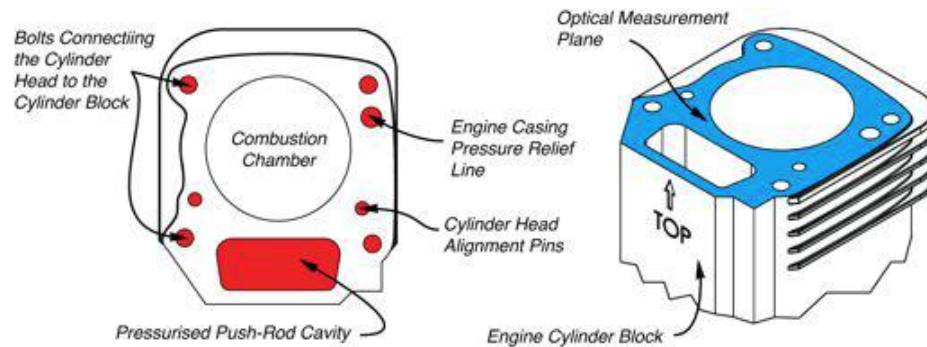


Figure 3. 19 The Sandwich Components including Cylinder head, Gaskets and Chamber.

## The body guard engine block

To ensure the engine running safely and stably, a 5 kg metal block is designed as a plate clamping unit to against the combustion pressure (Fig. 3.20). The highest pressure occurs in two places on the engine block, firstly at the interfaces between the cylinder head, OAG plate and chamber. The vertical pressure is up to a maximum of 41 Bar accompanying the high temperature combustion. Secondly force up to 20 N occurs at each fibre interface with combustion in a horizontal plane. To overcome the pressures, The engine block was desgined with two parts the upper plates and the lower plate. (Fig 3.20). The upper plate with engine block head are of great mass and coupled to the lower plate. The lower plate is designed to be installed outside the chamber and the interface with the OAG. The lower plate supports the OAG plate and fits the engine block head. The engine block head is to squeeze the cylinder, OAG

plate and chamber with a high iron plate. The iron plate has 8 shafts components for resisting the combustion pressure. To keep uniform pressure distribution on the OAG plate, 4 column sleeves are connected with the cylinder head. During testing the force on the shaft bolts is less than 13 KN. To ensure uniform pressure distribution on the plates, they are attached to the engine block carefully by carefully tightening opposite screws. Figure 3.21 illustrates the engine assembly. The large force from bolts makes the engine running safely and significantly reduces the pressure on the surface of the fibres. Super glue was used to hold the fibres firmly to the OAG plates.

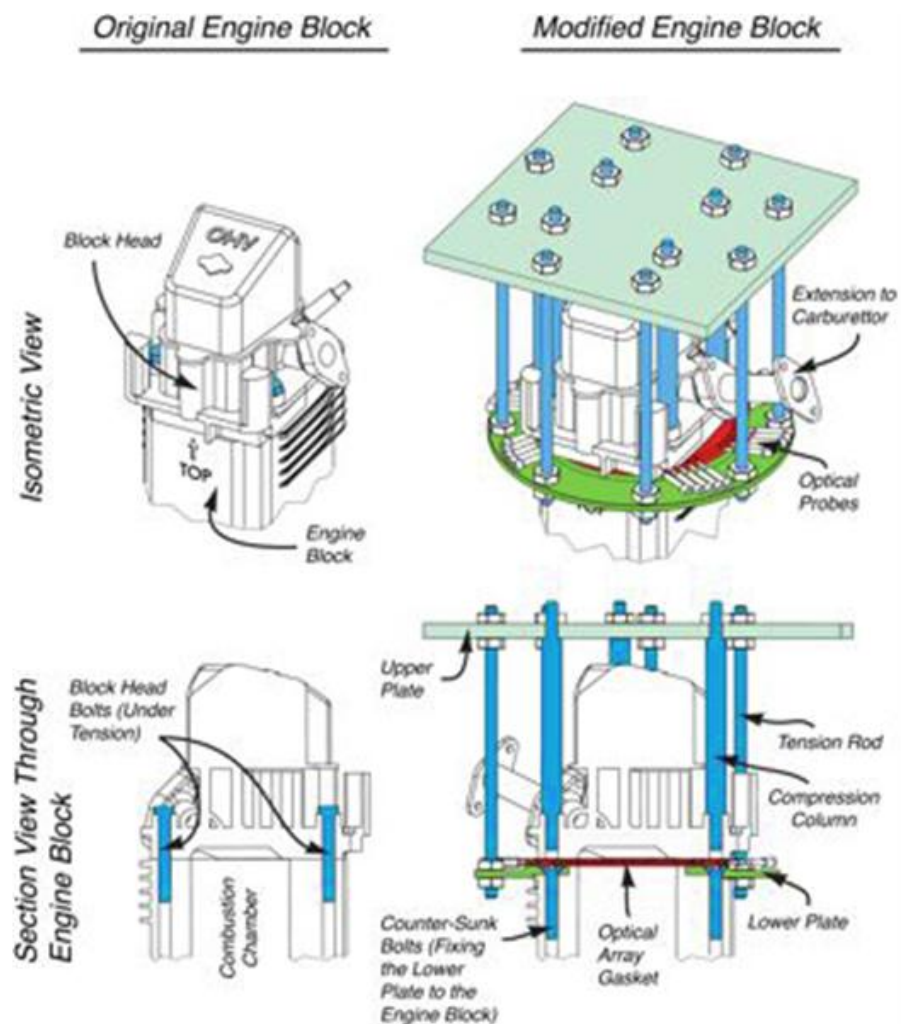


Figure 3. 20 Comparison of the Layout of the Original and Modified Engine

The sMART design of using a 'sandwich' method of OAG placement is achieved the requirement for tomography methodology in an internal combustion engine. Even through this presents a high quality modification to the original engine, it has been found that it could still be improved in some aspects which are discussed in further works section.

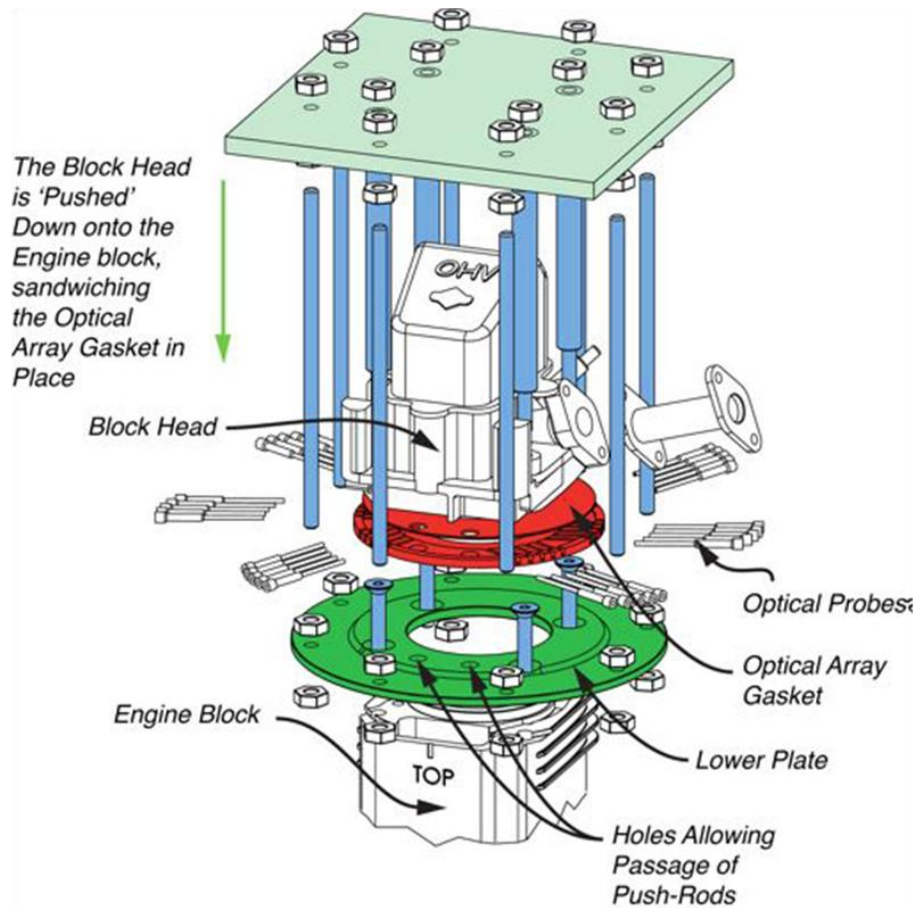


Figure 3. 21 The Modified Engine Assembly

## 3.3 PMT and Accessories Specification

### 3.3.1 Filter Selection

The combustion chemiluminescence is a chemical reaction and light emission process. The analysis of flame chemical reactants is significant to combustion research.

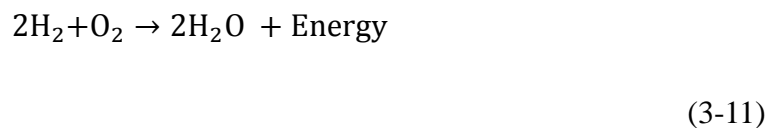
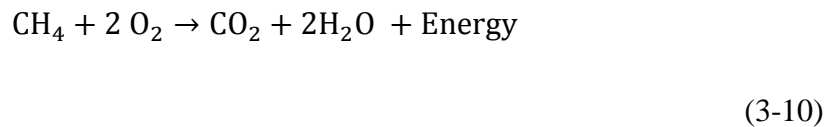


Thus, the composition and chemical reactions are briefly discussed as follows. Many quantitative measurements of hydrocarbon flame emission were reviewed by Gaydon [48]. In the test, natural gas is utilized as the fuel. Typically, the chemical composition of natural gas is:

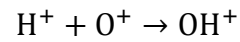
Table 3. 4 Chemical composition of natural gas [49]

Methane	CH <sub>4</sub>	70-90%
Ethane	C <sub>2</sub> H <sub>6</sub>	0-20%
Propane	C <sub>3</sub> H <sub>8</sub>	
Butane	C <sub>4</sub> H <sub>10</sub>	
Carbon Dioxide	CO <sub>2</sub>	0-8%
Oxygen	O <sub>2</sub>	0-0.2%
Nitrogen	N <sub>2</sub>	0-5%
Hydrogen sulphide	H <sub>2</sub> S	0-5%
Rare gases	A, H <sub>e</sub> , N <sub>e</sub>	Trace

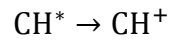
The main component of natural gas is CH<sub>4</sub>. The reaction between hydrocarbon and oxygen is an essential indicator of flame front propagation. The formulas of the main chemical reactions are:



During reacting, there are some interactive products:

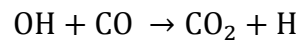


(3-12)

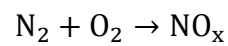


(3-13)

Other reactions occur, for example:



(3-14)



(3-15)

From the formulas it is found that the methylidyne radical ( $\text{CH}^*$ ) and hydroxyl radical ( $\text{OH}^*$ ) as main reaction components are the most important types of combustion explosion.

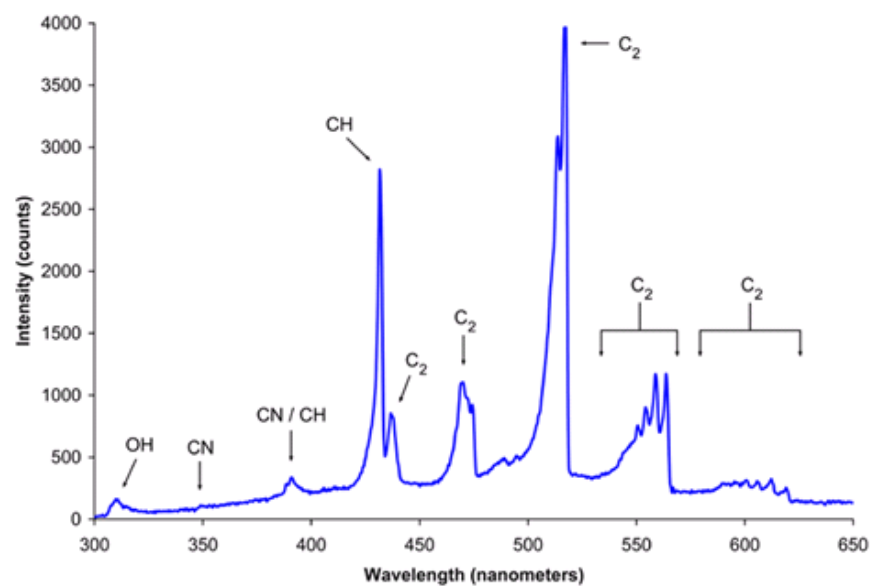
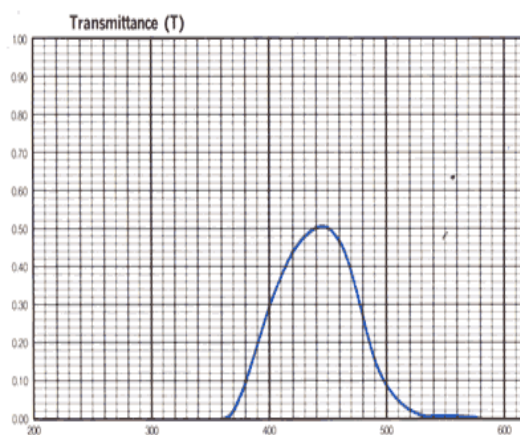


Figure 3. 22 Typical Blue Flame Spectrum [49]

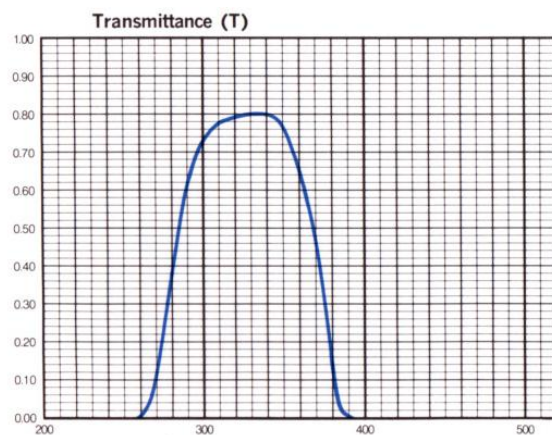


As it is illustrated (Fig. 3.22), the strongest intensity peaks represent CH\* and OH\* elements. CH\* has two emission peaks at 440 nm and 390 nm which corresponds to  $A^2\Delta - X^2\Pi$  and  $B^2\Sigma - X^2\Pi$  transitions in the range of blue flame spectrum; OH\* peak near 308 nm which corresponds to  $A^2\Sigma^+ - X^2\Pi$  transition in the UV range of electromagnetic spectrum [50].

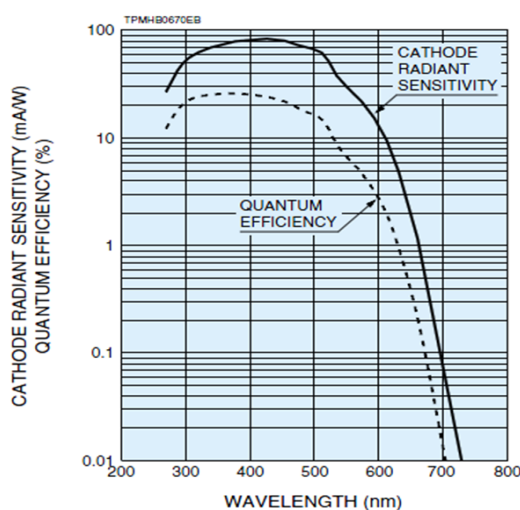
To analyze Blue flame and UV flame behaviors, two bandpass filters were used to trace the elements in practice: the HOYA B-440 blue filters are employed to trace CH\* (Fig. 3.23 a); the HOYA U-340 Ultraviolet (UV) filters are used to trace OH\* elements (Fig 1.3 b). In the experiment, it has been suggested to use UV filter with a wide bandpass range from 300 nm to 350 nm but not particularly at 308 nm to ensure capture the UV emissions (Fig. 3.23 b). The transmittance ratios of Blue and UV emissions have been evaluated before project set up. The blue filter specification has a peak transmittance nearby 440 nm and the ratio of transmittance is about 50% (Fig 3.23 a). The UV filter has a wide peak range from 300 nm to 350 nm and the ratio of transmittance is about 75% (Fig. 3.23 b). Combination with the transmittance ratios of PMT specification (Fig. 3.23 c), the Blue transmittance of PMT is about 75% and the UV transmittance of PMT is about 50%. Thus, the transmittance ratio of UV and Blue flame is approximate 35%. In the system, BH4001-PMMA fibre cables are used and their transmission loss is roughly less than 3% in the test (Fig. 3.23 d). Therefore, the transmission ratio of the POET system is generally 34%.



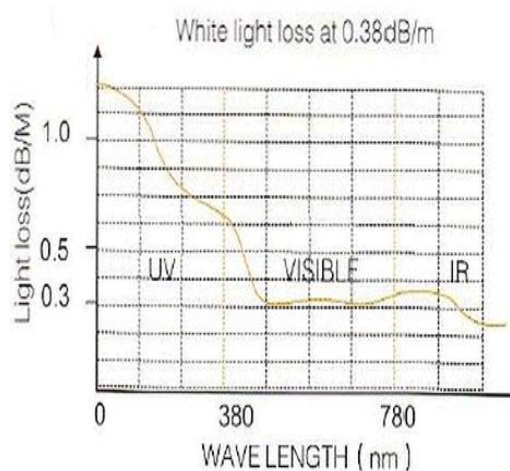
( a ) Blue Filter Spectrum



( b ) UV Filter Spectrum



( c ) PMT specification diagram



(d) PMMA fibre loss

Figure 3. 23 Blue, UV Filter, PMT and Fibre loss Specification Diagram (Appendix D)

Quantitatively, since Blue and UV chemiluminescence are significant phenomenon of combustion expands, many previous researches are basis of these two reactants and the studies are commonly using Plane Laser Induced Fluorescence (PLIF) technique [51-53]. Generally, Blue and UV flames yield the structure of the reaction region. The  $\text{CH}^*$  corresponds to the blue light which may excite the carbon reaction chain [54]. The CH and oxygen reaction produce  $\text{OH}^*$  which corresponds to the UV

emission region. Although the  $\text{CH}^*$  radical exists in a narrow spatial and temperature region for a short –life, it is recognized as a flame front marker which is present at the flame heat release location. UV chemiluminescence, known as a skin of the flame front, is recognized as a marker of the burning region and the unburnt region of flame whose behaviour contribute to the analysis of the velocity of the FFP. Figure 3.24 illustrates OH of UV flame and CH of Blue flame behaviours of a laminar burner flame in single shot by PLIF technique. The structure of CH radical is very thin in left image; the dark region in right image is OH radical.

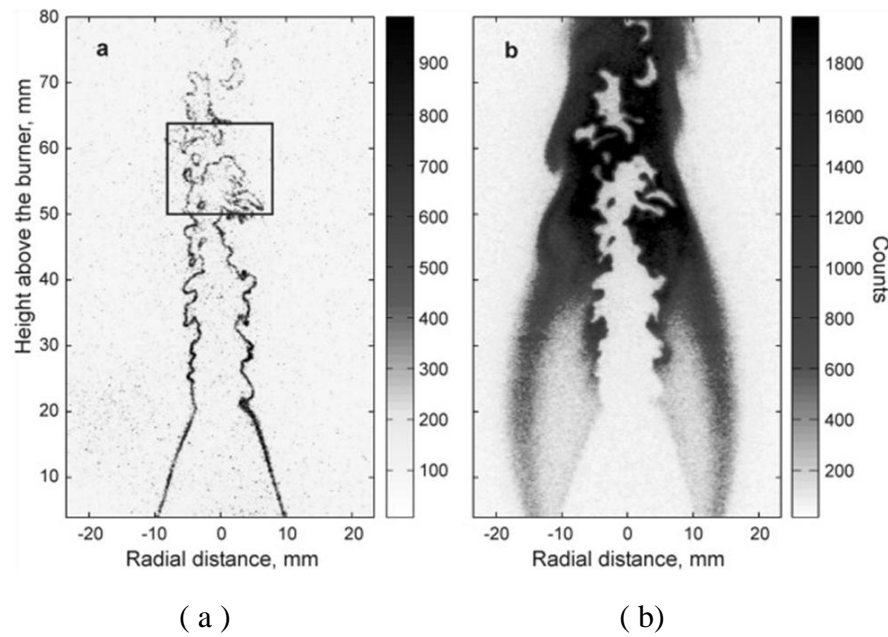


Figure 3. 24 Single-Shot PLIF Images of Flame: (a) CH and (b) OH [55]

Many earlier studies are based on a burner flame or laminar flame for analyzing UV and Blue flame chemiluminescence. However, there have been a few quantitative experiments for measuring UV and Blue performance inside engines. In this project, UV and Blue flame characters are traced and compared to investigate in-

cylinder combustion.

### 3.3.2 Optical Fibre

The 40 two meters long optical fibres and probes pass information about combustion from the cylinder to the PMT modules. The optical fibre probe instrument consists of a lens head, a silica fibre, steel cladding and a SubMiniature version A (SMA) connector. The two meter fibre is a Polymethyl-Methacrylate Resin (PMMA) type with a high light transmission. (Fig 3.25)

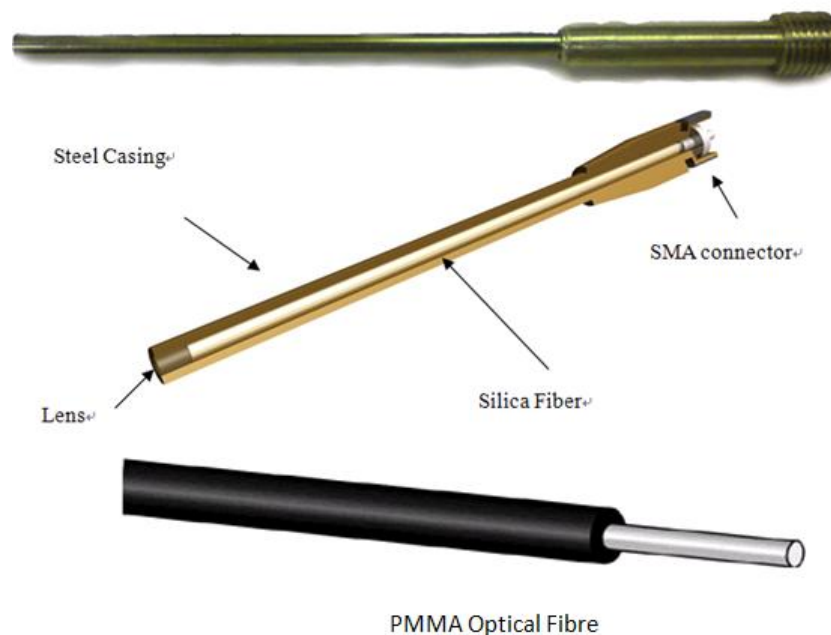


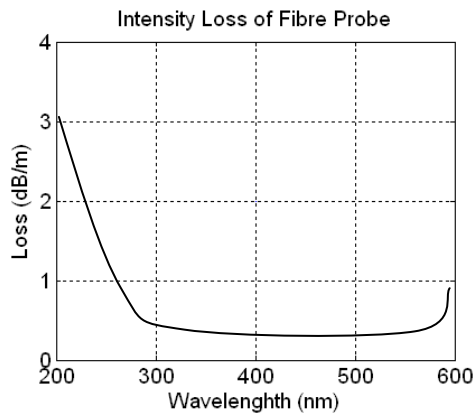
Figure 3. 25 Diagram of Fibre and Probe Structure

The fibre probe is 55mm long and has a 2 mm diameter core. The isolated fibre probe exhibited good performance under combustion pressure and temperature. The probe is subject to operation limits of 20N ejection force and a maximum ambient temperature of 200°C. If these are exceeded the lens front may pull out during engine

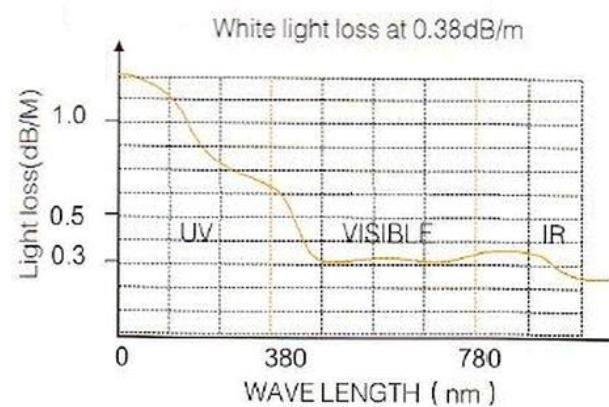
running. Table 3.5 is specifications of fibre and probe.

Table 3. 5 Specification of Fibre Probe and PMMA Fibre

Specification	Fibre Probe	PMMA Fibre
Fibre length	55 mm	2 meter
Core diameter	1 mm	1 mm
Casing diameter	2 mm	2.2 mm
Core materials	High Purity Synthetic Silica	Polymethyl-Methacrylate Resin
Casing materials	Steel	Fluorinated Polymer
Transition Spectrum	180 nm -1200 nm	300 nm – 1200 nm
Loss in Fibre	0.014 dB	0.3 dB
Connector	SMA	SMA
Aperture angle	$22^{\circ} \pm 2$	0.58



( a ) Fibre Probe



( b ) PMMA Fibre

Figure 3. 26 Signal Transmission Loss in Probe and Fibre

Furthermore, losses of signal occur when it is travelling inside the probe. The losses curve is illustrated the minimum loss locates in the range 400-500 nm spectrum

(Fig. 3.26 a) which is corresponded to the CH. The PMMA is suitable for short distant light transmission with a 0.25 dB/m loss at spectrum 450 nm (Fig. 3.26 b).

The acceptance angle of the fibre determines the scale of induced information from combustion. The fibre and OAG modification specification specifies a vertical acceptance angle of up to 10 degrees and a constant horizontal angle of 20 degrees (Fig. 3.27). The large volumes of combustion information obtained were sufficient for mathematic algorithm analysis. The vertical angle was reduced to less than 4 degrees sometimes by the pressure causing some information loss.

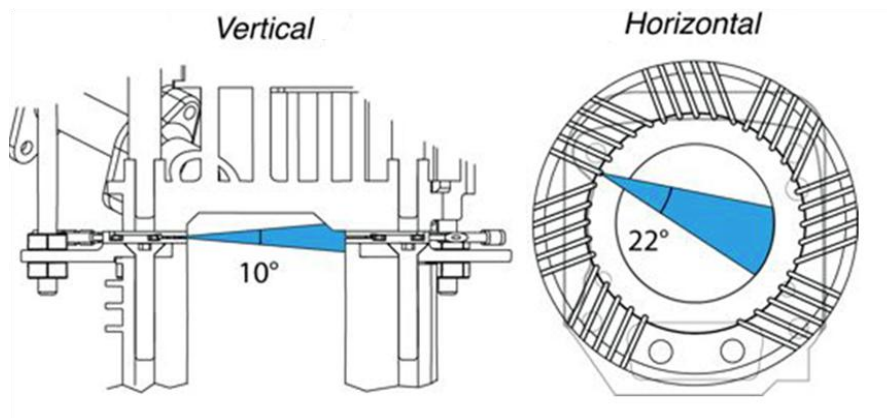


Figure 3. 27 The Aperture of Optical Fibre in Vertical and Horizontal

### 3.3.3 PMT Connecting Interface

A 1 meter fibre was used to connect the PMT detectors and optical fibre probes. The fibre is connected on one side to the probe by the SMA connector and the other side is connected with the PMT by an in-house designed interface for placing the filters (Fig 3.28). A black box, 5 mm depth and 5 mm width was designed to hold the filters. A small rubber o-ring was used to protect the filters from galling. The 1 meter

fibre was connected to a SMA connector to transmit the signals from the engine. Light losses occur within the 1 meter fibre, at the fibre-probe interface and at the filter to PMT interfaces. Light loss in the new OAG design is discussed in the further work section.

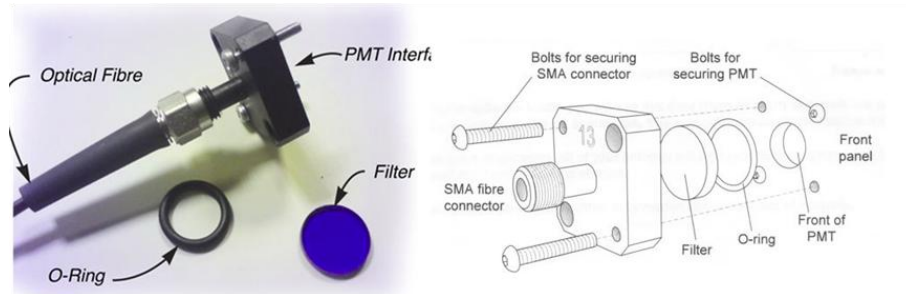


Figure 3. 28 Black Box Interface between Fibre and PMT

### 3.3.4 Photo Multiplier Tube

A tomographic array was constructed from 40 photo multiplier tubes (PMTs) to receive the transmission signal from the flame propagation of the engine. The PMT detector is a core component of the POET system whose function is mainly detecting combustion. The PMT specification and are now discussed.

#### Introduction

Photodetectors (photo sensors) can be classified in three types by their operating principle: external photoelectric effect, internal photoelectric effect and thermal types. The external photoelectric effect occurs when a semiconductor is subjected to a light source in a vacuum. Photons are emitted by energy stepping from the surface into the vacuum. The PMT is a highly sensitive external photoelectric type

sensor with an excellent response frequency. The PMT has a high frequency response, low noise and high gains especially in weak signal conditions. It is widely used as a vacuum photo sensor in laboratory measurements, medical treatments, particle physics and astronomy fields. The photodiode is a major internal photoelectric effect sensor. It is used in optical communication measurements because of its miniature size and high sensitivity. Thermal type sensors are used in temperature detection because of their low sensitivity and independence of wavelength.

Table 3. 6 Comparison of Photo sensors Performance

Photo sensor characteristics	Photo Multiplier tube	Phototransistor	Photodiode
Wavelengths range	115-1700 nm	200-2000 nm	400-1100 nm
Sensitivity	Excellent	Very Good	Very Good
Response Frequency	Excellent	Good	Good
Ambient Noise Performance	Fair	Very Good	Very Good
Stability	Very Good	Very Good	Good
Weak signal sensitive	Excellent	Poor	Poor
Size	Large	Small	Small

The photodiode which was used in previous test exhibited excellent performance for its small size and high sensitivity over a large wavelength range. The photodiode is very responsive typically in micro second level, sufficiently quick for use in measuring combustion propagation. However, the PMT response is in nanoseconds and it is much more sensitive to weak signals. Therefore, the PMT is utilized in experiment.



In a natural gas fuel engine, the internal combustion propagation is a complex chemiluminescence process accompanied by chemical reactions that mainly occur between methane and oxide. The major products of the energy release reactions are  $\text{CH}^*$  and  $\text{OH}^*$  elements. To investigate combustion propagation inside the chamber of the engine using optical diagnostics, it is necessary to measure some special elements that emit light during burning.  $\text{CH}^*$  has a peak wavelength value near 440 nm in the blue region.  $\text{OH}^*$  has a peak wavelength near 330 nm in the UV region. UV and CH elements are traced by a PMTs array with spectrum bandpass filters. The analysis was covered in section 2.1. After analyzing the capable of integrate of PMTs, a model R8900-00-C12 of Hamamatsu PMT are employed (Fig 3.29). It is present good response sensitivity from 300 nm to 650 nm of spectrum (Fig 3.29). This type of PMT is small enough to set up an integrated PMTs array with a powerful computer system module.

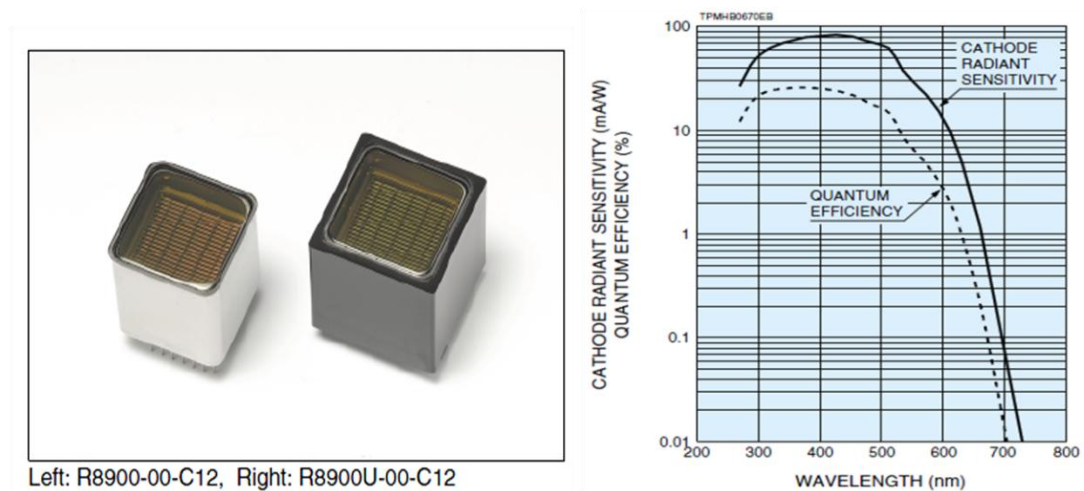


Figure 3. 29 The PMT Chips and the Spectral Response of PMT Module [56]

## Optical characteristics of the PMT

The PMT sensor is design for measuring the quantity of light radiation in intensity units. The relationship to the light energy is shown in equation 3-16.

$$E = h\nu = h \times \frac{c}{\lambda} \quad (3-16)$$

Where  $h$  is the Planck constant  $6.626 \times 10^{-34}(\text{J} \cdot \text{s})$ ;  $\nu$  is the frequency of light;  $c$  is the free space velocity of light  $3 \times 10^8 \text{m/s}$ ;  $\lambda$  is the wavelength (nm). The equation can be rewritten substituting  $E$  in  $eV$  where  $1 \text{ ev} = 1.6 \times 10^{-19} \text{ J}$  in equation 3-17 and the  $h, c$  are constants:

$$E(eV) = \frac{1250}{\lambda} \quad (3-17)$$

Where, the energy is proportional to the wavelength.

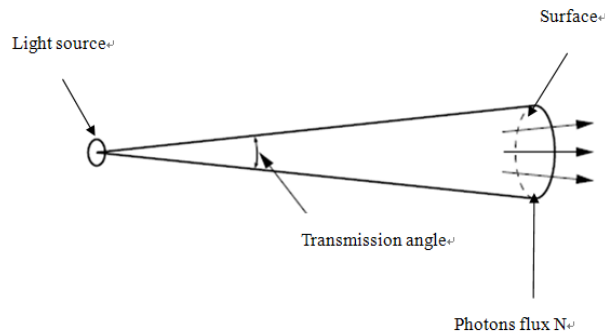


Figure 3. 30 PMT Intensity Units Principle

PMT light energy is calculated from the quantity of photons reaching a surface (Fig 3.30). If the photons in flux per second is  $N$  and the wavelength is  $\lambda$ , then the intensity  $W$  is:

$$W = NE = \frac{Nhc}{\lambda}$$

(3-18)

Hence

$$W = NE = \frac{N \times 2 \times 10^{-16}}{\lambda}$$

(3-13)

Light intensity can be represented in two ways: by power ‘Watts’ (  $W$  ) and by the quantity of light in Lumens (‘ $Lm$ ’) related to the visual intensity of light.

### 3.4 Compact POET Computer System

To achieve the implementation of PMTs tomography system in the lab, an intelligent PMTs embedded computer system was manufactured by Etalon Research Lab for embedding the PMT components with a computer (Fig 3.31). The POET computer system consists of 40 Hamamatsu PMT modules, a high speed DAQ card, a high speed computer with dual core 2.8 GHz Intel CPU, 4 Gigabytes of memory and windows XP OS. The PMT modules are mounted with a SMA fibre optic connector interface box which is used to place filters. The DAQ card transforms the optical signals from the PMT to a digital signal for processing by the computer. The flame front propagation of the IC engine was sampled by the DAQ card is fast to 350 ns.

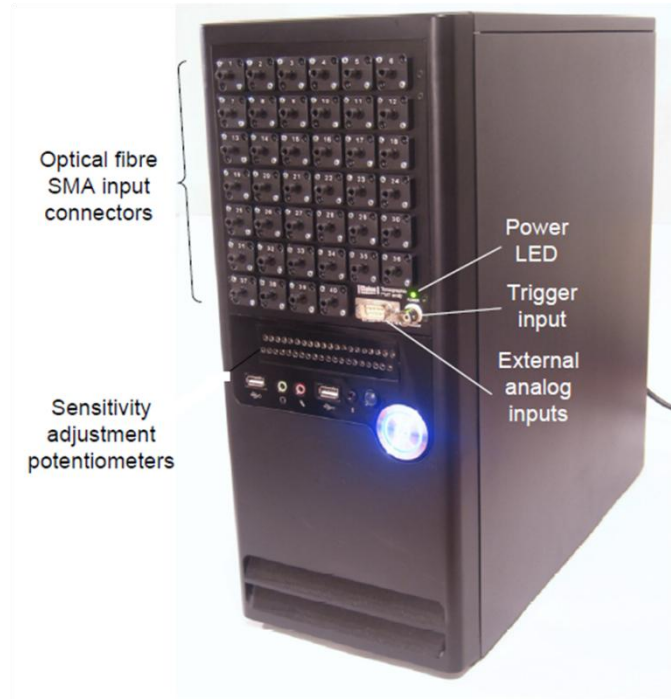


Figure 3. 31 Intelligent POET Tomography Computer System

### 3.4.1 Tomography Computer System Implementation

The implementation of a tomography computer system consists of hardware operation and software application.

#### Hardware operation

The interface components are controlling the system hardware. The SMA connector interface with behind PMTs is dismountable for changing filters (Fig 3.32). The SMA interface of each PMT can be removed by unscrewing the securing bolts. In the SMA Black box, a 2-3 mm thickness and 12.5 mm diameter glass filter can easily be changed. The filter is protected by a lactoprene o-ring placed front of PMT sensor.

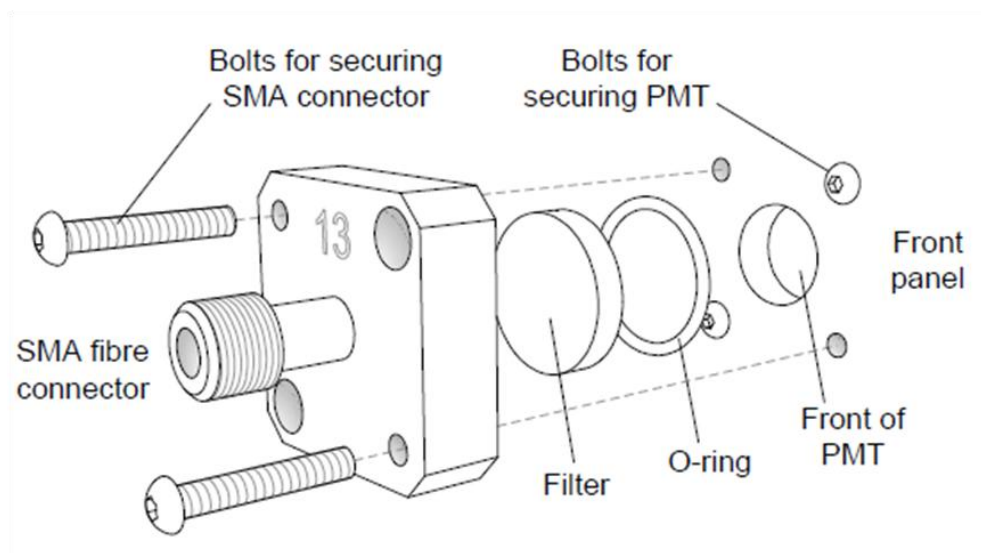


Figure 3.32 PMTs SMA Interface Schematic Diagram

A sensitive potentiometer was fitted to each PMT to adjust the gain. Turning the potentiometer screw clockwise increases the sensitivity to maximum after five rotations.

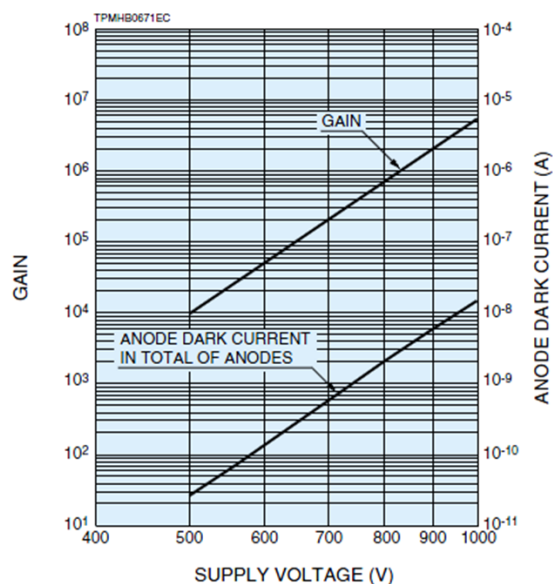


Figure 3.33 The Gain Characteristics of PMT versus Supply Voltage [57]

# Software application

The software was specially designed for tomography data recording. The software includes channel selection, recording, saving and signal viewing modules (Fig 3.34). The channel selection interface has 40 channel selection boxes for each PMT. 8 external input channels are preparing for external analogy input system. The input voltage panel is to alter the PMT gains. The range is divided into 4 levels: 0-1 voltages, 2 voltages, 5 voltages and 10 voltages.

The DAQ card records sampling signals from the PMT sensor. The inter time between each sample signal ranged from 350 ns to 100 us by operating the ‘Sampling freq.’ panel.

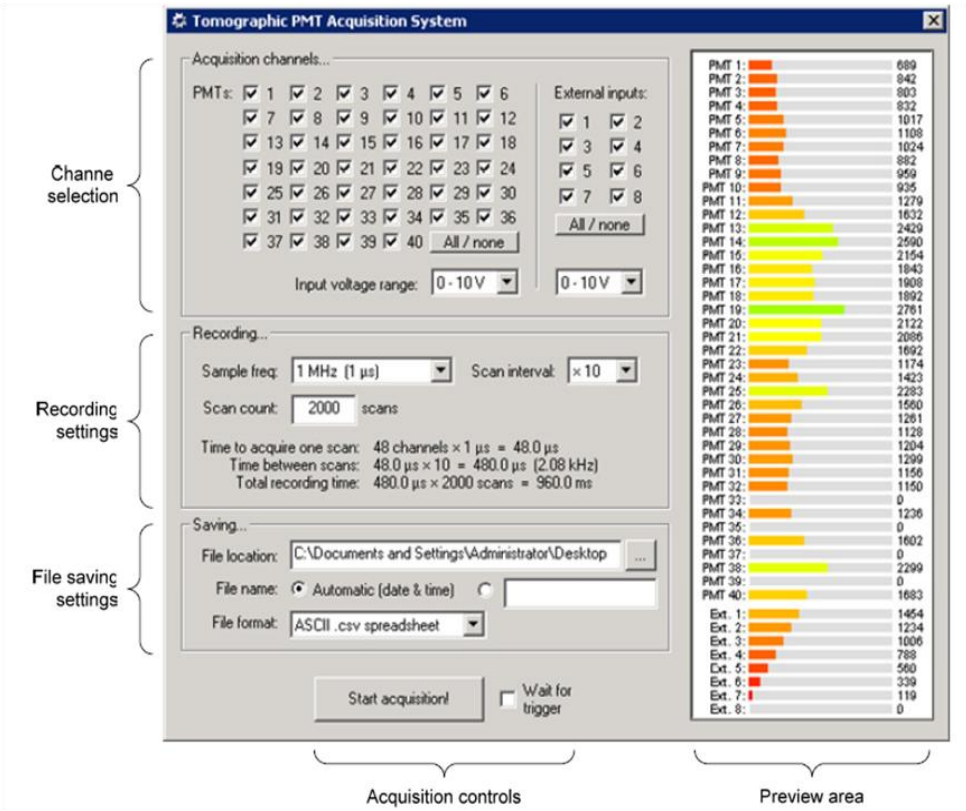


Figure 3. 34 Software Operation Interface

Furthermore, the sampling can be taken in three time intervals by controlling the scan interval panel (Fig. 3.33): 1 times, 5 times and 10 times. With the increasing of interval numbers, the sampling frequency rates decrease as 1, 1/5 and 1/10. Thus, the total scanning time can be expressed:

$$t = \left( \frac{1}{\text{sampling frequencies}} \right) \times \text{numbers of channels} \times \text{scan intervals} \quad (3-19)$$

The scan count is a count number that how many sampling time  $t$  has been expected to detect. Therefore, for instant, if the sampling frequency is 1MHz, the scan interval is 10 times and the scan count is 2000. Thus, the total scanning time is going to be:

$$T = 1\mu s \times 40 \times 10 \times 2000 = 800 \text{ ms}$$

The saving interface is the format of outputs signal and can be saved in three formats: Matlab profiles, Text note profiles and Micro excel profiles. The intensity viewing interface is a preview of instant signal intensities. The maximum displaying of intensities is 5000 in maximum.

### 3.4.2 Hardware Components

The embedded PMTs module comprises an independent power supply of PMTs, PMTs, PCB board power control, a sensitivity potentiometer with a ADlink connection to the DAQ card (Fig 3.35). In the embedded system there is a 15 voltages PMT bipolar power supply and a PCI-2208 ADlink CPCI board is for supporting the DQA card.

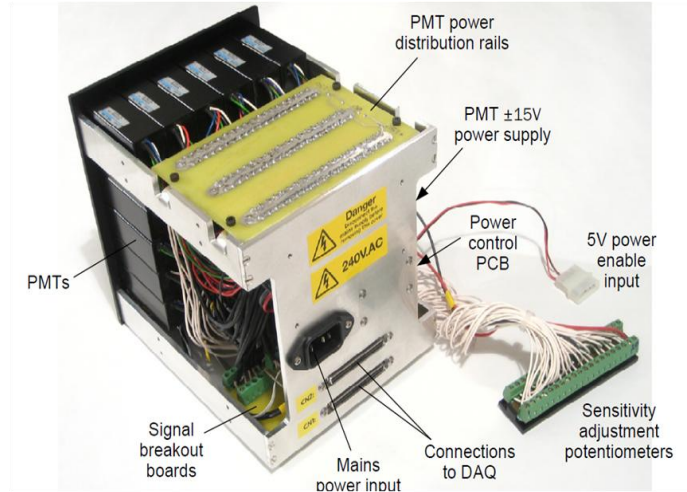


Figure 3. 35 PMTs Tomography Computer System Hardware Components

40 PMTs modules are employed and the Hamamatsu H5784-04 consists of 40 modules. Channels 33, 35, 37 and 39 are empty. Channels 1 to 6 have different sensitivities to the others. Prior calibration is therefore necessary.

Table 3. 7 PMTs Distribution of Embedded Module in Series Number

PMT channels	Serial number
1 to 6	58690025 to 58690030
7 to 32	60690002 to 60690027
34	60690028
36	60690029
38	60690030
40	60690031

## 3.5 Summary

Chapter 3 introduced the engine modification procedure and the compact POET system. In the experiment, a commercial OHV engine was modified for



combustion measurements purpose. In modification, the gasoline fuel system was substituted by a natural gas intake valve system. The ignition system was altered for setting up purposes. The OAG gasket was specially designed for placing the detector fibres. To make sure the safety of engine operation, a safety block was developed to anti the great pressure from combustion explosion. Since these modifications had changed the engine performance slightly, the altered engine was operated stably during testing. In the detecting system, a compacted PC was manufactured by Etalon research lab for collecting flame intensity. The system consists of 40 PMTs, DAQ card and a computer. 40 fibres were placed surrounding engine cylinder for tomography purpose. The flame tomographic projections were transmitted from fibres to PMTs. Then the signal had been converted from photons to numerical values. Therefore, the combustion was analyzed using these projections data. In conclusion, the POET system has a good performance to collect combustion signals even the flame is in fast turbulent.

## Chapter 4.

# Computational Methodology

The computational methodology of this project uses the Radon Transform Technique (RTT) and the Algebraic Reconstruction Technique (ART) to collect signals and reconstruct the flame front. In image reconstruction, the software named ‘Array MART’ has been developed to reconstruct the tomographic images. The software was initially designed and developed by previous OEL group students for other tomography projects. To ensure the old version Array MART software works well in the POET project, the software has been improved by two main aspects based on the previous version of source code. In this new version, firstly the intensity with spark ignition signals of one complete four stroke combustion can be automatically selected and filtered for reducing noise errors. Secondly, in the visualization part reconstructed images of initial version only use the default RGB (Red, Green and Blue) colourmap to present the results. However, in the new version, Jet and Hot colourmap have been applied in image visualization. Nevertheless, after evaluation and simulation of previous versions, the numerical results display low averaged errors (details in chapter 4.3.3). Thus, in the new version, the computation and algorithm of software have not been changed and the main algorithm is still MART (Multiplicative Algebraic Reconstruction Technique).

In the signal collections, when a parallel light beam crosses an object its outline

is projected at a constant angle on the screen. The tomography technique uses multi light array crossing at various angles. The 2D and 3D images of the object are reconstructed using algorithms. Since the light beams pass the object, the images mostly are approximate in terms of attenuations of luminescence. The attenuation coefficient (transmission loss) is the reduction in intensity of a luminous light beam by scattering and absorption while crossing a medium. The attenuation coefficients in dB/km are given by [58]:

$$\alpha = 10 \times \log_{10} \frac{I_0}{I} \quad (4-1)$$

where  $\alpha$  is the attenuation coefficient;  $I_0$  is the luminous intensity before attenuation;  $I$  is the luminous intensity after attenuation. The intensity after attenuation is given by the natural logarithm equation:

$$I = I_0 \exp(-\alpha) \quad (4-2)$$

The attenuation intensity  $I$  can be obtained in an exponential expression. If the attenuation position of an object is  $f(x, y)$  as shown in Figure 4-1, the expression can be rewritten as:

$$I = I_0 \exp \int f(x, y) ds \quad (4-3)$$

Assuming an Euclidean plane  $\mathcal{R}^2$ , the value of vector  $s$  can be expressed by:

$$s = x \cos \theta + y \sin \theta$$

(4-4)

Then, the projection point  $p(s, \theta)$  can be obtained:

$$p(s, \theta) = \iint_{-\infty}^{\infty} f(x, y) \delta(x \cos \theta + y \sin \theta - s) dx dy$$

(4-5)

This equation is known as the Radon Transform formula. If a parallel light beam crosses an object  $f(x, y)$  at an angle  $\theta$ , then the original value of the object can be obtained from the projection value using the inverse Radon transform technique.

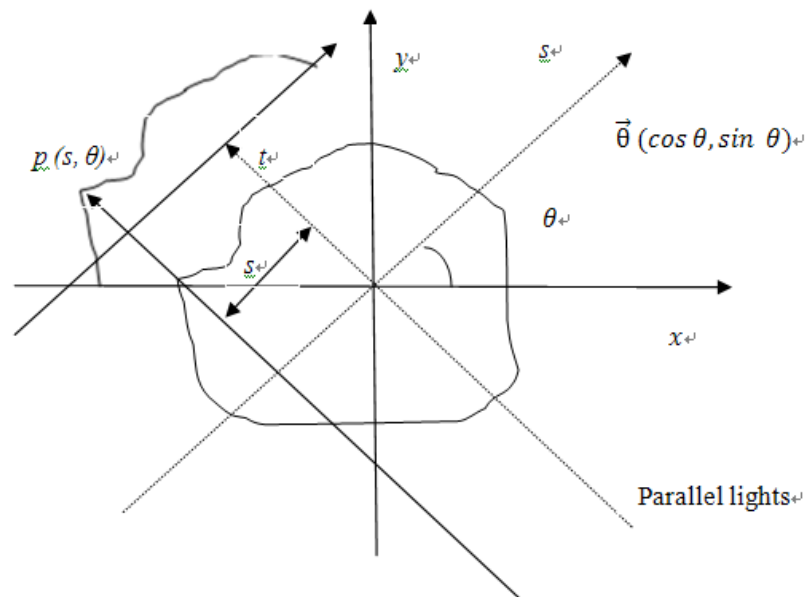


Figure 4. 1 Tomographic Reconstruction Technique in the Euclidean Plane

## 4.1 Computed Tomography

### 4.1.1 Computed Tomography Concept

Tomography is developed to visualize the internal structures of an object using parallel light beams or fan beam projections. It is typically used in Radon transform algorithms. The tomographic technique gives a physical solution to setting up

diagnostic systems to detect full view projections of a target. It provides a mathematical solution to simulate approximate models of objects. It is used in studying optics and in clinical research areas of Computed Tomography (CT). In Tomography, two solid triangles are viewed in a plane. When the objects are photographed from the side or front, only parts of the objects can be captured because the viewing angle is blocked by obstacles. The tomography technique is used to photograph the objects from both the side and front. Computational simulation methods can be applied to recreate a full view of the objects. ‘Tomography’ is to measure objects from different angles.

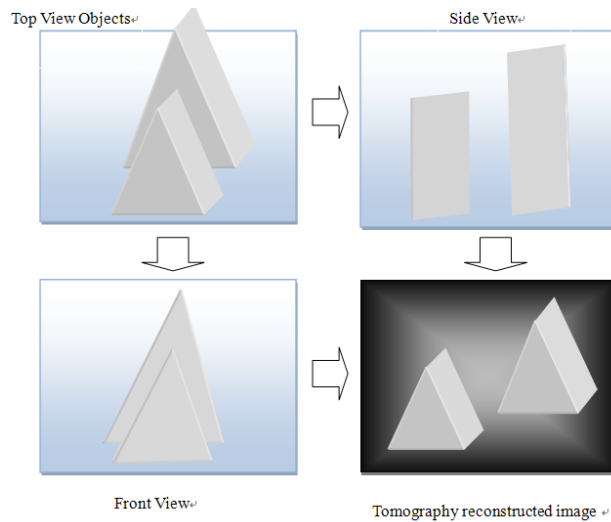


Figure 4. 2 Tomography Reconstruction Technique Concept Diagram

In computed tomography, the physical target is modeled mathematically. If the objects in Figure 4.2 are substituted by a  $2 \times 2$  matrix (Fig 4.3 (a)), the relationship between each variable is:

$$\begin{cases} x_1 + x_2 = 10 \\ x_3 + x_4 = 7 \\ x_1 + x_3 = 5 \\ x_2 + x_4 = 12 \end{cases}$$

(4-6)

Thus, the value of each variable is deduced:  $x_1=2$ ;  $x_2=8$ ;  $x_3=3$ ;  $x_4=4$ . A math matrix can then be constructed. (Fig 4.3 (d)) is ‘visualizing’ the objects mathematically.

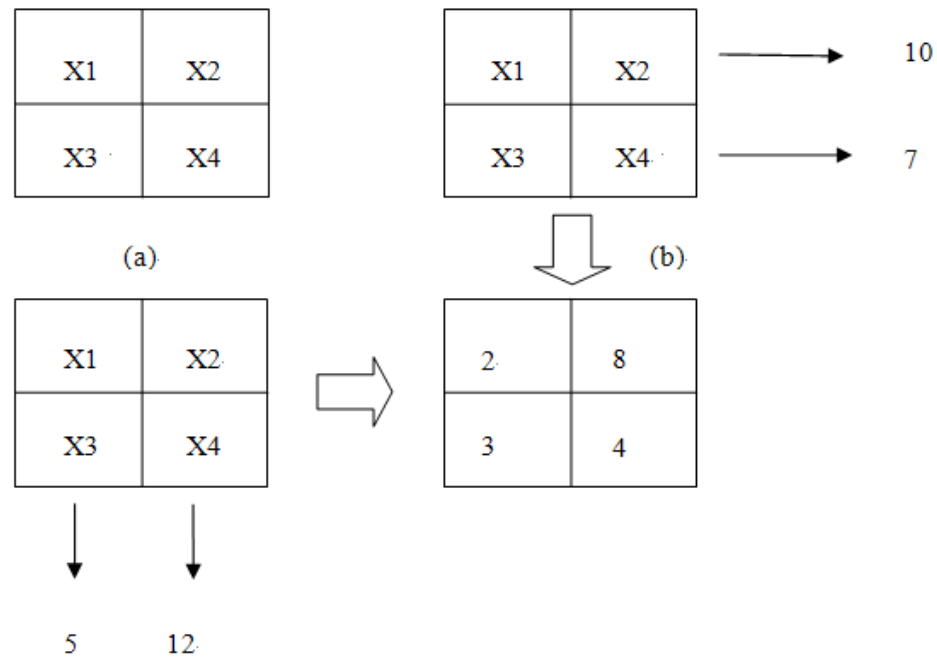


Figure 4. 3 Tomography Reconstruction Technique in Mathematics

### 4.1.2 Tomography Mathematics

Tomographic math is used to collect projections of the object, estimate the signal loss, calculate the back projections of the object, and compute an approximate model of the observed target.

#### Projection

In linear algebra mathematics, a projection is considered as a linear transformation of an object from a vector space to a plane. Points (x, y, c) of one slice of a 3 dimensional object can be mapped to points (x, y, 0) in two dimensions on a plane. The transformation of the 3D object linearity points to a 2D plane is a geometric

projection. When a uniform parallel light beam passes a transparent object (Fig 4.4), the outline of the object is projected on a background plane. The linear projection of a series of points  $(x_1, y_1)$ ,  $(x_2, y_2)$ ,  $(x_3, y_3)$ .....,  $(x_n, y_n)$  from a cylindrical object is at the position  $(\delta, \gamma)$  located on the background plane. The point  $(\delta, \gamma)$  is a point carried with subsequent information of linear points of the object slice.

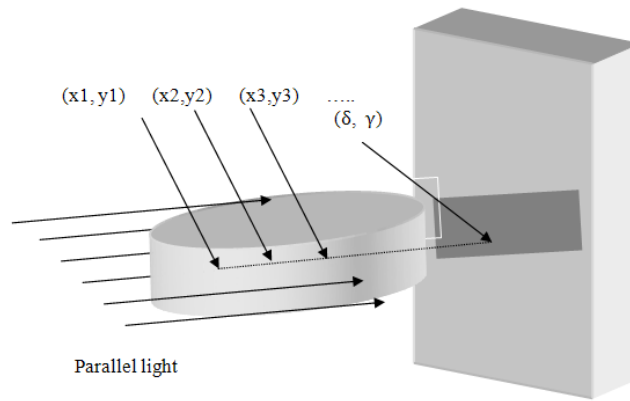


Figure 4. 4 The Rectangle Projection of Cylindrical Object on the Plane

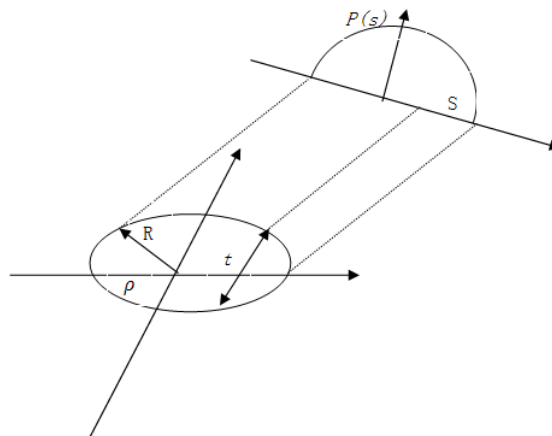


Figure 4. 5 Projection of Object in a Plane.

It is supposed that the cylinder consists of hundreds of discs. In the X-Y coordinate system, the density of disc is  $\rho$  (Fig 4.5). The time that light takes to cross

the object is  $t$ . The projections are on the  $(s, \theta)$  coordinate system plane. Then, the projection  $P(s)$  is expressed by the equation:

$$P(s) = \rho t = 2\rho\sqrt{R^2 - s^2} \quad (4-7)$$

Where  $R$  is the radius of the X-Y plane,  $s$  is the distance between each parallel light beam and  $|s| \leq R$ . If the light crosses the object at an angle  $\theta$  (Fig 4.1),  $s$  can be evaluated by  $\theta$  in the X-Y plane using equation 4-4. The value of the projection  $P(s)$  is only dependent on the incoming light angle  $\theta$ . Then, consider a light beam crossing several objects in  $(s, \theta)$  coordinate (Fig 4.6), the linear integrated projections of  $P(s, \theta)$  can be evaluated in equation:

$$P(s, \theta) = P(S_1, \theta) + P(S_2, \theta) + P(S_3, \theta) + \dots + P(S_n, \theta) \quad (4-8)$$

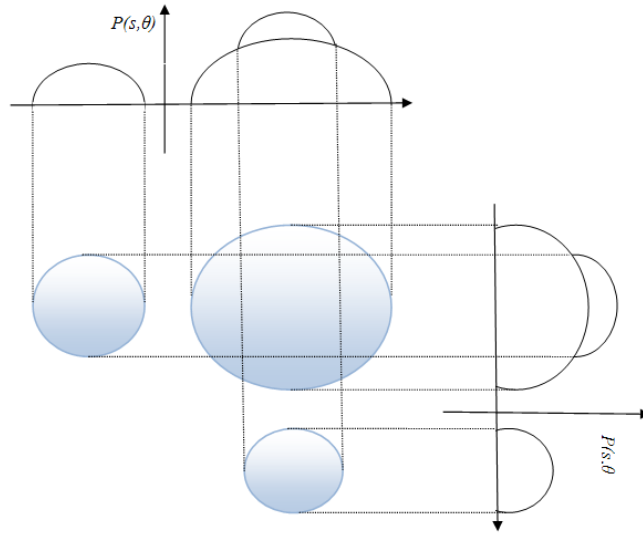


Figure 4. 6 Projections of Multi Objects in Different View Angles

The expression can be described in mathematics by a complex matrix. For



example, a given  $2 \times 2$  matrix (Fig 4.3) is employed to substitute the objects mathematically. The projection paths of the crossing section are described by variables  $a_{ij}$ , where  $i=1,2,3,4,\dots,n$ ,  $j=1,2,3,4,\dots,n$ . Then, from the equation 4-8,  $P(i, \theta)$  can be expressed as:

$$P(i, \theta) = a_{i1}x_1 + a_{i2}x_2 + a_{i3}x_3 + a_{i4}x_4 \quad (4-9)$$

As illustrated in Figure 4.7, the numbers of information in each integrated parallel  $P(i, \theta)$  are evaluated by crossing sections in a matrix square. Thus in a  $n \times n$  matrix, linear projections  $P(i, \theta)$  can be obtained. These are fundamental model of the ART algorithm.

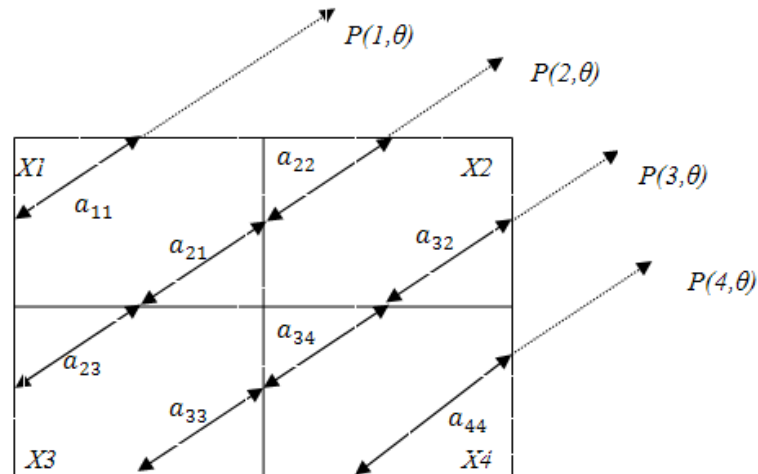


Figure 4. 7 The projections in 2X2 matrix math module

## Backprojection

Back projection is simply the inverse of projection. It has serious effects on image reconstruction. Since the signals are attenuated during transmission, selection of the correct estimation methods for backprojection is significant to the tomography

algorithm. In mathematics, multi projections of data are recognized as a  $N \times N$  matrix. This backprojection, called the Adjoint Matrix of projection is a linear algebra algorithm. A is a given matrix and its Adjoint matrix is simply the transposed matrix  $A^T$ . If the projection matrix vector X is a simple column matrix (Fig 4.3 and 4.7), the equation of projection is:

$$X = [x1, x2, x3, x4]^T \quad (4-10)$$

The projection is given by:

$$P = AX \quad (4-11)$$

Then, the backprojection can be evaluated as:

$$B = A^T P \quad (4-12)$$

Thus, if  $P = [5, 12, 10, 7]^T$  as Fig 4.3, the backprojection B is obtained:

$$B = \begin{bmatrix} 1 & 0 & 1 & 0 \\ 0 & 1 & 0 & 1 \\ 1 & 1 & 0 & 0 \\ 0 & 0 & 1 & 1 \end{bmatrix}^T \times \begin{bmatrix} 5 \\ 12 \\ 10 \\ 7 \end{bmatrix} = \begin{bmatrix} 1 & 0 & 1 & 0 \\ 0 & 1 & 1 & 0 \\ 1 & 0 & 0 & 1 \\ 0 & 1 & 0 & 1 \end{bmatrix} \times \begin{bmatrix} 5 \\ 12 \\ 10 \\ 7 \end{bmatrix} = \begin{bmatrix} 15 \\ 22 \\ 12 \\ 19 \end{bmatrix} \quad (4-13)$$

However, the matrix value of B is different from the original vectors matrix X.

The reason is explained below.

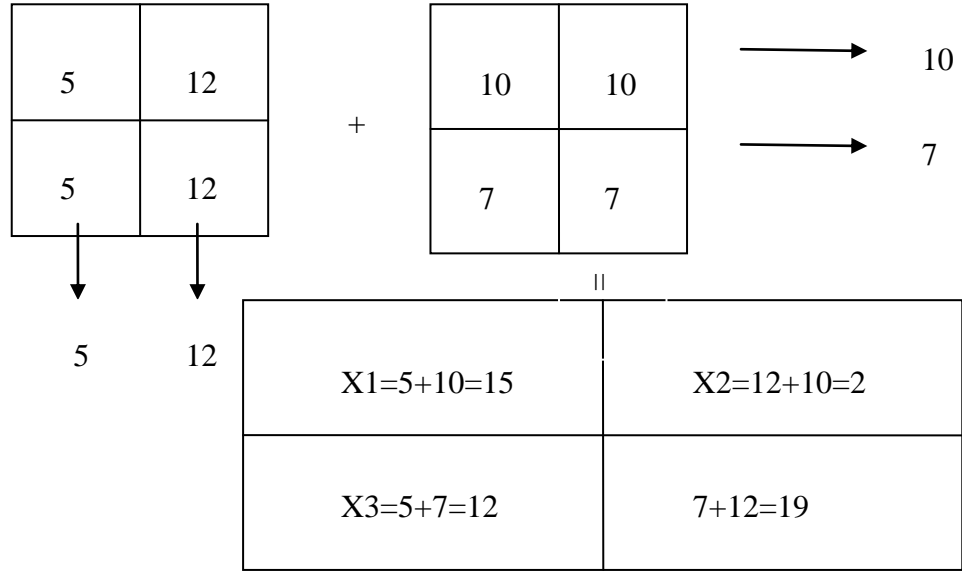


Figure 4. 8 Backprojection Evaluation Process

Though the backprojection value is different to the original single values, they have a strong interrelationship with each other in equation 4-13. The backprojection equation is:

$$B(x, y) = \frac{1}{2} \int_0^{2\pi} P(S, \theta)_{S=x\cos\theta+y\sin\theta} d\theta \quad (4-14)$$

## Image tomography reconstruction

The object captured by the camera is represented in an image by pixels. Each picture pixel contains intensity information indicating the differences in darkness and brightness of the object. Image tomography reconstruction locates the pixel positions of the original object by projection detection. The intensity values of each pixel can be evaluated according to the cross-correlation relationship of projection detections. For

instant, the point  $f(x, y)$  is substituted by a uniform light source and its projection  $p(s, \theta)$  carries the object intensity information (Fig 4.9).

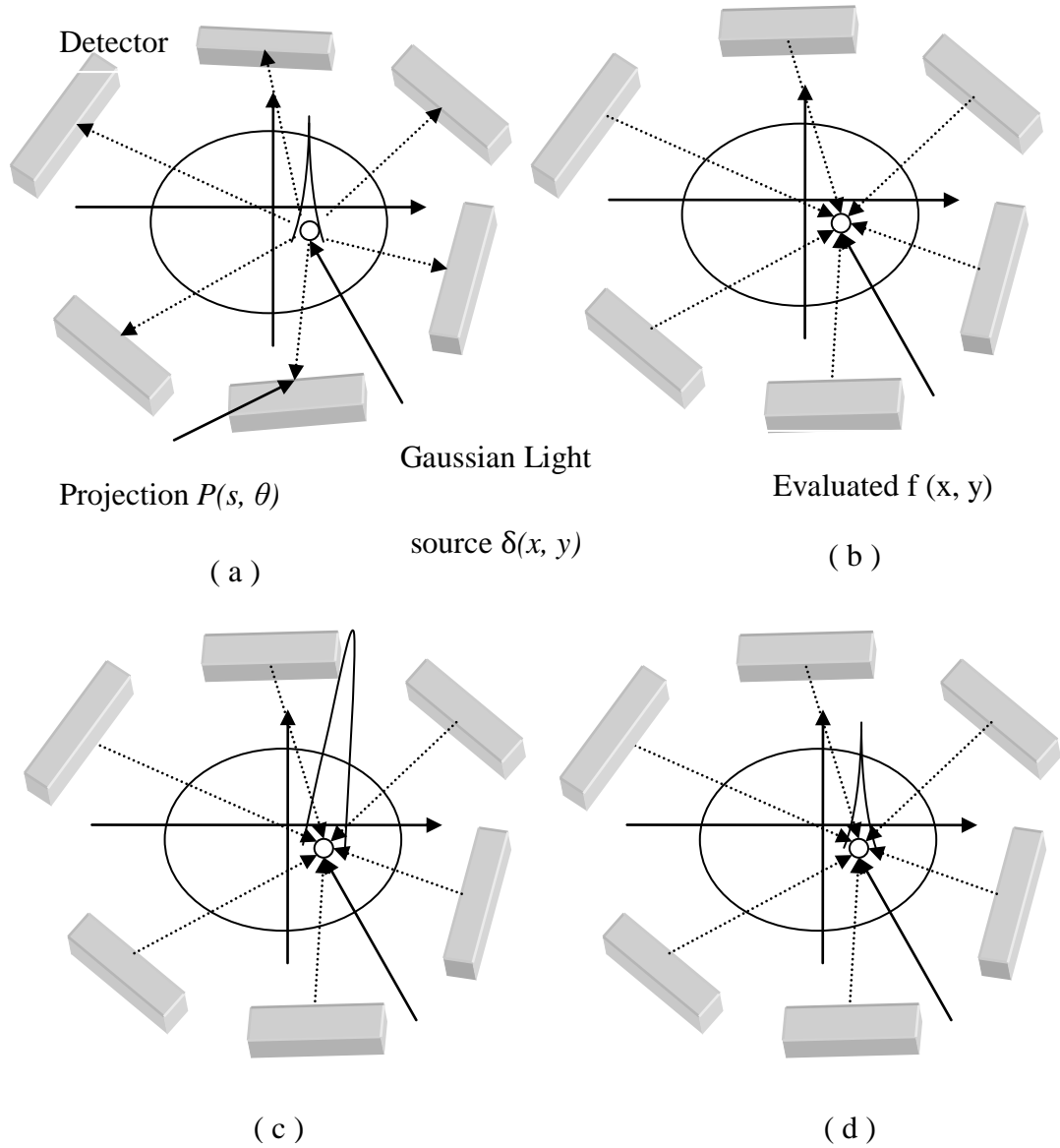


Figure 4. 9 Image Reconstruction Process by a Gaussian Intensity Light Source

The uniform light source intensity is denoted by  $\delta(x, y)$  in a Gaussian function. It is surrounded by detectors at angles  $\theta$  from  $0^\circ \sim 360^\circ$ . The locations of  $t$  are  $(x, y)$  in the X-Y plane. In Figure 4.9 (a), the projections of the light source  $P(s, \theta)$  are first recorded in both positions and intensity and then through the backprojection algorithm

technique. The position of  $f(x, y)$  is evaluated and located. Although the image has been relocated in the correct position, the value of the intensity has been distorted by the multiplicative backprojection technique. The reconstructed image can be corrected using a backprojection algorithm filter (FBP) in the evaluation.

To estimate the  $\delta(x, y)$ , the relationship between  $P(s, \theta)$  and  $\delta(x, y)$  was found.  $\delta(x, y)$ , a Dirac Delta function [59-62] is representative of a Gaussian intensity light source at  $(x, y)$ . Then, the  $\delta$  is defined as a Gaussian function in equation:

$$\delta(x) = \frac{N}{\sqrt{\pi}} e^{-Nx^2} \quad (4-15)$$

Where  $N$  denotes the integrated order, for a continuous function  $f(x)$ , the Lebesgue integral [63] with respect to the measure  $\delta$  is represented by:

$$\lim_{N \rightarrow \infty} \int_{-\infty}^{\infty} \frac{N}{\sqrt{\pi}} e^{-Nx^2} f(x) dx = \int_{-\infty}^{\infty} \delta(x) \cdot f(x) dx = f(0) \quad (4-16) [63]$$

Thus,  $\delta(x)$  has no values in the X-Y coordinate system plane but it is representative of the intensity value. Therefore, in an image, the  $\delta(x - x_0)$  is present at location  $x = x_0$ .

The Radon transform of  $f(X) = \delta(x - x_0) = \delta(x - x_0)\delta(y - y_0)$  is given as [64]:

$$P(s, \theta) = \int_{-\infty}^{\infty} \int_{-\infty}^{\infty} f(X) \delta(x \cos \theta + y \sin \theta - s) dx dy$$

Then,

$$P(s, \theta) = \int_{-\infty}^{\infty} \int_{-\infty}^{\infty} \delta(x - x_0) \delta(y - y_0) \delta(x \cos \theta + y \sin \theta - s) dx dy \quad (4-17) [64]$$

$$P(s, \theta) = \int_{-\infty}^{\infty} \delta(y - y_0) \delta(x_0 \cos \theta + y \sin \theta - s) dy \quad (4-18)$$

Thus

$$P(s, \theta) = \delta(x_0 \cos \theta + y_0 \sin \theta - s) \quad (4-19)$$

Where present, the projection is a sinuous waveform dependence of angle  $\theta$  in the vector space ( Fig 4.10).

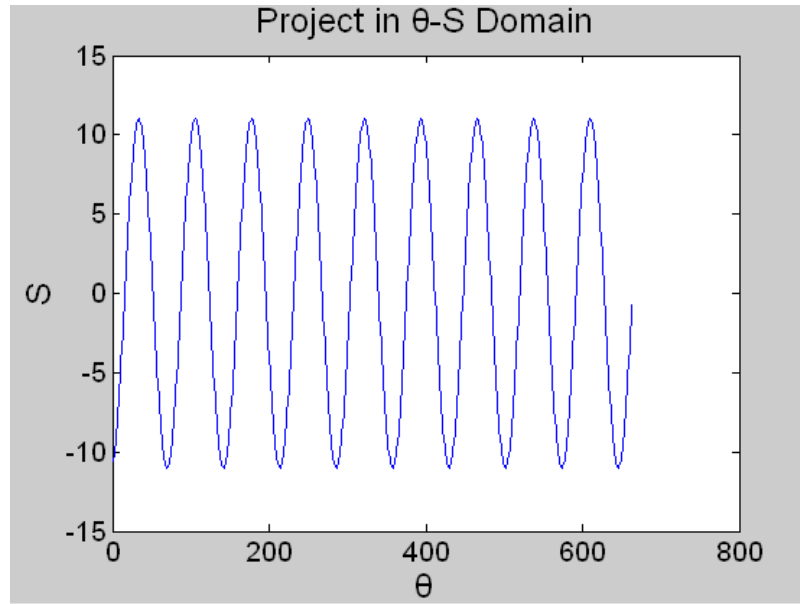


Figure 4. 10 Projection Behaviors in  $\theta \sim s$  Domain

## 4.2 Parallel Projection and Fan Beam Projection

Tomography projections are generally divided into two types: parallel projection and fan beam projection (Fig 4.11). Both projections rely on the Fourier transform theorem for transforming projection data from a spatial domain into a

frequency domain. The Fourier transformation transforms the signals to a uniform frequency. The kernel fundamental by Fourier transform used for tomography image reconstruction technique is Fourier slice transformation. The reviews of Fourier transform is in the appendix A. The Fan beam projection method is based on the parallel projection and is used to simplify the setup of system and the computational process.

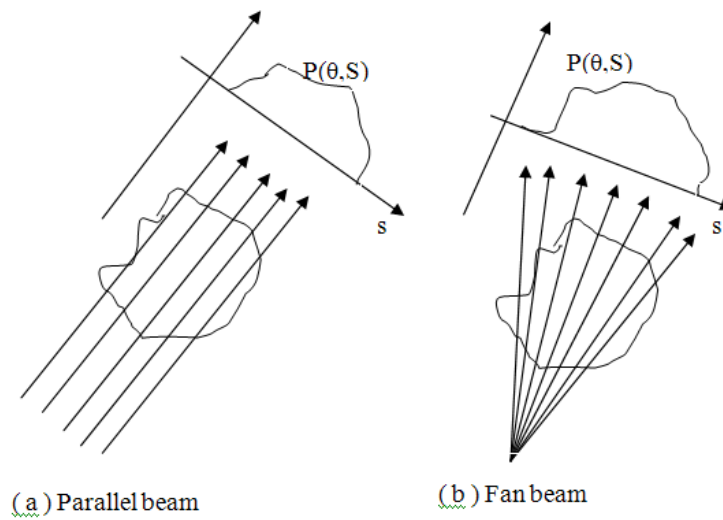


Figure 4. 11 Parallel Beam Projection and Fan Beam Projection

### 4.2.1 Parallel Beam Projection

The parallel beam projection is a simple method of image reconstruction. A parallel beam is passed through an object to obtain the information. The only dependence is on the projection angle  $\theta$  in algorithm (Fig 4.11 (a)). The 1D Fourier transform of the projection is expressed in following equation:

$$P(\omega) = \int_{-\infty}^{\infty} P(s)e^{-2\pi is\omega} ds$$

(4-20)

and the inverse Fourier transform is:

$$P(s) = \int_{-\infty}^{\infty} P(\omega) e^{-2\pi i s \omega} d\omega \quad (4-21)$$

The 2D inverse Fourier transform in polar coordinate system is:

$$f(x, y) = \int_{-\pi}^{\pi} \int_{-\infty}^{\infty} F(\omega, \theta) e^{2\pi i \omega (x \cos \theta + y \sin \theta)} \omega d\omega d\theta \quad (4-22)$$

Where  $\omega$  is the frequency; In a polar system, according to the symmetric property of Fourier frequency, the  $F(\omega, \theta) = F(\omega, \theta + \pi)$ . The equation 4-22 can be rewritten as:

$$f(x, y) = \int_0^{\pi} \int_{-\infty}^{\infty} F(\omega, \theta) |\omega| e^{2\pi i \omega (x \cos \theta + y \sin \theta)} \omega d\omega d\theta \quad (4-23)$$

From equation 4-21, the equation of image reconstruction from Fourier slice theorem is given by:

$$f(x, y) = \int_0^{\pi} \int_{-\infty}^{\infty} P(\omega, \theta) |\omega| e^{2\pi i \omega (x \cos \theta + y \sin \theta)} \omega d\omega d\theta \quad (4-24) [64]$$

Where  $|\omega|$  is the ramp filter [65-67].

From the equations, the image can be reconstructed from projection data with mathematics by employing a series of angles detectors from 0 to  $\pi$ . Fourier transform is used to reform the projections in the frequency domain to reproduce the frequency image. The inverse Fourier transform algorithm is then used to transform the frequency image back to spatial domain.



## Ramp filters

Although the image can be reconstructed from projection data using the Fourier transform and inverse Fourier Transform function, the reformed backprojection image is distorted (section 4.1.2). In Figure 4.15 (b) above, the centre is the origin of the polar coordinate system and represents low frequency. The frequency increases along the axis from the origin. The information is concentrated around the centre at low frequencies. The many low frequencies are irregularly distributed creating blurring similar to Gaussian blurring [68, 69]. Distortion occurs when the image is transformed into the frequency domain. The image displays blurring representing over-weighted frequency distributions. In math, the kernel operator is  $1/|\omega|$ , a reciprocal of  $|\omega|$  as denoted in equation 4-24. In a normal Fourier transform image the  $1/|\omega|$  is not uniform and causes the image to blur and scatter. A filter ramp operation  $|\omega|$  needs to be added to reduce the noise from  $1/|\omega|$ . The  $|\omega|$  is expressed as:

$$|\omega| = \sqrt{\omega_x^2 + \omega_y^2} \quad (4-25)$$

Using the ramp filter function in inverse Fourier transform backprojection reduces the distortion and blurring of the reproduced image. The filtered backprojection algorithms are generally classified by ramp filter types as described below.

### 1. Method 1

The simplest method is to add a ramp filter with the 1D Fourier transform of  $P(s, \theta)$  to

eliminate the noise operator  $1/|\omega|$ . Filtered slice projection data is obtained as denoted in  $q(\omega, \theta)$  and by multiplying the slice projection into tomography data  $Q(\omega, \theta)$ . Transforming the filtered projection data  $Q(\omega, \theta)$  by inverse Fourier transform gives the original image. The relation is:

1D Fourier transform	Multiply	Inverse Fourier transform
$P(s, \theta) \xRightarrow{\hspace{1.5cm}} q(\omega, \theta) \xRightarrow{\hspace{1.5cm}} Q(\omega, \theta) \xRightarrow{\hspace{1.5cm}} f(x, y)$		

## 2. Method 2

Similar to method 1, a filter is added in the  $(s, \theta)$  coordinate system without a Fourier transform. From the Fourier transform convolution property:

If

$$Q(\omega, \theta) = H(\omega, \theta) \times F(\omega, \theta) \quad (4-26)$$

Then

$$P(s, \theta) * h(s, \theta) = \int_{-\infty}^{\infty} H(\omega, \theta) \times F(\omega, \theta) d\omega d\theta \quad (4-27)$$

Therefore, the filtering process can be explained:

1D transform and multiply	Ramp filter	Reconstruction
$P(s, \theta) \xRightarrow{\hspace{1.5cm}} Q(\omega, \theta) \xRightarrow{\hspace{1.5cm}} P(s, \theta) * h(s, \theta) \xRightarrow{\hspace{1.5cm}} f(x, y)$		

### 3. Method 3

Considering the Hilbert transform [70-72] relationship with Fourier transform, the ramp filter can be denoted as a Signum function:

$$sgn(\omega) = \begin{cases} 1, & \omega > 0 \\ 0, & \omega = 0 \\ -1, & \omega < 0 \end{cases} \quad (4-28)$$

From the Hilbert transform and Fourier transform relationship:

$$F(H(\mu))(\omega) = (-isgn(\omega)) \cdot F(\mu)(\omega) \quad (4-29)$$

The ramp filter can be rewritten in equation:

$$H(\omega) = |\omega| = i2\pi\omega \times \frac{1}{i2\pi} sgn(\omega) \quad (4-30)$$

Where, the inverse Fourier transform of  $-isgn(\omega)$  is  $1/\pi s$ . Thus by reference to equation 4-27, the filtered data  $q(s, \theta)$  is denoted in equation:

$$q(s, \theta) = \frac{dP(s, \theta)}{ds} * \frac{-1}{2\pi^2 s} \quad (4-31)$$

Where the filtered data is a combination of the derivation and Hilber transform.

Table 4.1 summarizes the backprojection algorithms [73].

Table 4. 1 List of Parallel-Beam Backprojection Algorithms [73]

Method	Step 1	Step 2	Step 3
1	1D Ramp filter with Fourier transform	Backprojection	
2	1D Ramp filter with Convolution	Backprojection	
3	Derivative	Hilbert transform	
4	Backprojection	2D Ramp filter with Fourier transform	
	Backprojection	2D Ramp filter with 2D convolution	
5	Derivative	Backprojection	Hilbert transform

### 4.2.2 Fan Beam Projection

Fan beam projection is a popular but complex projection method implemented by Computed Tomography. It has a wider detection area and faster computational process compared to parallel beam projection (Fig. 4.12). The parallel beam (Fig. 4.12 a) only scans one vertical angle by crossing the object. The fan beam scans many angles by crossing the object (Fig. 4.12 (b)). In an emission tomography model, the parallel beam system has to use a series of parallel light sources to illuminate the object to obtain projection; by contrast, the fan beam is not restricted of using parallel light to obtain parallel projections.

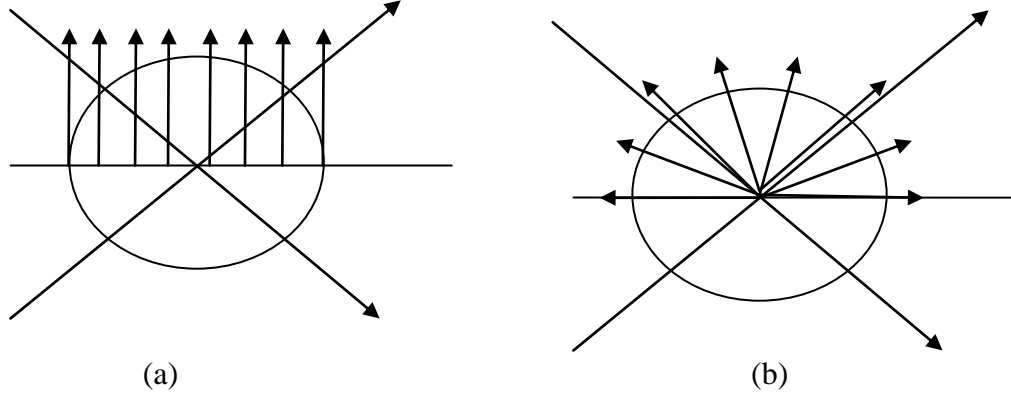


Figure 4. 12 Fan Beam Projection and Parallel Beam Scanning Area

The fan beam algorithm can be considered as a transformation from a parallel algorithm. The weighted frequencies are the same in a polar coordinates system for projections from both parallel and fan beam systems in a spatial domain. The only change is of the origin in a polar coordinates system by Fourier transform. The geometric relationship between each other means that the fan beam algorithm can be substituted with the parallel beam algorithm (Fig. 4.13). Assume that the distance between fan beam source and origin is denoted by  $D$ ; the  $\alpha$  is the angle between parallel and fan beam,  $\beta$  is the angle between the Y axis and the fan beam. Thus, the geometric transform is:

$$s = D \times \sin\alpha, \quad \theta = \alpha + \beta \quad (4-32)$$

Hence, the fan beam projection is expressed in equation:

$$P(s, \theta) = g(s, \alpha, \beta) \quad (4-33)$$

Thus, the reconstructed  $f(x, y)$  in X-Y coordinates system is rewritten in equation:

$$f(x, y) = \int_0^\pi \int_{-s_\alpha}^{s_\alpha} P(s, \theta) h(x \cos \theta + y \sin \theta - s) ds d\theta$$

(4-34)

Where the  $s_\alpha$  is the value of  $s$  which is belong to  $(-s, s)$ ; It can be rewritten in  $[0, 2\pi]$ , which is

$$f(x, y) = \frac{1}{2} \int_0^{2\pi} \int_{-s_\alpha}^{s_\alpha} P(s, \theta) h(x \cos \theta + y \sin \theta - s) ds d\theta$$

(4-35)

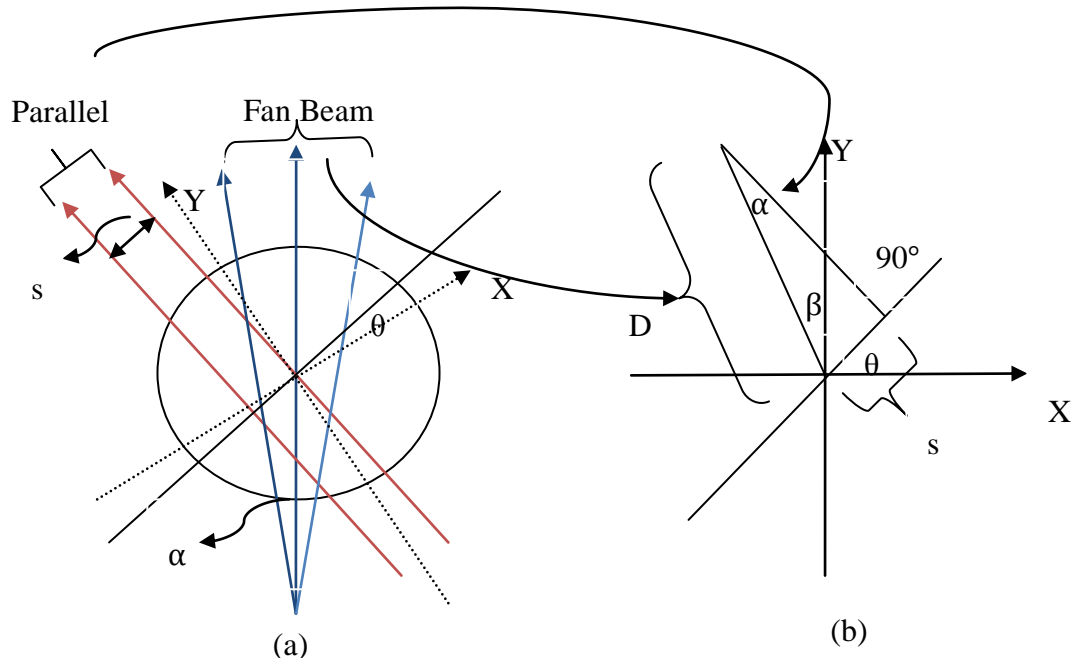


Figure 4. 13 Geometric Transform between Parallel Beam and Fan Beam

The features of the fan beam make the algorithm more complicated than that for the parallel beam. The fan beam can be recorded in detail by different placement of detectors (Fig. 4.14). In diagram 4.14 (a), the fan beams are equal distance from each other. In 4.14 b the fan beams are set at an equal angle to each other. Thus, the

projection algorithms are different because of the difference in the lengths of the projections. Firstly, the fan beam is analyzed in equal angles as (b). After the transformation (Fig. 4.13 b), the relationship of the fan beam and parallel beam is defined in equation 4-33. After deducing, it is much complex for algorithm (in equation 4-36) because of too many variables.

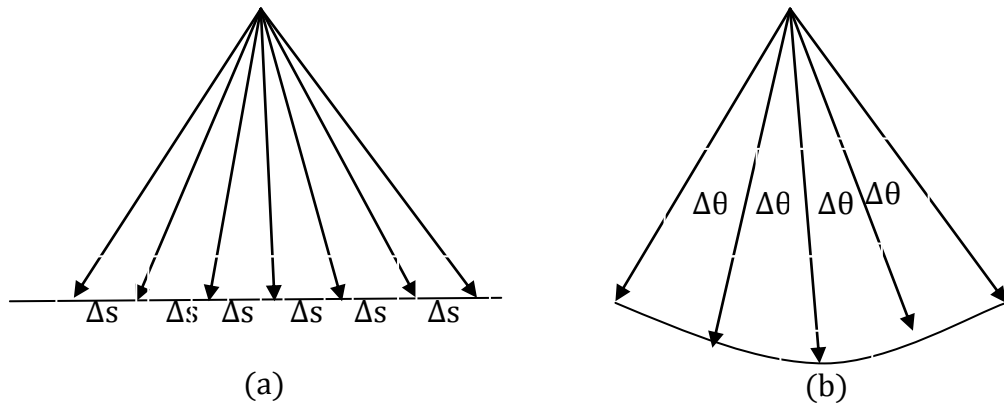


Figure 4. 14 Different Algorithm Methods for Fan Beam Projection

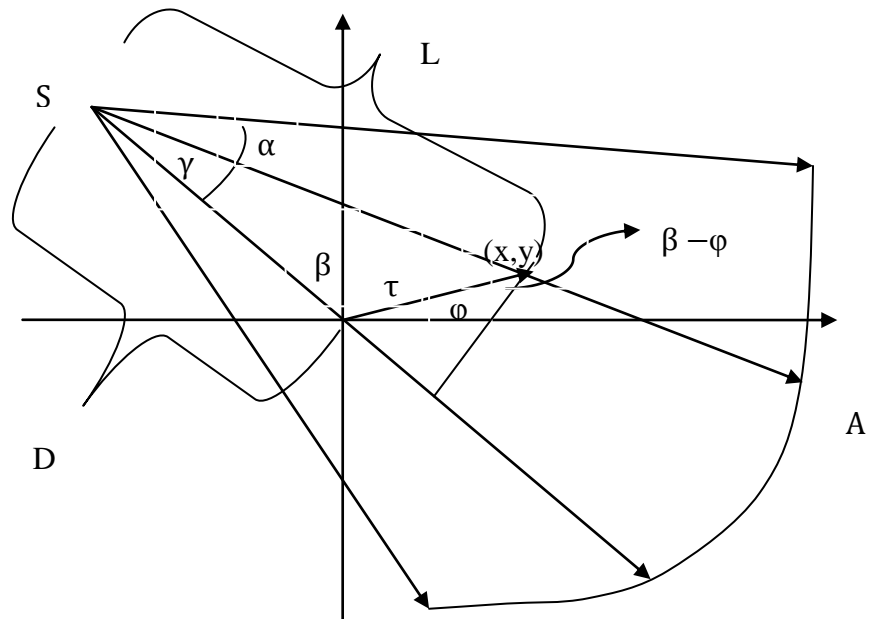


Figure 4. 15 Fan Beam Ray Point  $(x, y)$  Transformed into Polar Coordinates

To simplify the equation, the  $(x, y)$  point is represented in a polar coordinates

(Fig. 4.15). The point  $f(x, y)$  is denoted in a polar coordinate system by  $f(\tau, \varphi)$ , where  $\tau$  is the polar radius,  $x = \tau \times \cos\varphi$ ,  $y = \tau \times \sin\varphi$ . Then, the equation is rewritten from equation 4-35:

$$f(\tau, \varphi) = \frac{1}{2} \int_0^{2\pi} \int_{-s_\alpha}^{s_\alpha} P(s, \theta) h(\tau \cos(\theta - \varphi) - s) ds d\theta \quad (4-36)$$

Substituting  $\theta$  with  $\alpha + \beta$ , the equation is:

$$f(\tau, \varphi) = \frac{1}{2} \int_0^{2\pi} \int_{-s_\alpha}^{s_\alpha} g(\alpha, \beta) h(\tau \cos(\alpha + \beta - \varphi) - D \sin\alpha) D \cos\alpha d\alpha d\beta \quad (4-37)$$

Where  $D \cos\alpha d\alpha = ds$  according to the Jacobian Matrix function (or differential theorem) [74]. In fact, here  $s_\alpha = \sin(s/D)$  and it belongs to  $[0, \pi]$  rotation of fan beam. Hence, the projections inside the fan beam rays are a normalized projection named SA ray (Fig. 4.15). They can be evaluated using the transformed coordinates system. Assume that the length between source and evaluation point is  $L$ , and the angle of the ray is  $\gamma$ .

$$\tau \cos(\alpha + \beta - \varphi) = \tau \cos(\beta - \varphi) \cos(\alpha) - [\tau \sin(\beta - \varphi) + D] \sin(\alpha) \quad (4-38)$$

Thus,  $L \cos(\gamma) = D + \tau \sin(\beta - \varphi)$ ;  $L \sin(\gamma) = \tau \cos(\beta - \varphi)$ ;

Equation 4-37 is rewritten as:

$$f(\tau, \varphi) = \frac{1}{2} \int_0^{2\pi} \int_{-s_\alpha}^{s_\alpha} g(\alpha, \beta) h(L \sin(\gamma - \alpha)) D \cos\alpha d\alpha d\beta \quad (4-39)$$



If the fan angle of projection is given, then the fan projections can be evaluated from each fan ray projection. The ramp filter  $|\omega|$ , is expressed in a  $L\sin(\alpha)$  variable.

$$h(L\sin(\alpha)) = \int_{-\infty}^{\infty} |\omega| e^{i2\pi\omega L\sin\alpha} d\omega \quad (4-40)$$

The derivation equation of the ramp filter is:

$$h(L\sin(\alpha)) = \left(\frac{\alpha}{L\sin\alpha}\right)^2 \times h(\alpha) \quad (4-41)$$

Therefore the backprojection algorithm of fan beam is denoted in equation:

$$f(\tau, \varphi) = \int_0^{2\pi} \frac{1}{L^2} \int_{-s_\alpha}^{s_\alpha} g_\beta(\alpha) g'(\gamma - \alpha) D \cos \alpha d\alpha d\beta \quad (4-42) [66]$$

Where

$$g'(\alpha) = \frac{1}{2} \left(\frac{\alpha}{\sin\alpha}\right)^2 \quad (4-43)$$

The fan beam projections algorithm is extended by many investigators, for example Kak and Slaney's work [75, 76]. In the experiment, the differences between equal angle and equal displacement of detectors have little effect on the results. In POET system, the detectors are placed at equal angles.

## 4.3 Interactive Reconstruction Algorithm and Array MART Software Implementation

The Array MART software used in POET is an iterative Algebraic

Reconstruction technique (ART). Array MART processes linear integrated fan beam intensities of in cylinder combustion using a 40 detectors tomographic array. The region of interest is divided into  $10 \times 10$  pixel areas to display integrated intensities for evaluation in the MART algorithm. It is simple to model the intensity distribution using this software. However the simulation algorithm with the system operating errors can only produce a general image of combustion. Improvements to the software are discussed in the further work section.

### **4.3.1 Transmission and Emission Tomography Technique**

In clinical diagnostics two scanning techniques are employed to obtain information about an object of interest: transmission tomography and emission tomography.

#### **Transmission tomography**

The transmission technique is a popular method of X-ray diagnostics. The X – rays are passed through the patient’s body and the X-ray energy is recorded by detectors. The energy  $I$  of the X –ray passing through a patient is attenuated by the interaction between the photons and electrons of the body. The attenuated intensities are recorded by the detectors. After tomography reconstruction, the reformed image is displayed and the doctor is able to identify the diseased region of the body. The attenuation coefficient follows the Beer-Lambert Law [77] and is expressed:

$$A = -\log_{10} \left( \frac{I}{I_0} \right) \quad \text{For a liquid}$$

$$A = -\ln \left( \frac{I}{I_0} \right) \quad \text{For a gas}$$

(4-44)

## Emission tomography

In emission tomography, the patient is given an injection of radiopharmaceuticals. The radiation and inner body information is measured using outside detectors. In combustion detection, an emission tomography technique is used. The different chemical reactants CH\* and OH\* elements are considered as the radiant center in-cylinder and they pass through various densities of air-fuel mixture. The attenuation coefficient for the Beer-Lambert law is [78]:

$$I = I_0 \exp (-m(\tau_a + \tau_g + \tau_\omega + \tau_r + \tau_{o_3} + \tau_{NO_2}))$$

(4-45)

Where

- a refers to characteristics of the atmosphere;
- g is a uniform mixed gas
- $\omega$  is the water vapour absorption;
- r is the Rayleigh scattering from molecular oxygen and nitrogen.
- M is the air mass factor.

The equation evaluates the atmosphere attenuation coefficient [78, 79]. However in the

complexity of combustion, a simplified attenuation coefficient calibration method called inverse-square law is used instead of the Beer-Lambert law.

### **4.3.2 Iterative Reconstruction**

In computational mathematics, the iterative method [80-82] is a convergent algorithm. In a direct methods algorithm such as solving the equation  $x^2 = 4$ ,  $x = \pm 2$ ; the solution is found in a finite sequence of operations. If the problem is not solvable in a finite sequence then a sequence of approximation operations is required to obtain the best approximate solution. For example, to obtain a point (x,y) within a nonlinear line in a Cartesian coordinates system (Fig. 4.16 a), it is difficult to find a direct algorithm operation. A sequence of solutions through a series of vertical lines of operation is evaluated. An approximate point (x1,y1) is estimated to approach the original point (x,y). Iterative methods are useful for solving irregular functions in complicated operations whether it is a point, a curve or complex modules (Fig. 4.16 b).

The iterative image reconstruction technique [83-86] is based on iterative algorithms. In image reconstruction, the image is reformed using the backprojection of an object. The complex model of the object is an unknown math model that is difficult to evaluate using simple math algorithms or simulate directly. Iterative algorithms are used to simulate an approximate ‘guess’ model and to find a close or in math relationship model of the original object. Using compensating algorithms, the image of the object can be reconstructed.

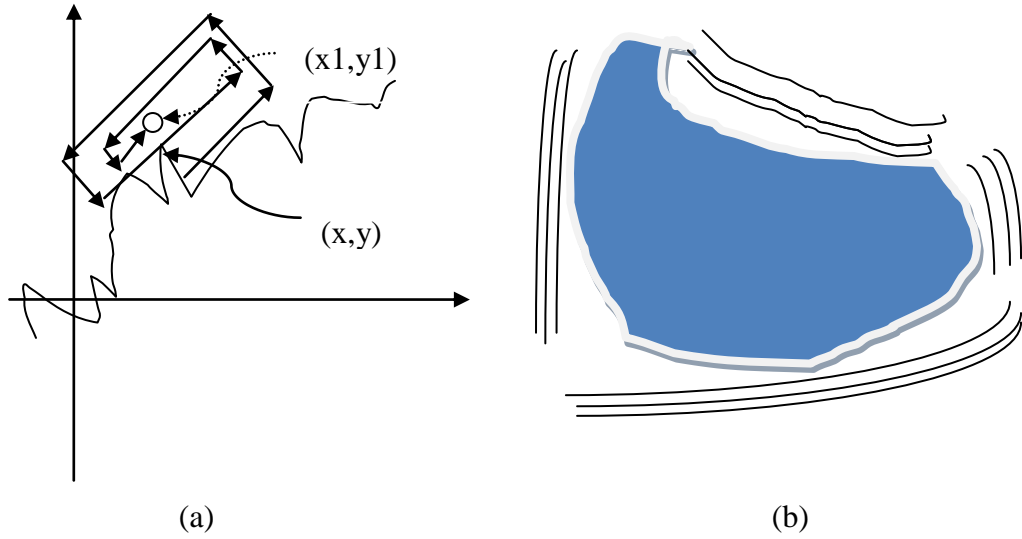


Figure 4. 16 Iterative Method Algorithms Concept Diagram

The iterative reconstruction consists of four steps:

- 1) Since the model of the target is unknown, a general model has to be established by employing the projection data with an unknown series coefficient:

$$f(x, y) = \sum_{n=1}^{\infty} e_n x_n^i + e_n y_n^i + c$$

(4-46)

where  $i = 1, 2, 3, \dots, m$ ;  $c$  is the coefficient.

- 2) To estimate the results, an ideal model solution has been built firstly.
- 3) Estimate the noise by comparing the ideal module with the projection data.  
Simulate a noise function to eliminate the noise from the projection data.
- 4) By using the iteration algorithms, the image is reconstructed through computational operations, using maximum likelihood (ML) or Expectation Maximum (EM) functions.

The advantage of iterative methods for image reconstruction is that the reconstructed model of the image is independent of the noise from the projections. Even with incomplete projections or with missing object information, the image can still be reformed from the ‘statistics’ model and iteration of object projections. For a complex model, it is difficult to find a suitable statistical model of noise and an operator to optimize the computer operations.

In iterative image reconstruction techniques, Kaczmarz [87] developed an iterative algorithm to solve algebraic problems of image reconstruction. This method is called the Algebraic Reconstruction technique (ART) [87]. Two main methods are employed in Computed Tomography (CT) image reconstruction: Maximum likelihood (ML) reconstruction using Expectation Maximization (EM) algorithm or MLEM technique; and the Ordered Subsets-Expectation Maximization (OSEM) methods or OSEM technique. The ML-EM is a combination of two algorithms: Maximum likelihood and Expectation Maximization. The likelihood algorithm can find an approximate model of object using the joint probability density function of Poisson random variables. To maximum the approaching of original object by likelihood function, a ML algorithm is applied to optimize the simple likelihood algorithm. However, the optimal likelihood function is still too complicated to be computed, the expectation of ML algorithm are employed. The final algorithm for maximization the EML function is called ML-EM algorithm. In the terms of OSEM, the projections are divided into several ordered groups in ordered and it is called ordered-subsets. One

subset projection of each iteration is used to reduce the time taken to reconstruct the object. This accelerates the convergent process but increases the noise.

## Algebraic Reconstruction Technique

The ART method uses a basic algorithm of iterative reconstruction techniques. An arbitrary value is used for the attractor point to solve unknown model problems in math. For instant, to find the solution of the crossing section of three linear algebraic lines, an initial supposed location is  $x_0$ , then a sequence of solutions is generated to find solutions approaching the crossing point by iterations (Fig. 4.17).

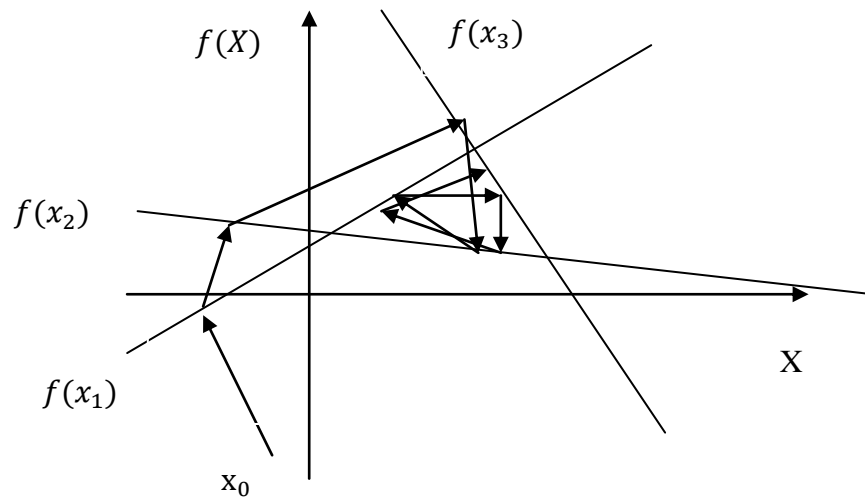


Figure 4. 17 Schematic Approximate Solutions Found by ART Algorithms

In image reconstruction, the images are unknown math matrix models but with known projections in columns and rows. This algorithm is named ART (Fig. 4.18). If the image is  $P$  and the coefficient of  $P$  is a  $3 \times 3$  matrix called  $A$ , the solution to  $P$  is:

$$AP = B$$

(4-47)

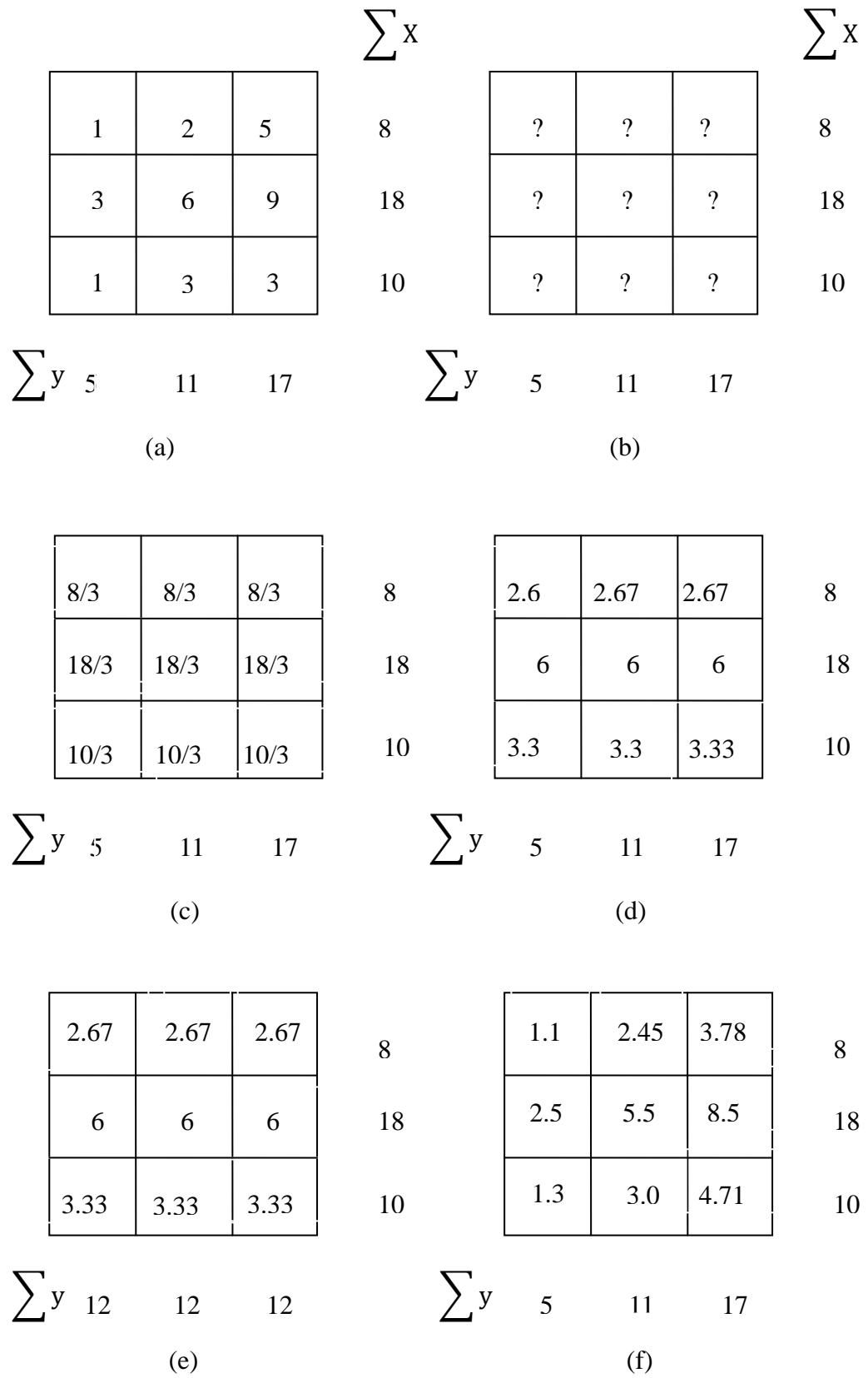


Figure 4. 18 ART Algorithms Explanation Schematic Diagram



The operation of finding a solution B to P can be achieved by the ART algorithm (Fig 4.18). In the expression, the ideal coefficient A is a 3x3 matrix where the value of P is given as 1 (Fig 4.18 a). Guesses for an unknown 3x3 matrix with column and row sums are shown in Figure 4.18 (b). By dividing the row projection sum equally into three elements in each grid, a new matrix from the row average is obtained (d). Each column of the new matrix can be summed to generate new column projections in (e). Then an approximate matrix of the ideal model is created using the row average value to multiply the proportion of new generated column projections and original projections. This algorithm process is the basis of ART technique during one iteration. The approximate matrix approaches the ideal model, though it may still have a ‘noise function’ error compared to the ideal one (Fig 4.18 (f)). To acquire a maximum expected value, more iterations of the algorithm are needed to reduce the noise. The ART is employed to design the OAG plate and program Array MART software.

## **Multiplicative Algebraic Reconstruction Technique (MART)**

Multiplicative ART is a simple method to optimize the ART and correct the calculated values using the experiment data. The initial approximate values are computed using equation 4-47. The general MART is as follows:

- a) For each iteration  $l$ ,
- b) The calculated value  $P_j^c$  is approximated for each sample  $i$ .

- c) All samples pass through the given cell. The total number of samples per cell  $N$  corresponds to  $i$ ,  $W_{ij}$ ,  $P_j$ ,  $P_j^c$ . Where  $W_{ij}$  is the weighting factor;  $P_j$  is the measured projection value;  $P_j^c$  is the calculated value.
- d) The product of all correction terms are computed for each cell  $j$ .

Thus, after a complete  $l^{th}$  iteration, it has

$$f_i^l = f_i^{l-1} + \prod_N W_{ij} \left( \frac{P_j}{P_j^c} \right)$$

4-48

There are four different ways of correction terms shows as follow [88]:

- Brooks MART:  $f_i^l = f_i^{l-1} + \prod_N \lambda W_{ij} \left( \frac{P_j}{P_j^c} \right)$
- MART method 1:  $f_i^l = f_i^{l-1} + \prod_N [1 - \lambda(1 - \left( \frac{P_j}{P_j^c} \right))]$
- MART method 2:  $f_i^l = f_i^{l-1} + \prod_N [1 - \lambda W_{ij}(1 - \left( \frac{P_j}{P_j^c} \right))]$
- MART method 3:  $f_i^l = f_i^{l-1} + \prod_N \left[ \frac{P_j}{P_j^c} \right]^{\lambda W_{ij}}$

Where  $\lambda$  is the coefficient of experiment model.

Follow the Figure 4.19, the model has an initial matrix as Figure 4.19 (a) and the evaluated matrix after three iterative corrections as Figure 4.19 (e). In step 1, (b) is the evaluated values after one iteration. In step 2, the rows and columns projection values by summarizing present in (c); and they are different from initial projections (a). Thus in step 3, by multiply the proportions of  $(I_{initial}/I_{evaluated})$ , the corrected values are obtained in (d). Then, repeat the step 3, the evaluated values after three times iteration is illustrated in (e). As it is demonstrated in figure 4.19, the values have been corrected with the increasing of iteration numbers.

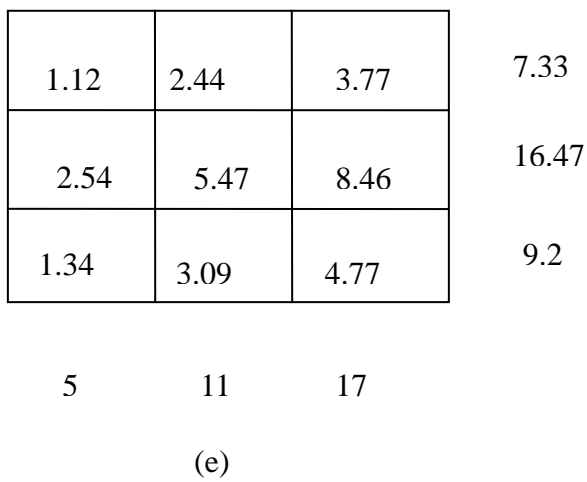
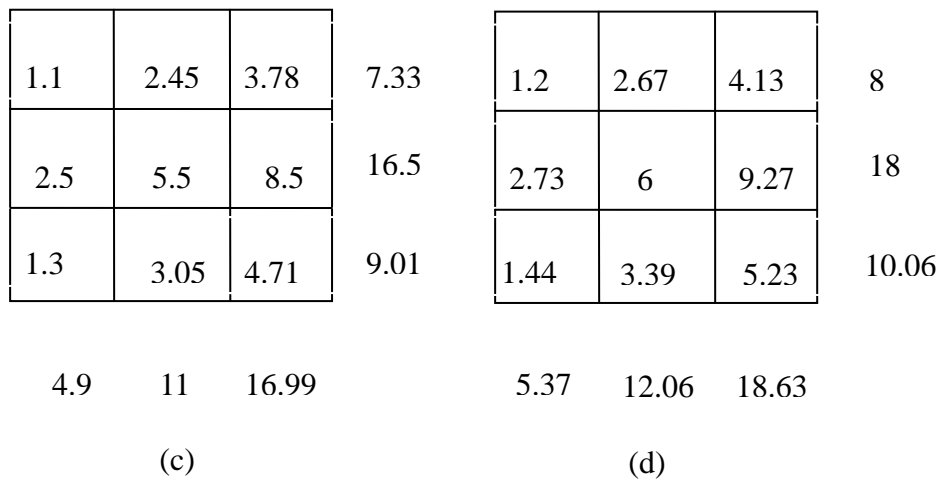
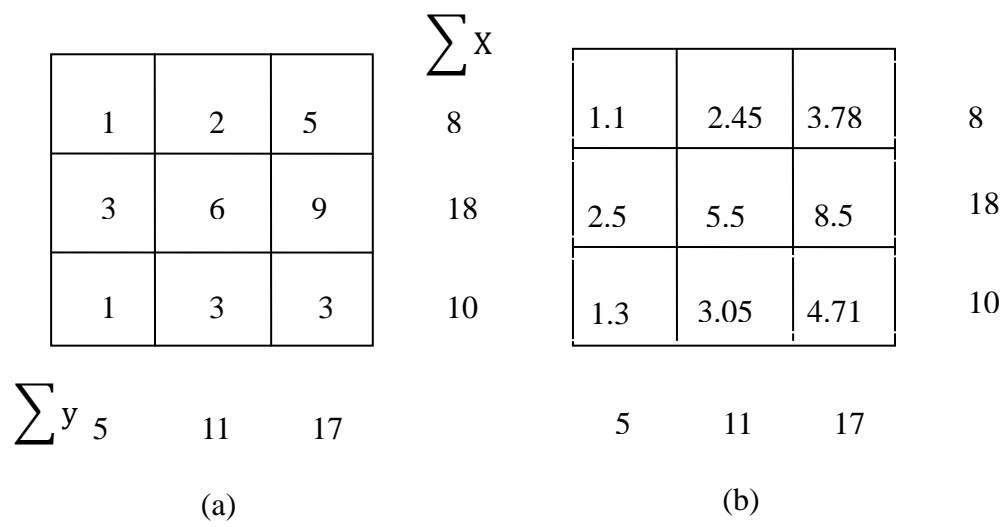


Figure 4. 19 MART Algorithm Illustration Diagram

The errors of the MART results are slightly compared with other general ART

methods which are proved by Ko and Kihm (1999) for three projection cases [89]. However, the errors of the ARTs and the MART are comparable for five projection cases, showing poor performances of the MART than the ART for some cases [89]. The limitation of MART is that the calculated value must be positive. In the experiment, the designed of OAG ensure the intensity measurements are all positive.

### 4.3.3 Array MART Software

The Array MART software is specially programmed for image reconstruction of in-cylinder combustion research. The software utilizes the ART algorithm and intensity interpolation method to simulate the combustion intensity distribution. The function of the software is to record the synchronized intensity signals of real time combustion transmitted by the tomographic projections of the 40 PMTs. Five 20° fan beam projections in each group and totally eight groups are collected by detectors. In using the ART algorithm estimation, the projection signals are redistributed in a 10x10 pixels image by intensity gradients to study the instant flame propagation. The software flow is illustrated in Figure 4.20.

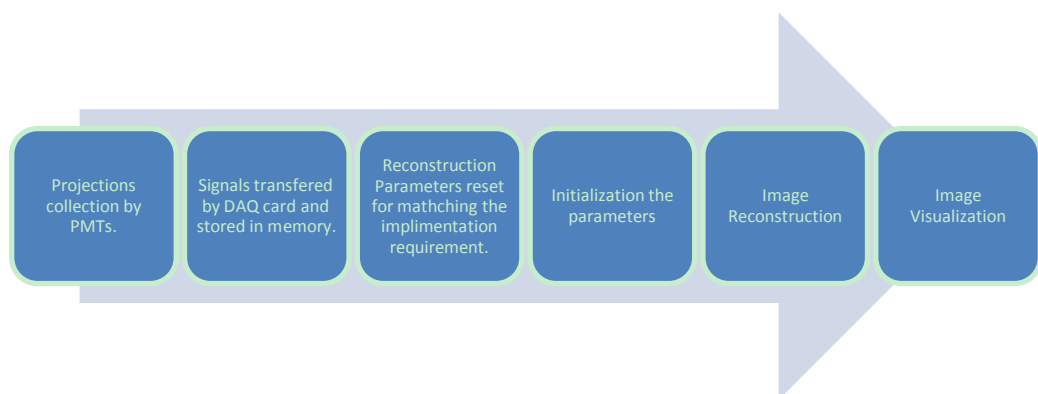


Figure 4. 20 Flow Chart of Array MART Software Processing

## Array MART Software Algorithm

There are two parts to the Array MART algorithm: the estimation of fan beam back projections and the simulation of intensity distributions. In the modified Engine section, the circular shape of the cylinder is a good fit for the tomography array using the OAG gasket. The intensity sensors are divided into 8 groups of 5 to collect information of combustion in 'tomo'. To cover the whole chamber reaction field, the detection views are arranged intercrossing with each other. The engine starts with spark ignition. The spark ignition ignites the gas mixture in the chamber. The radiation crosses the burned and unburned gas field and the intensities are collected by detectors. After ignition, combustion starts as an explosion and spreads from the ignition point to the edges of the chamber. The path traveled runs the distance from the combustion centre to the interface between unburned gas and burning gas (Fig. 4.21). In theory, images of flame propagation and combustion can be obtained if the locations of flame front and the intensities of combustion are known. Then function  $f(x, y)$  corresponding to the shape of combustion can be simulated.

The Array MART software uses intensity interpolation to generate an approximate model. The observed information from the projection is a sum of the flame intensities at different angles. The simple shape of the intensity distribution is able to be roughly simulated by utilizing the interpolation algorithm. The observing chamber field is divided into  $200 \times 200$  grids. In each grid, a value of intensity  $I_{ij}$  exists.  $I_{ij}$  can be estimated using interpolation methods starting with a 'arbitrary' value  $I_s$

from two or more cross section intensities at different angles . After iterations, the approximate values of each grid is determined and placed into each pixel to achieve combustion visualization.

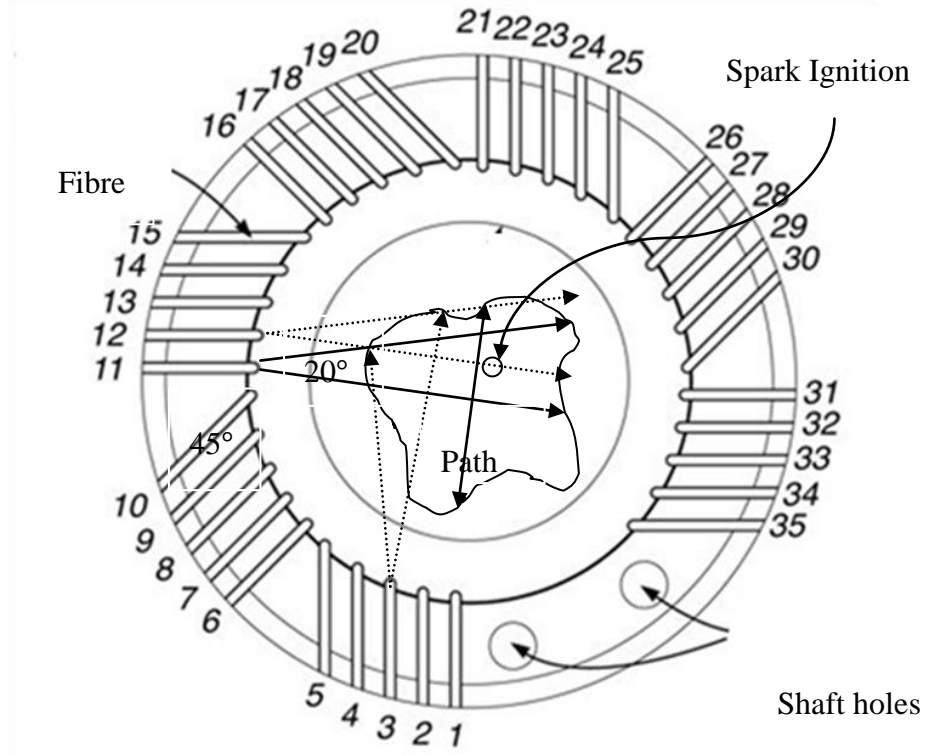
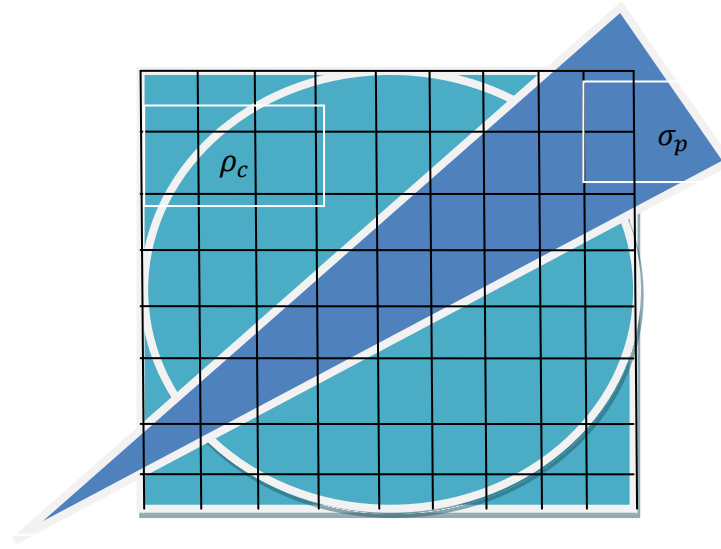


Figure 4. 21 The Schematic of Combustion Distribution Measurement by OAG Ring

In the software algorithm the whole chamber radiation field is denoted as  $\rho_c$ . Since the chamber radiation is divided into  $200 \times 200$  grids, the fan beam projection coverage is represented by  $\sigma_p$ . The summed intensities of one projection is.

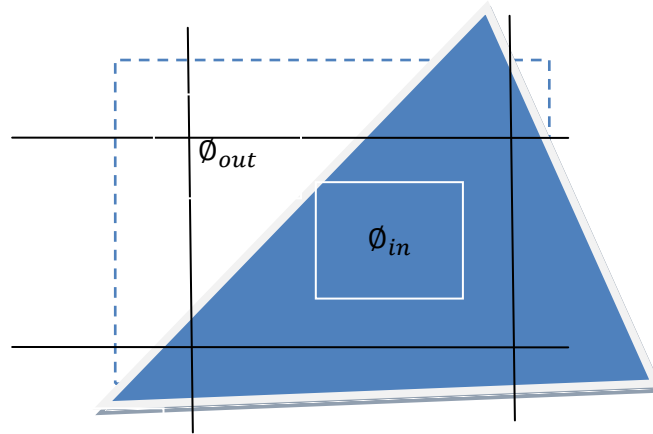
$$I_{\sigma_p} = \int_{\rho_c} I_{i,j} di dj \quad (4-49)$$

Where  $i=1,2,3,\dots,200$ ;  $j=1,2,3,\dots,200$ . Shown in Figure 4.22.



Projection

Figure 4. 22 The Projection and Radiation Distribution Diagram



Projection

Figure 4. 23 Projection Coverage in One Pixel

To evaluate a single projection, only the area covered by the projection and the radiation area need to be considered. Each grid can be covered by one pixel; the coefficient  $\phi_{i,j}$  is the coverage ratio for each pixel (Fig. 4.23). If the projection area is completely covered by pixels, the coverage ratio is 1. If the projection area is only

partly covered by pixels, the covered area is denoted by  $\phi_{in}$ , the uncovered area is denoted by  $\phi_{out}$ , where the ratio is between 0 and 1.

The fan beam projection is:

$$I_{\sigma_p} = \sum_{i=1}^n I_i * \phi_{i,in} \quad (4-50)$$

To overcome the attenuation of intensities, a coefficient index  $a^2/R^2$  by Inverse-square Law of a point source luminous is induced to evaluate the intensity loss of combustion; where  $a$  is the aperture of the fibre and the  $R$  is the distance from the element pixel to the fibre. The sum intensity of projection can be rewritten as:

$$I_{\sigma_p} = \sum_{i=1}^n I_i * \phi_{i,in} \times \frac{a_i^2}{R_i^2} \quad (4-51)$$

Using iteration to obtain an approximate solution,

$$e_{new_i} = \left\{ \frac{I_{measured}}{I_{P_i}} e_{P_i} \phi_{in_i} \frac{a^2}{R_i^2} \right\} + \left\{ e_{P_i} \phi_{in} - e_{P_i} \phi_{in_i} \frac{a^2}{R_i^2} \right\} + \{ e_{P_i} \phi_{out_i} \} \quad (4-52)$$

Where  $e_{new_i}$  is the emission coefficient after iteration;

- $e_{P_i}$  is the previous iteration emission coefficient;
- $I_{measured}$  is the measured intensity of projection.;
- $I_{P_i}$  is the evaluated value of previous iteration;
- $\phi_{in_i}$  is the coverage ratio of projection in each pixel;
- $\phi_{out_i}$  is the uncoverage ratio of projection in each pixel.

The iteration coefficient is divided into three in each bracket of equation 4-53. The first



term is the difference between the detection intensity and evaluated intensity. The second term is a value that represents the Inverse-square Law reduction of distance intensity attenuation. The third term is the projection uncovered ratio. Equation 4-51 can now be rewritten with the emission coefficient:

$$I_{evaluated_i} = \sum_{i=1}^n I_i * e_{old_i} \times \phi_{i,in} \times \frac{a_i^2}{R_i^2} \quad (4-53)$$

## Array MART Software Implementation

The software was designed to implement tomography image reconstruction from projection data. Software implementation consists of Initialization, data operation by iteration and visualization. Initialization is a debugging process to prepare the operation parameters of the system. The parameters are the interval angle between each fibre group, the aperture angles, the number of connected fibres and the cylinder bore diameter. To improve the system accuracy and reduce the algorithm operating times, the OAG schematic was considered in simplified characteristics for the initialization algorithm (Fig. 4.24). If the diameter of the chamber radiation area is 1, the length of the outside chamber is denoted by  $a_i$ ; the diameter of the OAG is designed as  $\sqrt{2}$  in length. The initialization of projection coverage is:

$$\begin{bmatrix} X \\ Y \end{bmatrix} = [b_i \pm (1 - a_i) \tan(\frac{\theta}{2})] \quad (4-54)$$

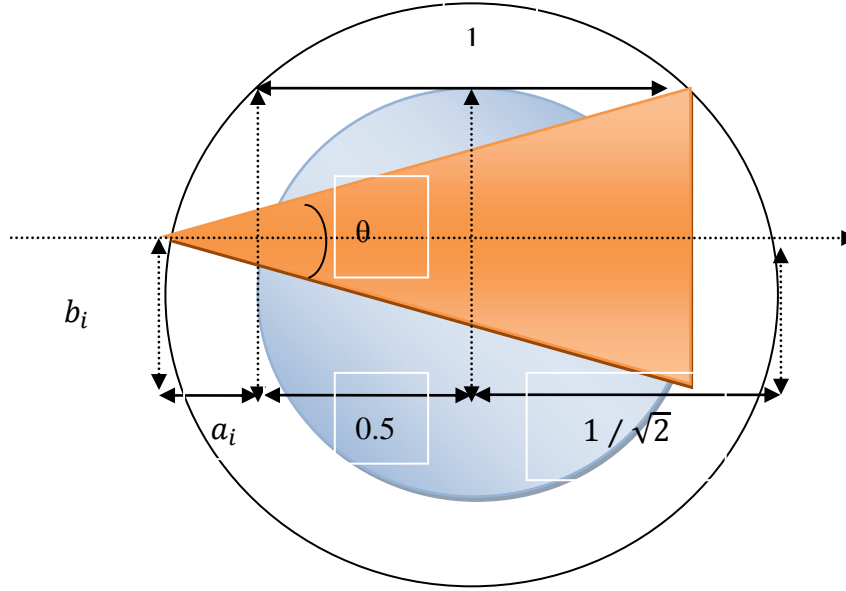


Figure 4. 24 Array MART Software Initialization Algorithm of OAG Design

After the initialization debugging process, the software starts processing the signals to prepare image visualization. The program algorithm executes a single iteration of equation 4-52. It starts with one projection, the coverage ratio and the crossed times of each pixel are recorded in memory, then the program loops for the number of iterations and sum the intensities of each projection. Finally the average intensities of each pixel are distributed in pixels to achieve visualization. The initial ‘guess’ function of each pixels is expressed in equation 4-55:

$$I_{initial} = \int_{-b}^b \int_{a-(y-b)\tan\theta}^{a+(y-b)\tan\theta} \frac{f(x,y)}{(y-b)^2} dx dy \quad (4-55)$$

Where the  $(y-b)^2$  is the following the inverse square law and it can not be zero.

The 200×200 resolution image of combustion visualization is too complex to process by computer. The visualization resolution is set to 10×10. The intensities

distribution in each pixel uses bilinear interpolation methods (Fig. 4.25). Since the evaluated intensities are discrete signals; to display intensities as continuous, 55 values are interpolated between two neighborhoods intensities. The interpolations are average values based on the difference between two neighborhoods.

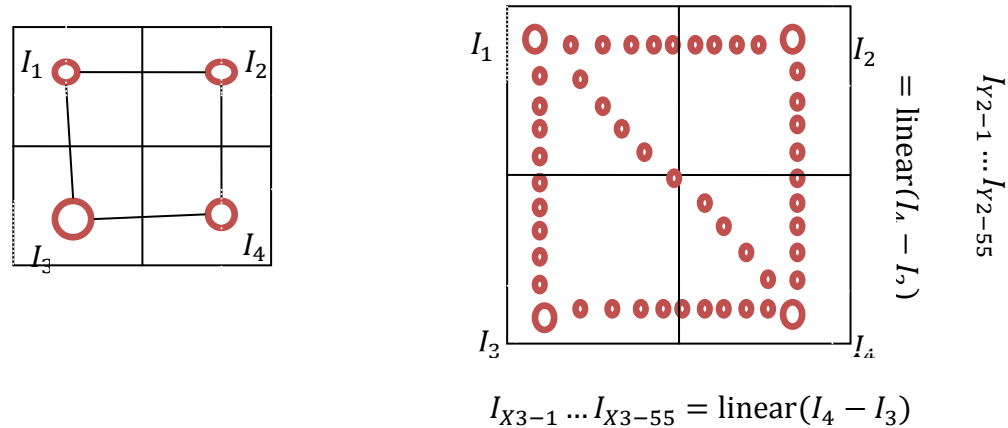


Figure 4. 25 Continuous Visualization Transformed by Intensity Interpolation

#### Algorithm Diagram

The original image reconstruction was in jet colourmap with blue background in Figure 4.26 (a). To visualize the combustion in more comparative chromatogram, the results images are displayed in jet colourmap with black background (Fig. 4.26 b).

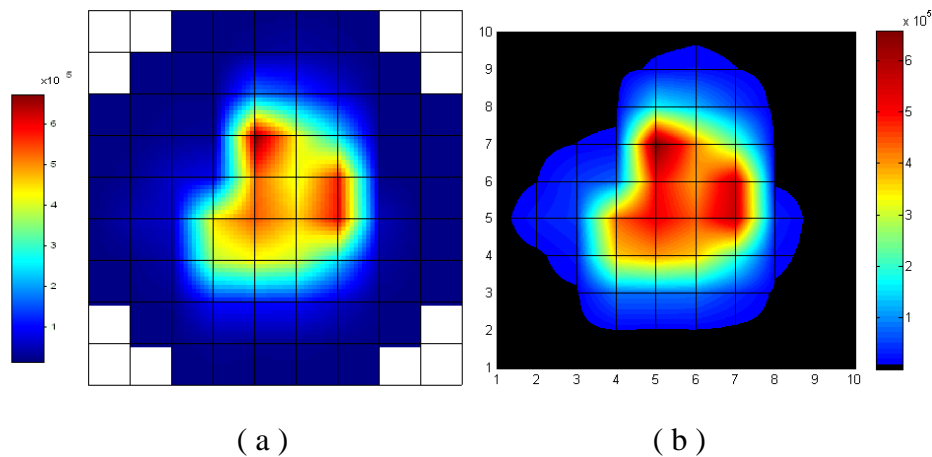


Figure 4. 26 Visualization of Object in Colour Map

## Array MART software testing

To test its performance, the Array MART software was first applied to several ideal models. Since combustion is considered in a linear projection, a linear module is simulated and tested (Fig. 4.27).

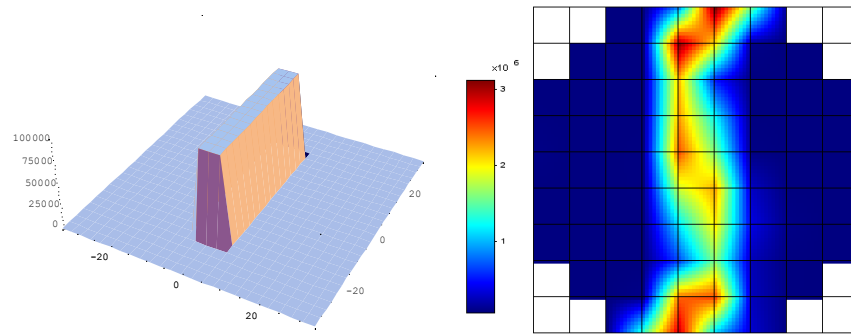


Figure 4. 27 A Linear Simulated Model Tested by Software

The intensity image reconstructed by the software for a linear object is displayed (Fig .4.27). Serious distortions were observed between different intensities at the interfaces in comparing the image of the initial model and the reconstructed model. The flame is commonly represented using a Gaussian function. Thus, the Gaussian function flames are simulated in various situations below. The signal from a simple Gaussian flame is:

$$f(x,y) = 100e^{\omega(x^2+y^2)} \quad (4-56)$$

Where  $\omega$  is the frequency of the Gaussian flame.

Table 4. 2 A Single Gaussian Flame Image Reconstruction by Numbers of Iterations

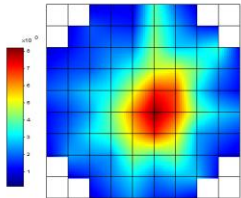
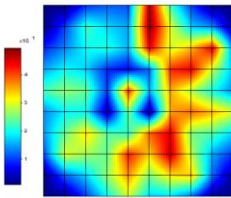
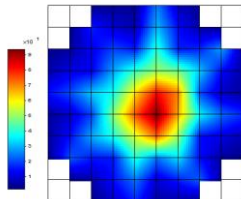
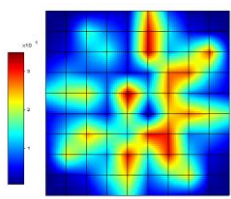
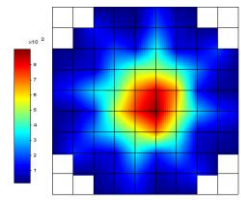
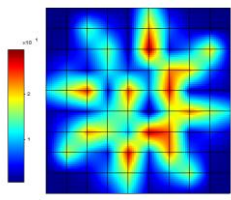
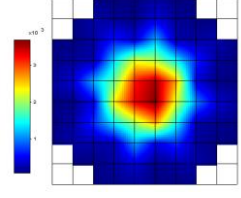
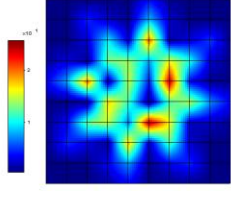
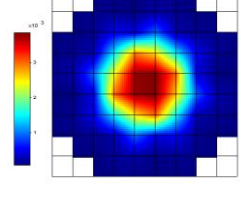
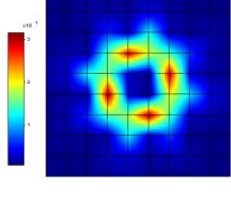
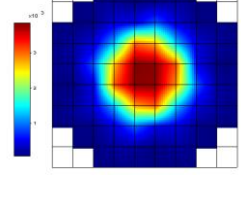
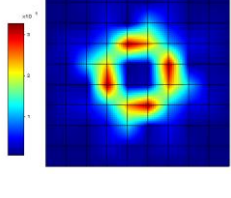
Iteration	Reconstruction	Error Plot	Average Error	Maximum Error
1			21.62%	48.70%
10			11.62%	33.74%
100			8.17%	28.63%
1000			4.48%	24.01%
10000			4.07%	30.13%
100000			4.14%	31.58%

Table 4.2 illustrates image reconstruction of the Gaussian flame using numerical iteration. Initial errors during the image reconstruction, were sharply reduced by increasing the iterations. The software performed the flame reconstruction well. The Error Plot Images is obtained by the reconstructed image minus the initial image.

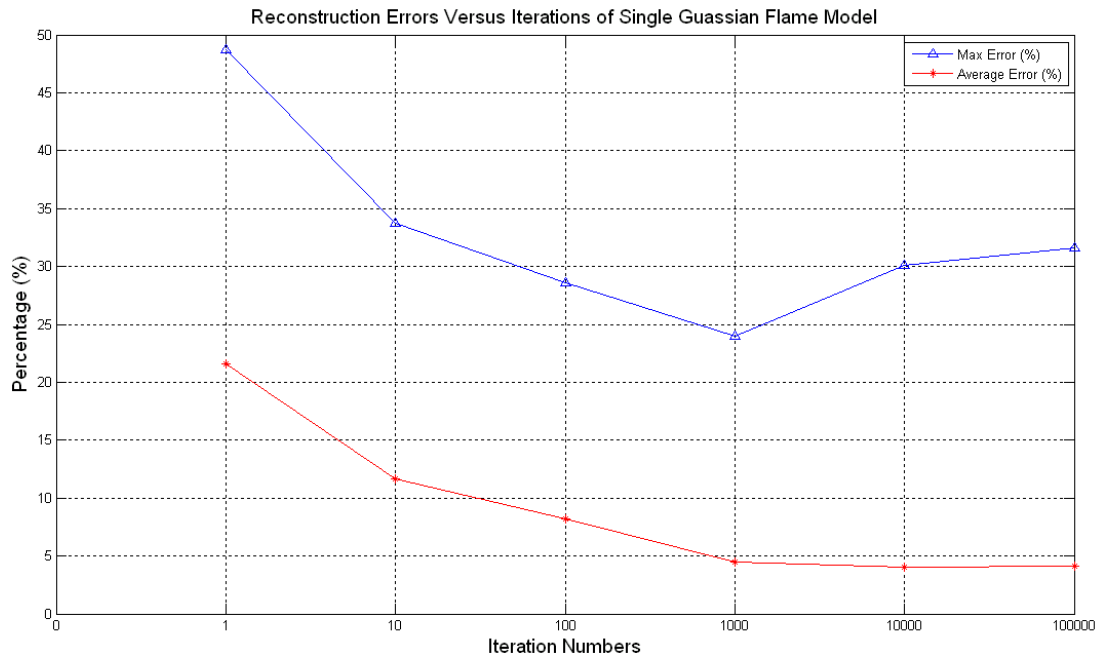


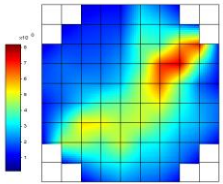
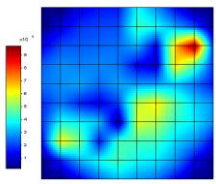
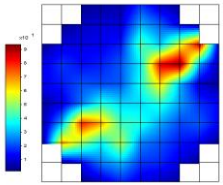
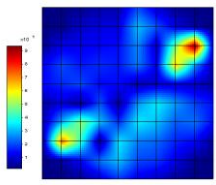
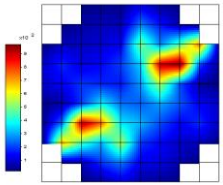
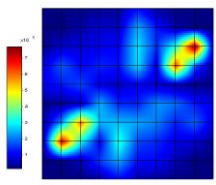
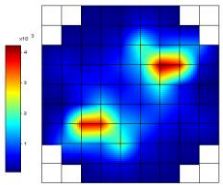
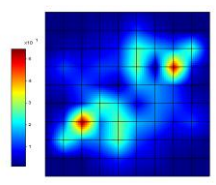
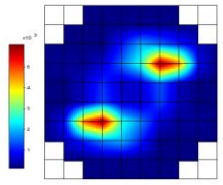
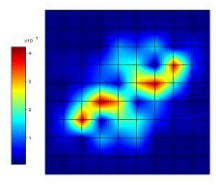
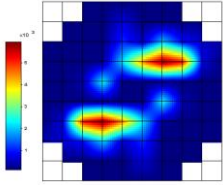
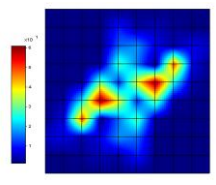
Figure 4. 28 Error Characteristics of Single Gaussian Flame Model

To consider multiple Gaussian flames, two Gaussian flame models were simulated to test image reconstruction. The multiple flame model is given by the equation:

$$f(x, y) = 100e^{\omega((x+1.5)^2+(y-1.5)^2)} + 100e^{\omega(x-1.5)^2+(y+1.5)^2} \quad (4-57)$$

Table 4.3 and Figure 4.33 show the results.

Table 4. 3 Two Gaussian Function Flames Reconstruction by Numbers of Iterations

Iteration	Reconstruction	Error Plot	Average Error	Maximum Error
1			26.87%	93.00%
10			15.45%	90.82%
100			11.91%	75.73%
1000			7.59%	52.41%
10000			5.43%	40.21%
100000			7.35%	59.54%

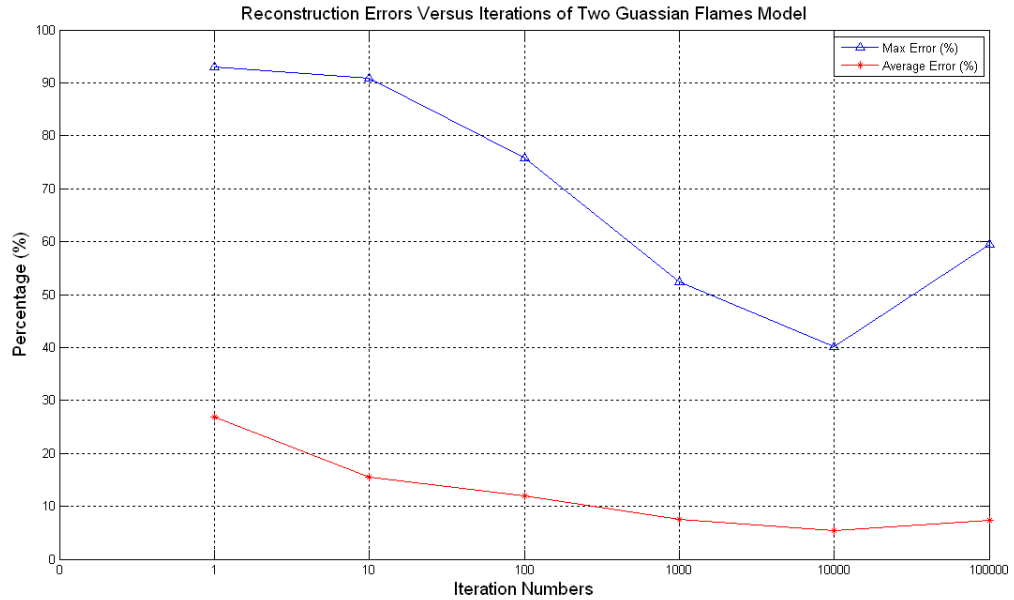


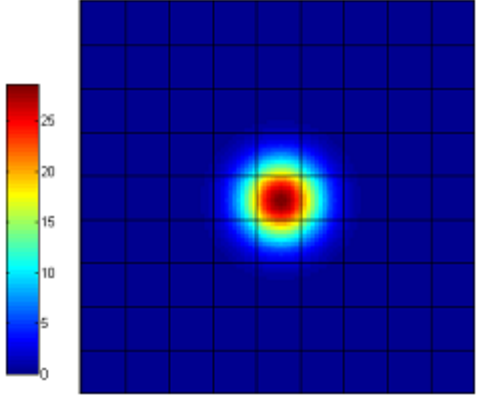
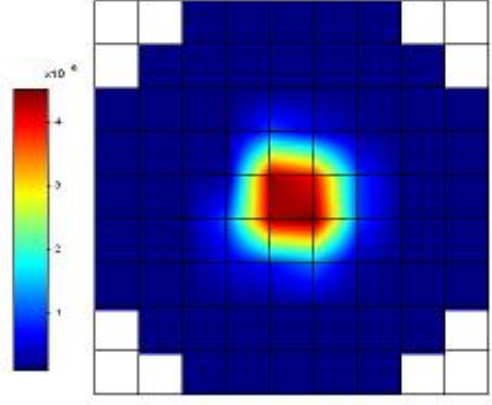
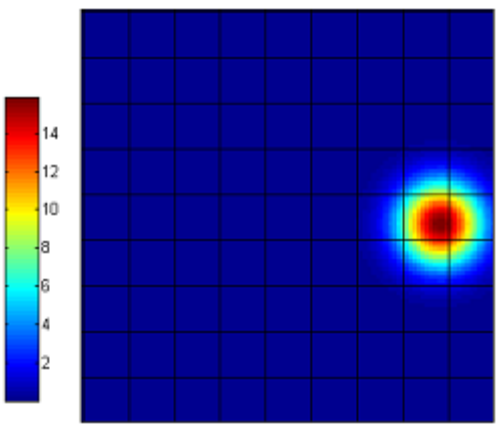
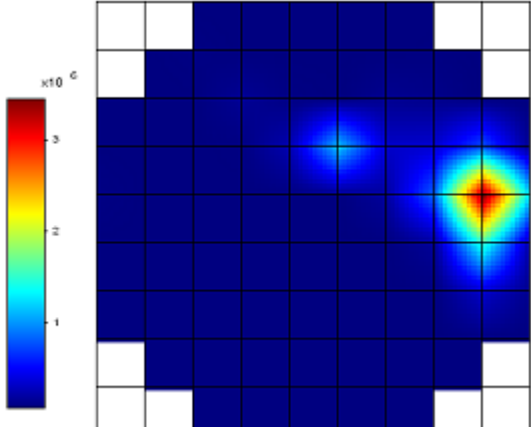
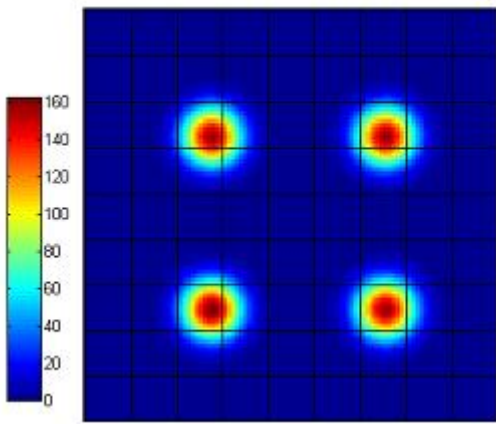
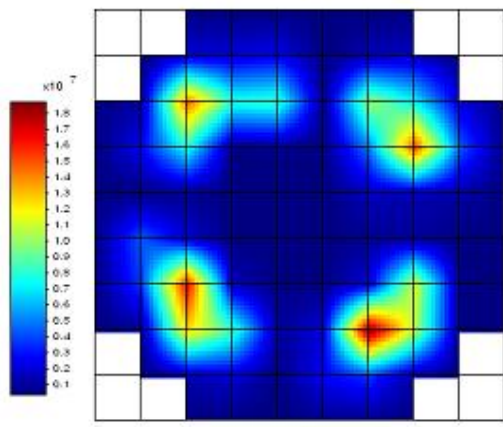
Figure 4. 29 Error Characteristics of Two Gaussian Function Flame

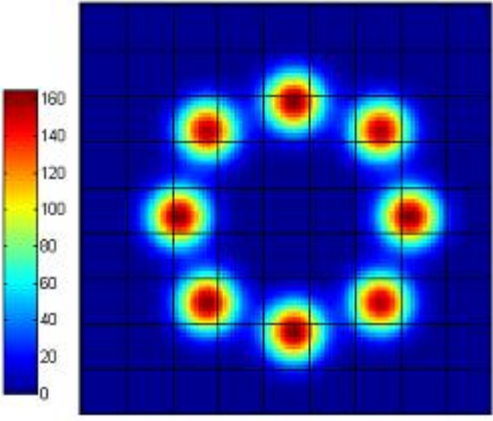
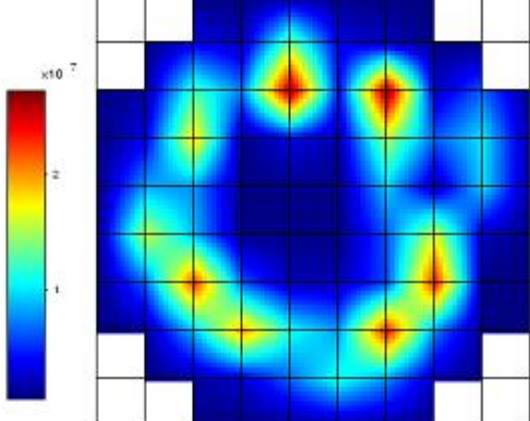
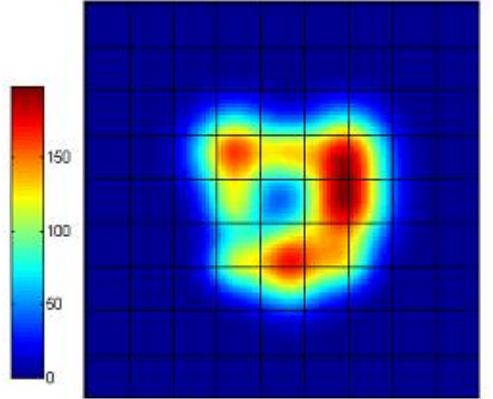
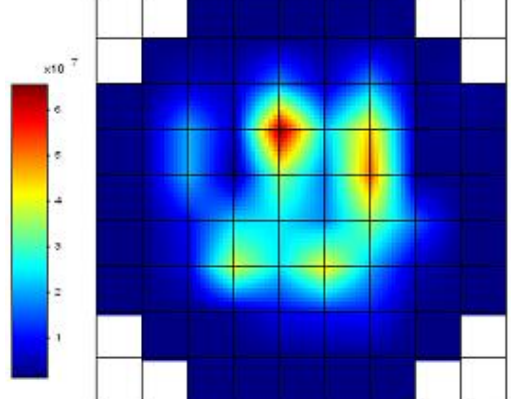
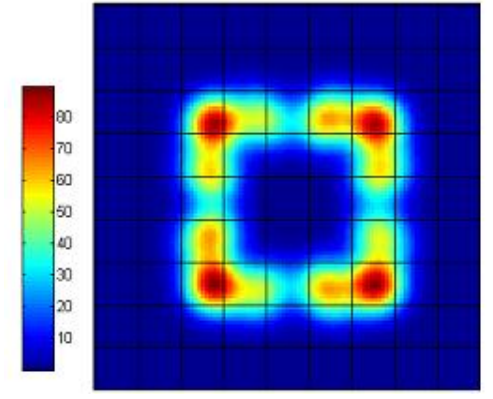
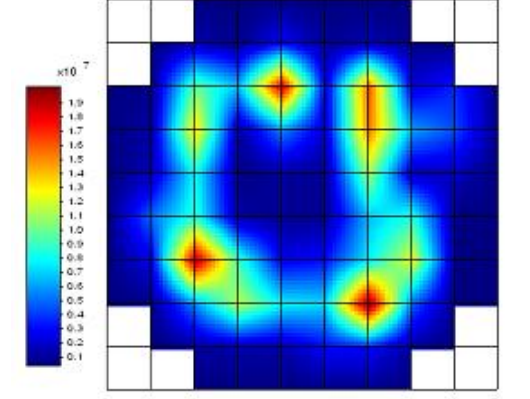
The software performed less accurately for multiple Gaussian functions flame. The reconstructions became more stable after 1000 iterations. Table 4.4 demonstrates a sequence of images to verify the MART by variety simulation models. The left images are simulated models: Gaussian Flames, Flames by Multiple Discrete Gaussian Turbulences and Flames by Multiple Continuous Gaussian Turbulences. The right figures are reconstructed images after 1000 iterations.

After verifying, the MART technique performs reconstructed images for all of models after 1000 iterations. In the reconstructed Gaussian flame models, the software is sensitive to the size varying of models and to the displacement of models. There is small distortion when the flame is close the eddy of chamber, for instant the reconstructed image of 'Gaussian Flame On Right'. It caused by less cross-correlations at the boundary of chamber.



Table 4. 4 MART Software Evaluations

	
Gaussian Flame Size in Center	Reconstructed Gaussian Flame in Center
	
Gaussian Flame On Right	Reconstructed Gaussian On Right
	
Four Discrete Gaussian Turbulences	Reconstructed Four Discrete Gaussian Turbulences

 <p>A heatmap showing eight distinct, localized Gaussian-like peaks arranged in a circular pattern on a dark blue background. A color bar on the left indicates values from 0 to 160.</p>	 <p>A heatmap showing the reconstructed version of the eight discrete Gaussian turbulences. The peaks are slightly blurred compared to the original. A color bar on the left is scaled by <math>\times 10^{-7}</math> and ranges from 0 to 3.</p>
<p>Eight Discrete Gaussian Turbulences</p>	<p>Reconstructed Eight Discrete Gaussian Turbulences</p>
 <p>A heatmap showing a continuous function Gaussian flame, which appears as a single, irregular, and somewhat elongated bright region. A color bar on the left indicates values from 0 to 150.</p>	 <p>A heatmap showing the reconstructed version of the continuous function Gaussian flame. The bright region is more diffuse and less defined than the original. A color bar on the left is scaled by <math>\times 10^{-7}</math> and ranges from 0 to 6.</p>
<p>Continuous Function Gaussian Flame</p>	<p>Reconstructed Turbulent Flame</p>
 <p>A heatmap showing a continuous square turbulent Gaussian flame, which forms a bright, somewhat irregular square shape. A color bar on the left indicates values from 0 to 80.</p>	 <p>A heatmap showing the reconstructed version of the continuous square turbulent Gaussian flame. The square shape is visible but with more internal detail and noise. A color bar on the left is scaled by <math>\times 10^{-7}</math> and ranges from 0.1 to 1.9.</p>
<p>Continuous Square Turbulent Gaussian Flame</p>	<p>Reconstructed Continuous Square Turbulent Gaussian Flame</p>

In the reconstructed models of multi-discrete turbulent flames, the reconstructed figure visualizes the discrete Gaussian turbulences perfectly in both spatial distributions and the turbulent sizes. However, there are some distortions by iterations. In the continuous models, some small size Gaussian turbulences are ignored since the software sensitivity is  $5\text{mm} \times 5\text{mm}$ . For instants, the ‘Continuous Square Turbulent Gaussian Flame’ is continued using 20 Gaussian flame models. After reconstruction, only distinct peaks are visualized. Other small turbulences are substituted using linear intensities. Nevertheless, in multiple turbulences test, the reconstructed results are still well sensitive to the turbulences locations and size. The shape of objective is demonstrated though the objective is much complicated.

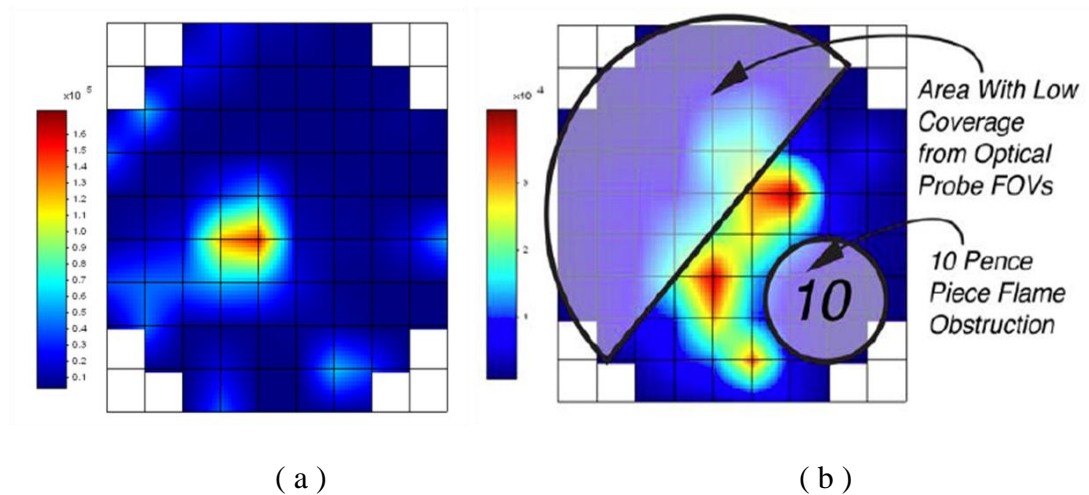


Figure 4. 30 Visualization of Candle Flame and Laminar Flame ( a is a reconstructed image of candle flame; b is a reconstructed image of burner flame )

The Figure 4.30 displays reconstruction images of candle and premixed burning flame in the test. The laminar candle flame displays a small turbulence and its flow direction distinctly. The premixed flame displays the distributions of turbulence

concentrations in intensity and reveals the varying locations of the flame front.

## 4.4 Summary

Chapter 4 specifies the computational methodology of the POET system design.

In tomography, the projections of objective are classified into parallel beam projection and fan beam projection by scanning methods. In the experiment, the fan beam projection had been adopted by its fast scanning property. To consider the cost of system, 40 projections had been employed in the experiment. In combustion reconstruction, the MART algorithm had been applied to evaluate the unknown model of flame front. In simulation of flame turbulent, the Array MART software had been used. The reconstructed images illustrate a minimized averaged error by the use of 1000 iterations. Nevertheless, the programming is originally designed for turbine flame measurement by MEng. students in 2002. Thus, the software has several limitations of in-cylinder combustion visualization: the start time of combustion can not be recognized by software; the signal noise can not be filtered using this programming; the weak signals are dominated by strong signals because of the poor image visualization function. Thus, the software is partially reprogrammed to overcome these limitations in this project but still using MART algorithm.

## Chapter 5.

# Experimental Results Analysis

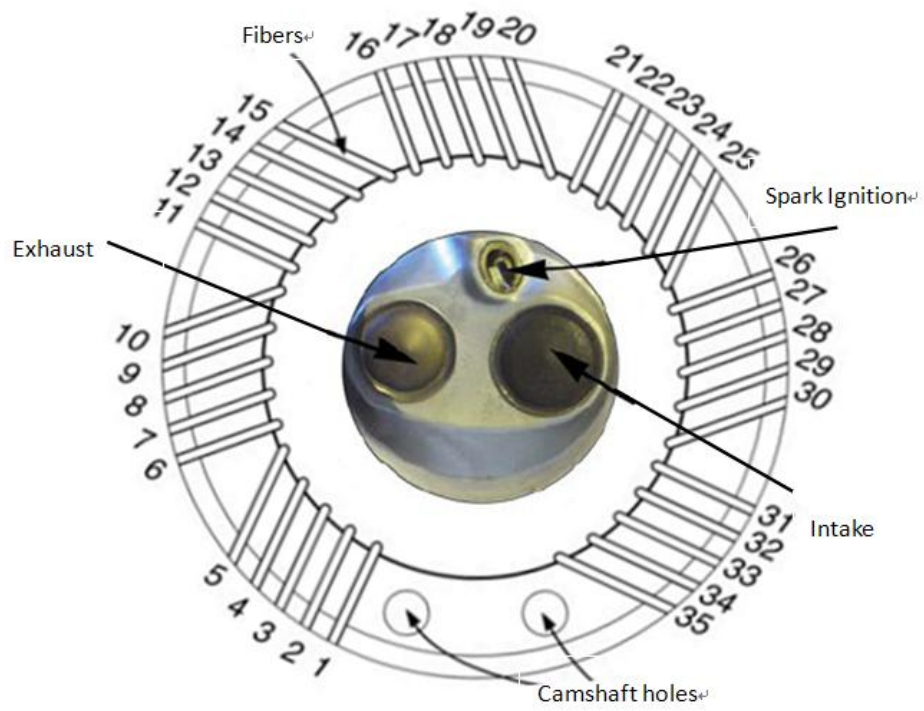
This chapter is the analysis of combustion process by three experiments: the Shack Hartmann system, the photogrammetry and POET system. The Shack Hartmann technique demonstrates the wavefront of different types of turbulent flame. Photography result produces a sequence of images to show the combustion process. In the photographic experiment, the flame was captured by UV filtered and Non-filtered CCD camera. These two experiments give the fundamental investigations of turbulent flame front. It supports the result analysis of the POET system.

In the POET experiment, the analysis is using the data collected from PMTs. The flame front propagation speed is evaluated using projection data. Then the in-cylinder combustion process is reconstructed by the MART techniques. In velocity evaluation, two types flame front turbulence are discussed: UV filtered flame and Blue filtered flame. In each flame, individual projection is taken for analyzing the flame propagation speed. Since the PMTs are tomographically surrounding the chamber in different angles (Fig 5.1 a), each projection has different values of the flame front intensities in time and space (Fig 5.1 b). Thus, the flame turbulent differences are observed and analyzed based on the projections varying. According to displacement of flame front propagations in time varying, the speed is appraised.

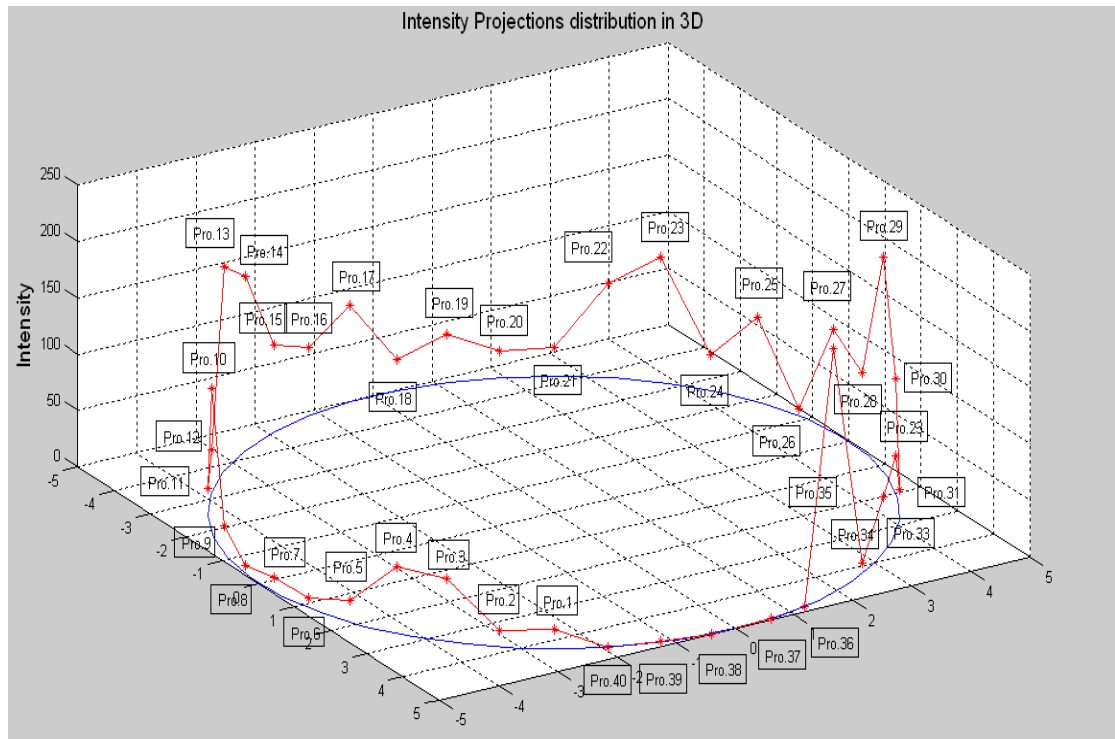
After the measurements of flame front velocity, the combustion process is

reconstructed by MART. To analyze the combustion process, several results are illustrated:

- i. The brief description of result images. This section is to explain the result images and how to use images to analyze the combustion.
- ii. The analysis of UV flame combustion. In this section, the reconstructed images using UV filtered data has been used to evaluate the turbulences. One iteration and 1000 iteration images have been compared by Crank Angles to discuss the combustion process. The selected combustion images starts from spark ignition time  $-27^\circ$  and ending at  $180^\circ$  which is a complete combustion explosion stroke. One iteration images demonstrate the rough structure of turbulent combustion. After one iteration, the brief combustion distribution has been confirmed by averaging cross-sectional intensities. The 1000 iteration images illustrate the corrected images by iterative coefficient correction.
- iii. The analysis of Blue combustion. In this section, the Blue flame data has been employed to evaluate the different turbulences compared with UV flame. One iteration and 1000 iteration images have been shown by Crank Angles to compare with UV combustion process.
- iv. The analysis of combustion in different equivalent ratios is dependent on changes of air/fuel mixtures. In this section, the combustion is analyzed in four different engine revolutions: 2280 RPM in rich fuel condition; 1550 RPM, 1200 RPM and 1090 RPM in lean fuel condition.



( a )



( b )

Figure 5. 1 POET O-Ring Gasket Layout diagram (a) and an Example of 3D view of Projections Distribution (b)

## 5.1 Shack-Hartmann Camera Applied to the Study of Flame Turbulent Density

A variety of optical methodologies have been applied to measuring the flame density gradient, including Schlieren and Interferometry methods. These methods perform well with thermal changes which correspond to the distribution of flame density. Experiments are often subject to flame turbulence but it is difficult to remove environmental vibrations during operation that caused inaccurate results. Further, these methods have distinct tomographic limitations for investigating in cylinder combustion in the reasons of their complicated implemental system. A new technique was needed which is sensitive to wavefront aberrations in temporal and spatial dimensions but insensitive to the vibration caused by the environment [90]. Two techniques have been identified to overcome the limitations: The Shack-Hartmann Wavefront Sensor (SHWF) technique and the PMT (Photomultiplier Tube) technique in the experiments. Both of two techniques have been evaluated by testing. SHWF presents a great performance for investigating the small turbulences. However, the PMT system has been adopted since the SHWF system is more complicated and its great costs of equipments.

The SHWF device which commonly consists of an optical sensor and a micro lenslet array is an adaptive optics for the measurements of object density and it is robust, stable and sensitive. SHWF sensor has developed rapidly in recent decades because of its accurate implementation and reliability of phase shifting measurements. Small thermal gradients are difficult to measure using classic quantitative



methodologies. SHWF is sensitive to the spatial distribution of the surface of the turbulence and insensitive to the vibration errors. The system can be easily setup to diagnose flame density under a variety of conditions in implemental environments. Tests were conducted under laboratory conditions for comparison with other methodologies.

In the Shack Hartmann camera system, hundreds of microlenses are focused on the camera and create a grid of focal spots on the sensor. By passing the flame, the focus spots are shifting and defocusing due to the varying of density of burning flame. Because lenses are multiple and small enough to detect these changes, the slope of each microlens focuses are recorded on the camera (Fig 5.2). Thus, the flame density gradients can be calculated depending on the average slope of the locations of the subaperture of the lenslet array. Assume the wavefront aberration angle  $\alpha$  and it is:

$$\tan \alpha = \frac{z}{y} = \frac{\Delta y}{f} \quad (5-1)$$

if  $w_{(x,y)}$  is the wavefront, the wavefront tilts is in following expressions:

$$\begin{aligned} \frac{\partial}{\partial x} W_{(x,y)} &= \frac{\Delta_x}{f} \\ \frac{\partial}{\partial y} W_{(x,y)} &= \frac{\Delta_y}{f} \end{aligned} \quad (5-2)$$

The wavefront  $w_{(x,y)}$  is calculated from the deviations of subapertures to reconstruct a 2 D image of the distortion of the flame density distribution (Fig 5.3).

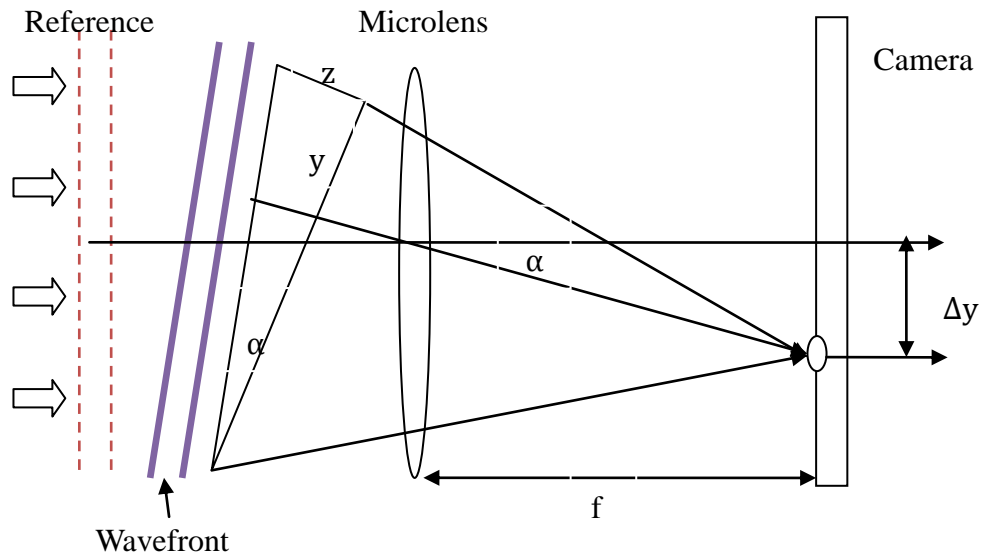


Figure 5. 2 Slope of Tilt Measurement by Single Microlens

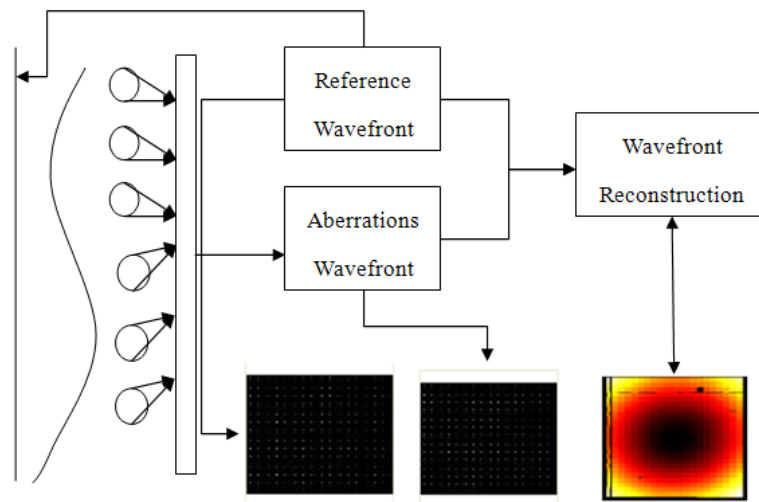


Figure 5. 3 Flame Density Gradients Reconstruction Process

### 5.1.1 Flame Density Distribution Implementation using SHWF Technique

To test the feasibility of using a SHWF sensor in a tomographic reconstruction system the aberration of flame density gradients was measured. A WFS (Wavefront

Sensor) 150C camera consisting of a  $31 \times 39$  lenslet array and a  $1280 \times 1024$  resolution CCD camera was employed. The pixel size is up to  $4.65 \mu\text{m} \times 4.65 \mu\text{m}$  and the frequency of maximum resolution is 15 Hz. The testing procedure used a 35 mW Helium-neon laser as an emitter to generate a collimated parallel beam through the density detection region. The SHWF camera recorded the created wavefront. System set up is shown in Figure 5.4. A Neutral Density filter reduces the intensity of the 3 mm laser beam. The laser beam is then enlarged and collimated to a 10 mm diameter parallel beam to increase the observing region. By crossing the flow density, the output tilted beam is carried with flow density information. The WFS 150C camera records the density gradient for wavefront reconstruction.

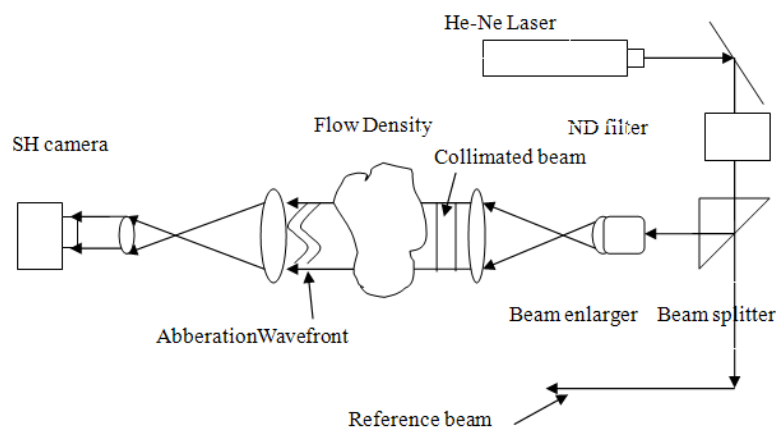


Figure 5. 4 Flow Density Measurement Set up

### 5.1.2 SH Experimental Results Analysis

A SH camera has been used to evaluate the flame density and flame front intensity distributions. In experiments, a candle with soot burning, a premixed diffusion flame by Bunsen burner and a gas flow without burning are analyzed. The

candle and premixed flame are measured in order to evaluate the SH sensitivity of flame turbulence in spatial and temporal domain. The measurement of unburned gas flow is aim to estimate the optical system intensity errors which are caused by flame chemiluminescence.

The SWHF technique is well known for its measurements of wavefront aberration using small lens arrays to detect the Cartesian displacements and phase shifts. In a Cartesian coordinates, the aberration wavefronts change the location of lenses focus. Thus the deformation induced by density gradients can be measured quantitatively and accurately. In the results of lenses defocus, the phase shifts of the wavefront can be measured using Zernike Polynomials [91, 92].

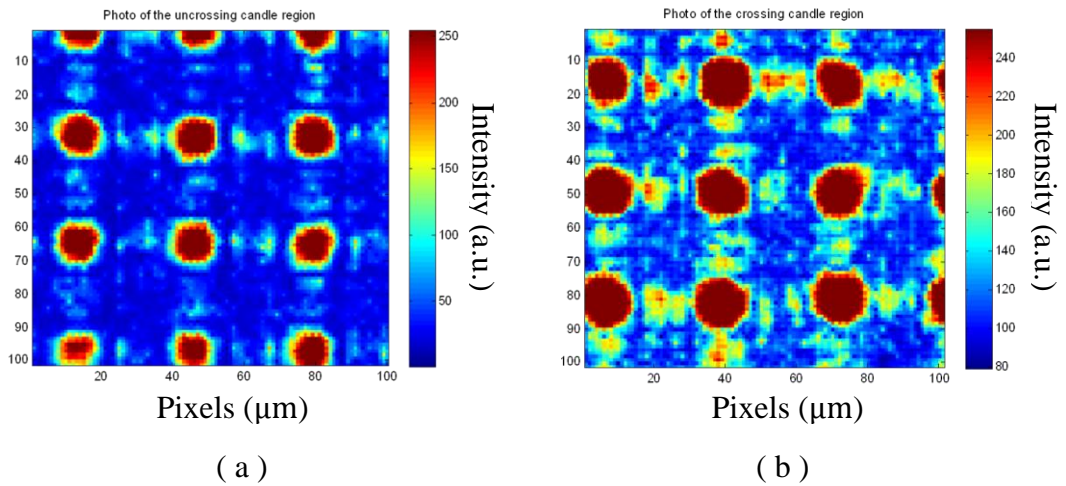


Figure 5. 5 Comparison between uncrossed and crossed regions of candle

In candle flame, the great luminosity of soot may affect the measurements of intensity by the S-H camera. The slow turbulence has little influence on wavefront deformations. Thus, it is easy to capture aberration photos of the candle. Generally, the flame intensity is discussed in Gaussian distribution. In the SH camera, it is

accompany with significant diffractions because of the small size of lens (Fig. 5.6). By comparison of image (a) and (b), a small change to size, location of lens focus and diffraction spots between focus is strongly deformed due to the varieties of optical path difference. Even the candle is in small turbulence, the changes in the candle flame front were still clearly recorded in  $\mu\text{m}$  (Fig 5.7). In the Figure, cyan represents negative differences and yellow is the positive differences. The general structure and detail of the flame can be observed (Fig 5.8).

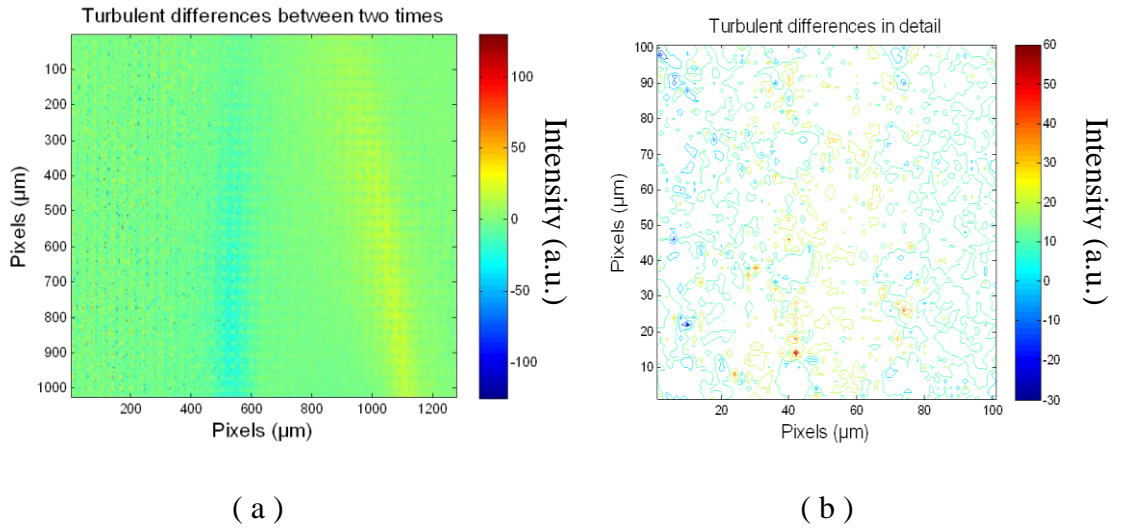


Figure 5. 6 Varying of Turbulences. (Image a is the displacement between two instantaneous time; Image b is the contour map of small turbulences)

Moreover, though the aberration of candle is not intense, the curve of surface is slightly uneven (Fig 5.7). In the Figure, owing to the great sensitivities of small tilts, the refractive index of density gradients and the defocus intensity are described in  $\mu\text{m}$  by 3D images. Candle front turbulence can clearly be seen in both spatial and frequency domains.

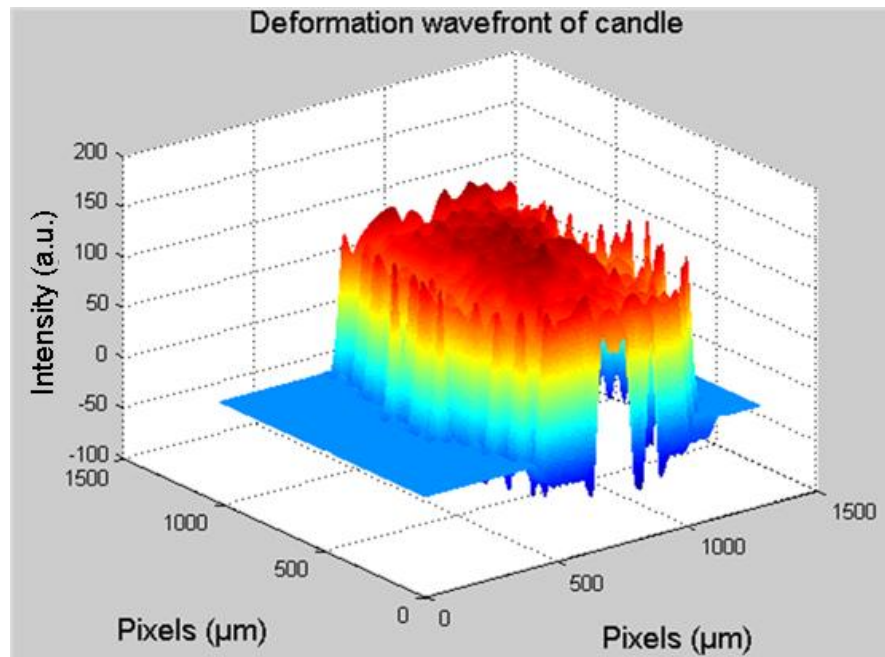
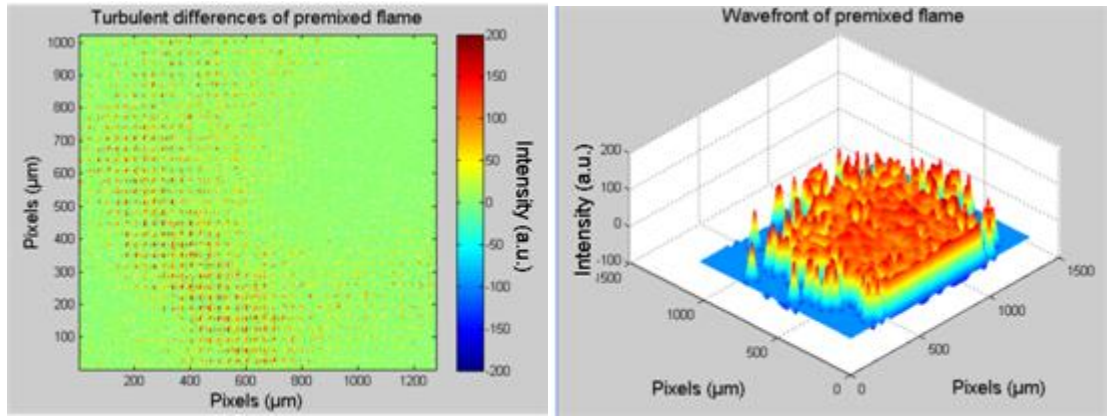


Figure 5. 7 The Aberration Wavefront of Candle in 3D

In comparison, the premixed flame is more turbulent than candle soot flame. For testing SHWF using in premixed flame, a Bunsen burner with premixed fuels was used to observe the flame aberration using an S-H camera. The premixed flame rich in oxygen gives a less sooty diffusion flame. The outline of the turbulence flame was photographed by a normal high resolution CCD camera. The small spatial turbulence was difficult to capture and a Shack Hartmann camera was used to the problem. In Figure 5.8 (a), the displacements are shown by red scatters. Although more discrete than for a candle (Fig 5.6 a), the deviations of focus spots still significantly explain the flame turbulence in both outline and particulars. In the 3D mesh model the changes of premixed flame is less uniform than for a candle. The phase shifts are greater than for a candle according to the observation of surface uneven. It is present the greater refractive index of premixed flame (Fig. 5.8b).

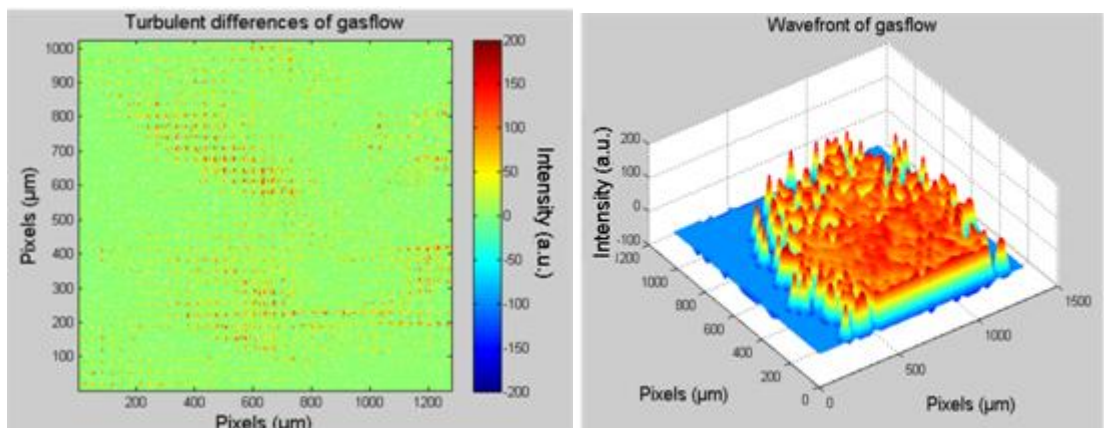


( a )

( b )

Figure 5. 8 Deformation Wavefront of Premixed Flame in Rich Fuels (Image a is the turbulent displacement between two instantaneous flames; Image b is the wavefront of flame turbulences)

In the test, the chemiluminescence of candle and premixed flame creates background optical noise and adds extra intensities on wavefront singles. Thus, estimate and dispel these errors, an unburned gas flow is utilized.



( a )

( b )

Figure 5. 9 Deformation Wavefront of Gasflow Turbulence (Image a is the turbulent displacement between two instaneouse flames; Image b is the wavefront of turbulent flame)

In comparison, the gas flow turbulence has been clearly recorded and reconstructed (Fig. 5.9). The background noise is at  $\pm 10$  a.u. intensities (varying by distances) but with low affects on lens defocus and focus displacement. Thus, the SH camera can be applied in the investigation of combustion gradients. Meanwhile, it has been found that the premixed flame is more turbulent than unburned gas flow in the same experimental conditions.

## **5.2 Flame Front Analysis by Photogrammetric Technique**

Many methods have been developed to analyze the chemiluminescence of combustion and they use different parameters to trace the behavior of flame propagation. Flame intensity as the critical parameter is not only relevant to the temperature of the flame, but presents in variations of combustion over time, spatial and frequency domains.

Historical method of combustion measurement is to photograph the flame by a high speed camera. Visual interpretation of the flame surface is intuitive but often difficult to apply. In this experiment, the combustion process is directly observed using a high speed CCD camera through a transparent Quartz Windows as cylinder head (Fig. 5.10). A sequence of  $512 \times 512$  pixel combustion propagation photos is captured through a transparent cylinder head by a 20k Hz CCD camera in Figure 5.11. To analyze the detail, a contour image of the combustion is used (Fig 5.12). The spark is



ignited at 0 second, and the flame propagates towards the boundary of the chamber crossing the intake valve. Then the flame spreads through the exhaust valve with less intensity.

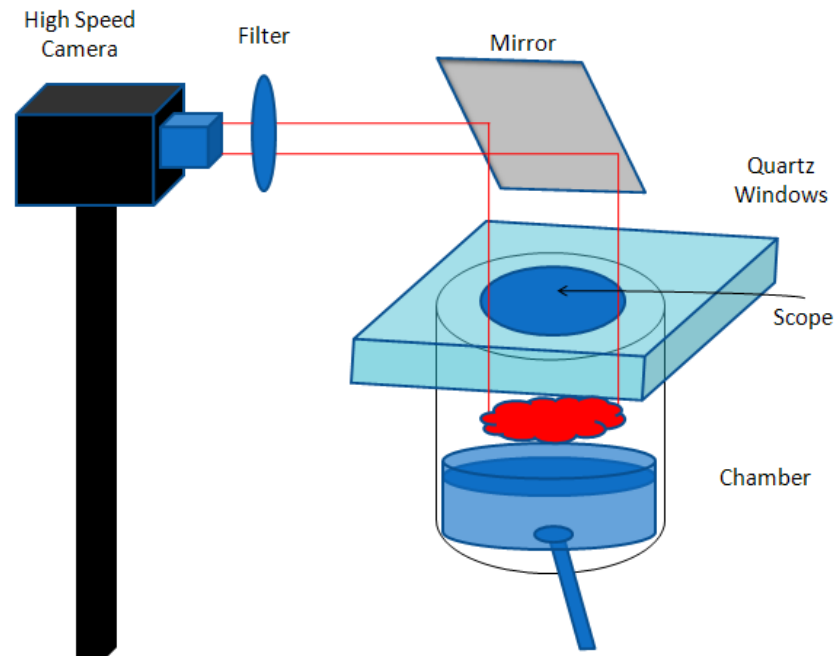


Figure 5. 10 Photogrammetric Measurement System (In the experiment the filter is a 310 nm bandpass UV lens. The frequency of CCD camera is up to 2 kHz)

In Figure 5.11, flame front propagates fast from CA 0° to 45° and takes 3.75 ms to reach the chamber boundary. Propagation speed is approximately calculated as 18.7 m/s in average. Flame density varied through the chamber. The explosion initially occurred at the site of ignition spark corresponding to CA 0° photo. Then it fronts through the intake valve with intensity firstly increasing and then decreasing. Synchronously, it crosses exhaust valve side of chamber to boundary with intensity decreasing in general.

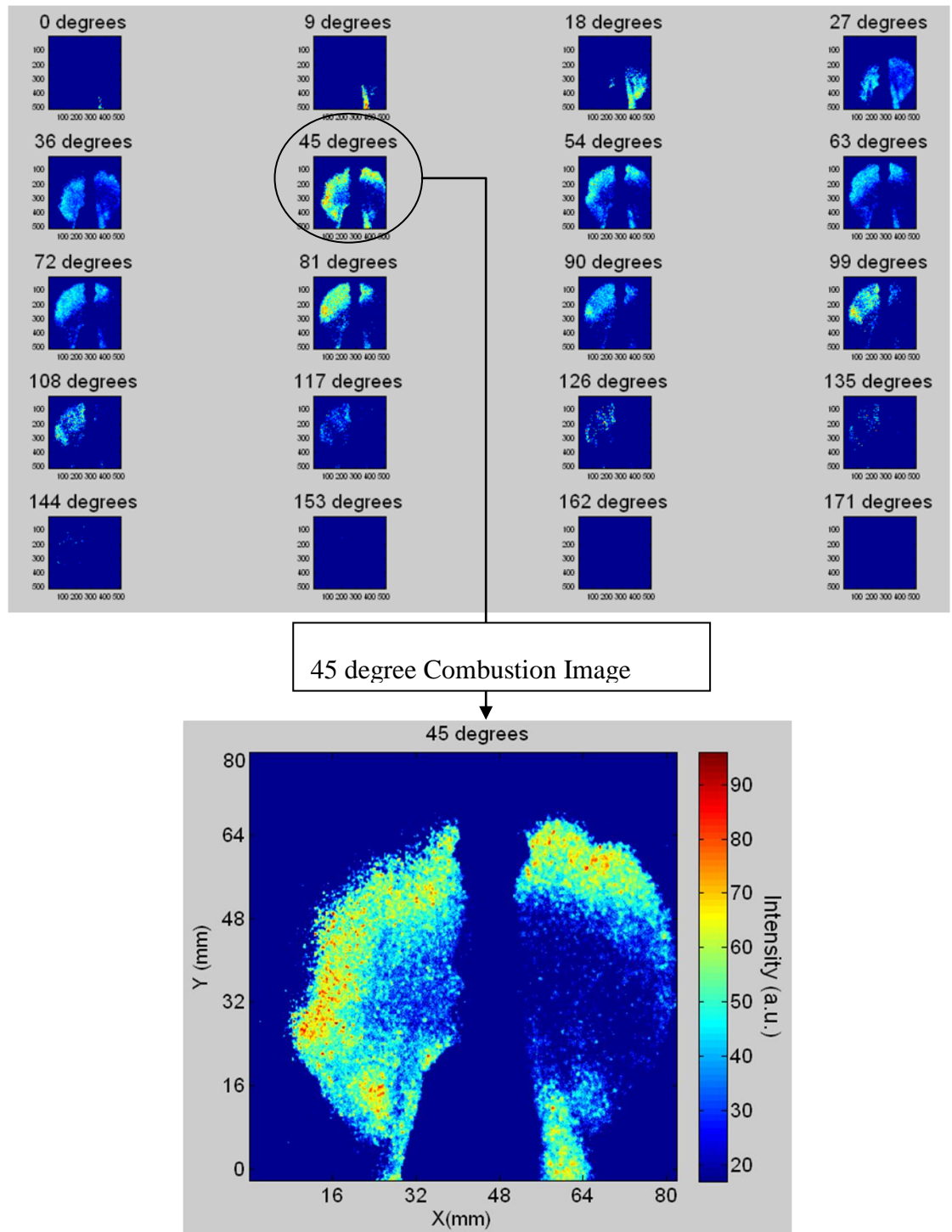


Figure 5. 11 Photographic Images of Combustion Propagation without Filter (Top Views of Combustion Process using a sequence of different Crank Angles images taken by non-filter high speed camera)

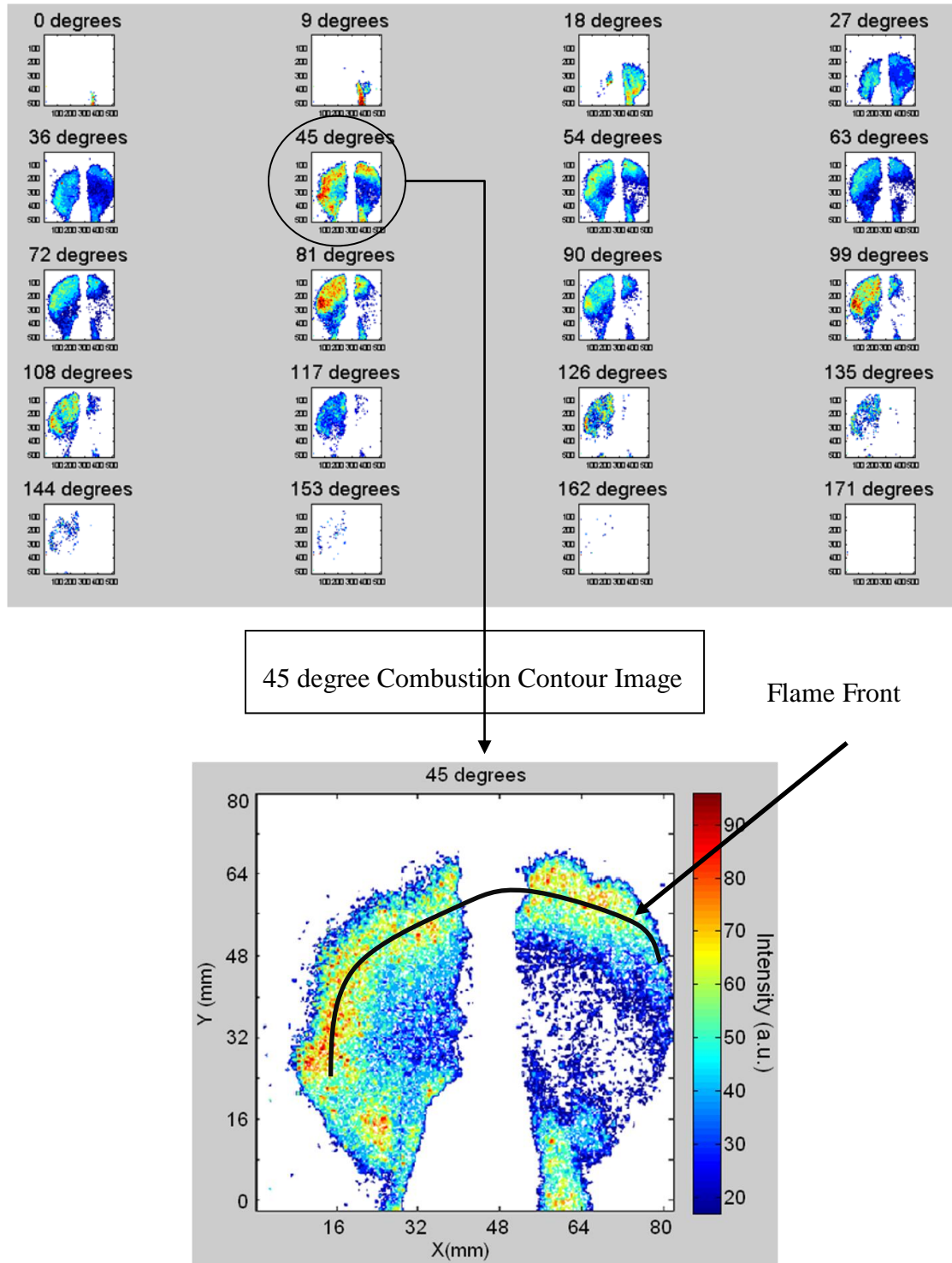


Figure 5. 12 Contour Images of Combustion Propagation without Filter (The black curve has been recognized as flame front which is with high intensities and also is an interface between burnt gas and unburnt gas)

The flame propagation outline is determined by the combustion photograph. Chemiluminescence is a complex chemical process and several reactants have significant effects on combustion efficiency, output power of the engine and exhaust pollution. The investigation of reaction elements is required. Investigators are commonly interested in the  $\text{CH}^*$ ,  $\text{OH}^*$ ,  $\text{NO}^*$  etc. elements because of their different functions in the chemical reaction. In the photography experiment, a camera with an UV bandpass filter is employed to record the flame propagation by UV elements. UV elements as intermediate product of reaction significantly affect the reaction ratio. It represents the contour of flame front and is named as a 'skin' of combustion. In test, the UV chemiluminescence profile is found to be approximately the same as irregular circle of the turbulence curve line (Fig. 5.13). The UV flame is more concentrated than non filtered combustion (Fig. 5.13) in intensity. According to the concentration of UV intensities distribution, flame propagation process is distinctly revealed.

Comparing UV with non filtered intensity profiles of combustion propagation in different reactants, features of rough flame front are described. For further comparison, sums of intensity values of both UV photography and non filter photography were calculated (Fig 5.14). The rapid increasing intensity in the two photographs occurred before the 60 degree crank angle and then fell in a gentle sloping curve. The UV curve represents more flat than the non filtered.

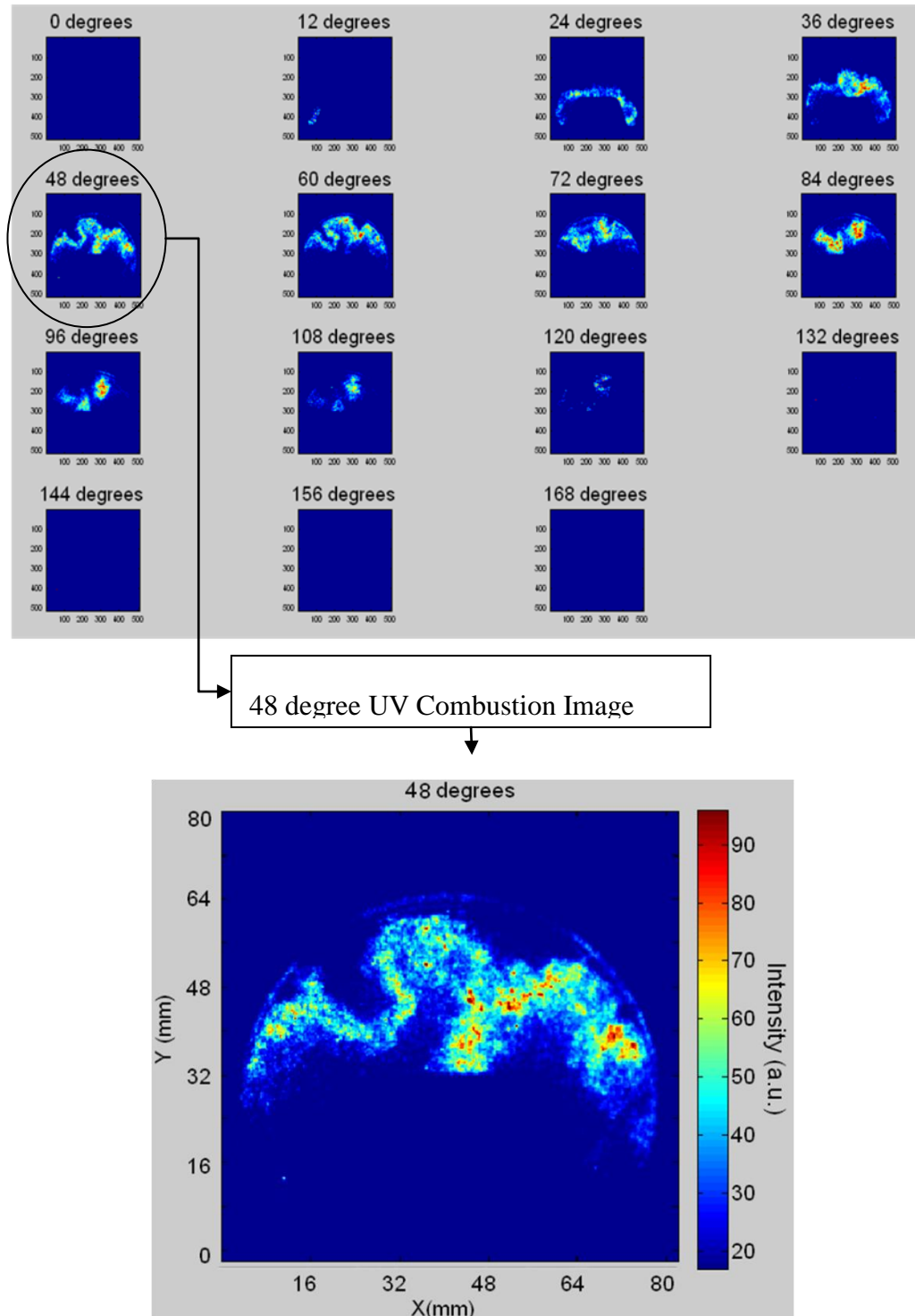


Figure 5. 13 Photographic Images of Combustion Projections by UV Filter (Top Views of Combustion Process using a sequence of different Crank Angles images taken by the UV filtered high speed camera)

However, this method for observing combustion has two limitations. The intensity profile only reveals the surface of combustion propagation from top views although the spatial resolution is sufficient to measure the turbulence of the flame. Direct photography is a qualitative measurement of flame turbulence. A more accurate measurement method is needed to obtain combustion information. Nevertheless, the photos are valuable in understanding flame propagation and provide a reference model for image reconstruction using PMTs diagnostics technique.

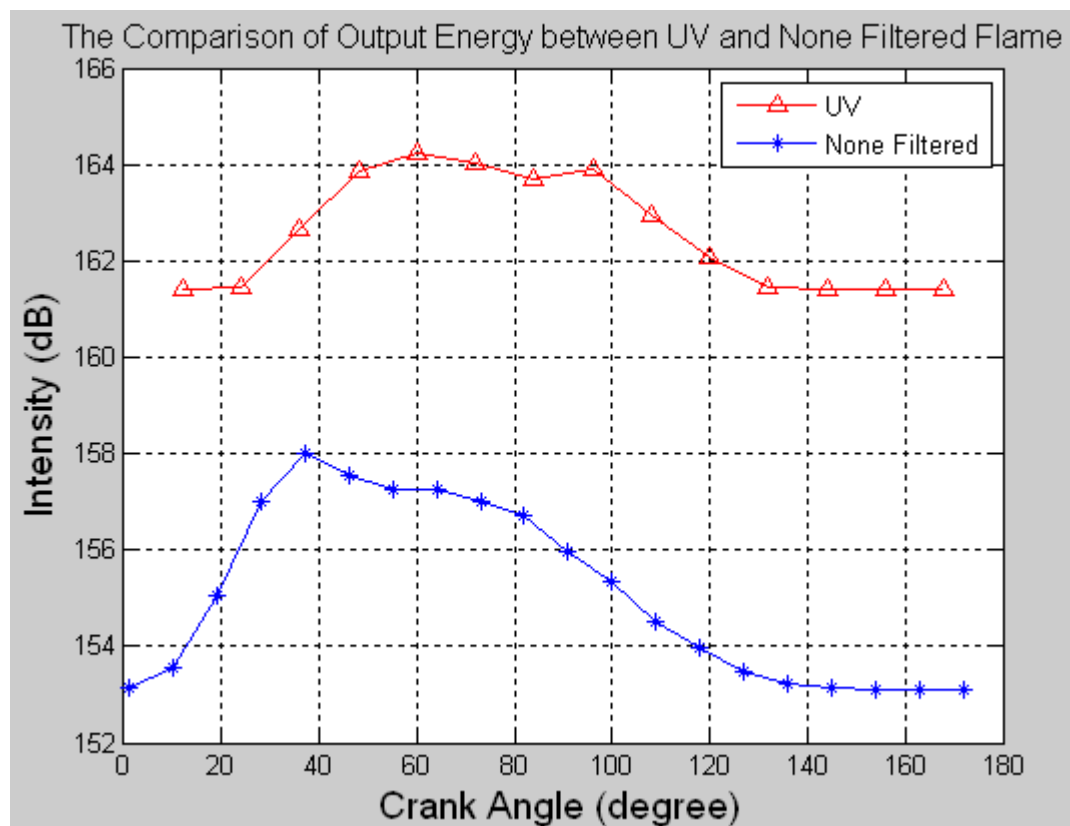


Figure 5. 14 Sum Intensities Comparison between UV and None-filter Combustion

(Note: UV intensities are higher than non filter combustion but in different set up.

In the PMT, it is shown that UV intensities are less than non filter intensities at same combustion temperature.)

## 5.3 Simulated Model of Flame Propagation

Combustion occurs after spark ignition in the engine chamber and its burning fuel is chemiluminescent. The flame front spreads following the explosion path. Thus, the flame front speed can be measured using optical diagnostics techniques to trace the combustion process quantitatively. The combustion within an IC engine is difficult to observe because of the turbulence and quenching. Many scientists recognize the importance of these phenomena in flame propagation analysis [93, 94]. The movement of piston in the cylinder causes the flame to swirl therefore, the analysis starts from a vortex model. During the intake stroke, the gas is let into the chamber in a vortex flow. When piston is moving down during the explosion stroke, combustion causes a similar swirl but turbulence is more complex and different in each engine type (Fig. 5.15). These engine photos (Fig 5.11) shows that combustion starts nearby the spark ignition. It then spreads to the boundary of chamber bore by crossing intake valve and exhaust valve. The propagation can be seen as a vortex model (Fig. 5.15). The flame velocity increases rapidly in the intake valve area because of the high density of compressed gas mixture. Simultaneously, the flame radiates through the exhaust valves with lower speed. The averaged intensities first increase rapidly and then gradually fall (Fig. 5.14).

In the test, the assumption model is proved and supported by PMT measurements. According to the O-Ring Gasket design, the detection area of the fibre probe of each PMT is a fan beam region which is beginning with an  $20^\circ$  aperture from

sensor side and ending at the opposite side. Moreover, the detection regions of sensors are overlapped and correlated. The two face to face groups of fibres are aligned to cover the whole chamber. For example, the top five fibres 11 to 15 are placed by one side and the other five fibres 31 to 35 are placed on the opposite in order to cover the whole chamber bore (Fig. 5.16 b). There are 8 groups of five fibres and they are placed at intervals of each  $45^\circ$  angles. Thus, the intensities of over-crossed region can be evaluated by cross correlation algorithm.

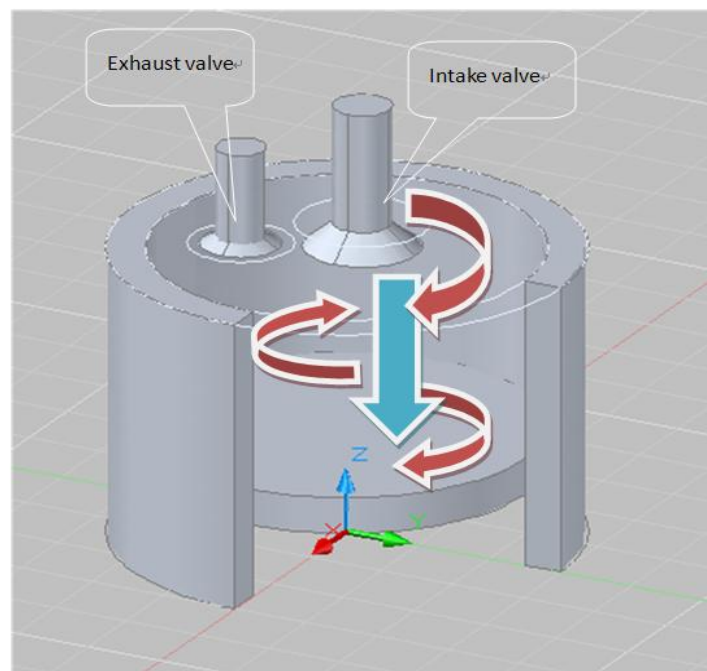
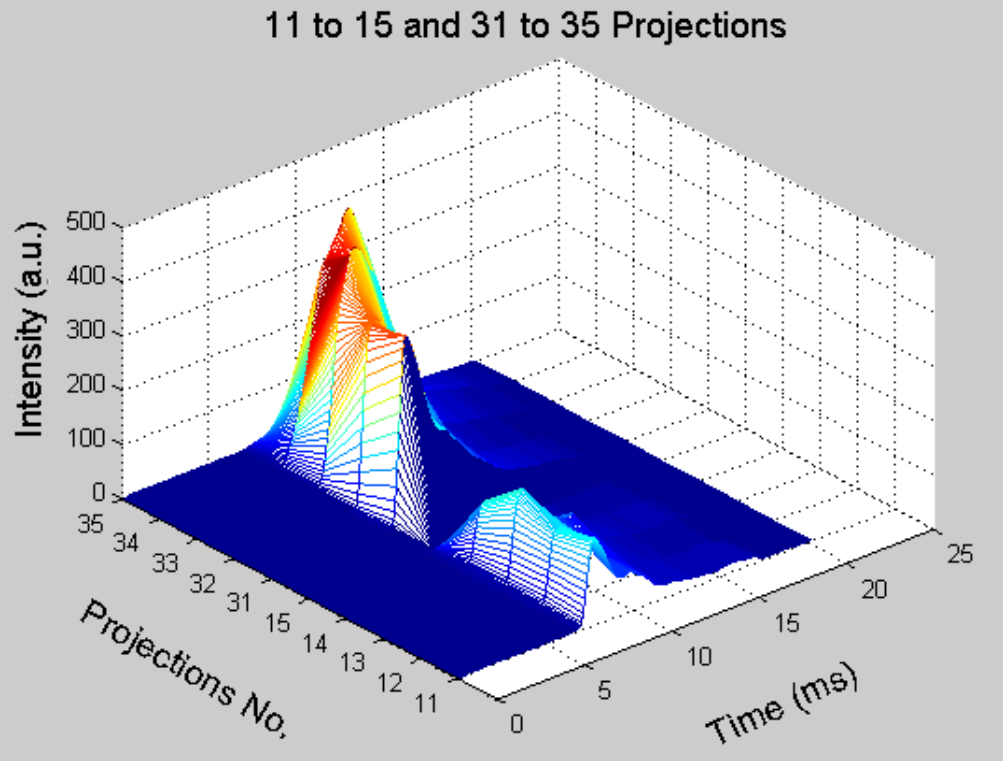


Figure 5. 15 Vortex Modeling of Combustion in the IC Engine

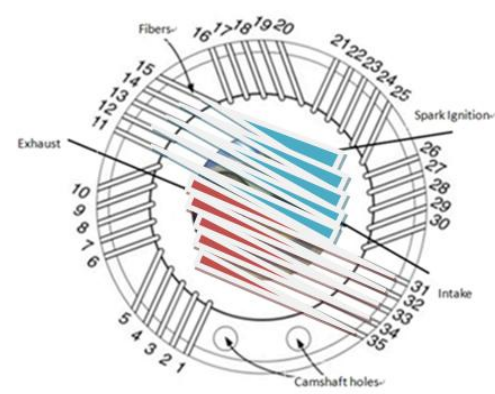
In Figure 5.16 (c), the projections of number 31 to 35 clearly delayed in time compared with other data profiles. The different intensities are denoted by different colours (Fig 5.17 a). Fibres 11 to 15 cover the top section of bore which is opposite to the group of fibres 31 to 35 (Fig 5.16 b). There are small time delays between 11 to 15 projections and apparent time delays between with 31 to 35 profiles. Flame



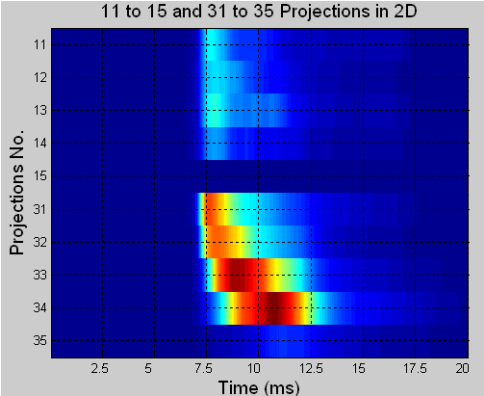
propagation starts at the spark ignition point and spreads from the central of chamber to the edges of bore. In the 31 to 35 group, distinct time delays between each fibre demonstrate the turbulence propagation in both temporal and spatial.



( a )



( b )



( c )

Figure 5. 16 No. 11 to 15 and 31 to 35 Projections Radiation Diagram and Intensity Plots in 2D, 3D

Then, the group 21 to 25, which is perpendicular to groups 11 to 15 and 31 to 35 shows flame behaviors surrounding intake valve rapidly increase to the maximum intensity (Fig. 5.17).

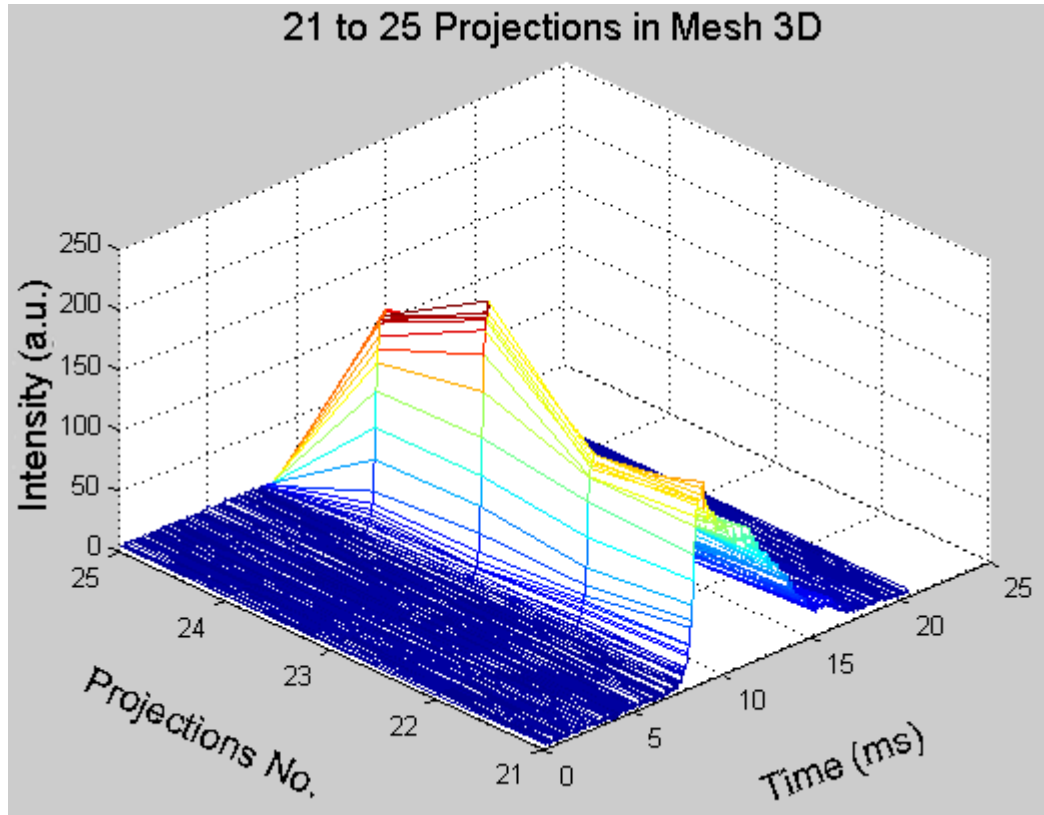


Figure 5. 17 21 to 25 Projections Intensity Plot in Mesh 3D

From the earlier qualitative analysis of combustion propagation, blue flame behavior in the OHV pro 206 Otto IC engine with gas fuels could be roughly described within chamber (Fig 5.18). The flame starts nearby the spark, then quickly pass the intake valve area. The first significant turbulence appears. By summarizing intensities, the first eruption of heat release occurs (Fig. 5.19). Flame flows to the exhaust valve at lower speed. After the first peak, owing to the lean of mixture gas of intake valve region and other factors, the distinct combustion turbulence starts appearing in exhaust

valve in the second peak eruption; then the flame spreads to the bottom of chamber and the third peak eruption occurs.

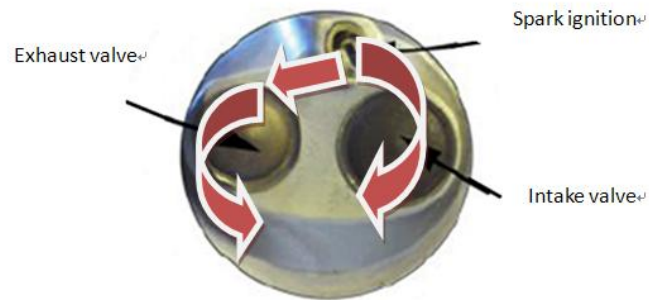


Figure 5. 18 Combustion Propagation Movements Diagram in the Test Engine

The three significant turbulences of burning eruptions are shown in Figure 5.19 below. The qualitative analysis of flame front propagation combined with photography observation supports the later quantitative measurement of flame velocity.

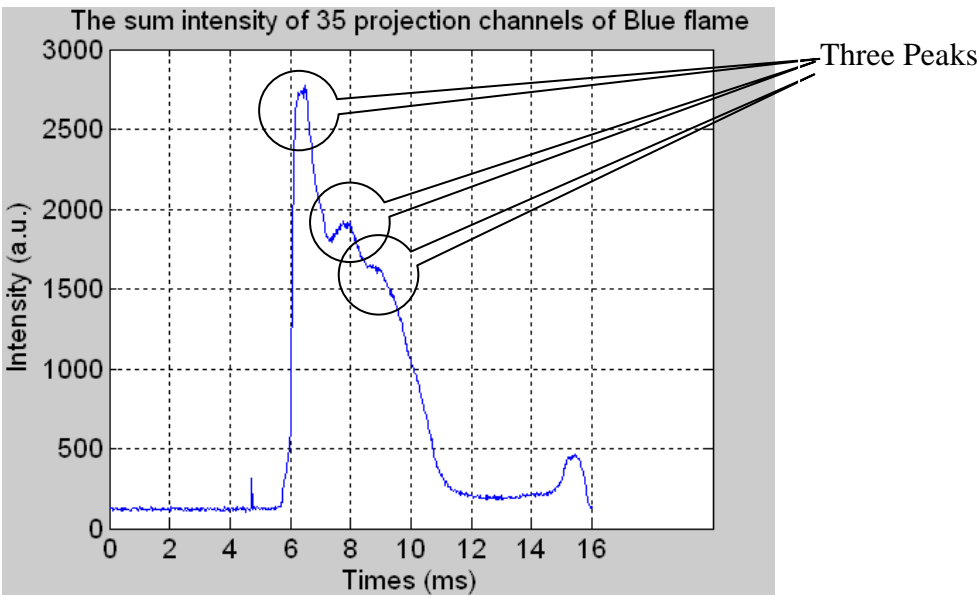
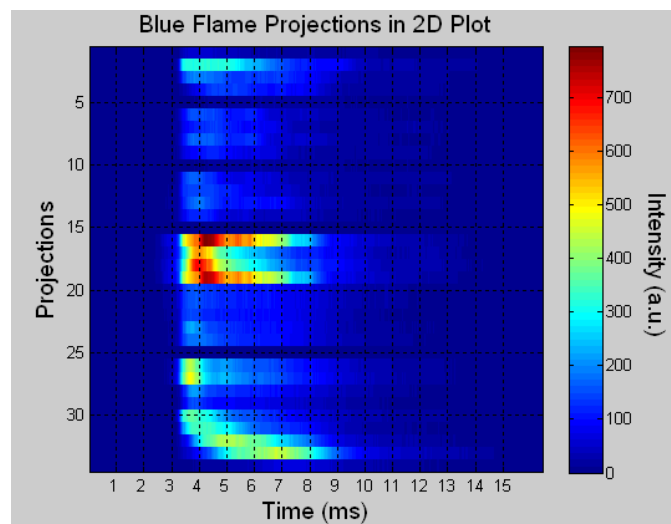


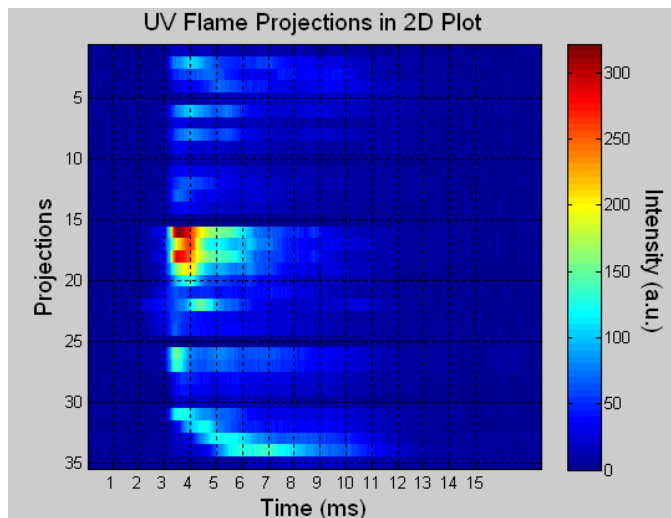
Figure 5. 19 The Three Orders of Summarized Intensities Peak Eruption Diagram

The UV flame propagation demonstrates some differences by comparing with Blue flame. Figure 5.20 (a) and (b) show the comparison of Blue and UV flame

intensities of 35 Projections. Both these two types of flame have the time delays between each projection. The intensities of Blue flame are more concentrated and at the beginning of combustion are more intense. The intensities of UV flame are more averaged than the Blue flame intensities (proved by photometry method in Fig. 5.14). The UV is a 'skin' of combustion and its profiles act as a dual ring outline in a thinner layer compared with the blue flame. UV intensities are distributed more evenly.



(a)

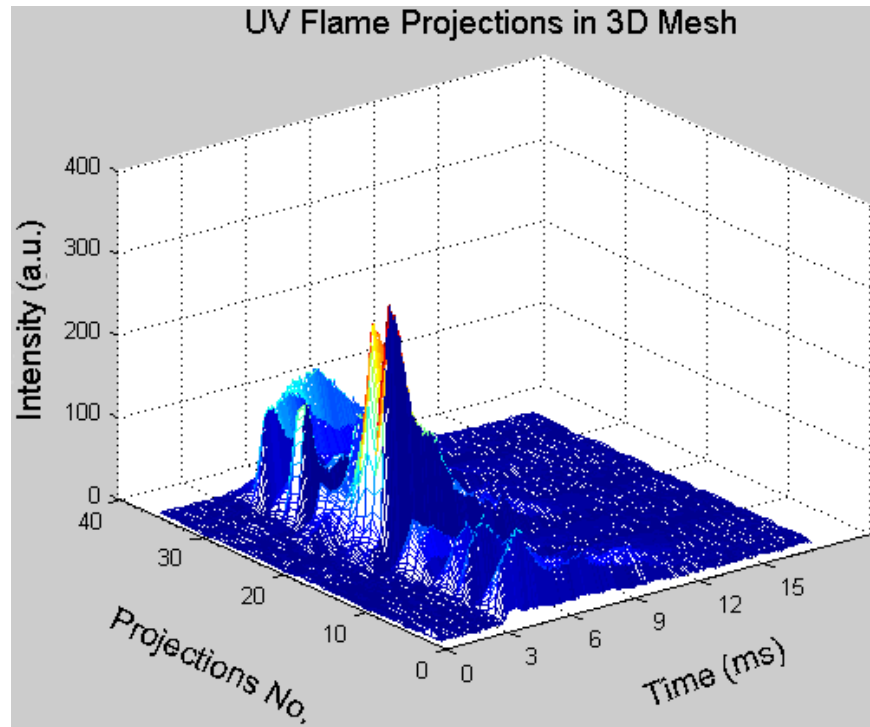


(b)

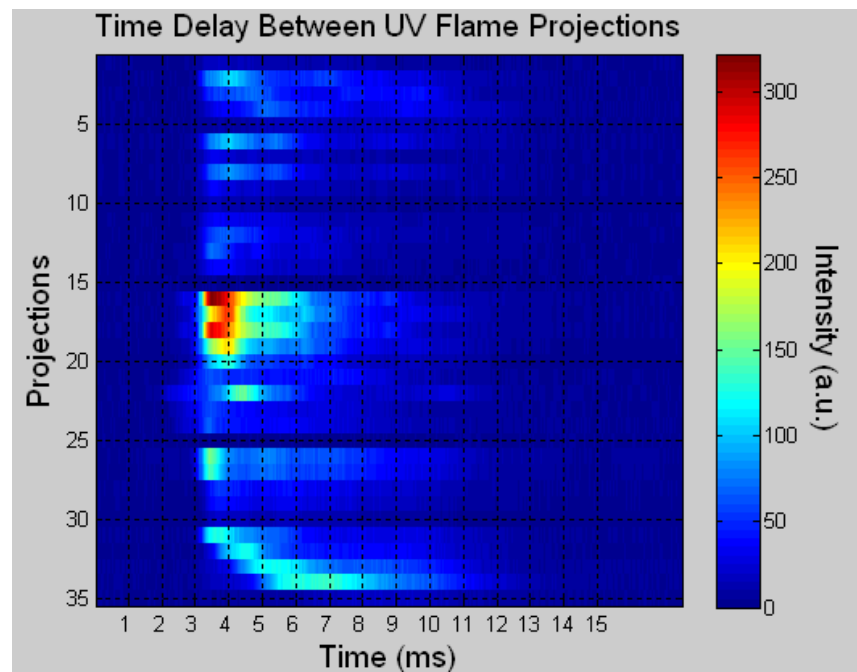
Figure 5. 20 UV flame propagation behaviors in IC engine

## 5.4 Flame Propagation Analysis by POET Projections

As a result of their sensitivity, PMTs are used to measure flame propagation speed. In the experiment, 35 fibres which are placed surrounding the OAG plate are utilized to detect the flame intensities from multiple angles of cylinder chamber (Fig. 5.1). The method of flame front velocity measurement is that the flame intensities are changing and the locations of burning flame are moving within chamber at all times. Therefore, according the varying of flame intensities in both of temporal and spatial domains, the flame front propagation speeds are able to be evaluated. In practice, the position of spark ignition is locked and it has been assumed as a reference point. So the combustion intensities at a time are received from different angles by PMTs. By finding the differences of time between two peaks of flame intensities and locations of PMT, the flame propagations speed can be roughly evaluated. However, the high sampling frequency of PMT has improved the accuracy of this method and has reduced the evaluation errors. In the 3-D image of intensity projections obtained from 35 PMTs (Fig 5.21), the intensities of one complete circle of engine running is displayed in mesh plot. The X axis denotes the time of the engine revolution which is sampled. The projection of each PMT at different intensities is the sum of fan beam projections from a constant observation angle. The time delay between each projection is seen in Figure 5.21 (b).



( a )



( b )

Figure 5. 21 3D and 2D Intensity Images of UV Combustion Projections

For speed measurement, the propagation velocity algorithm is:

$$v_f = \frac{(P_{a_{i,j}} - P_{b_{i,j}}) * D_L}{\Delta t} \quad (5-3)$$

Where  $v_f$  is the flame speed;  $P_{a_{i,j}}$ ,  $P_{b_{i,j}}$  are the positions in the chamber of average intensity peak;  $D_L$  is the chamber diameter;  $\Delta t$  is the time difference between the two peaks. The data were recorded by PMTs to give a quantitative measurement of the flame propagation speed. The data was analyzed in sequence from the No. 1 probe to the No. 35 probe corresponding to angle alterations from 0° to 360°. According to POET frequency settings, the revolution of engine speed is 2280 RMP; thus one revolution takes 15 milliseconds and 7.5 milliseconds for the explosion stroke (combustion stroke) since the engine is four strokes. The measurement temperature was about 800-1000 °C and the pressure nearly 25 bars.

Table 5. 1 System Parameter Initialization of Velocity Measurement

Parameters	Settings
Engine revolutions	1000 ~ 2500 RMP
Scan sampling frequencies	1MHz
PMT input voltage	+5 V
Time sampling	$1\mu s \times intervals$
Scanning counters	50000
Scanning Times	2.5 second

### 5.4.1 Flame Turbulences Analysis

Flame information is carried by each projection of collecting data. Flame

propagation analysis begins with identifying single projection activities. To investigate projection, its data are selected from three special angles (Fig. 5.22) determined by the three eruption locations. Projection at number 17 crosses the intake valves. Projection at number 3 measures the exhaust valve intensity behavior. Projection 34 is a projection to measure the bottom part of chamber which is far away from spark ignition. The three projections are separately analyzed between the blue flame and UV flame.

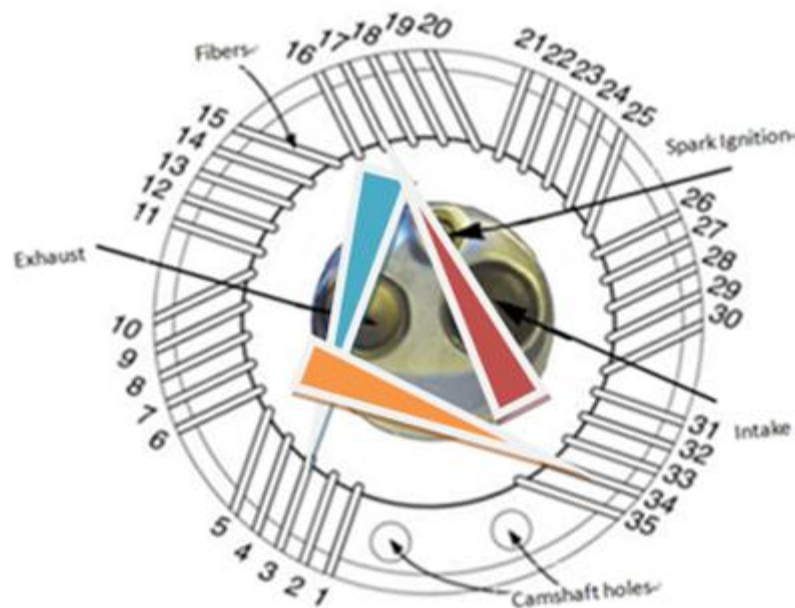


Figure 5. 22 No. 3, 17, and 34 Projections Radiations Schematic Diagram

## Blue flame

Blue flame measurement observes  $\text{CH}^*$  luminescence using 440 nm bandpass filters. Figure 5.23 is a diagram of number 17 projection data for 4 engine revolutions. Number 17 is a special position near to the spark ignition and crosses the centre of the chamber in a vertical direction. Hence, it is more sensitive to the spark ignition at great



intensities. After a small ignition delay, the intensity increases in a sharp curve that represents the combustion starts surround number 17 at a higher temperature. Engine intensities over the four cycles differ by inconsistent factors of inlet gas mixture equilibrium ratio, the mixture gas density in the inner chamber and the combustion start locations. These turbulences may be caused by unstable engine system performance.

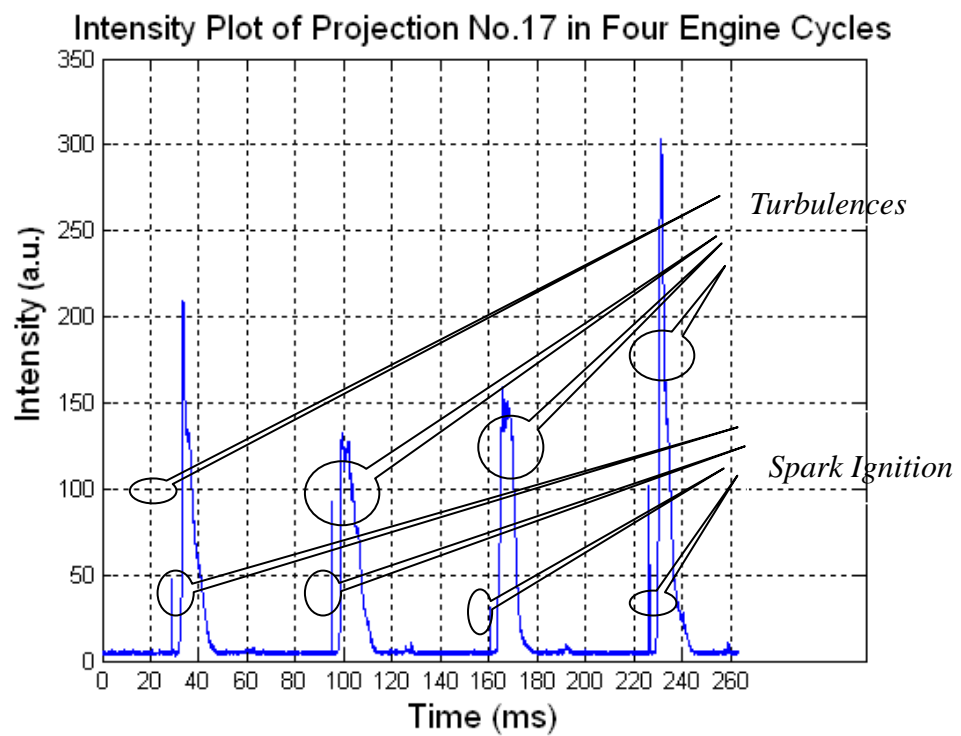
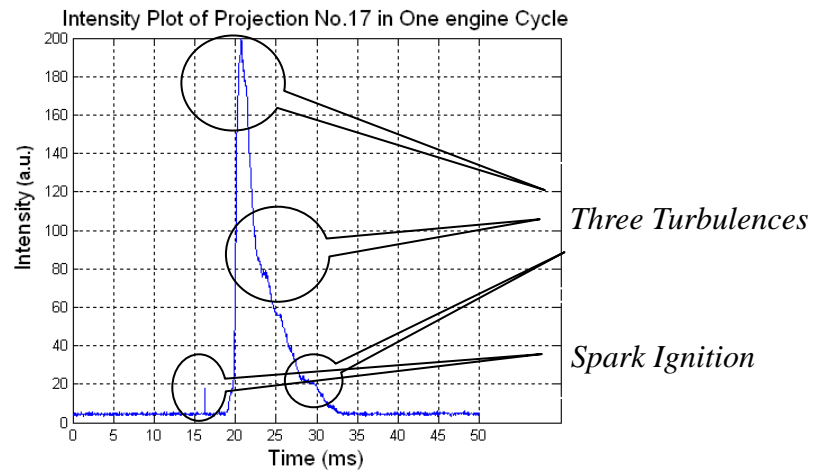
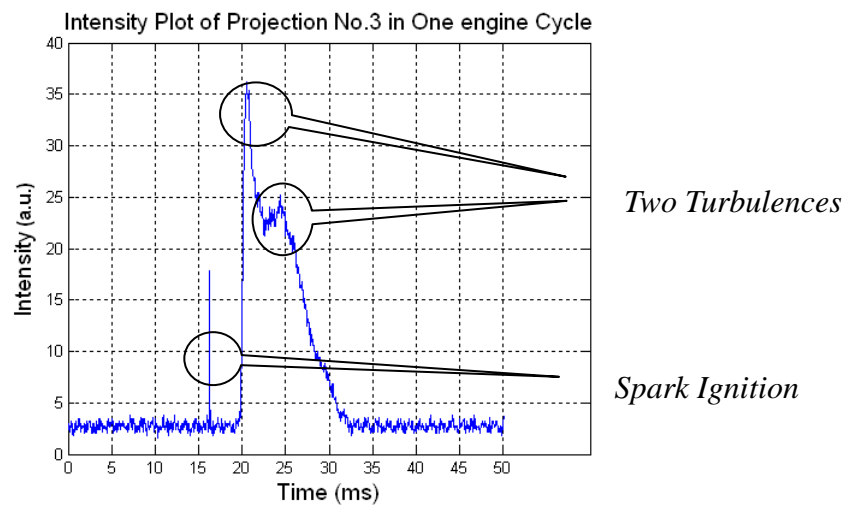


Figure 5. 23 No. 17 Projection Intensity Plot of Four Engine Cycles

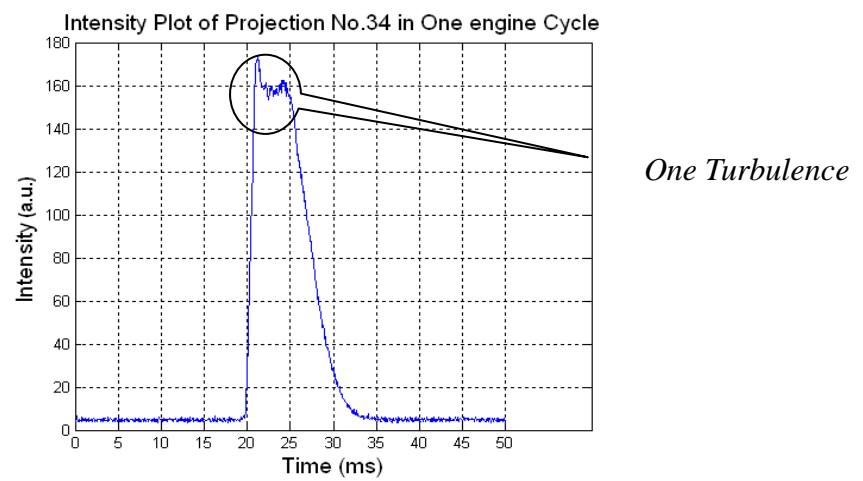
Figure 5.24 illustrates a diagram of 17, 3, 34 projection profiles. The maximum intensities of number 17, 3 and 34 were approximately 200, 40 and 180 respectively. By comparison, the spark ignition appears on projection No. 17 and No. 3 projections but disappear No. 34 projections.



( a )



( b )



( c )

Figure 5. 24 Intensity Plots of No. 3, 17 and 34 Projections in One Engine Cycle

That indicates the spark ignition occurs within the No. 17 and No. 3 PMT fibre detection range but outside No. 34. It particularly demonstrates the location of Spark ignition. The sharp increase of the first peak for number 17 shows combustion starts close to the number 17. The flame then spreads to the right chamber with lower intensities within number 3 projection area. Flame propagates back to number 17 projection denoted by its second peak value. Then the combustion begins increasing and fast propagation on the left part of chamber where the number 3 projection is increasing. After that, the combustion is front to the bottom of chamber where the number 34 is starting increasing with high intensity. These observations are in line with the previous qualitative analysis of flame propagation behaviours.

Through the measurements, one stroke of the engine takes 15 ms at 2300 rpm. The delay of combustion from ignition is 2.2 ms. The first peak eruption of turbulent flame intensity for number 17 is 1.6 ms after the start of combustion. The number 3 peak takes 2.3 ms after combustion and the number 34 takes about 5.5 ms (Fig 5.25). Assuming spark ignition in the centre of the chamber bore, then the radiation distance  $R_d$  to No.3, No. 17 and No.34 is a quarter of bore diameter:  $R_d = 68 \text{ mm}/4 = 17 \text{ mm}$ . The number 17 is the intake valve; number 3 denotes the exhaust valve side and number 34 is the bottom boundary of chamber. The speed of flame propagation from the ignition point to intake valve was 10.63 m/s. The flame then spreads to the exhaust valve at a velocity of up to 7.39 m/s. The speed of combustion from the centre to the bottom is approximately 3.09 m/s. Speed propagation on the exhaust side and intake

side are very similar but higher than velocities at the bottom valve. The flame explosion speed decreases as the density reducing.

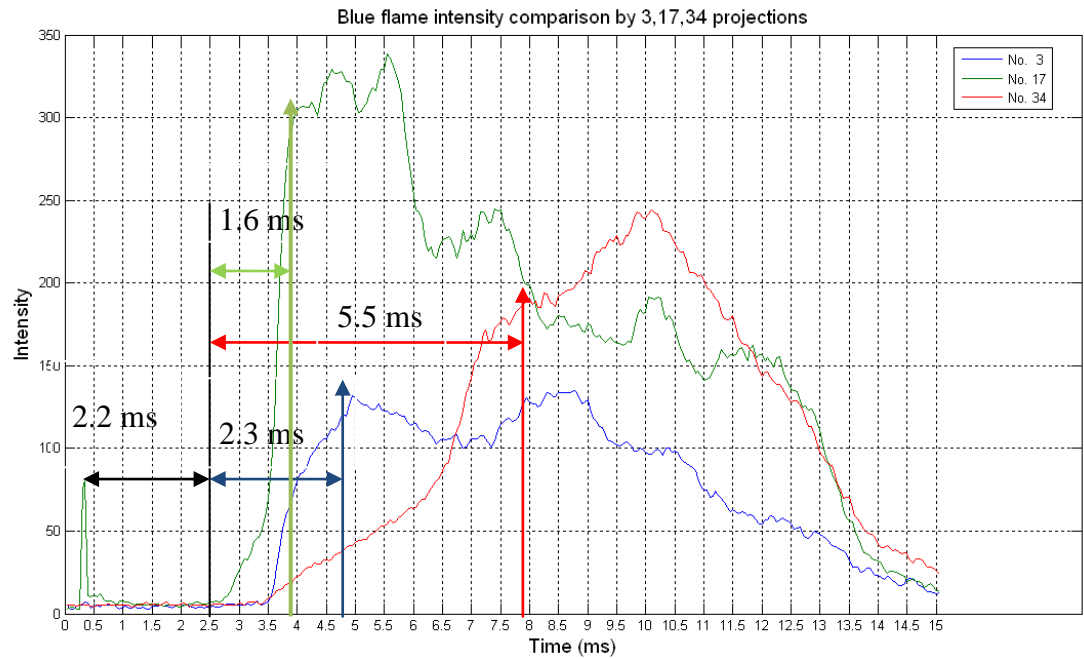


Figure 5. 25 Comparisons of Blue flame in Time Coordinate System

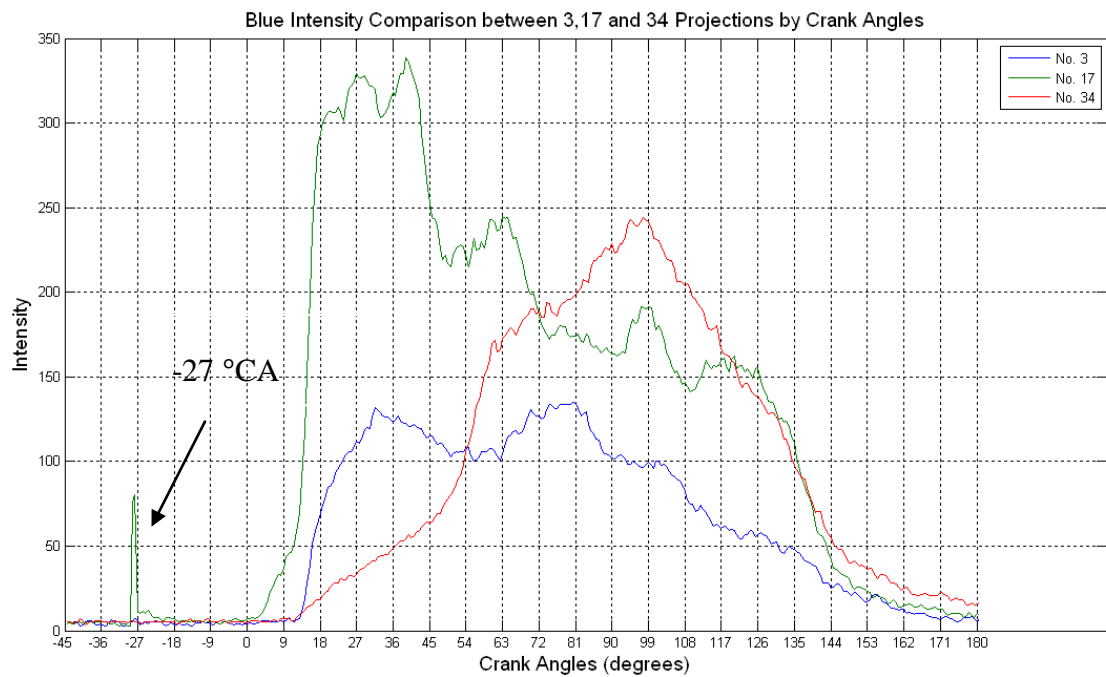


Figure 5. 26 Crank Angle Delays between No. 3, 17 and 34 Projections in Blue Flame

The spark ignition time is around - 27 degrees of CA before combustion in test. It takes about 18 degrees moving from beginning of explosion to first peaks of intensity. In fact, the burning flame is completely full of chamber after 12 degrees because all projections start to have apparent signals after 12 degrees. From 18 to 45 degrees, the combustion is burning intensively. After 45 degrees, the flame heat release starts falling.

## **UV flame**

The UV combustion is a 'skin' of flame front propagation and coats outside of the blue flame, the UV elements burning in a reaction layer ahead of flame front (Previously discussed in Fig. 3.24). Thus, in flame velocity evaluation, the UV has been used to increase the accuracy.

UV flame projections taken at number 17 (Fig. 5.27) are similar to those for the blue flame (Fig. 5.23). The combustion has lower energy and less heat releasing compared to the blue flame because of spectrum energy differences between Blue and UV elements. In Figure 5.27, the UV behavior seems more turbulent and more complex than blue one by its outline diagrams. The 17, 3 and 34 projections of the UV flame (Fig. 5.28) are present similar curves to the blue flame (Fig 5.24) but at lower energy.

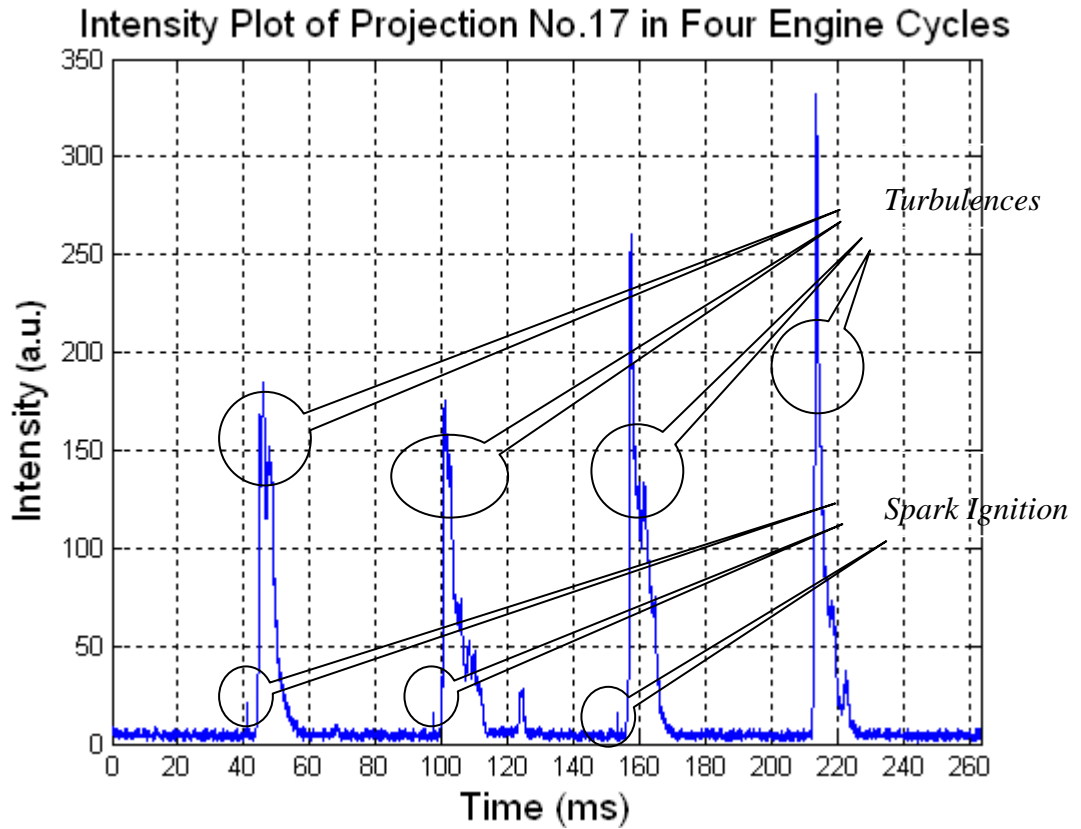
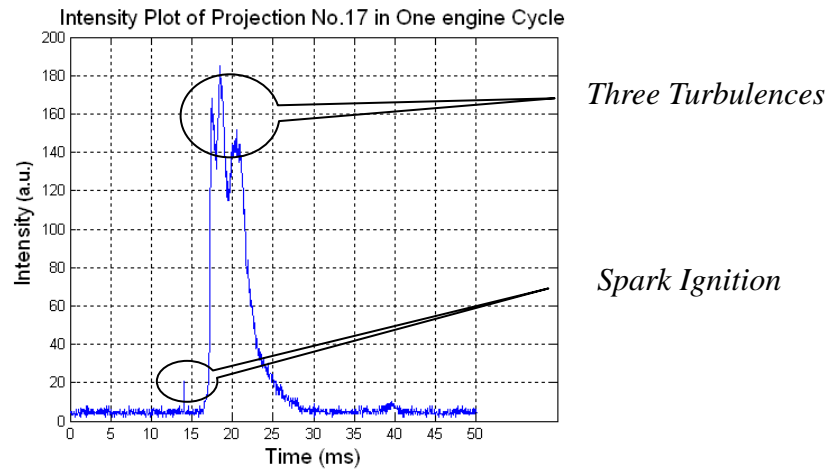


Figure 5. 27 UV Flames of Four Cycles Measurement by PMT Number 17

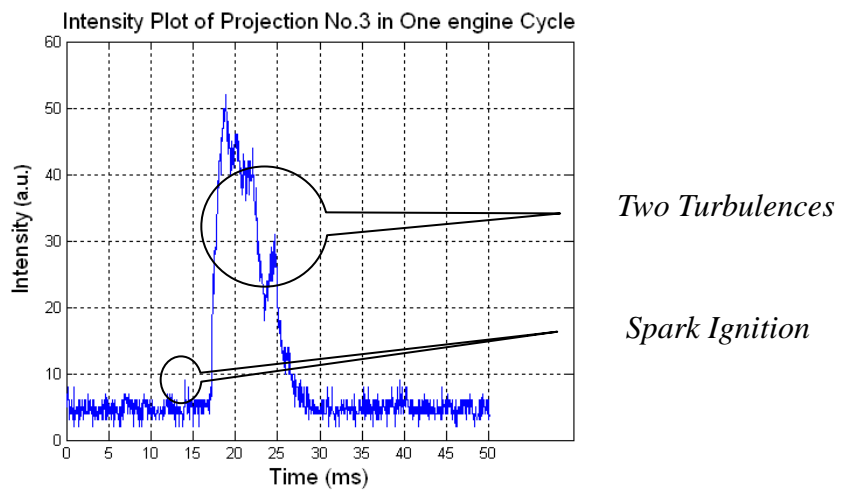
Several differences between UV and blue flame have been suggested (Fig 5.29 and Fig 5.25).

1. The slope of UV curves is steeper than those of the blue flame. It suggests UV emissions are more concentrated than Blue emissions.
2. The UV curves are narrower than the blue flame. It may owe to the low energy of UV emissions.
3. The time delays of UV flame between turbulences are shorter than blue flame.

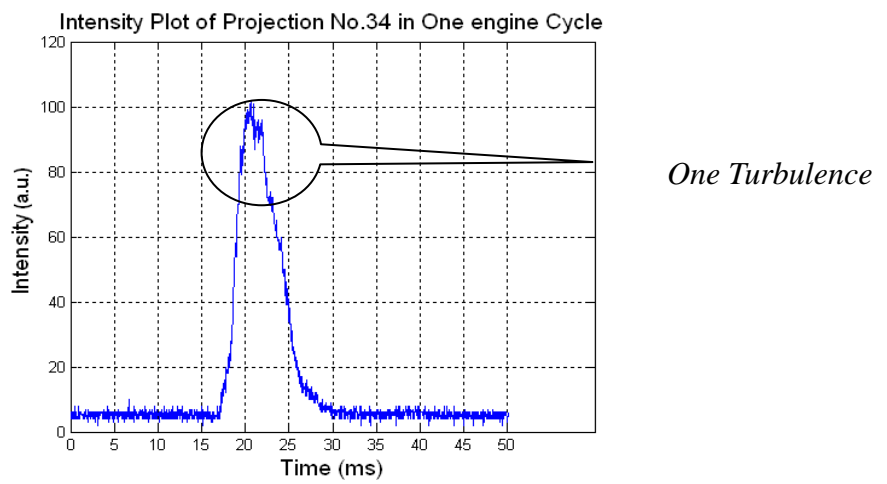
It presents the UV flame is more turbulent than blue flame.



( a )



( b )



( c )

Figure 5. 28 UV Flames in One Cycle of the Number 3, 17 and 34 Projections

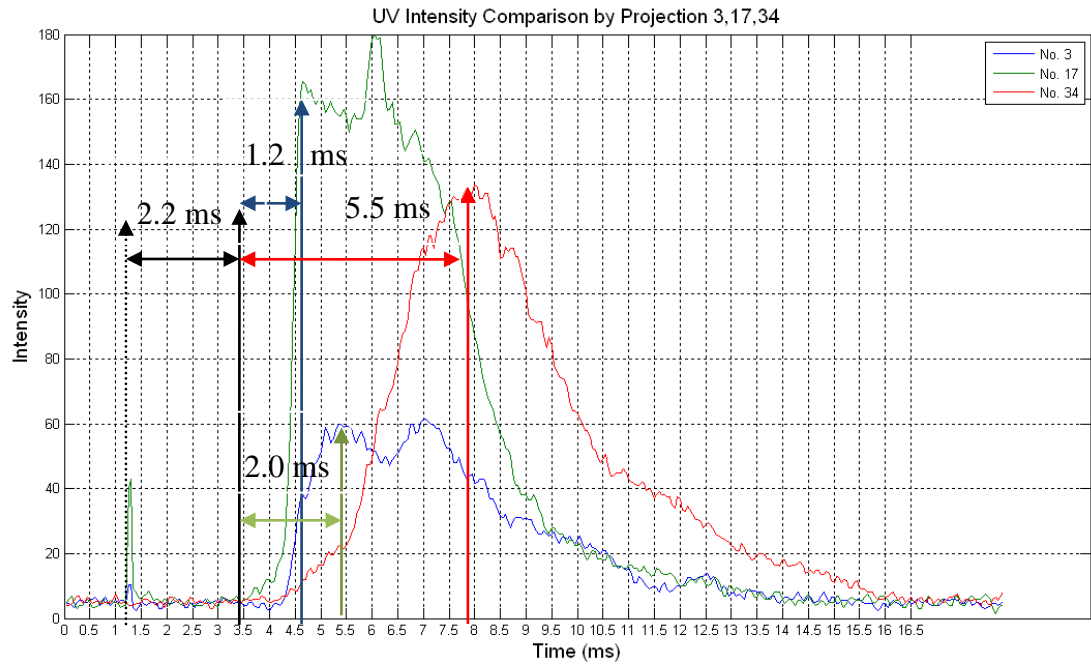


Figure 5. 29 Comparisons of UV flame in Time Coordinate System

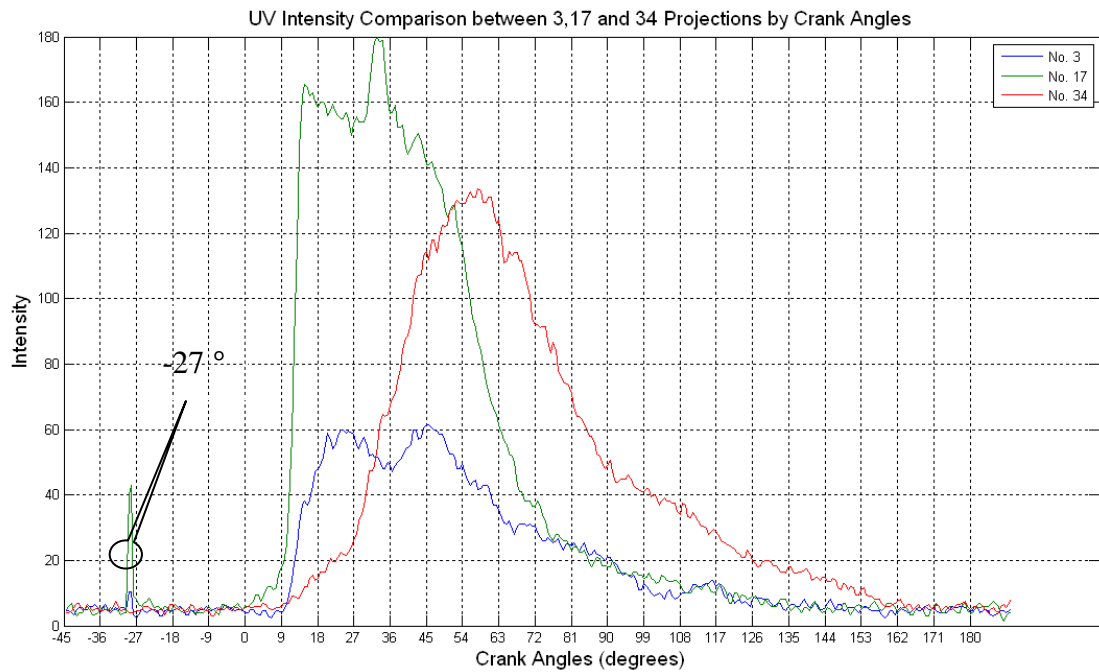


Figure 5. 30 Crank Angle Delays between No. 3, 17 and 34 Projections in UV Flame

In the analysis of flame propagation speed, the Blue flame represents brief reactions of combustions. Thus, UV projections are applied to evaluate the flame front velocity for improving the accuracy. The UV flame speed is slightly different from the



Blue's. Combustion timing is the same with a 2.2 ms delay after spark ignition. However, the extension time of the flame from spark to the intake valve side is reduced to 1.2 ms with a flame speed of 14.17 m/s. The flame spread time within the exhaust section is reduced to 2.0 ms with an increased speed up to 8.5 m/s. The propagation time to the bottom of the chamber is slightly reduced to 5.5 ms with a speed of 3.09 m/s. Only a little difference in the speed measurements for the 17 and 3 projections were observed but the number 34 projection presented a wide variety of speed measurements. These were rough measurements of flame velocity. To improve accuracy, statistical measurements of projections are employed in following discussions.

With the UV flame (Fig. 5.30) the main combustion heat release is still within the first 45 degrees. The second gentle heat release occurs from angle 45 to 72 angles. Then, the OH chemical reactions are going to disappear from 160 angles to the end. In comparison with the blue flame (Fig. 5.26), the average heat release of OH is less than CH emission properties.

### **5.4.2 Flame Propagation Velocity Evaluation**

The statistics calibration methods improve the accuracy of flame velocity evaluation. The PMTs are fitted to the OAG plate in 8 groups of 5 fibre probes. The radiation of flame is from the spark ignition point to the boundary of chamber. In the experiment, three regions of interest (ROI) within the bore are identified for flame

velocity measurements. Combustion starts at the spark position and propagates to both left, right and bottom sides of chamber. The right side flame front behaviors in intake valve ROI are measured by projections of number 21 to 26. The left part is able to be measured independently from 1 to 5 projections. The bottom part is studied using projections of number 31 to 35 (Fig. 5.31). There is a time delay for the bottom projections compared to the other projections. Although there are some crossing areas, the projections of 31 to 35 and 1 to 5 do not affect each other's velocity measurements. To further improve measurement accuracy, the average values of speed are taken over 50 cycles of engine running. Thus, the measurement method is to evaluate the time differences of intensity peaks between each projection.

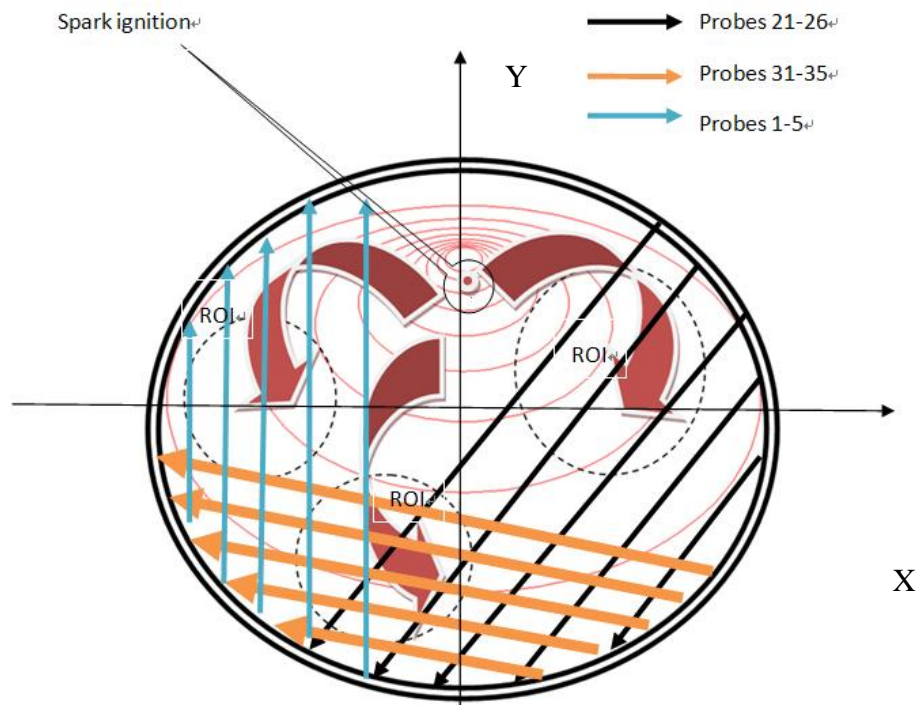


Figure 5. 31 Flame Velocity Evaluation Method Schematic Diagram

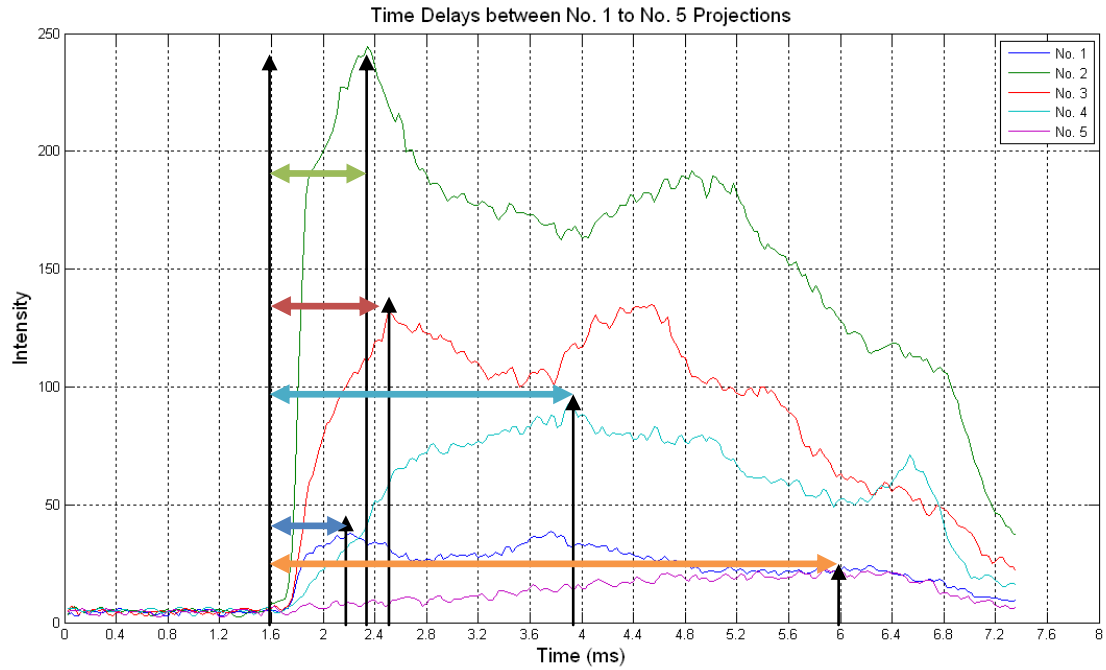


Figure 5.32 Time Delays between No. 1 to No 5 Projections

The algorithm filters signals from projections to reduce noise. Two measurement methods are used: one is an individual investigation between two projections to find the speed's difference; another is to find the displacement between the first touching of chamber boundary and combustion kernel to calculate the average velocity. All the measurements are under the UV flame condition since it is more sensitive to the flame extension. Table 5.2 is the list of statistics velocities from displacements between each projection. The table shows that the high speed flame is concentrated on the intake side owing to the rich gas mixture and high pressure at the beginning of combustion. After the reduction in pressure and density, the speed on the left exhaust valve side decreases although it is still high speed. The propagation at the bottom is much slower than in other parts because they are lean combustion reactions.

Table 5. 2 UV Propagation Velocity between Each Projection (Combustion Kernel passing the Number 2, 17 and 23 Projections)

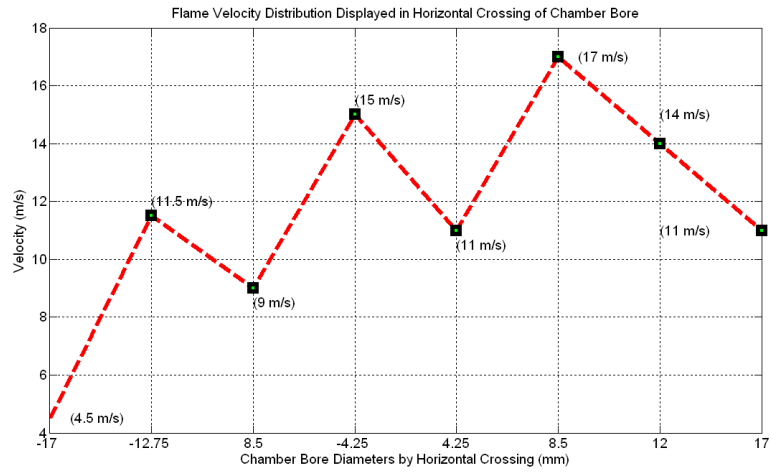
PMTs	Velocity
Number 1 to 2	17 m/s $\pm$ 3 m/s
Number 2 to 3	9 m/s $\pm$ 2 m/s
Number 3 to 4	12.5 m/s $\pm$ 1 m/s
Number 4 to 5	4.5 m/s $\pm$ 0.5 m/s
Number 11 to 12	10 m/s $\pm$ 3 m/s
Number 12 to 13	10 m/s $\pm$ 2.5 m/s
Number 13 to 14	9 m/s $\pm$ 2 m/s
Number 14 to 15	5.5 m/s $\pm$ 1 m/s
Number 21 to 22	11.6 m/s $\pm$ 4 m/s
Number 22 to 23	20 m/s $\pm$ 7 m/s
Number 23 to 24	15.4 m/s $\pm$ 7 m/s
Number 24 to 25	12 m/s $\pm$ 3 m/s
Number 31 to 32	11.6 m/s $\pm$ 2 m/s
Number 32 to 33	9 m/s $\pm$ 1.5 m/s
Number 33 to 34	6.4 m/s $\pm$ 0.5 m/s
Number 34 to 35	3.2 m/s $\pm$ 0.5 m/s

Table 5.3 gives the average flame propagation velocities. High speed flames occur on the intense reaction region of the intake valve parts, and the low speed flame on both left and bottom sides of the chamber.

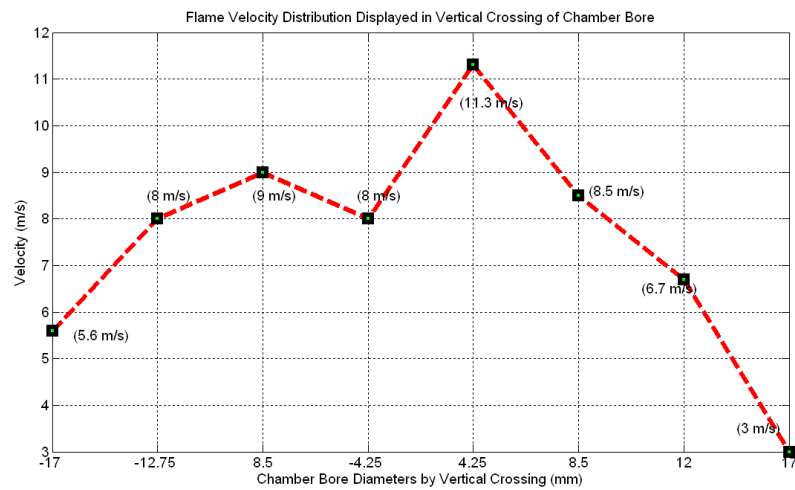
Table 5. 3 Averaged Flame Speed (From the Central of Combustion to Chamber Boundary)

PMT	Velocity
Number 16 to 1	11.2 m/s $\pm$ 3 m/s
Number 16 to 25	17 m/s $\pm$ 5 m/s
Number 16 to 35	12 m/s $\pm$ 2 m/s

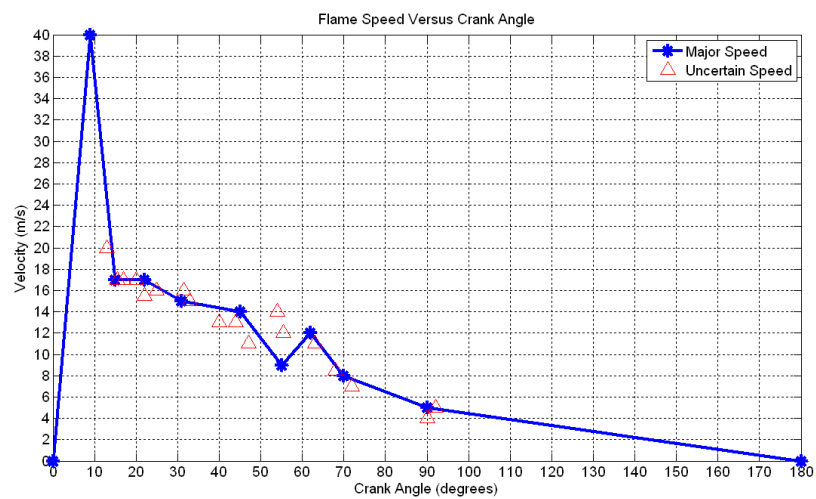
The flame speed evaluated in three coordinates consists of horizontal flame propagation in X direction on the upper region of cylinder chamber covering the intake and exhaust valves, the vertical flame extension of left chamber part in Y direction and the velocity in crank angle coordinate system (Fig. 5.33). Figure (a) and (b) illustrate the high speed flame occurs in intake valve area. Then flame propagates to the left at a lower speed. Finally the flame spreads through the whole chamber at the lowest spread velocity. The intense combustion reactions occur with increasing speed from a crank angle of 15 to 25 degrees. Then the velocity rapidly reduces from 35 to 50 angles (only half of maximum speed). Then, the speed gradually reduces to zero after 55 degrees. Figure 5.34 is a quiver velocity description of flame front to present the flow acts. Combustion starts at the red kernel and rapidly extends at speed up to 17 m/s crossing the right parts. Simultaneously, the flame spreads left at a reduced average speed of 9 m/s. The green parts occur after combustion in the blue area. The flame speed is lowest because of the lean reactants and low density of gas mixture.



( a )



( b )



( c )

Figure 5. 33 Flame Speed Display in X, Y and CA Coordinates System

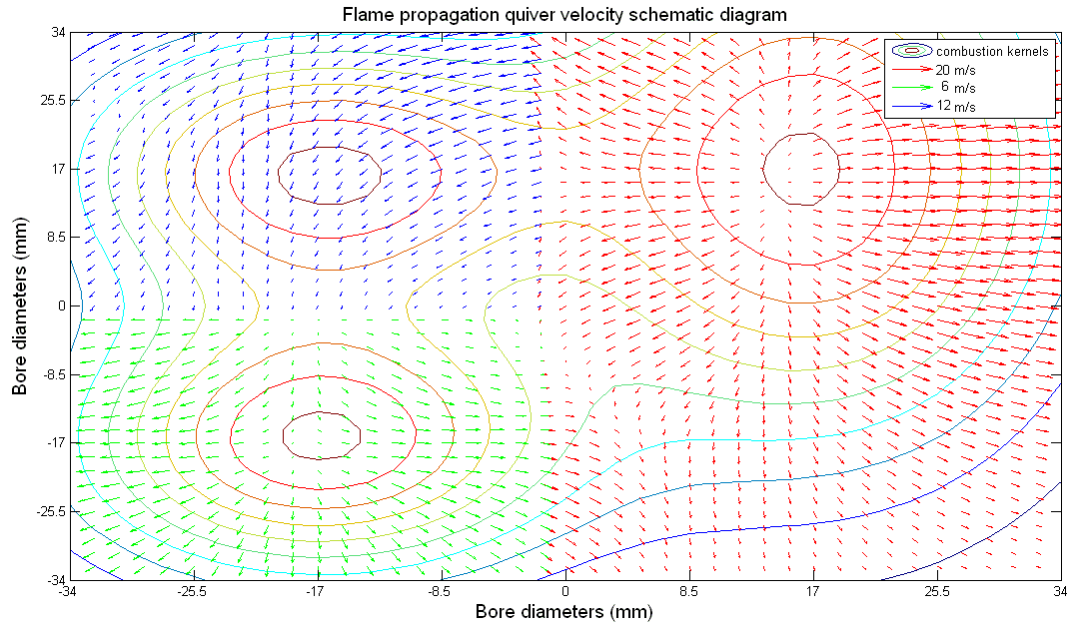


Figure 5. 34 The Averaged Speed of Flame Propagation In-Cylinder

Under different air-fuel conditions, the flame front activities of combustion are diverse by different engine revolutions. Thus, the engine is implemented in four speeds to investigate different combustion front propagations (Fig 5.35): 2280 RPM is a rich combustion in cyan line, 1550 RPM is a regular combustion in blue line, 1200 RPM is less lean combustion in red line and 1090 RPM is dead speed for engine running in green line. Flame intensity is reduced following the decrease in engine speed. The flame speed increases more quickly and combustion duration is shorter at higher revolutions than at lower revolutions (Fig 5.36). Figure 5.36 is the diagram of combustion front speed at different equivalent ratios.

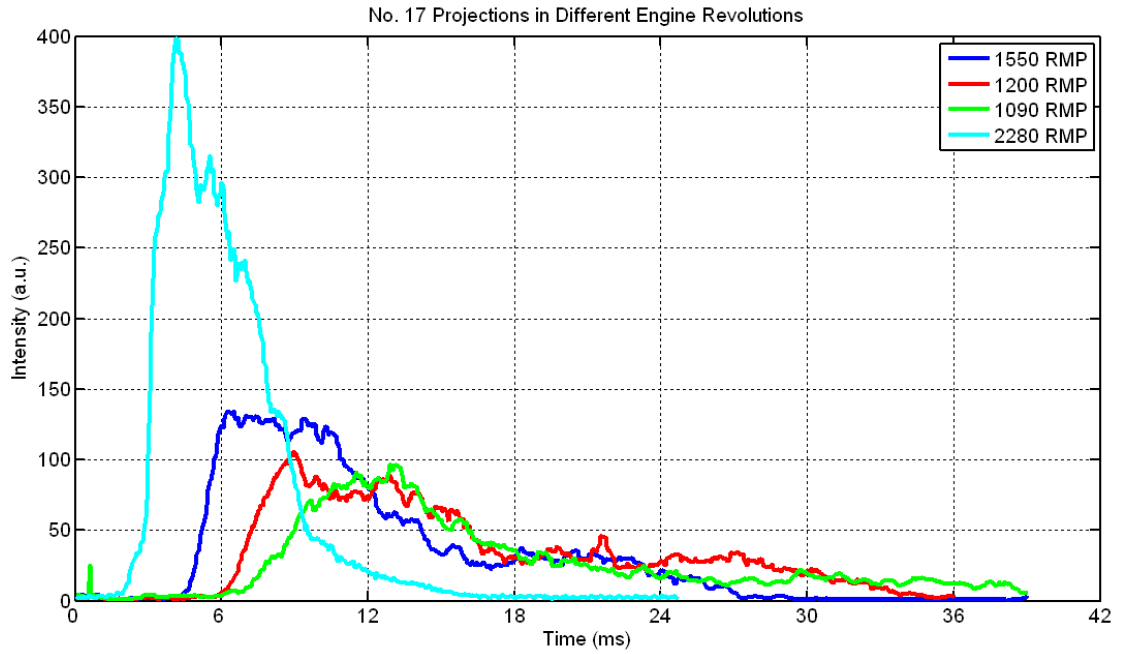


Figure 5.35 No. 17 Projection Intensity Plot at Different Engine Speeds

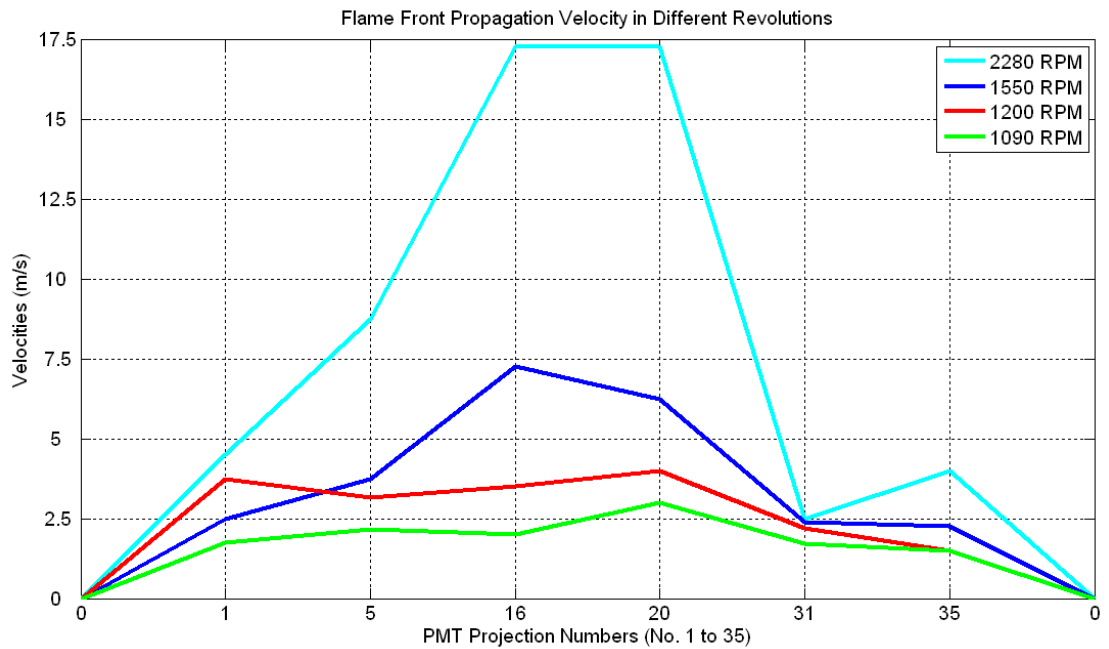


Figure 5.36 Flame Propagation Speeds at Different Engine Revolutions

In the test, the engine is initially running with rich fuel at 2280 rpm. The equivalent ratio is  $\phi \approx 1.6$ . The propagation speed is up to 17 m/s from projections 16 to 20. The speed is around 8 m/s from projections 1 to 5. The speed reduces under 5



m/s from projections 31 to 35. The blue line denotes the flame front velocity at the equivalent ratio  $\phi \approx 1$ ; the velocity falls to 7 m/s. The red curved line is the speed at the equivalent ratio  $\phi \approx 0.79$ ; since the ratio reduces, the average speed is lower than blue line. The green line represents very lean fuel at the ratio  $\phi \approx 0.64$  close to the minimum ratio for engine running. Under very lean fuel conditions, the flame velocity is much lower and the velocities curve tends to be flat indicating that the flame propagates across the chamber at constant speed.

In the analysis of flame propagation process, as the start of combustion, the explosion occurs nearby spark ignition. Then it expands toward to the edge of chamber bore in higher speed (up to 40 m/s) but with weak intensities. After the  $15^\circ$  CAs, the combustion is full-filled the chamber bore. Then several burning points appears surrounding chambers by different intensities. The intensive energy releasing firstly happens in intake valve region due to the concentration of air-fuel is particularly compressed in this region. After the intensely burning, the intensities in the intake valve region start falling and they are increasing in other regions. In visualization, it demonstrates the turbulences are shifting from the intake valve to the rest of regions and it ends nearby exhaust valve. Nevertheless, in the detection of combustion flame, the captured signals are fan beam projections crossed by other projections. The intensity covers a large region of the bore and seriously influences precise velocity evaluation. To overcome the complexity of the combustion process and the difficulty of measuring absolute flame speed accurately, an average optimum flame speed is

adopted. A new design that gives more accurate velocity measurement is discussed in further work chapters.

## **5.5 Combustion Process Reconstruction and Flame Front Propagation Analysis**

The combustion density distribution is another characteristic for analyzing the flame front and heat release. Three density investigation methods were initially considered for combustion visualization: Multiplicative Algebraic Reconstruction Technique (MART), Radon transform technique and Shack-Hartmann lens array application in flame visualization. The MART is an advanced iterative computed tomography algorithm for unknown object reconstruction (discussed in chapter 4.3). Since combustion is complex and turbulence occurs instantly, it is difficult to simulate a likelihood function for computational combustion. This method can be used to analyze instant flame propagation. The Radon transform technique (chapter 4.2) is an important algorithm for image reconstruction and is popularly used in medical CT systems. Radon transform is an accurate method using several projections of the target to reconstruct a full image of target. In the experiment, the MART has been selected as first option due to the turbulent flame is hard to simulate. Thus, the Radon transform technique can be used to optimize MART technique and reduce the errors in further work. A Shack-Hartmann lens array is used to observe the particular ROIs of flame turbulence. The combustion is turbulent and it is minimum to 5mm in spatial

resolution for observing. Since Shack-Hartmann lens array are suitable for measuring the small turbulence by its small size and multiplicative lenses, thus the new method of using SHWF technique is worth considering in further study.

The MART technique is an algebraic algorithm that has many benefits in reconstructing an unknown object using several projection slices surrounding the target. For example, the combustion is a sequence of random models in different time with great turbulence. It is impossible to use simple math functions to simulate. While a high speed camera to record the overhead combustion information from the top, but it is difficult to observe the flame under the combustion surface (Fig 5.11 and 5.12); especially in a commercial engine. Tomography methods are developed to research the different layers of combustion using projections from the target. In this project, the fibres connected with PMTs are tomographic placed surrounding the engine chamber in order to collect combustion signals. Therefore, two key parameters can be obtained: one is the location of each projection region because of the tomographic displayment of fibres; another is the sum values of intensities of each projection by receiving from PMTs. However, these two parameters are still not enough to evaluate the combustion. In the visualization of combustion, the unknown intensities distribution on the projection line has to be 'guessed' to establish modeling functions of combustion. The MART algorithm is a good solution to deal this situation. It is used to find solutions of a sequence of relevant equations and give the values of each point of the object. Assume math function of the object is  $F(x, y)$  ; the projections is

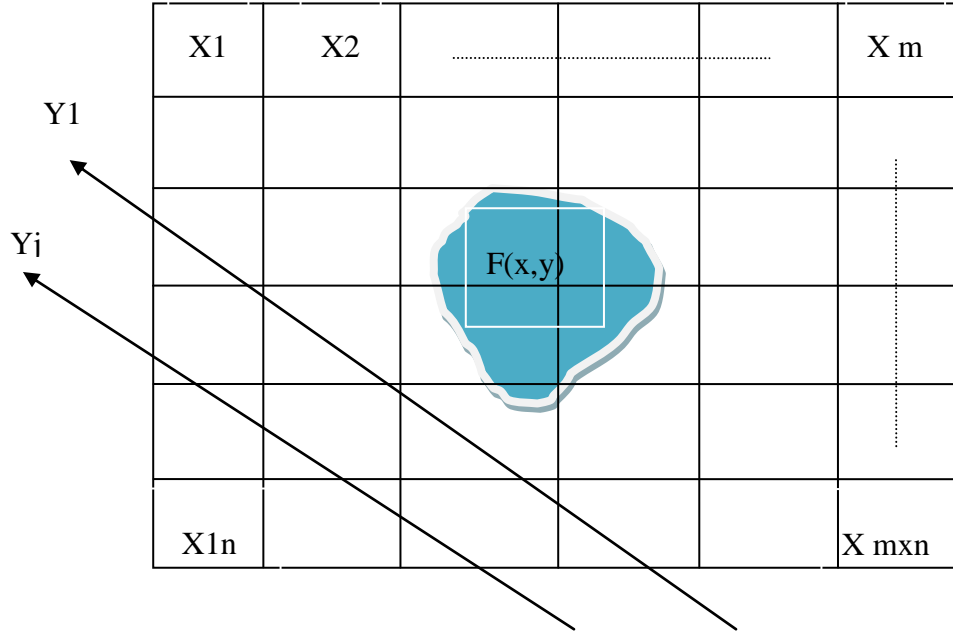


Figure 5. 37 MART Schematic Diagram

from  $Y_1$  to  $Y_j$  where  $j=1:n$ ; the object is in a  $m \times n$  matrix whose values are constant.

Since the matrix is at constant values and the projections are obtained by detections,

$F(x, y)$  can be evaluated as:

$$a_{11} * X1 + a_{12} * X2 + \dots + a_{1n} * Xm = Y1$$

... ..

$$a_{j1} * X1 + a_{j2} * X2 + \dots + a_{jn} * Xm = Yj$$

(5-4)

Where  $a_{j1}$  is the coefficient number of projections in each pixel.

If two projections are obtained by detections and the coefficient numbers are known in

the result of the projection covering area are known, then  $X1$  and  $X2$  can be calculated.

$$a_{11} * X1 + a_{12} * X2 = Y1$$

$$a_{21} * X1 + a_{22} * X2 = Y2$$

(5-5)

The MART technique gives a combustion visualization solution that approaches the real flame in an ideal condition. However it is difficult to find the correct coefficient number for the equations. Also the computational progress is slow. For example, if the model is in a 128 x 128 pixels matrix, the coefficient number matrix is up to 16384 x 16384. The MART is not popular in chemical diagnostics because of its slow computational process. MART may also be influenced by signal error of the algorithm. However, it is suitable for this experiment since the high capability of complex turbulence simulation and can support other simulation techniques.

To improve the measurement resolution, an OAG was specially designed with rearranged optical fibre probes (Fig 5.38 (a)). In the conceptual design, 40 PMTs in 8 groups are 'tomo' around the chamber by 45 degrees. The special design increases the spatial resolution of the flame front to approximately 5 mm × 5 mm and is very sensitive to the distortion of combustion front (Fig 5.38 (b)). However, this array design is not very sensitive at the boundary of chamber, because the aperture angle of fibre probe is only 20 degrees and has a small radiation area. In the kernel of the chamber bore, the region is divided in to 7 mm × 7 mm rectangles of 10 × 10 pixels resolution by vertical and horizontal orientation projections. The boundary resolution

is low because the edge of chamber only has 40 projections and they overlap less than the center.

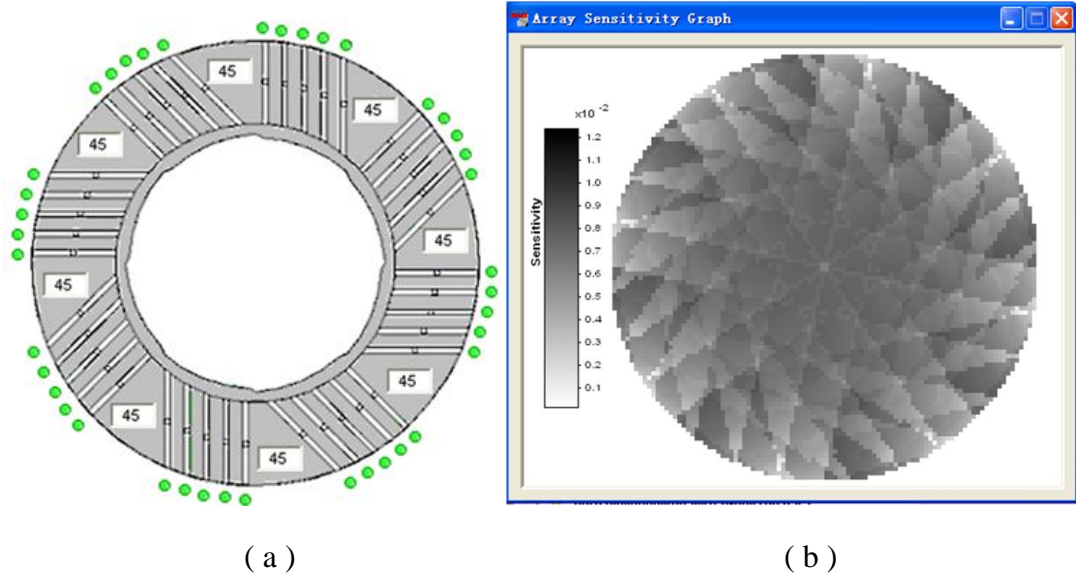


Figure 5. 38 Fibre Distribution Panel and System Sensitivity Diagram ( a is the conceptual arrangement of fibre channels; b is the sensitivity diagram of reconstruction system and it is evaluated by the overlapped times of cross sectional region of interest.)

### 5.5.1 Combustion Visualization

In this section, sequences of images are created to illustrate the combustion process in several conditions. The UV filtered combustion is firstly visualized by one iteration and 1000 iterations. Then Blue filtered combustion is shown by one iteration and 1000 iterations. To compare combustion in different engine revolutions, three sequences of images are shown by 1000 iterations. All of the results are layout using tables. The subsequence images are generated in crank angles from spark ignition time

–27° to 180 °. The system was operated under the following conditions.

Table 5. 4 System Specifications

Engine	OHV 206 OHV IC engine
Fuels	Natural gas and Air mixture
Revolutions	Rich Fuel:2280 RPM Lean Fuel: 1550 RPM, 1200 RPM and 1020 RPM
Measurement objective	Blue and UV flame front
Chamber bore size	68 mm
Fibre probe aperture	20°
Data acquisition	35 PMTs
Sampling Frequency	1 MHz ( $1\mu s \times intervals$ )
Samplings	50000 counts
Number of reconstruction Iterations	1000

The combustion front information was recorded as a high frequency discrete sampling at 1M Hz. The samples were processed using the MART iterative algorithm for 1000 iterations to give optimum results (referred in Fig. 4.28 and 4.29). The resolution of the flame turbulence is up to 5 mm  $\times$  5 mm . The reconstructed combustion is in a 10  $\times$  10 pixels image and the turbulence is displayed in spatial 7 mm  $\times$  7 mm resolutions. Figure 5.39 (a) is a sample image of the flame front at the start of combustion. Using the algorithm to evaluate the projection data produces an inverse image of combustion (Fig 5.39 (b)).

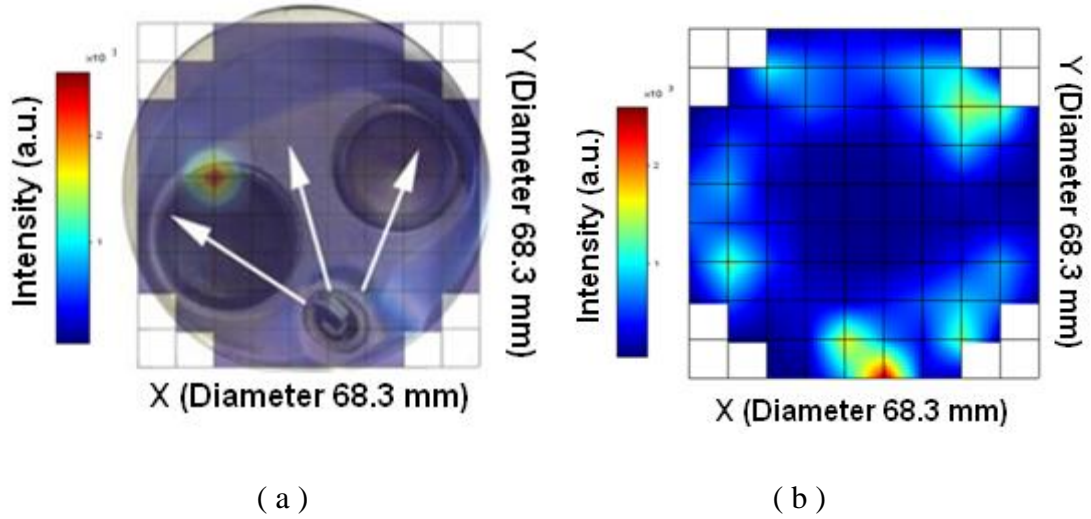


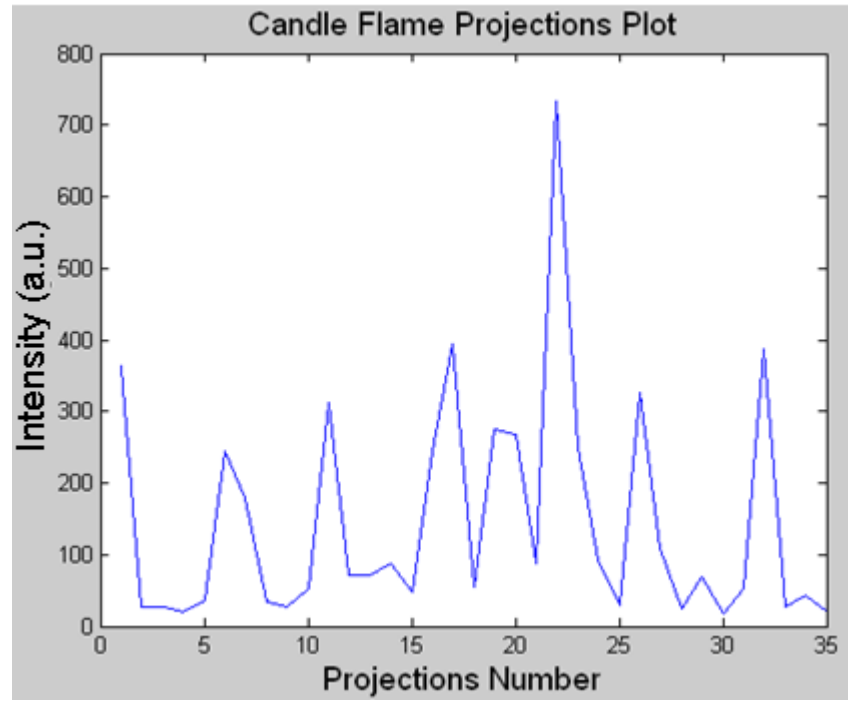
Figure 5.39 Combustion Visualization Schematic Diagrams (On the image a, Spark Ignition locates at the central of chamber bottom. The intake valve is on the left and the exhaust valve is on the right. The chamber diameter is 68.3 mm. The b is a reconstruction image of combustion in  $10 \times 10$  pixels and 1 pixel is equal to 7 mm.

The combustion projection intensities are full-filled in average. After iterations cross-correlation, the evaluated combustion images are reconstructed to represent the instant behavior of combustion. The colour bar on the left of image displays the intensity levels and the hottest area presents the maximum of intensity occurred in intensive reactions regions. The spark ignition position is the hottest region at the bottom of the image. At the start, combustion was concentrated around the ignition point and the region close to the ignition is in great intensity. The displaying of intensity distribution is a discontinued ring by the turbulent intensities. The shape of burning spot is present the size of turbulence of flame front.

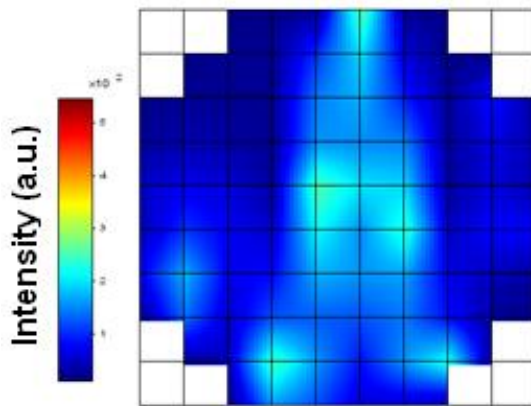
In following analysis, two sequences of images are shown to explain the UV



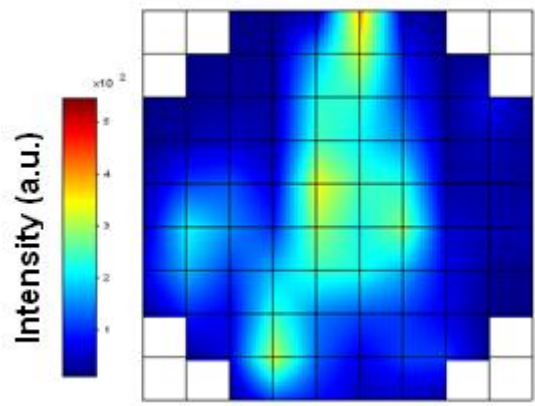
combustion and Blue combustion: reconstructed images after one iteration and reconstructed images after 1000 iterations. For example, figure 5.40 (a) and (b) are one iteration images of candle in different times. Figure 5.41 (a) and (b) are 1000 iterations images in different times.



( a )



( b )



( c )

Figure 5. 40 Reconstructed Candle Images after One Iteration

After one iteration cross-correlation, the candle projections are displayed the

intensities without error corrections. It is found that intensities of candle are briefly distributed in the center of images since the candle are uniform. However, the reconstructed images only briefly distribute the outline by one time correlation.

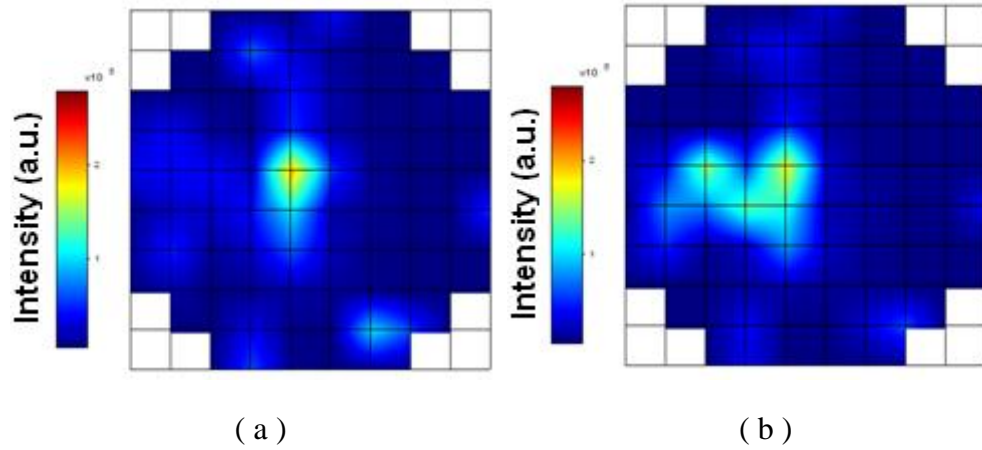


Figure 5. 41 Reconstructed Candle Images after 1000 Iterations

Figure 5.41 are reconstructed images after 1000 iterations. It represents clearer distribution of candle intensities. 5.41 (a) is more uniform than (b) since it is non turbulent at that moment. 5.41 (b) displays a distorted candle flame of the turbulent flow.

To illustrate results more visually, images have been improved using two colourmap formats: jet colourmap images in Matlab (Fig. 5.42 a) but in black colour background and hot colourmap in Matlab (Fig. 5.42 b). In the jet images, the 30000 has been set as the threshold of maximum intensity in case low intensities of images are lost by some over high intensities (Fig. 5.32 c). The hot Figures demonstrate the heat release of combustion. In hot Figures, the colourbar threshold is set to 3000 (Fig. 5.32 d). Despite some peak values are dominated by 3000, it represents the general

heat releasing process. In map visualization, some weak signals are represented in black colour caused by Matlab colourmap function. The colourmap index is 64 in total, the background of map is black. Since the black is taken a 1/64 value of maximum intensity, thus the 1/64 intensity value is visualized as black. For instant in figure 5.34 a, the maximum value threshold is 30000 and the 1/64 of 30000 is 470. Thus the value under 470 is visualized as black colour. In Figure 5.34 b, the maximum intensity threshold is 3000, thus the value under 47 is visualized as black colour.

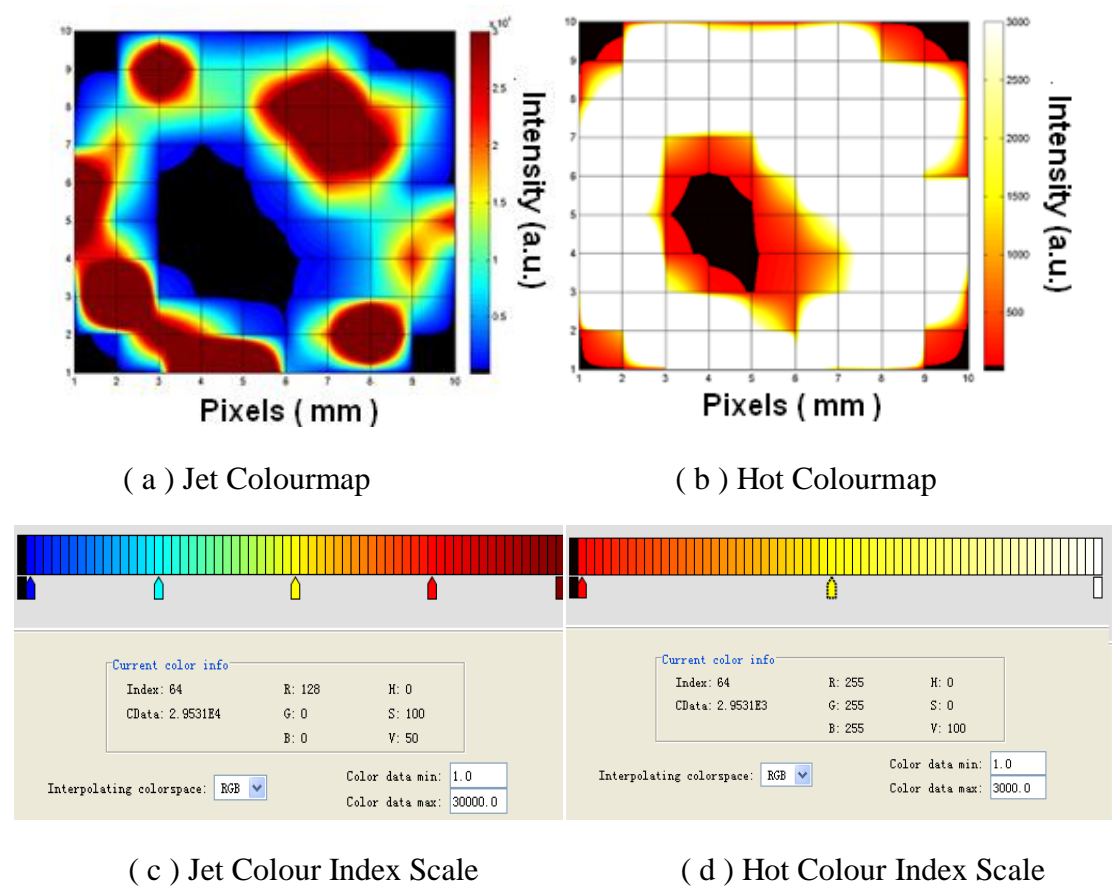


Figure 5. 42 The Same Instant Combustion Images Visualized in Jet and Hot Colourmap Formats (Note: 1 pixel = 7 mm and the intensity unit is a.u. of all following images)

### 5.5.2 UV Combustion Images Reconstruction

In this section, UV projections were employed to create the combustion process. It has two sequences of images: images after only one iteration and images after 1000 iterations. After the one iteration, the shape of combustion has been roughly confirmed by ART algorithm. After 1000 iterations, the distributions of combustion turbulence have been corrected by MART algorithm. It gives more accuracy reconstructed images to illustrate the combustion turbulent. In particular, the UV and blue projections data are sampled at approximate 2300 rpm of engine in rich fuel condition. Figure 5.43 is an intensity plot image of PMT projections.

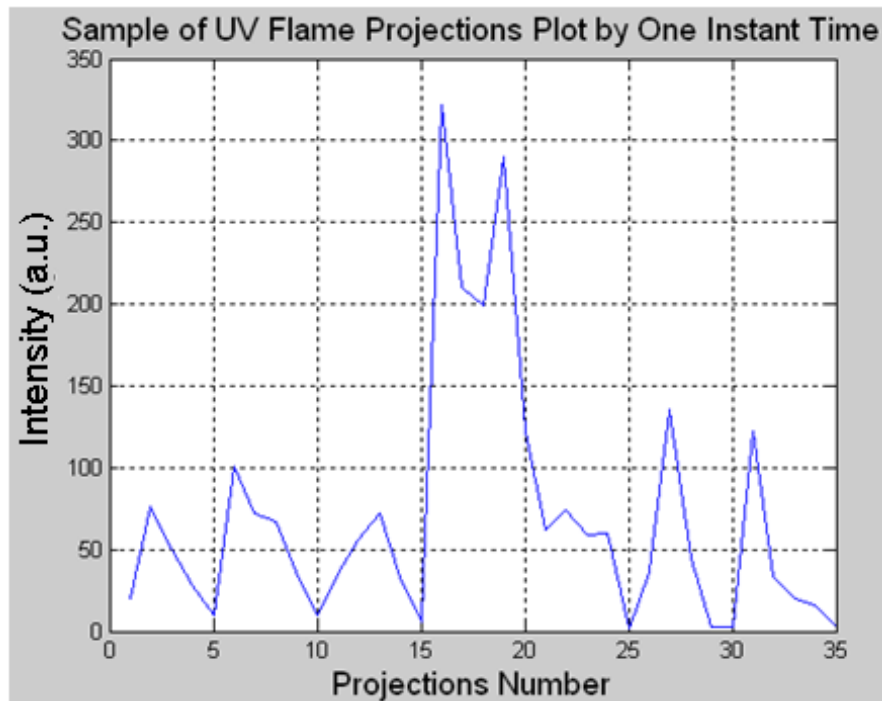


Figure 5. 43 The Intensity Response of PMTs of UV Flame by 1 MHz Sampling Frequency

## Reconstructed images of UV combustion by one iteration

As mentioned above, the one iteration briefly gives the shape of UV combustion turbulences after one iteration. The sampling image in table 5.5 gives the turbulences at one peak time during combustion expansion. Two results have been found by observing the images. Firstly, three distinct turbulences have been found surrounding spark ignition location. Secondly, the UV intensity is distributed in a Gaussian rings model of several turbulences. Comparing with the Anikin, et.al simulation of Burner flame in 2010 (Fig. 5.44), they set up a tomographic system to simulate UV flame front using Radon transform algorithm. In Burner flame, intensity distributions are more average due to its little turbulent characteristics comparing with in cylinder combustion. The POET results verify the performance of test engine according to turbulences distribution. In ideal model, the intensity should be uniform distribution without distinctive turbulences. In test engine, It is presents some significant turbulences. It may be caused by the spark ignition location and fuels distribution in cylinder.

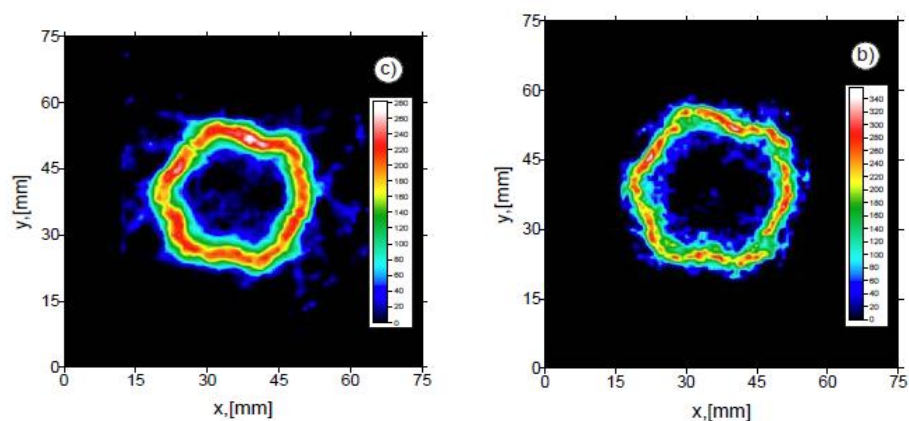
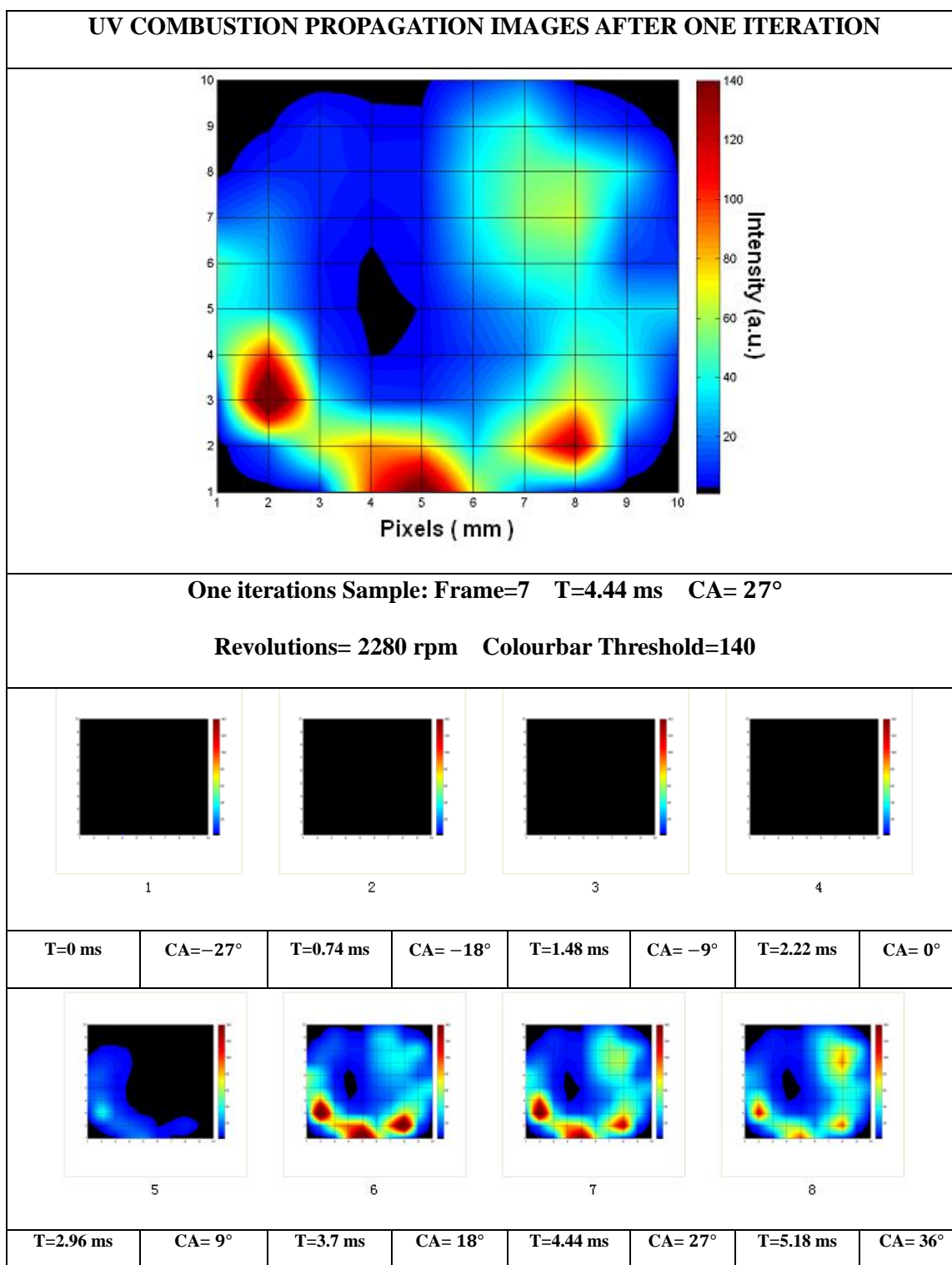
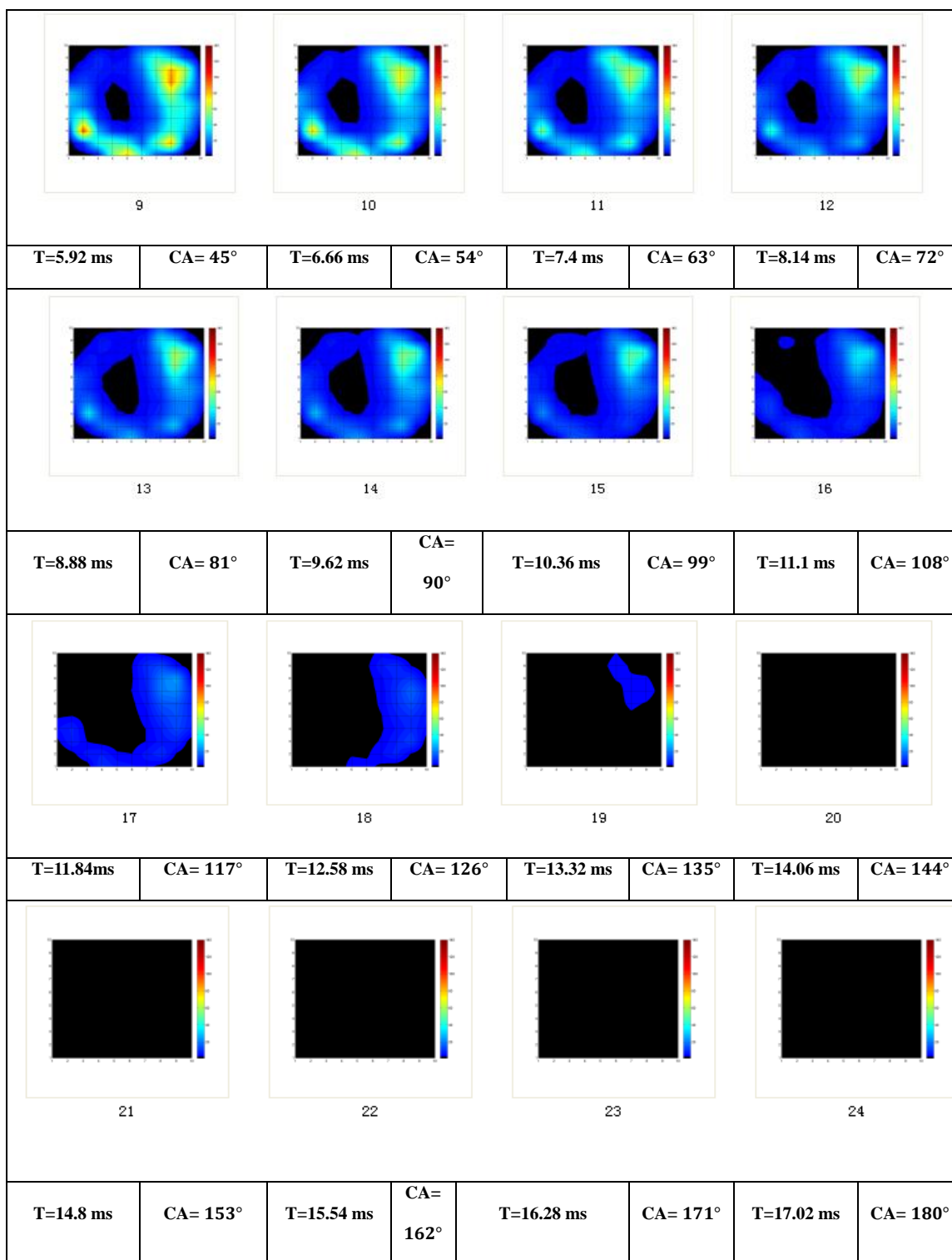


Figure 5. 44 UV Burner Flame Simulations by Karlsruhe University [32]

Table 5. 5 Reconstructed Images of UV Combustion Process after One Iteration





In analysis of combustion process (Table 5.5), subsequent images start from spark ignition time at  $-27^\circ$  Crank angles, and ends at  $180^\circ$  in a complete explosion stroke. The complete four strokes take approximate 30 ms and it takes 7.5 ms for a complete explosion stroke.

By comparing the images, the combustion turbulence distinctively occurs at  $9^\circ$  CAs surrounding chambers. Three significant turbulences occur in the bottom of images. One less significant turbulence appears at the top of images. After the  $18^\circ$  CAs, the intensity values of the three turbulences are decreasing, the intensity value of turbulence in the top of image becomes more distinct than others. During the propagation, the rapid reducing of pressure and fuels lead the entire intensities drop fast. After  $45^\circ$  CAs, the intensity decreases gradually. After  $130^\circ$  CAs, the intensities start disappearing. The flame front propagation is evaluated and it is approximate 15 m/s.

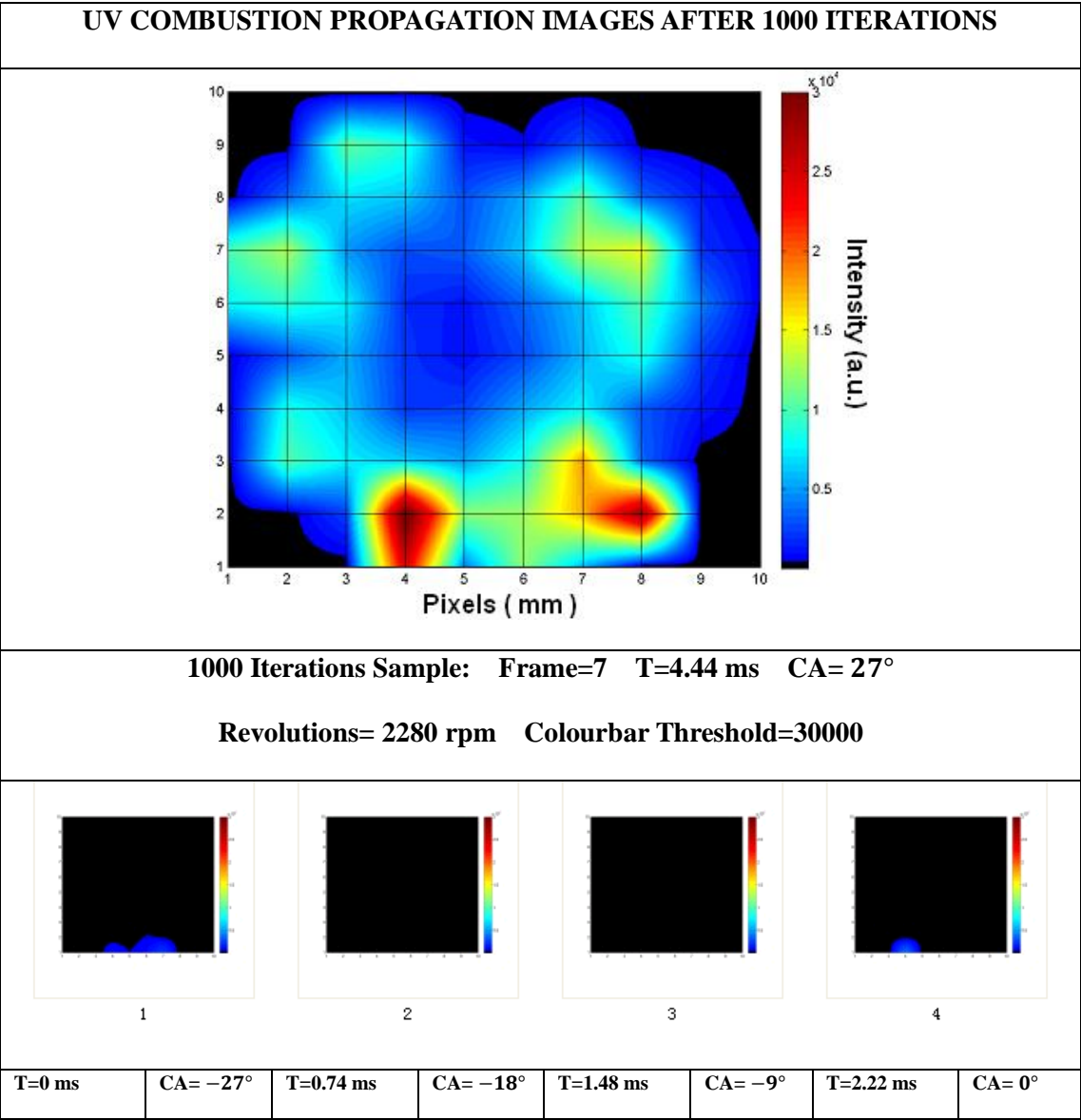
### **Reconstructed images of UV combustion by 1000 iterations**

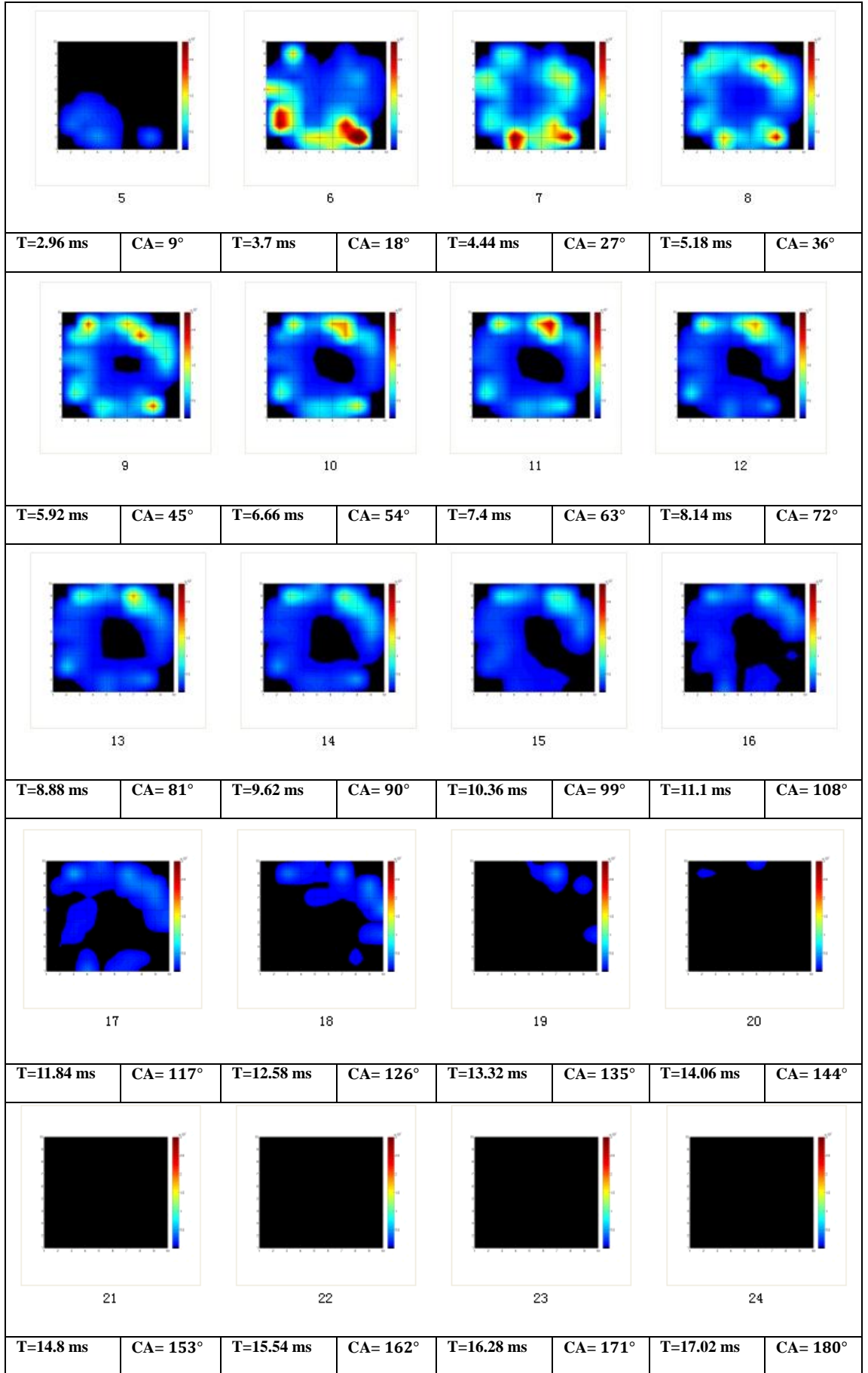
Table 5.6 as follow illustrates the combustion process using a sequence of reconstructed images after 1000 iteration. It gives several differences by comparing with one iteration images. The first difference is 1000 iteration images are more discrete than one iteration images, since some particular turbulent intensity is higher than others. After the iteration, the intensity has been corrected and placed in computational positions. The maximum values increased from  $10^2$  to  $10^4$ . Moreover,



the number of turbulences after 1000 iterations is different from one iteration. For instants, the sampling images of one iteration from table 5.5 are only present three distinct turbulences surrounding bottom of images. After 1000 iteration, six clear turbulences appear surrounding chambers (Table 5.6). In the comparison of reconstructed images, it has been found that the reconstructed images after 1000 iteration has the minimum averaged errors.

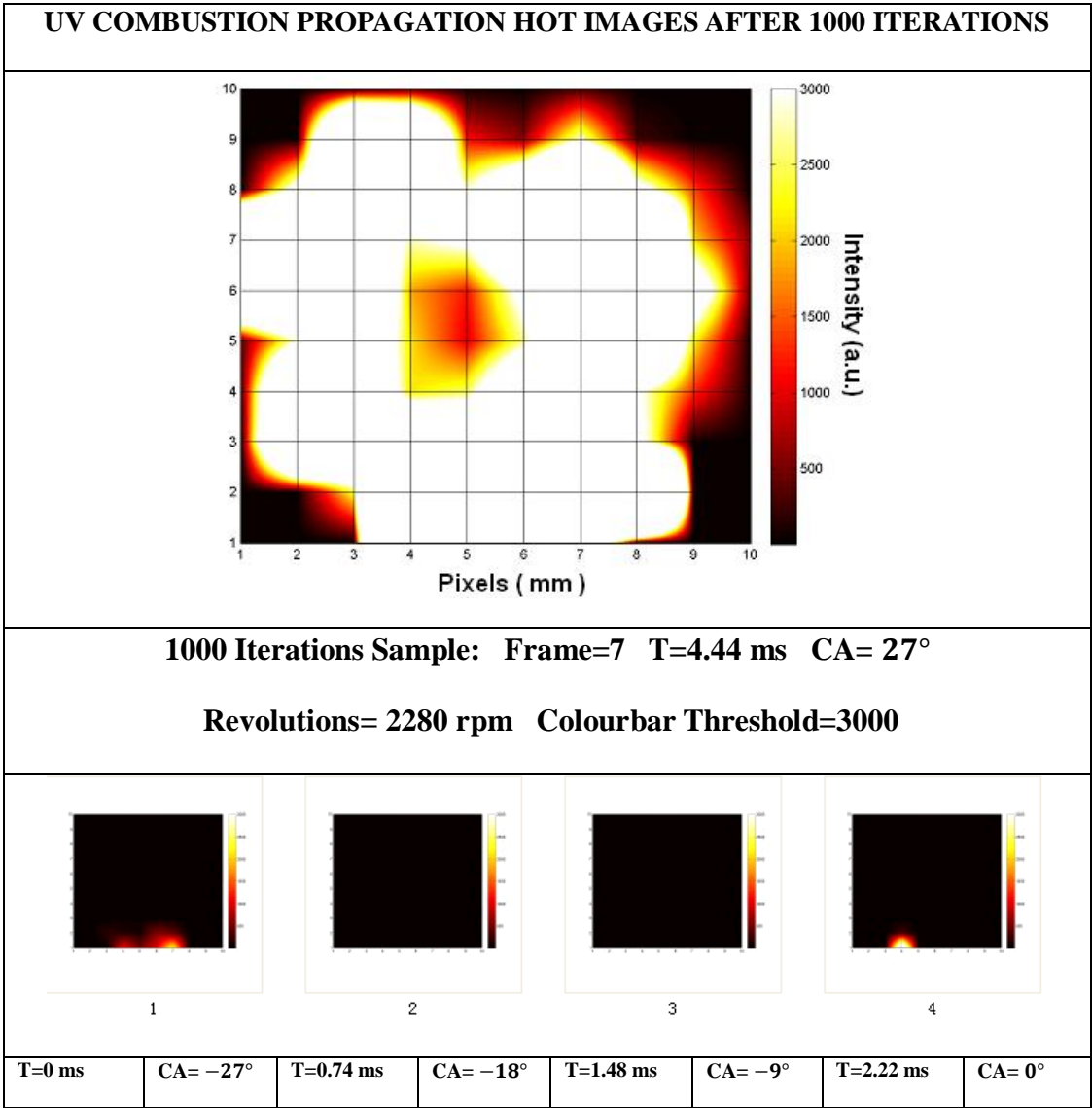
Table 5. 6 UV Combustion Process Images after 1000 Iterations

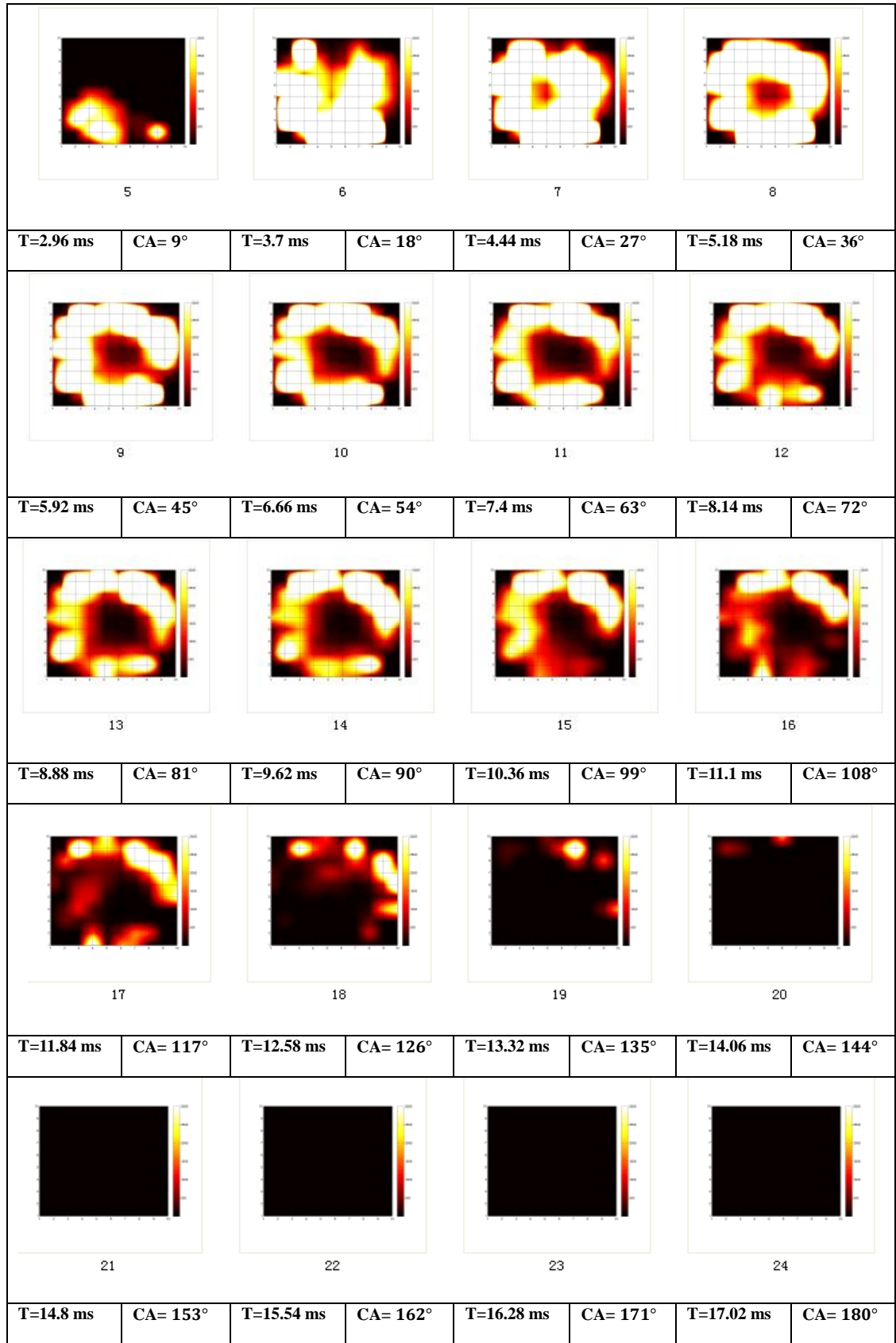




To demonstrate the heat releasing of combustion energy, a sequence of hot colour format images are figured in table 5.7. The maximum value is set to 3000. As the images illustrate, the critical heat releases occur from 18° to 45° Crank Angles. The size of top turbulences is wider than the bottom turbulences. Refer to the table 5.6 images, despite the turbulences are wider, values of bottom turbulences are greater than tops. This implies the initial air/fuel density distribution of bottom is richer than top's.

Table 5. 7 UV Combustion Process Hot Images after 1000 Iterations



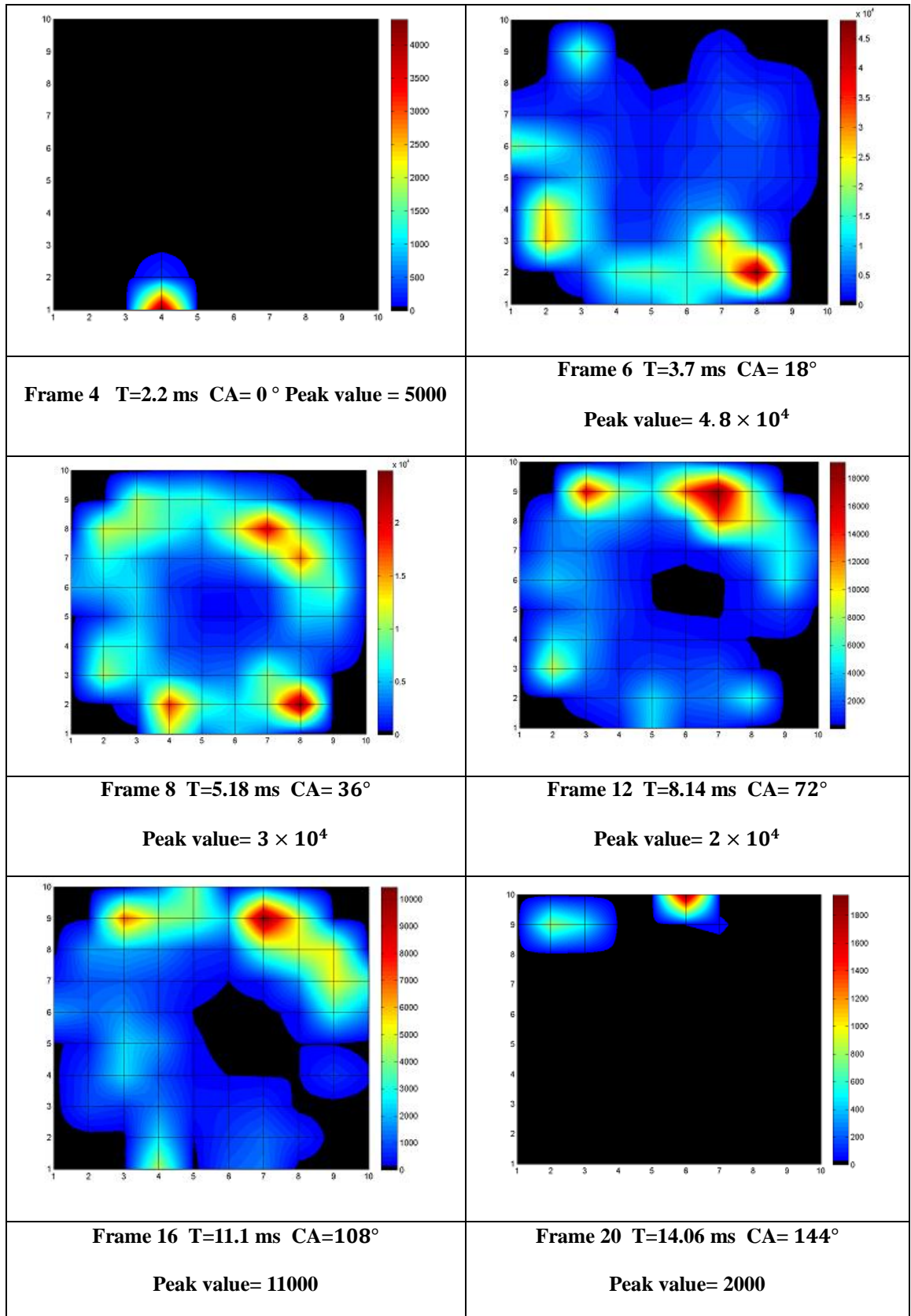


## **Reconstructed images of UV combustion by 1000 iterations by free colourbars**

Table 5.6 displays a sequence of images to illustrate the combustion process. The images are reconstructed in the same colourbar threshold scale. For example, as the sample image in table 5.6, the intensity value is up to  $6 \times 10^4$  in maximum. Thus, some images are present blue without distinctive turbulences in low intensities. To help understanding these images, several images are shown in free colourbars as follow (complete version in appendix E).

It has been found from table 5.8: the Frame 4 as the starts of combustion has low intensity turbulences at the bottom of image surrounding intake valve. At the frame 6, the intensity increases to  $4.8 \times 10^4$ . The significant turbulences still surround intake valve. At frame 8 the  $36^\circ$  crank angles, the intensities start falling. The apparent turbulences appear on the top of chamber. At frame 12, the intensities sharply drop to 20000 after  $72^\circ$ . Then it is to disappear after frame 20 at  $144^\circ$ .

Table 5. 8 UV Combustion Images by Free Colourbars



### 5.5.3 Blue Combustion Images Reconstruction

The Blue combustion represents the main heat releasing and information of turbulences distribution. To compare with UV combustion, the two sequences of images are to illustrate the combustion as the same as UV images: one iteration images and 1000 iterations images. The engine running parameters of Blue combustion are the same as UV combustions.

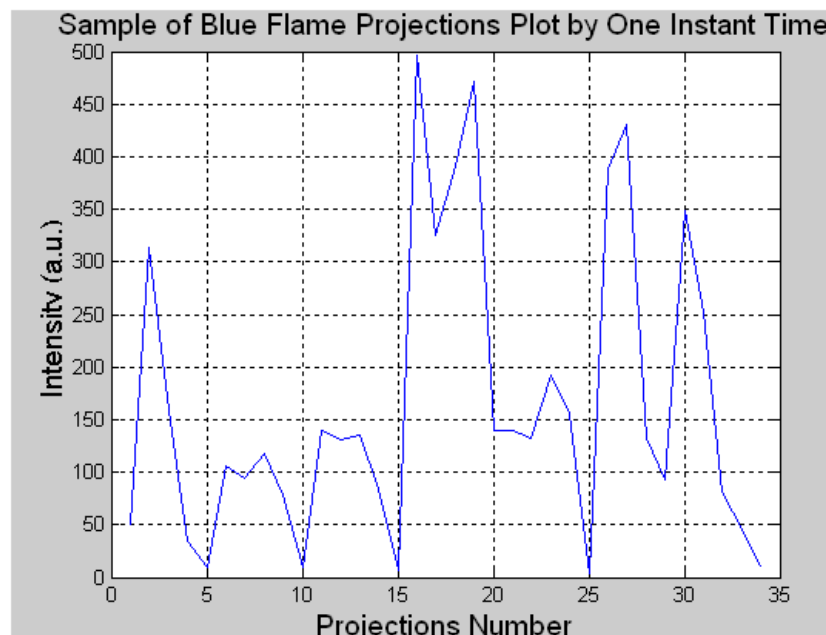


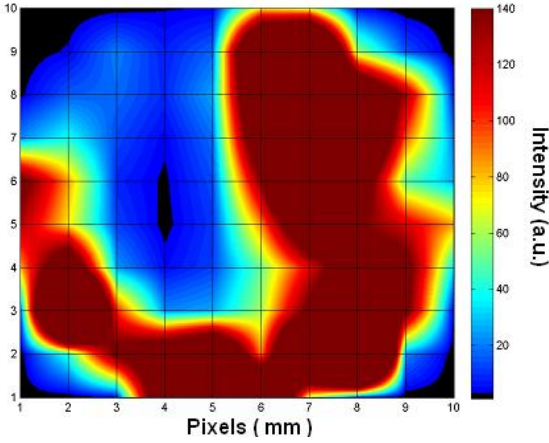
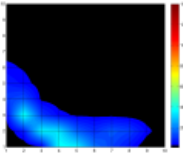
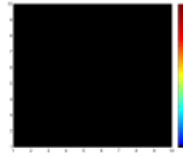
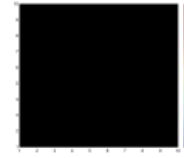
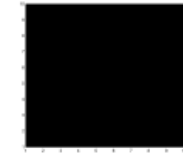
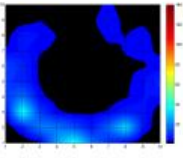
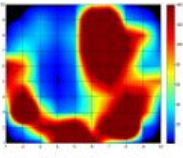
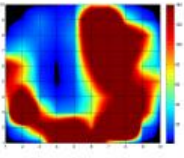
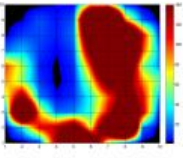
Figure 5. 45 The Intensity Response of PMTs of Blue Flame by 1 MHz Sampling Frequency

#### Reconstructed images of Blue combustion by one iteration

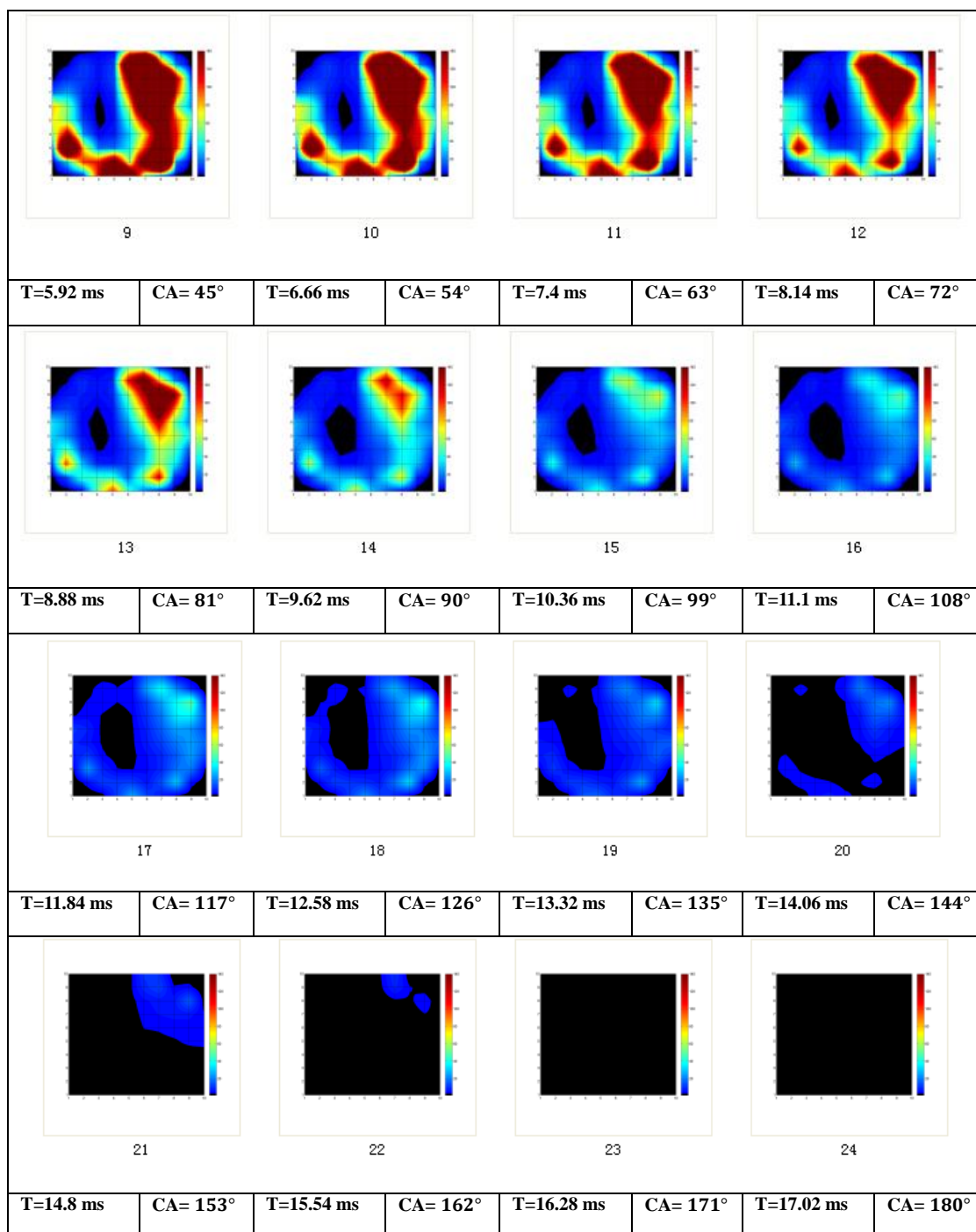
In this section, the image of Blue combustion has been reconstructed by one iteration. In comparing, the sample image in table 5.9 below is some different from UV sample image in table 5.5. The intensities of Blue are higher than UV. The Blue

turbulence on the top of images is much brighter than UV. However, the more information can be retrieved by numerical results.

Table 5. 9 Blue Combustion Process Images after One Iteration

BLUE COMBUSTION PROPAGATION IMAGES AFTER ONE ITERATIONS							
							
<p>One iterations Sample: Frame=7 T=4.44 ms CA= 27°</p> <p>Revolutions = 2280 rpm Colourbar Threshold =140</p>							
<div>     </div> <div> 1234 </div>							
T=0 ms	CA= -27°	T=0.74 ms	CA= -18°	T=1.48 ms	CA= -9°	T=2.22 ms	CA= 0°
<div>     </div> <div> 5678 </div>							
T=2.96 ms	CA= 9°	T=3.7 ms	CA= 18°	T=4.44 ms	CA= 27°	T=5.18 ms	CA= 36°

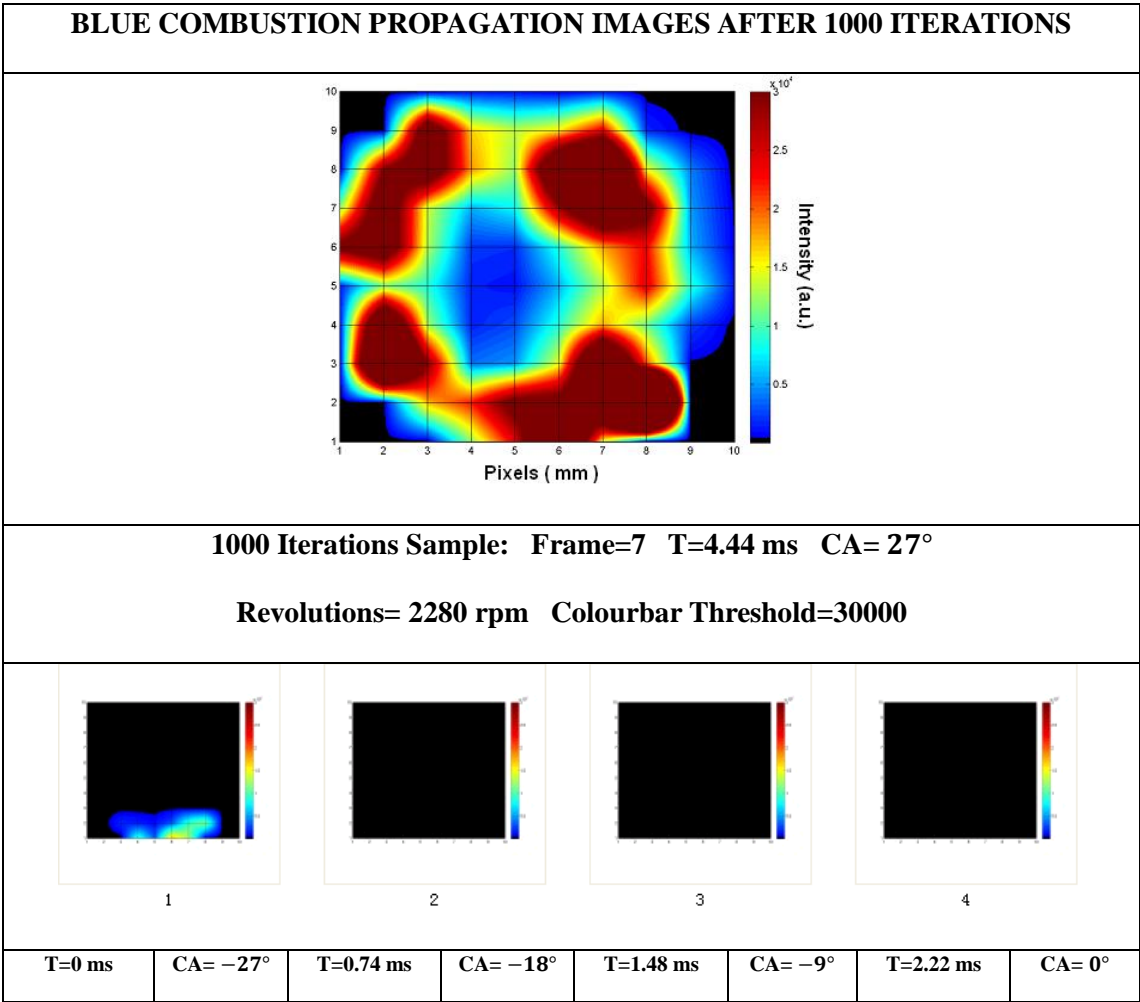




# Reconstructed images of Blue combustion by 1000 iterations

The table 5.10 illustrates a sequence of images of Blue combustion after 1000 iterations. Compare with UV combustion, it presents some differences. The maximum intensity of Blue is  $13 \times 10^4$  which is higher than UV  $6 \times 10^4$ . More distinct turbulences appear than UV. The turbulences are more continuous compare to the discrete UV turbulences. It has been proved that the intensity distribution of blue flame is more uniform than UV's. That suggests the UV combustion is more turbulent and intensive than Blue combustion.

Table 5. 10 Blue Combustion Process Images after 1000 Iterations



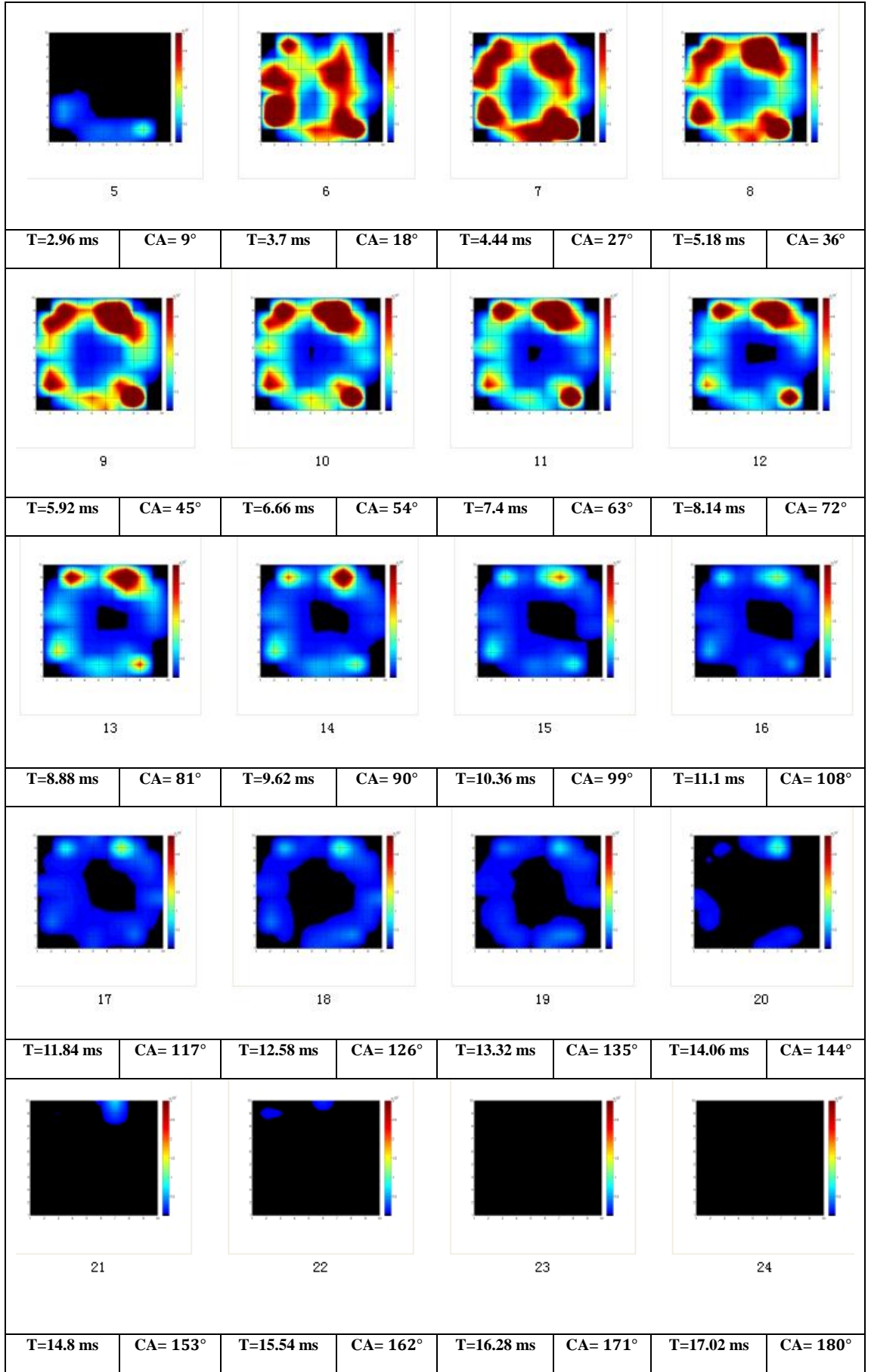
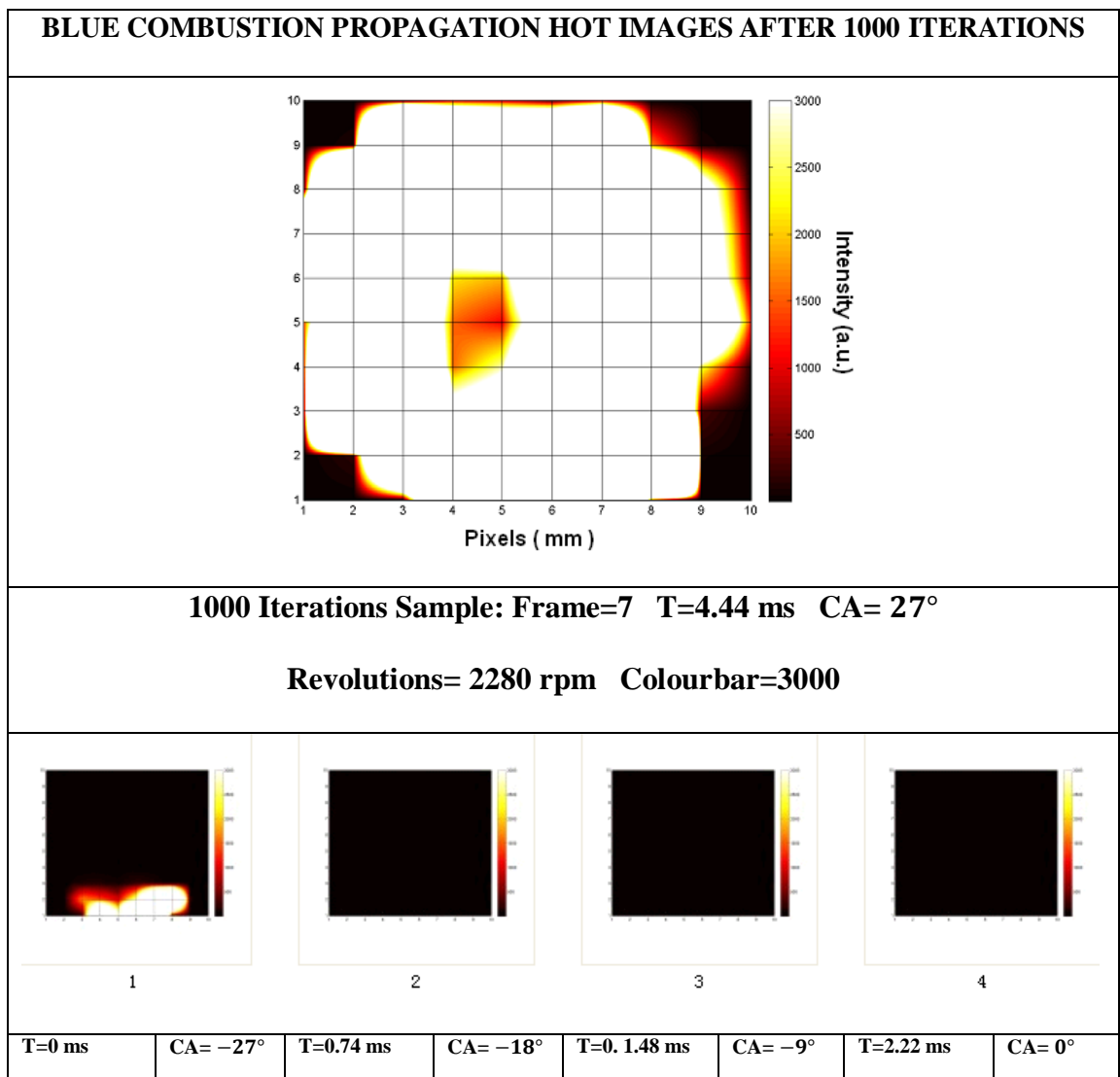


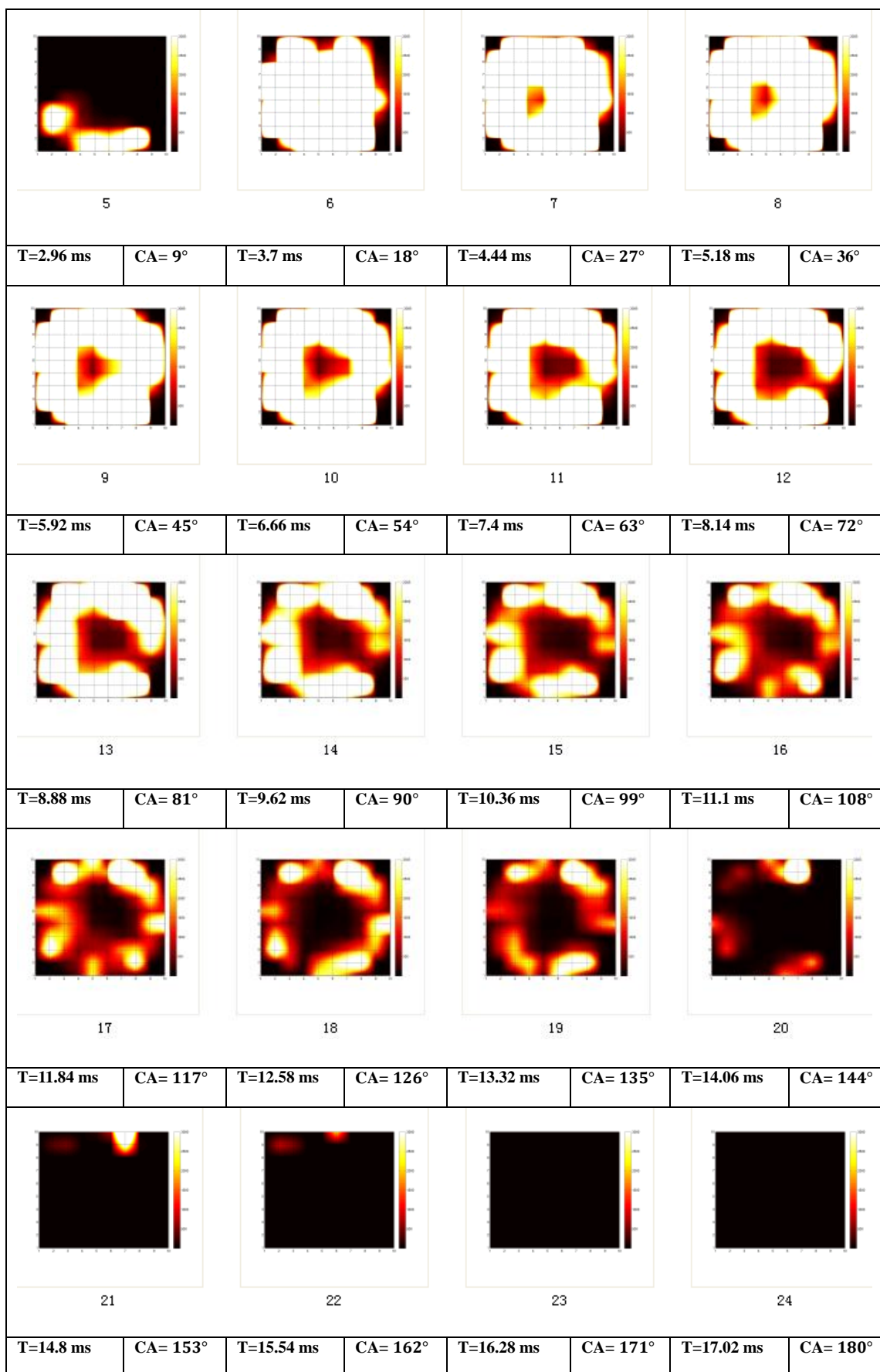
Table 5.11 illustrates the hot images of blue combustion after 1000 iterations.

By comparison with UV hot images, the heat release of blue is much more than UVs.

The shape of turbulences is wider than UV combustion. The turbulences are more linear than UV. It has been suggested that the UV combustion is much turbulent than Blue combustion.

Table 5. 11 Blue Combustion Process Hot Images after 1000 Iterations





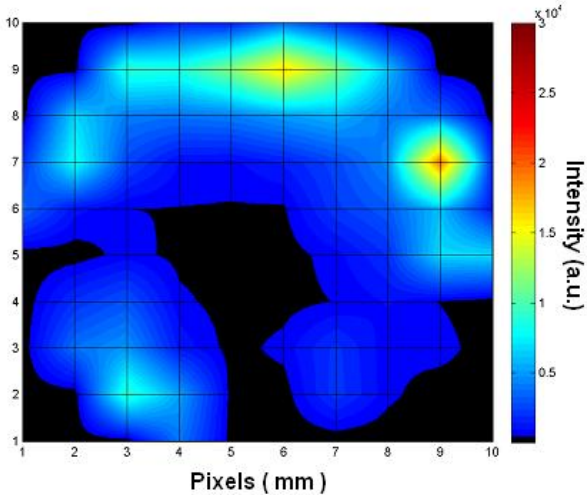
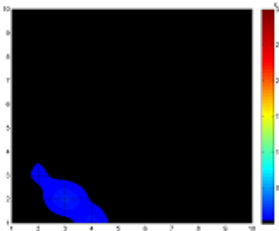
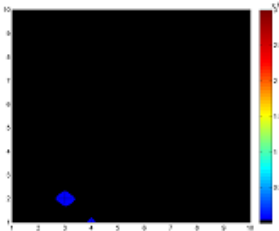
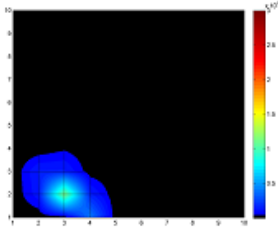
## 5.5.4 Combustion Reconstruction in Different RPMs

In different equivalent ratios, the engine runs at different revolutions. In experiment, the engine has been tested running at air/fuel ratios  $\phi \approx 0.64$ ,  $\phi \approx 0.76$  and  $\phi \approx 1$ . Corresponding to the revolutions, they are 1090 rpm, 1200 rpm and 1550 rpm respectively. In different revolutions, the flame front propagations speed is varying in the changes of fuel-air. These changes cause the performances of engine alter due to the heat release changing. Thus, the analysis of combustion in different revolutions is significant to study the engine heat releasing. In following, three subsequences of reconstructed images in different ratios have been illustrated to identify the varying of turbulent combustion (Table 5.10). The time of interest is from  $t = 2.8$  ms to 32 ms after spark ignition. For comparing the heat releases in different revolution speeds, several critical time of combustion images are focused. At the  $t = 4$  ms, the 1550 RPM image start to appear distinct signals. After the  $t = 22.4$  ms, the 1550 RPM combustion disappear. After the  $t = 28.8$  ms, the combustion of revolutions 1200 is completed. After the  $t = 32$  ms, the combustion of revolutions 1090 is end.

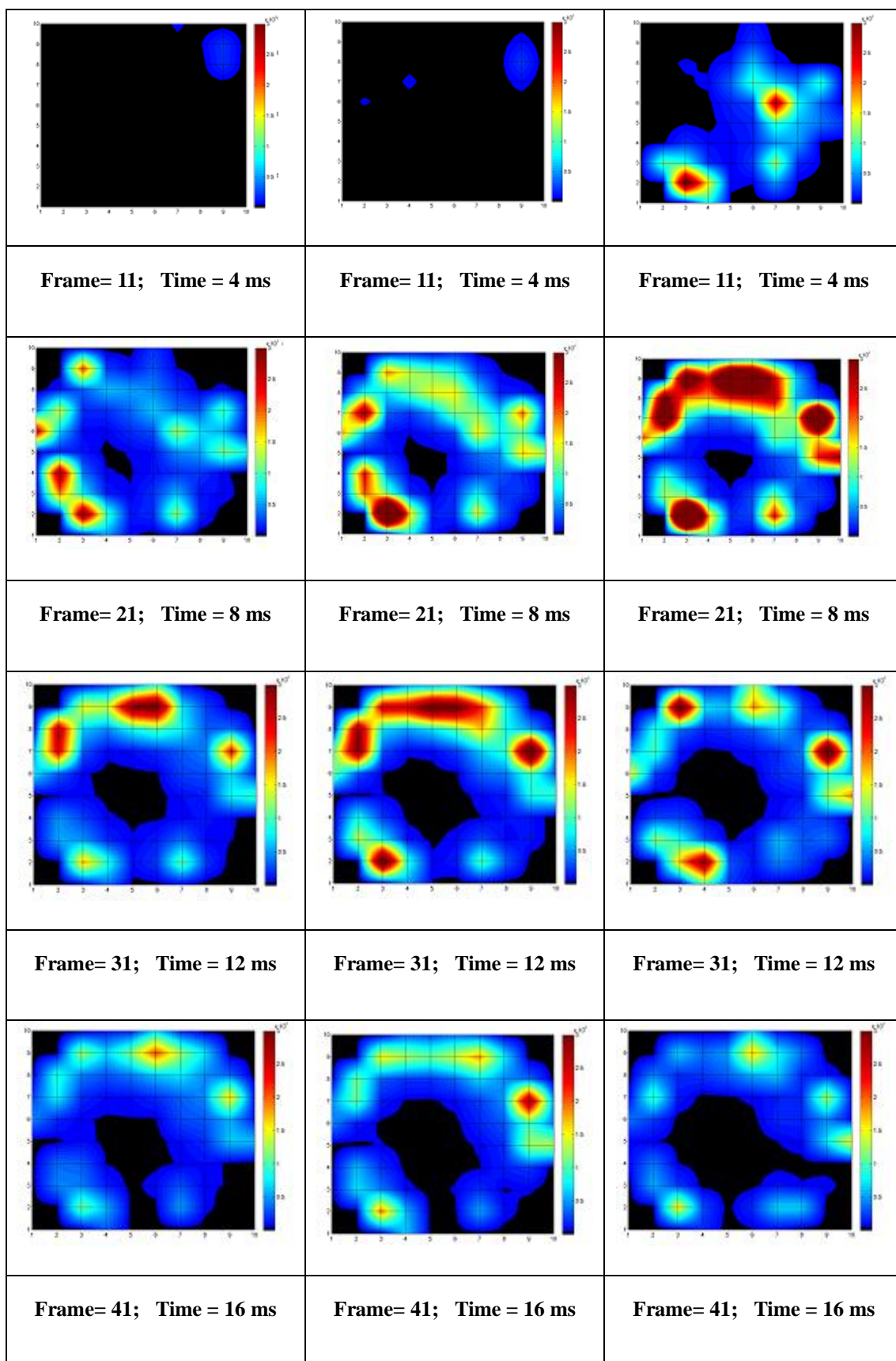
As the table illustrates, distinctive signals occur in 1550 rpm image at 2.8 ms. Other two images have no apparent emissions. At 4 ms, the flame emission values reach the maximum turbulences in both 1200 rpm and 1550 rpm. By comparison, the sum of intensity values of 1550 rpm image is higher than 1200 rpm. At the  $t = 8$  ms, the 1090 rpm flame emissions are reach the maximum. The 1550 rpm and 1200 rpm emissions start falling. After 22.4 ms, the 1550 rpm emissions disappear. The 1200 rpm

and 1090 rpm combustions keep burning. After the 28.8 ms, the 1200 rpm combustion is completed. After the 32 ms, the 1090 rpm emissions are finished. Therefore, the heat release of different power out in varying times can be evaluated using the numerical data of reconstructed images. However, it is discussed in further works section.

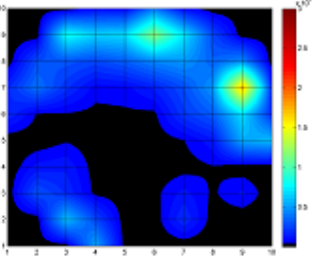
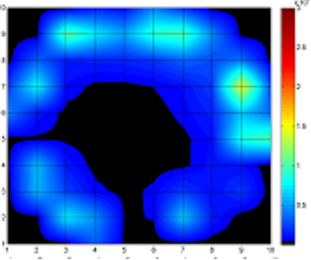
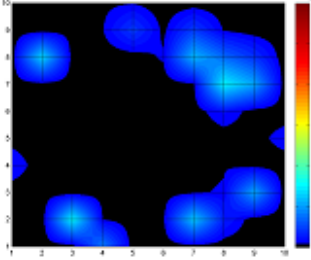
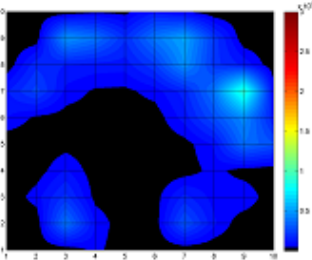
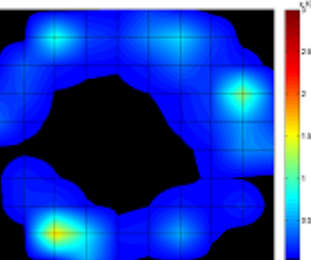

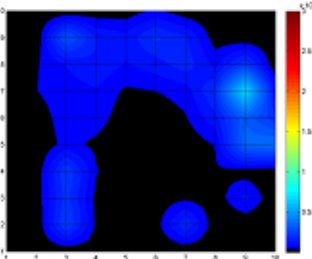

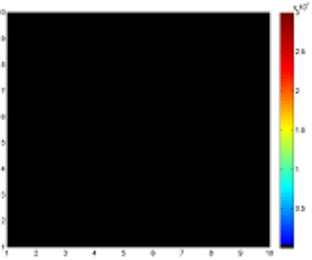
Table 5. 12 Reconstructed Images of Combustion Propagation by Different Engine Revolutions

Blue Combustions for Different RPM			
<div>  </div>			
<div> Sample:   Revolutions= 1090      Frame=45      Time= 31.5 ms  Colourbar Threshold=30000 </div>			
Revolutions=1090	Revolutions=1200	Revolutions=1550	
<div>  </div>	<div>  </div>	<div>  </div>	
Frame= 1;   Time = 0 ms	Frame=1;   Time = 0 ms	Frame= 1;   Time = 0 ms	







		
Frame= 51; Time = 20 ms	Frame= 51; Time = 20 ms	Frame= 51; Time = 20 ms
		
Frame= 61; Time = 24 ms	Frame= 61; Time = 24 ms	Frame= 57; Time = 22.4 ms
		N/A
Frame= 71; Time = 28 ms	Frame= 73; Time = 28.8 ms	N/A
	N/A	N/A
Frame= 81; Time = 32 ms	N/A	N/A

## 5.6 Summary

This chapter has discussed the flame front propagation speed measured by PMT projections. The expand flame front speed of flame is 12 m/s on average within cylinder. By comparison in different revolution speed, the velocities decrease gradually as the revolution speed falls.

In combustion reconstruction, UV and blue flame are compared. It has been found the UV turbulence is more intensive than Blue turbulence. However, the POET system suggests blue filtered flame intensity is greater than UV filtered flame briefly. In comparison of different air-fuel ratios, the reconstructed images of three engine revolutions present different propagation in both time and spatial. The varying of heat release in different revolutions has been suggested by observing the reconstructed images.

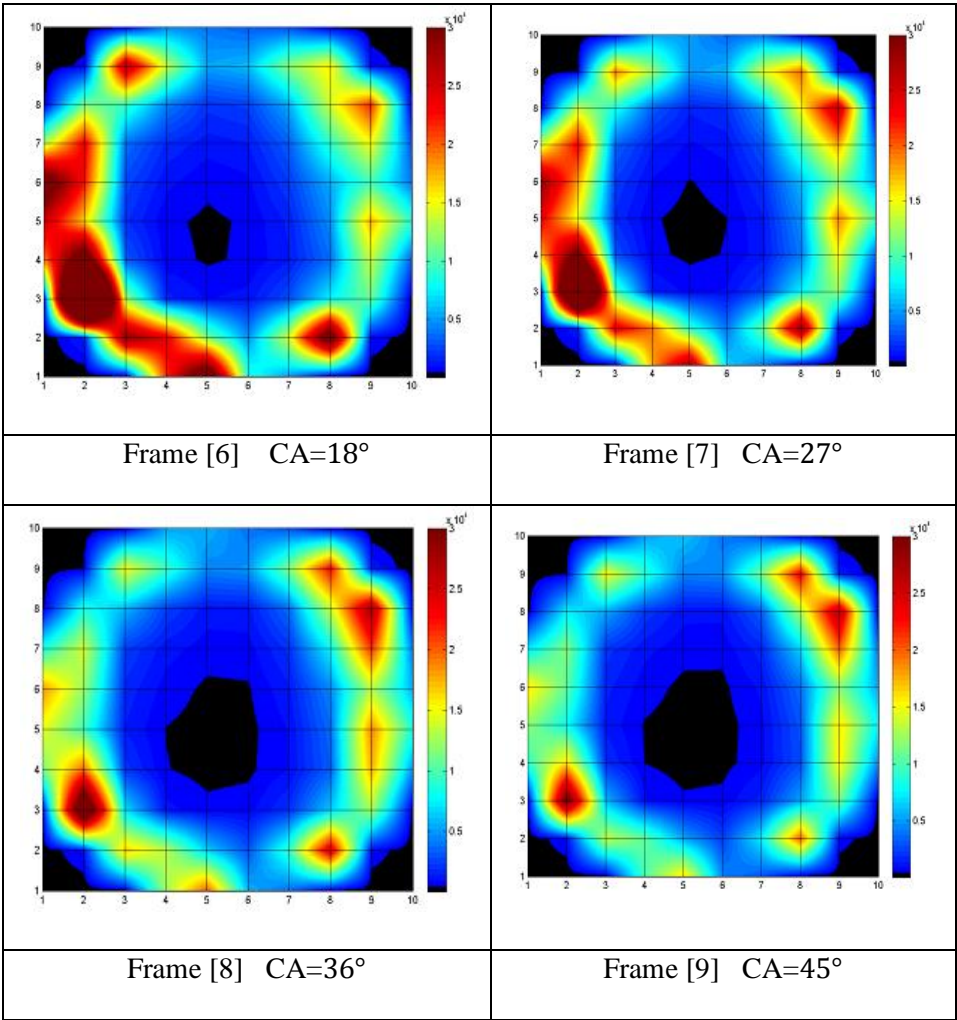
### 5.6.1 Optimized Combustion Images

The combustion process is the significance to identify the performance of engines. In the ideal engine, it is supposed the fuel fills the whole chamber in averaged distribution. Then the burning turbulences are not significant varying. Thus, the engine is running in stable and efficiency. However, the test engine is poor performance. The intensity distribution is more variable in different locations. To give a comparison, the result data have been optimized to reconstructed ideal engine combustion images. The reconstructed images from 13° to 45° are figured (table 5.13). The complete images

are in the appendix E.

The optimized images (table 5.13) are apparently different from previous results. It presents continuous Gaussian ring model. Though some distinct turbulences are distributed follow the ring, their intensities are not significant different from others. It suggests that the combustion occurs uniformly surrounding the chamber. The optimized images have changed the initial experiment data and they are simulated data. If a better performance engine is employed in further, the combustion images will be similar as these optimized images.

Table 5. 13 Optimized Reconstructed UV Images



# Chapter 6.

## Conclusion and Recommendations

### 6.1 Conclusion

The central aspect of this thesis states that the combustion process can be reconstructed in 2D images using the tomographic POET system. Through the analysis of these images, the model of combustion turbulence has been measured and reconstructed. The performance of a research modified engine has also been evaluated.

In this dissertation, several methods of flame front measurements have been reviewed in chapter 2. Following reviews of the relevant methods, the POET chemiluminescence approach has been developed and applied to make in-cylinder combustion measurement (Fig. 6.1).

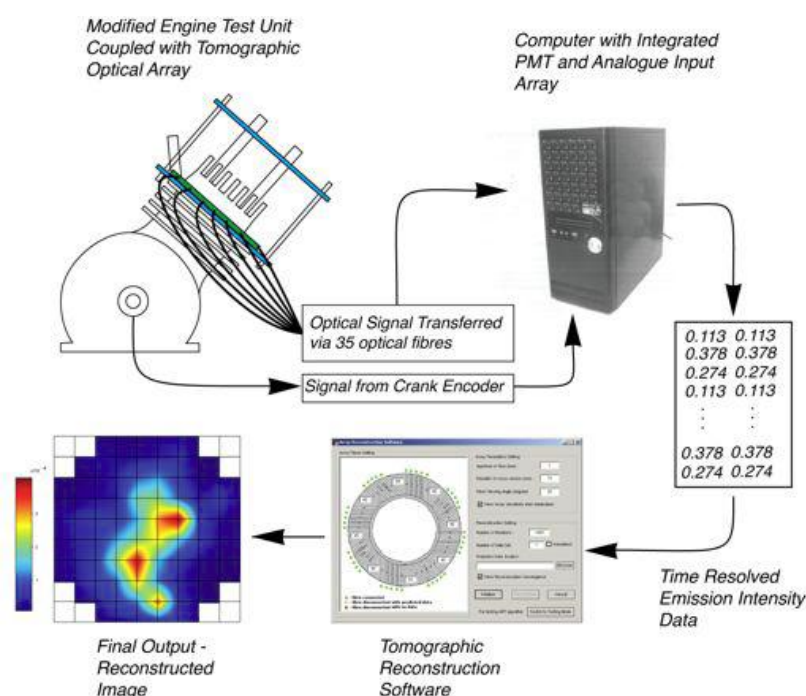


Figure 6. 1 POET System

Furthermore, through the study of tomographic system in chapter 4, two alternated techniques have been evaluated using PMTs and a Shack Hartmann lens array. The POET presented a non-intrusive approach does not require a laser-camera system. This advantage makes it excellent for in-cylinder combustion measurements. Therefore, the POET system has been adopted to measure the flame front.

In the project, a Briggs and Stratton OHV Pro 206 commercial engine has been modified to couple with the measurement system (Fig. 6.2). In the experiment, natural gas has been employed to fuel the engine. 35 PMTs has been placed surrounding chamber as optical detectors. PMTs present good performance to collect signals when the combustion is turbulent which is up to 4 kHz at frequency and up to 1500 °C in temperature. A compact PMT-PC system has been manufactured by Etalon Research Lab to achieve requirements of laboratory purpose.

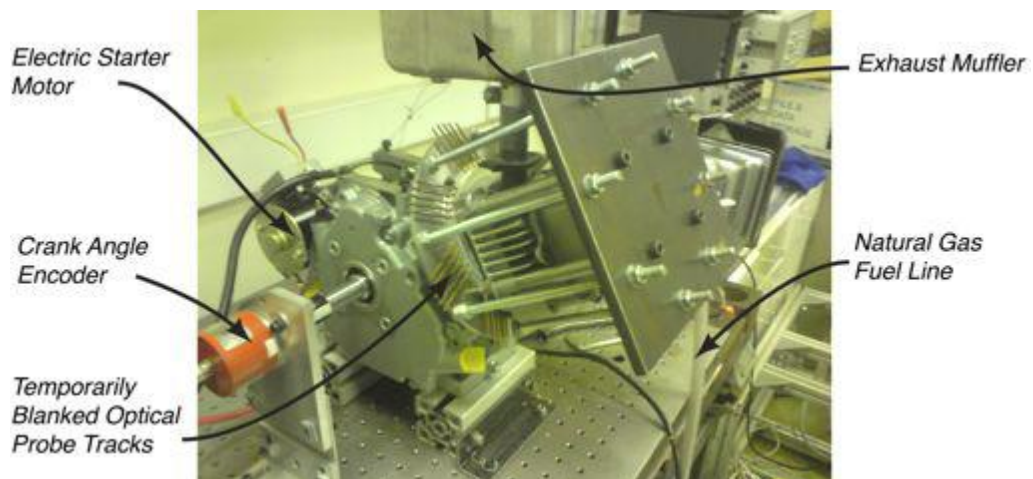


Figure 6. 2 Modified Engine Coupled with O-Ring Gasket

In the experiment, the flame front has been detected in both UV and Blue filters to verify the differences between varying spectrum wavelengths. The combustion has

been sampled in different equivalent ratios to evaluate the engine performance in varying revolutions. In previous projects, D. Wilson and P. Dunkley two PhDs had set up a tomographic system using photodiodes to measure a side valve modified engine [3]. In their system, there were two distinct unsolved problems. The signal was dominated by the spark ignition noise because of the electronic performance of the photodiode system. For the gas turbulence, the system had a 2:1 noise to signal ratios caused by the complex A/D transfer system design. However, in this project, the use of PMTs has a fast sampling response to the resolved time of 20 kHz. The SNRs of the PMT is 100:1. Therefore, the limitations of previous project have been overcome in this 2<sup>nd</sup> generation POET system.

In the results, the velocity of flame front propagation has been evaluated. The speed of flame front presents varying within the chamber caused by engine performance. Initially, the propagation speed is up to 17 m/s surrounding the spark ignition location at the beginning. Following a high turbulent expansion, the speed falls to 8 m/s. Then the speed decreases to less than 5 m/s (Fig 6.3) at the cylinder wall. In the four different revolutions: 2300 RPM, 1550 RPM, 1200 RPM and 1090 RPM, the averaged speed decreases from high revolutions to low revolutions. In 2300 rpm, the propagating speed varies from 17 m/s to 5 m/s in both temporal and spatial domains. In low revolutions, the propagation speed fluctuates approximately 5 m/s.

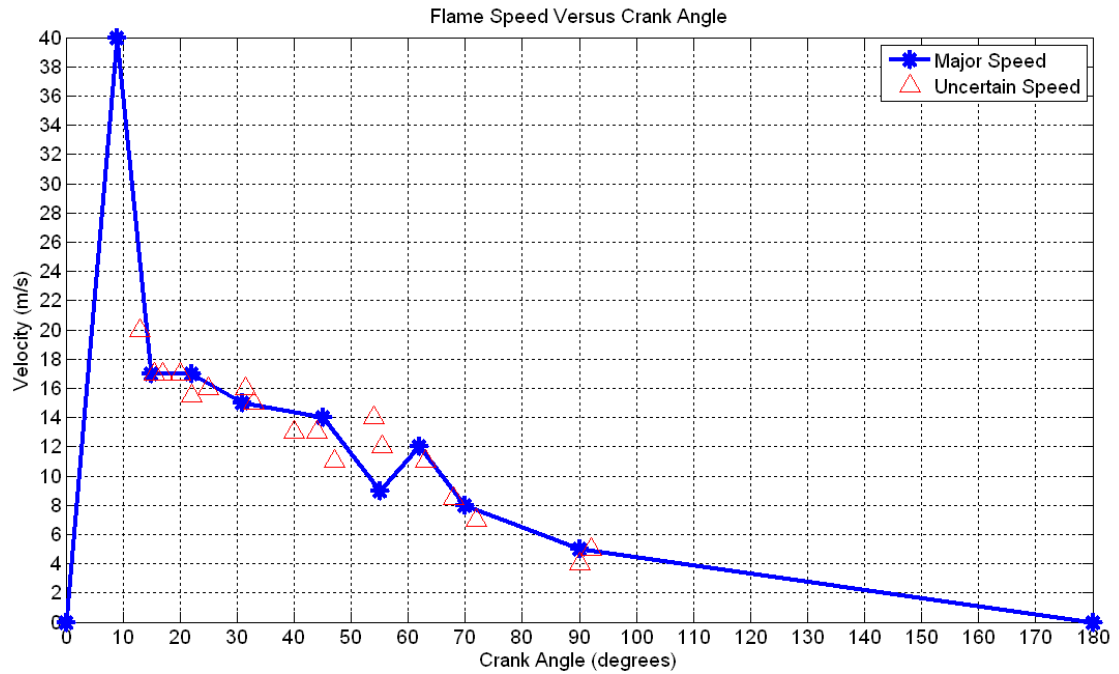
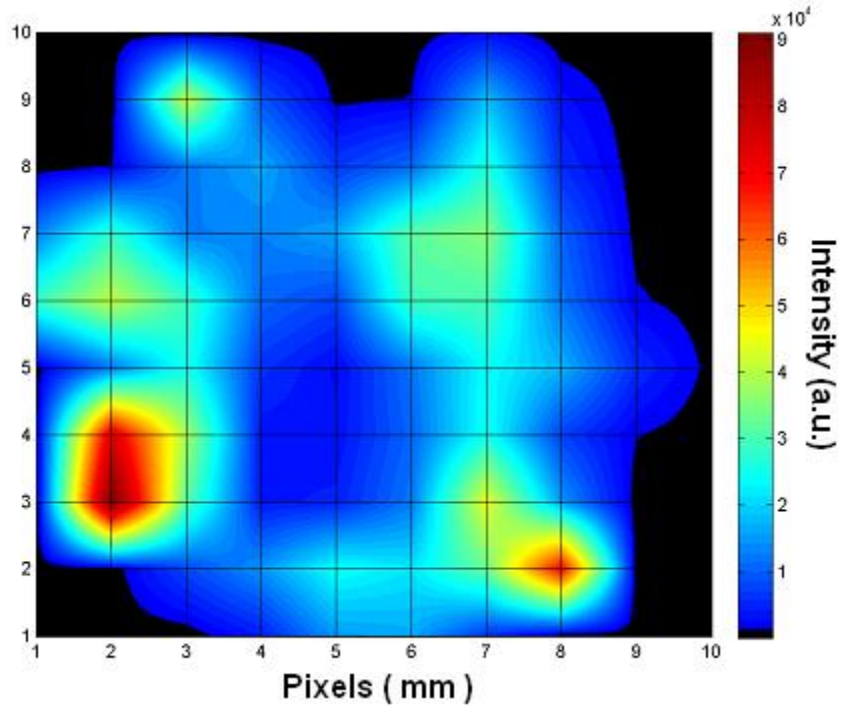
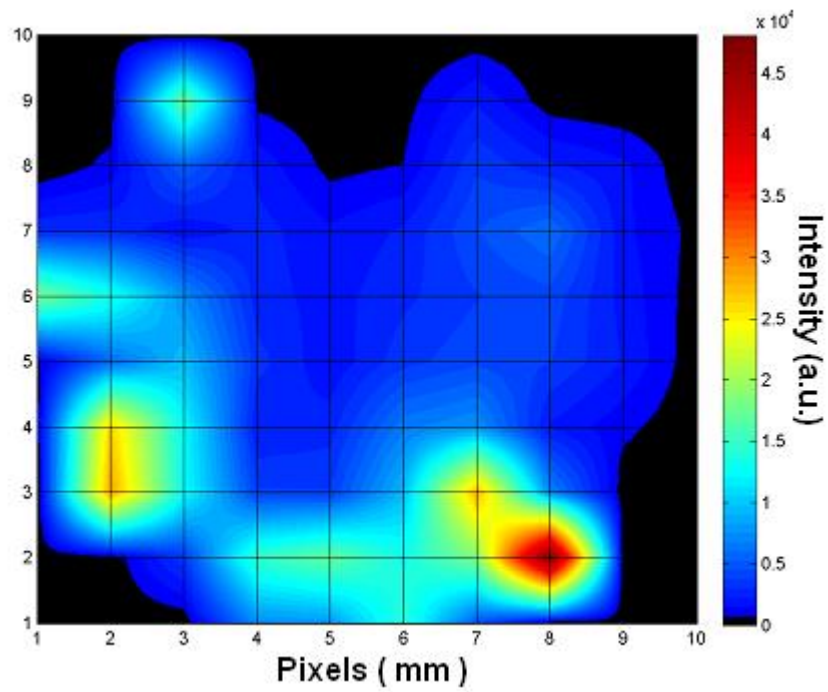


Figure 6. 3 Flame Propagation Velocities by Crank Angles

In combustion reconstruction, the Array MART tomographic software which was initially programmed by a MEng Group of students [95] has been improved and applied to reconstruct the combustion process in this project. In computational and simulation, an initial calculated combustion matrix model was guessed using PMT projections by inverse square law of light radiation. After iterations, the matrix combustion has been corrected by correlation coefficient to present an approximate combustion. After computation, a sequence of images of combustion process has been created to demonstrate the heat release and performance of the tested engine. The software uses  $10 \times 10$  pixels images to display the combustion turbulences in size of  $7 \text{ mm} \times 3 \text{ mm}$ . The size of turbulence has been calculated roughly is  $5 \text{ mm} \times 5 \text{ mm}$  (Fig 6.4).



( a ) Reconstructed Image of Blue Combustion by 1000 Iterations

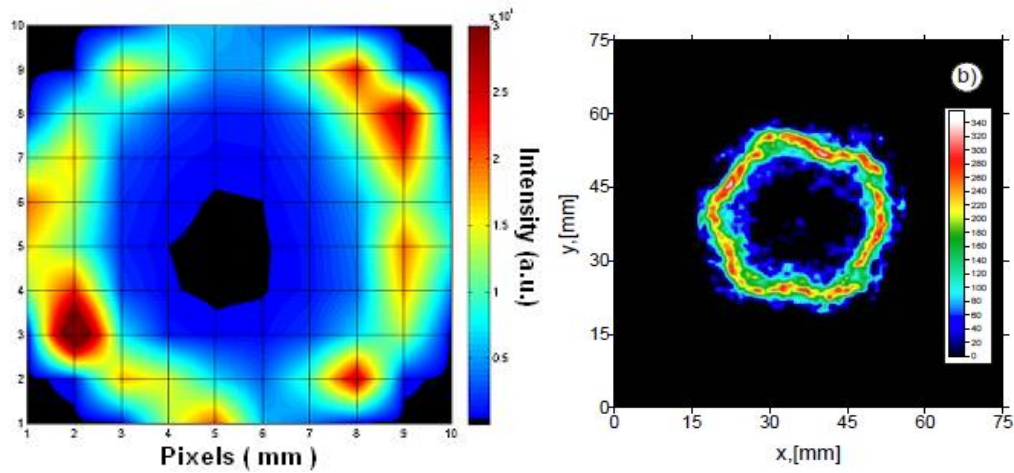


( b ) Reconstructed Image of UV Combustion by 1000 Iterations

Figure 6. 4 Reconstructed Images of UV and Blue Combustion at the Same Time



After the analysis of the combustion process, it has been founded the heat release of UV reactants are different from Blue elements. The energy of Blue emissions is great than UV emissions. The turbulence propagating in a Gaussian Ring has been proved Anikin, Suntz and Bockhorn have simulated a Burner flame using a camera tomography system in 2010 [32]. They demonstrate the OH turbulence shape in Gaussian ring as well (Fig 6.5 b). Moreover, the POET results imply that the flame front is fast propagating as beginning and it approximately takes 1 ms to cross the chamber bore at 2300 RPM engine speed; then the flame turbulences are locally growing surrounding the boundary of chamber and they are not propagating anymore.



( a ) Optimized UV combustion image      ( b ) Karlsruhe University Reconstructed

Figure 6. 5 A Comparison between Optimized POET UV Image and Karlsruhe University Simulation

In conclusion, the POET project is successful to verify the flame front propagation speed using PMTs. In flame turbulence study, the combustion process has been reconstructed and demonstrated using MART algorithm. The shape of

combustion wavefront has been reconstructed and discussed. The performance of combustion has been evaluated through analyzing of the reconstructed images. The recommendations of improving the system are suggested in further work as follows.

## 6.2 Further Work

The analysis of synchronized signals of engine combustion revealed the characteristics of flame front propagation in the time domain. The POET system presents a good performance for collecting and analyzing chemiluminescence signals. Since the special design of the OAG, the combustion process has been spatially covered mapped. Using the MART technique provides a relatively quick mathematic algorithm for flame simulation. However, the overall performance still has several major limitations.

1. The POET system is only designed for the response of signal intensity. During setups it may have operation errors. Thus, in further research, a pressure indicator and air-fuel accuracy mass sensor are suggested to add into the system for comparison and enhancing the system performance. A dynamometer is also needed for the calculation of engine heat release.
2. Current OAG is a fan beam projection design. However, in the measurement of flame front propagation, parallel beam projection has a better accuracy than fan beam projection. Therefore, parallel light beam projection OAG is advised to be redesigned for the precise measurement of flame front propagation velocity.

Nevertheless, the algorithm has to change for the new OAG design.

Table 6. 1The limitation of POET system and Recommendations of further works

	Limitation s of Current Project	Further Work Recommendations
Engine Modifications	Simple SI engine	The POET can be applied in other types of engine by different fuels
	Natural gas fuel	
	Inaccurate controller of air and fuel mixture intake	Digital scales of gas intake controller are necessary
	Only have PMT sensors to collect intensity signals	Need a pressure and a heat transfer sensor for the comparisons with Intensity results
	Engine running without Loads	Need a dynamometer to evaluate the system by different loads
OAG design	Only 40 channels and the reconstruct resolution is 5 mm × 5 mm.	More channels can be achieved but it will increase the cost of POET system.
	Fan beam projection design for receiving signals. It is inaccurate for the measurement of flame speed	Need parallel projection channels to reduce the errors of speed evaluation.
Algorithm	MART algorithm has errors during multiplication	LFBP-ART algorithm can improve the current algorithm and reduce errors

Thus, further work is needed on the engine modifications, OAG designs and the mathematical algorithm. The following sections are based on discussions for further work.

### **6.2.1 The Parallel Signal Collection Method and Radon Transform Algorithm in Application**

The POET system is a special design for flame front visualization that performs well in combustion reconstruction. However, the system can be improved to provide a greater accuracy. In combustion visualization presented in this thesis, the design of the OAG plate was based on fan beam Radon transform algorithm to collect signals. The fan beam approach provided good results because of its wide angular coverage range. The current OAG design and MART algorithm was found to have some limitations. Improvements to the system are discussed in the following sections.

### **Engine modification**

Further modifications are needed to the OHV gas engine used for the combustion experiments.

1. A high frequency pressure indicator needs to be added to monitor the variations of pressure of the flame front with engine performance.
2. The air intake system is controlled by the choke system. This does not control the air-fuel ratios accurately. Replacing the choke system by an air control valve will improve control of the air-fuel mix.

3. The system can be improved by connecting a generator to compare the flame front at different loads and find the relationship between heat releases and power outputs.
4. In further work, the 3D combustion visualization simulation can be achieved by utilizing 2D combustion visualization. Combustion in the engine can be identified layer by layer vertically. 3D simulation can be obtained by plugging optical fibres vertically into the side of the engine chamber. There are two methods of fibre plugging: a rough simulation plugging 4 more fibre probes on the side of engine. The 2D combustion reconstruction information is obtained at the first level. The 3D combustion can then be simulated using the additional intensity information from the different levels recorded by the other four fibres. The other method of 3D combustion simulation is complicated for the simulation algorithm. Flame front variation is generally caused by the spark ignition position. If the cylinder head of the engine could be rotated more intensity information could be obtained at the different levels by changing the spark ignition locations (Fig 6.1). However, 3D combustion is better simulated using the ART - Radon transform algorithm rather than the MART algorithm as discussed in the algorithm improvement part below.

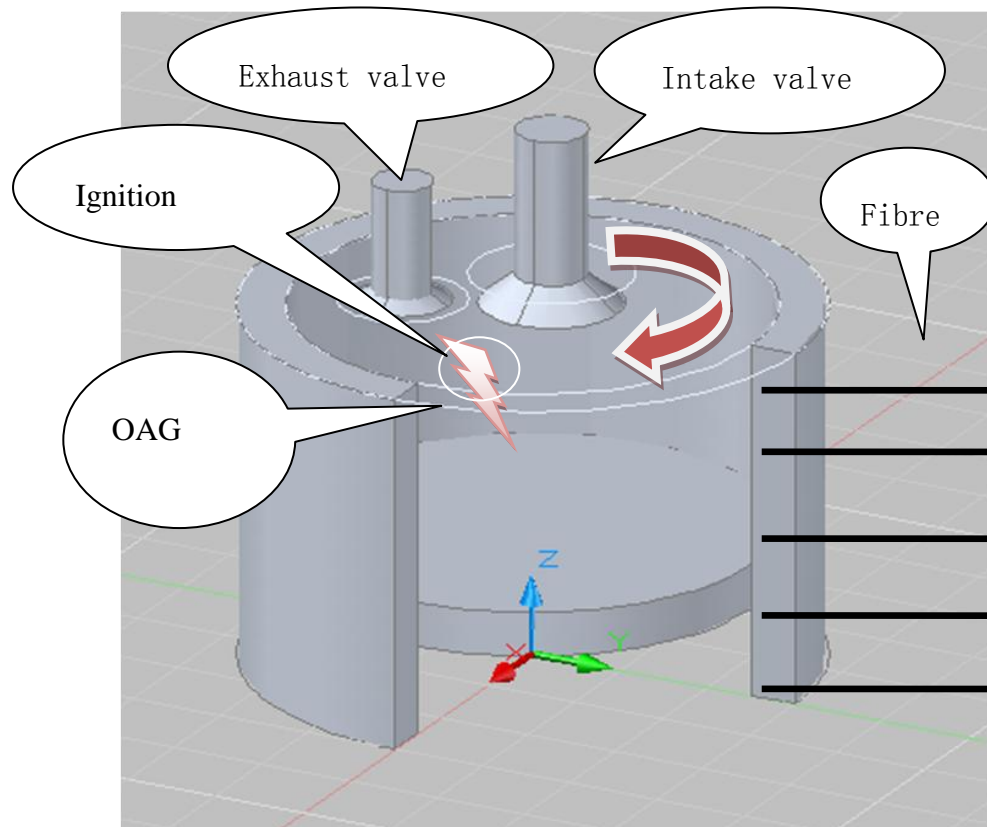


Figure 6. 6 3D Model Schematic for Combustion Simulation

## OAG kits promotions

The design of the OAG plate is critical to two aspects of the experiment: data collection for connecting the engine and the PMTs system; the other is relevant to the math algorithm of signal processing. Although the initial OAG plate design worked well, some improvements can be made to protect the system and improve the performance of POET system.

1. The system needs to be protected from high temperature damage. The alumina coat of optical fibres is connected to the lens using super glue. The unprotected fibres are easily damaged by high temperature. Two types of filters were

installed in front of the PMT sensors. A new OAG design with an O-ring filter placed in front the fibres to isolate them from combustion might improve performance (Figure 6.2). This design would also improve the accuracy of the system. The high pressure causes the OAG plate to deform. Then the observation apertures are changeable. In the new design, the pressure are afforded by the O-ring, thus the observation aperture is firmed.

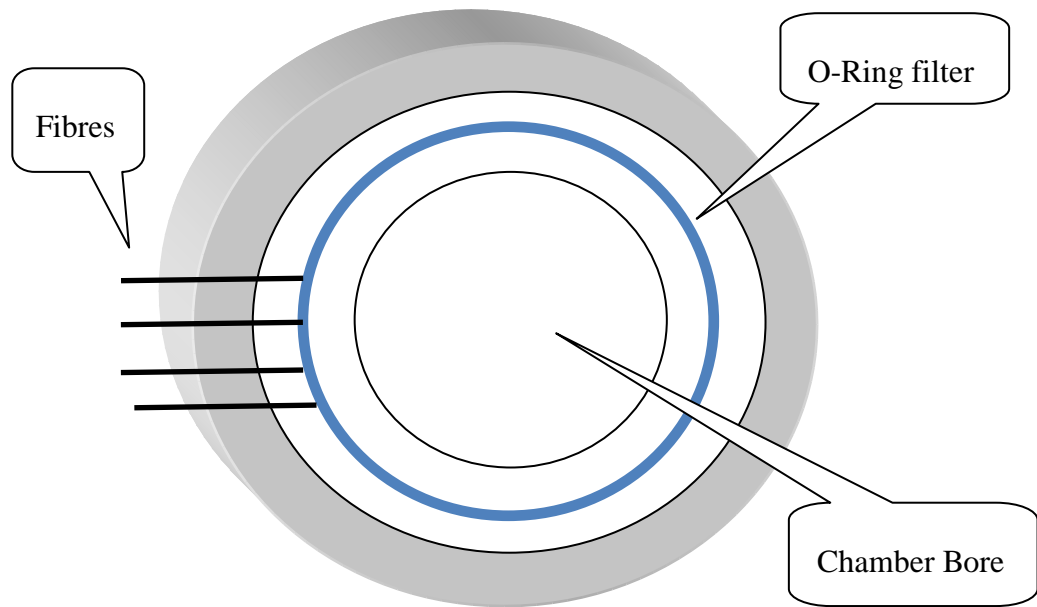


Figure 6. 7 O-Ring Filter OAG Plate Schematic Diagram

2. The POET system is based on a flame fan beam radiation design for detecting flame signals. The advantages of the fan beam system are that the fan beam covers the whole bore of engine combustion and the spatial resolution of the detection area is up to  $5\text{mm} \times 5\text{mm}$ . The disadvantages are that the system is less sensitive to the boundary of the bore and the system is influenced by the initialization of system since the detection areas overlapping. The system can

be altered using a parallel beam to collect signals of the flame radiations. As the structure diagram of parallel beam is shown in Figure 6.3, if the O-ring filter is coated with a special material the parallel flame can be focused on the fibre. Signal accuracy is improved because the parallel beam is independent with each other. When the group of five fibres is used the detection area is a square region compared with the fan beam crossing section in Figures 4.27 and 4.28. The new OAG design improves accuracy and reduces the computational time compared to the fan beam system. However, spatial resolution is reduced to  $6.4 \text{ mm} \times 6.4 \text{ mm}$ .

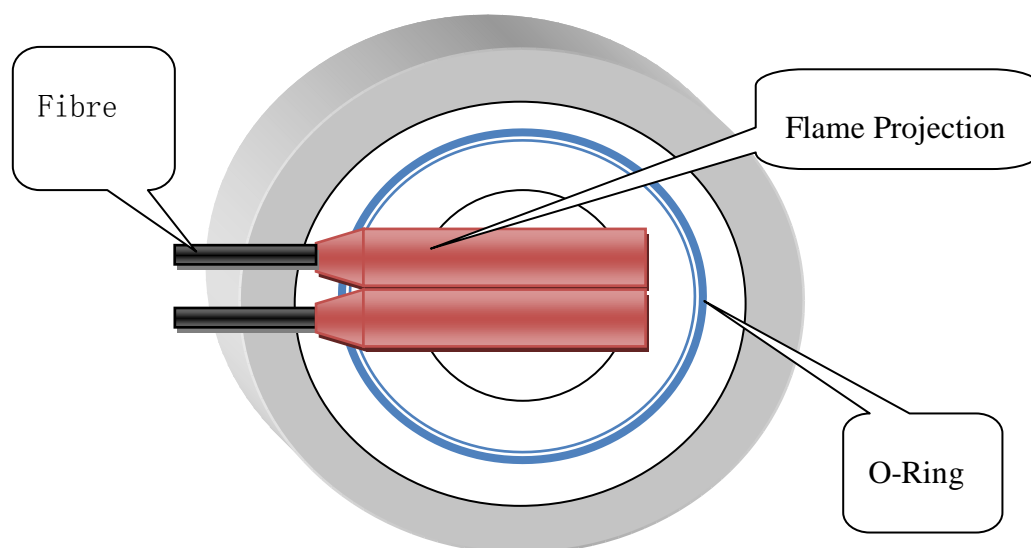


Figure 6. 8 Parallel Beam Detection Schematic Diagram

## Radon transform application in the system

The math methodology chapter covered the POET system algorithm was explained. The combustion reconstruction was based on the MART technique and the intensity interpolation method was adopted to estimate the flame intensity distributions.



The interpolation and iteration of the MART technique greatly improves the accuracy of the solution to an unknown flame function. The MART technique has two disadvantages. It is difficult to produce a collimated fan beam projection manually so that system operation errors are increased. Also the MART mathematics is not cross-correlated with other samplings. To overcome these problems, a parallel beam projection using the Radon transform technique is suggested for further work. Figure 6.3 shows the OAG has to be promoted by parallel beam projection design. The original OAG is designed by 45 degrees between each groups, the degrees has to be decreased to 20 degrees for better resolution with 5 fibres in each group. If the OAG was designed with 9 groups of 5 fibres the spatial resolution is increased to  $3\text{mm} \times 3\text{mm}$ . Using the Radon transform method the algorithm can be alternated to simulate the function with a large number of samplings using the least square rule. This could provide a better model for unknown functions for observing the variety of intensity distributions.

### **6.2.2 Tomography System Update Using Shack-Hartmann Cameras**

In the POET tomography system the MART technique is used to find an approximate function for an unknown flame model. Shack Hartmann cameras can be used to directly capture the image of chemiluminescence phenomenon to study the flame and reconstruct the combustion image.

Shack-Hartmann cameras have hundreds of lens arrays and each lens is very small. The camera is very sensitive to density gradients in great turbulence. The Shack-Hartmann is well suited to study high turbulence combustion in the time and spatial domains. The experiment is undertaken for research flame and the theoretical test has been done and mentioned in chapter 2. The purpose of employing Shack-Hartmann cameras is going to implement a tomography system to study flame front propagations. The description of setting up is in schematic diagram 6.4 and 6.5.

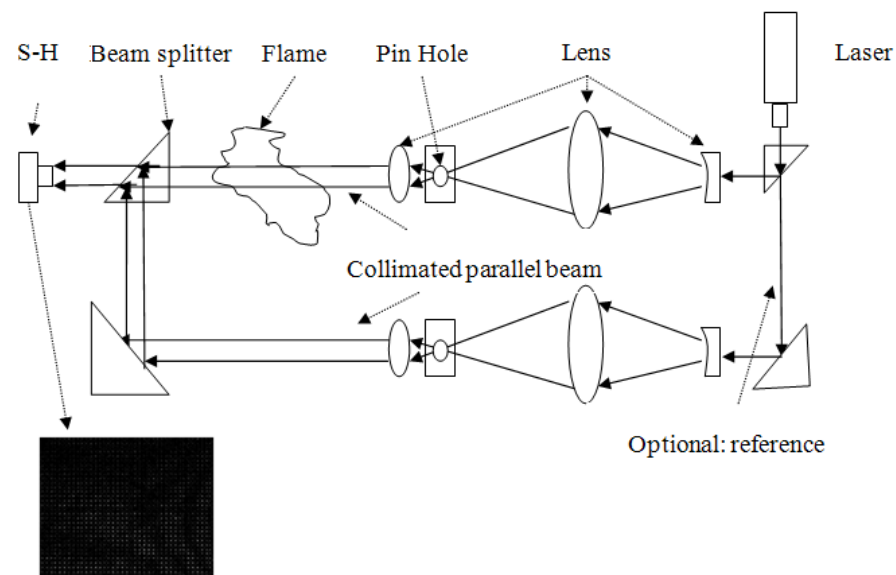


Figure 6. 9 Flame Front Study System by Employing Shack-Hartmann Camera

The system uses a collimated parallel light to cross the object density region (Figure 6.9). The S-H camera captures the small aberrations caused by density changes that represent the flame front behavior. To measure the phase shifts, a reference beam is added to the system to construct the interferometric images of the flame phase shifts. If several S-H cameras are used, the combustion models can be simulated using tomographic algorithm (Fig 6.10). The POET system is a reference to setup the S-H

cameras tomography.

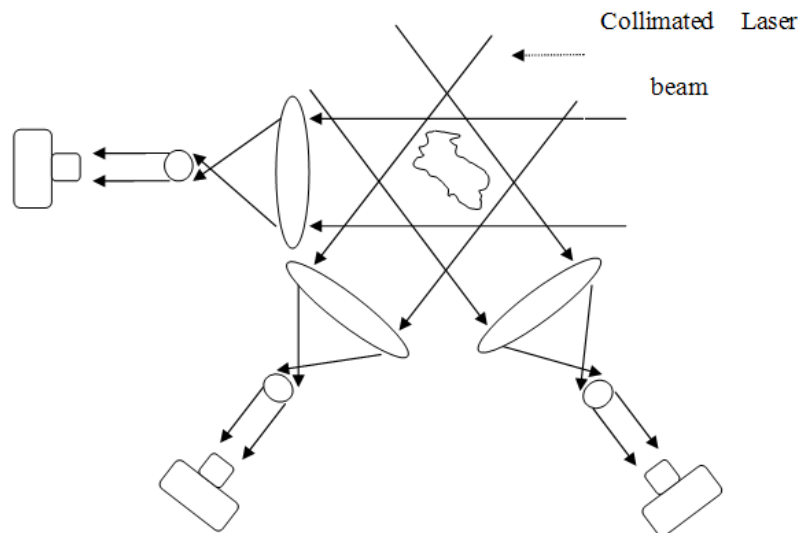


Figure 6. 10 Tomography Schematic Diagram of Shack-Hartmann Method

The S-H system combines qualitative and quantitative measurements for flame study. The system presents direct visualization of the object and using S-H cameras enable the details of aberrations to be obtained. However, the S-H camera is very expensive and modification of the engine is more complicated.

## Reference

- [1] P. Bryanston-Cross, M. Burnett, B. Timmerman, P. Dunkley and W.K. Lee, "Intelligent Diagnostic Optical for Flow Visualization," in *Optics & Laser Technology*, vol. 32, pp. 641-654, 2000.
- [2] N. Docquier and S. Candel, "Combustion control and sensors: a review," in *Progress in Energy and Combustion Science*, vol. 28, pp. 107-150, 2002.
- [3] P. Dunkley, "The investigation and application of OET (optical emission tomography) as a combustion diagnostic," in *PhD thesis of Warwick University*, 2002.
- [4] S.B. Kumar and M.P. Dudukovic, "*Chapter 2 - Computer assisted gamma and X-ray tomography: Applications to multiphase flow systems*," USA: St. Louis, 1997.
- [5] H.S. Koa, S.S. Ahnb and H.J. Kimc, "Measurement of impinging butane flame using combined optical system with digital speckle tomography," in *Optics and Lasers in Engineering*, vol. 49, pp. 1320-1329, 2011.
- [6] H.M. Hertz, "Experimental determination of 2-D flame temperature fields by interferometric tomography," in *Optics Communications*, vol. 54, pp. 131-136, 1985.
- [7] S.N. Soid and Z.A. Zainal "Spray and combustion characterization for internal combustion engines using optical measuring techniques e A review," in *Energy*, vol. 36, pp. 724-741, 2011.
- [8] W. Demtroder, *Laser Spectroscopy: Basic Concepts and Instrumentation*, 3 ed., Germany: Springer, 2002.
- [9] T. Vo-Dinh and D. Eastwood, *Laser techniques in luminescence spectroscopy*, Chelsea: MI, 1990.
- [10] Z. Huang, L. Jin, J.C. Sanders, Y. Zheng, C. Dunsmoor, H. Tian and JP. Landers, "Laser-induced fluorescence detection on multichannel electrophoretic microchips using microprocessor-embedded acousto-optic laser beam scanning," in *IEEE Trans Biomed Eng*, vol. 49, pp. 859-866, 2002.

- [11] S. Kostka, S. Roy, P.J. Lakusta, T.R. Meyer, M.W. Renfro, J.R. Gord and R. Branam, "Comparison of line-peak and line-scanning excitation in two-colour laser-induced-fluorescence thermometry of OH," in *APPLIED OPTICS*, vol. 48, pp. 6332-6343, 2009.
- [12] P.G. Aleiferis and M.F. Rosati, "Flame chemiluminescence and OH LIF imaging in a hydrogen-fuelled spark-ignition engine," in *International Journal of Hydrogen Energy*, vol. 37, pp. 1797-1812, 2012.
- [13] N.T. Nguyen and S.T. Wereley, *Fundamentals and applications of micro fluidics*. USA: Norwood, 2002.
- [14] P.A. Lebbin, "Experimental and numerical analysis of air, tracer gas, and particulate movement in a large eddy simulation chamber," in *PhD dissertation of Kansas State University*, 2006.
- [15] J.H. Li, "Characterization of Flow, Particles and Interfaces," in *Advances in Chemical Engineering, Volume 37*, pp 1-287, UK: Elsevier Inc., 2009.
- [16] J. Wang, "A new velocimetry algorithm for optimizing ultrasonic PIV imaging method," in *Information Technology and Applications in Biomedicine conference*, pp. 164-166, 2008.
- [17] P.S. Greenberg and M.P. Wernet, "Quantitative velocity field measurements in reduced-gravity combustion science and fluid physics experiments," in *Proceedings of the 16th IEEE Instrumentation and Measurement Technology Conference, Vols. 1-3*, pp. 391-396, 1999.
- [18] M. Reeves, D.P. Towers, B. Tavender and C.H. Buckberry, "A high-speed all-digital technique for cycle-resolved 2-D flow measurement and flow visualisation within SI engine cylinders," in *Optics and Lasers in Engineering*, vol. 31, pp. 247-261, 1999.
- [19] B. Peterson, D. L. Reuss, and V. Sick, "High-speed imaging analysis of misfires in a spray-guided direct injection engine," in *Proceedings of the Combustion Institute*, vol. 33, pp. 3089-3096, 2011.
- [20] C.J. Sung, J.S. Kistler, M. Nishioka and C.K. Law, "Further studies on effects of thermophoresis on seeding particles in LDV measurements of strained flames," in *Combustion and Flame*, vol. 105, issues 1-2, pp 189-201, 1996.

- [21] C. Appel, J. Mantzaras, R. Schaeren, R. Bombach and A. Inauen, "Turbulent catalytically stabilized combustion of hydrogen/air mixtures in entry channel flows," in *Combustion and Flame*, vol. 140, pp 70-92, 2005.
- [22] B.K. McLain, *Application of Laser Doppler Velocimetry and Particle Image Velocimetry to the Hydrodynamic Investigation of Three-phase Fluidized Beds*. USA: Ohio State University, 2000.
- [23] T.O.H Charrett and R.P Tatam, "Single camera three component planar velocity measurements using two-frequency planar Doppler velocimetry (2 v - PDV)," in *Meas. Sci. Technol.*, vol. 17, pp 1194-1206, 2006.
- [24] C. Willert, I. Roehle, R. Schodl, O. Dingel and T. Seidel, "Application of planar doppler velocimetry within piston engine cylinders," in *11<sup>th</sup> International Symposium on Applications of Laser Techniques to Fluid Mechanics*, vol. 8-11, pp 38-2, 2002.
- [25] A. Omrane, G. Juhlin, M. Alden, G. Josefsson, J. Engström and T. Benham, "Demonstration of two-dimensional temperature characterization of valves and transparent piston in a GDI optical engine," in *SAE Technical Papers*, vol. 2004-01-0609, 1994.
- [26] C. Robert, *X-Ray Computed Tomography in Biomedical Engineering*. London: Springer, 2011.
- [27] H.B. Jiang, *Diffuse optical tomography: principles and applications*. Boca Raton: CRC 2011.
- [28] P. Gall, "Review of laser scanning tomography in S, Sn and Fe doped InP and study of scattering defects in Fe doped InP," in *Indium Phosphide and Related Materials*, pp. 73-76, 1993.
- [29] G. Gilabert, G. Lu and Y. Yan, "Three-dimensional tomographic reconstruction of the luminosity distribution of a combustion flame," in *IEEE TRANSACTIONS ON INSTRUMENTATION AND MEASUREMENT*, vol. 56, pp. 1300-1306, Aug 2007.
- [30] P. Wright, C. A. Garcia-Stewart, S. J. Carey, F. P. Hindle, S. H. Pegrum, S. M. Colbourne, P. J. Turner, W. J. Hurr, T. J. Litt, S. C. Murray, S. D. Crossley, K.B. Ozanyan and H. McCann, "Toward in-cylinder absorption

tomography in a production engine," in *APPLIED OPTICS*, vol. 44, pp. 6578-6592, Nov 1 2005.

- [31] P. Wrighta, N. Terzijaa, J.L. Davidsona, S. Garcia-Castilloa, C. Garcia-Stewart, S. Pegrumb, S. Colbourneb, P. Turnerb, S.D. Crossley, T. Littc, S. Murrayc, K.B. Ozanyana and H. McCanna, "High-speed chemical species tomography in a multi-cylinder automotive engine," in *Chemical Engineering*, vol. 158, pp. 2-10, 2010.
- [32] N.B. Anikin, R. Suntz and H. Bockhorn, "2-D Tomographic Reconstruction of Instant OH – Chemiluminescence Distributions in Turbulent Flames," in *Chia Laguna, Cagliari, Sardinia, Italy*, 2011.
- [33] J.M. Desse and R. Deron, "Shadow, Schlieren and Colour Interferometr," in *Optical diagnostics of Flows*, vol.1, The Onera Journal Aerospace lab, 2009.
- [34] P. Krehl and S. Engemann, "Toepler, August - the First Who Visualized Shock-Waves," in *Shock Waves*, vol. 5, pp. 1-18, Jun 1995.
- [35] F. Gires and P. Tournois, "Interféromètre utilisable pour la compression d'impulsions lumineuses modulées en fréquence," in *Comptes Rendus de l'Académie des Sciences de*, vol. 258, pp. 6112–6115, 1964.
- [36] M.V. Klein and T.E. Furtak, *Optics*. New York: John Wiley & Sons, 1986.
- [37] X.B. Zou, Z.G. Mao, X.X. Wang and W.H. Jiang, "Two different modes of wire explosion for nano-powder production," in *EPL (Europhysics Letters)*, vol. 97, 2012.
- [38] J.M. Desse, "Recent contribution in colour interferometry and applications to high-speed flows," in *Optics and Lasers in Engineering*, vol. 44, pp. 304-320, 2006.
- [39] G. Dennis, "A new microscopic principle," in *Nature*, vol. 161, pp. 777-778, 1948.
- [40] D. Gabor, "Microscopy by reconstructed wavefronts," in *Proceedings of the Royal Society* vol. 197, pp. 454–487, 1949.

- [41] Y.N. Denisyuk, "On the reflection of optical properties of an object in a wave field of light scattered by it," in *Doklady Akademii Nauk SSSR*, vol. 144, pp. 1275–1278, 1962.
- [42] J.C. Robert, B.B. Christoph and H.L. Lawrence, *Optical Holography*. New York and London: Academic Press.
- [43] H.J. Tung, L.F. College and L.F. Illinois, "Basic Principles and Applications of Holography," in *Fundamentals of Photonics Module* vol. 1, p. 10, 1999.
- [44] K.S. Chana, T.S. Wilson, P. Bryanston-Cross and M. Burnett, "High Bandwidth Heat Transfer Measurements in an Internal Combustion Engine under Low load and Motored Conditions," in *Heat Transfer and Cooling in Propulsion and Power Systems*, AGARD, Norway, 2001.
- [45] D. Maurice, *Scientific Instruments of the Seventeenth and Eighteenth Centuries and Their Markers*, Portman Books, London, 1989.
- [46] J.B. Heywood, *Internal Combustion Engine Fundamentals*. New York: McGraw-Hill 1988.
- [47] E.F. Ober, *Internal Combustion Engines and Air Pollution, Chap. 2*. New York: Intext Educational 1973.
- [48] Alfred Gordon Gaydon, *The Spectroscopy of Flames*. London, UK: Chapman and Hall, 1957.
- [49] C.K. Law, *Laminar premixed flames*. England: Cambridge University Press, 2006.
- [50] K.T. Walsh, M.B. Long, M.A. Tanoff and M.D. Smooke, "Experimental and Computational Study of CH, CH\* and OH\* in an Axisymmetric Laminar Diffusion Flame," in *Twenty-Seventh Symposium (International) on Combustion, The Combustion Institute*, 1998.
- [51] Z.S. Li, B. Li, Z.W. Sun, X.S. Bai and M. Aldén, "Turbulence and Combustion Interaction: High Resolution Local Flame Front Structure Visualization using Simultaneous Single-Shot PLIF Imaging of CH, OH, and CH<sub>2</sub>O in a Piloted Premixed Jet Flame," in *Combustion and Flame*, vol. 157 2010.



- [52] P.S. Kothnur, M.S. Tsurikov, N.T. Clemens, J.M. Donbar and C.D. Carter, "Plane Imaging of CH, OH, and Velocity in Turbulent Non-premixed Jet Flames," *Proceedings of the Combustion Institute*, vol. 29, pp. 1921-1927, 2002.
- [53] J.Y. Hwang, Y.S. Gil, J.I. Kim, M. Choi and S.H. Chung, "Measurements of temperature and OH radical distributions in a silica generating flame using CARS and PLIF," in *Journal of Aerosol Science*, vol. 32, pp. 601-613, May 2001.
- [54] H.N. Najm, P.H. Paul, C.J. Mueller and P.S. Wyckoff, "On the adequacy of certain experimental observables as measurements of flame burning rate," in *Combustion and Flame*, vol. 113, pp. 312-332, 1998.
- [55] J. Kiefer, Z. S. Li, J. Zetterberg, X. S. Bai and M. Alden, "Investigation of local flame structures and statistics in partially premixed turbulent jet flames using simultaneous single-shot CH and OH plane laser-induced fluorescence imaging," in *Combustion and Flame*, vol. 154, pp. 802-818, Sep 2008.
- [56] "R80900-00-C12 specification form," in *Photomultiplier Tubes: Basics and Applications*, 3th ed, Hamamatsu Photonics K.K, 2006.
- [57] "PMT Handbook.", Hamamatsu Photonics K.K.
- [58] Z.V. Vardeny, "Telecommunications: A Boost for Fibre Optics," in *Nature*, vol. 416, pp. 489–491, 2002.
- [59] C. Richard and H. David, "Methods of Mathematical Physics," in *Wiley-Interscience*, vol. 2, 1962.
- [60] H.T. Davis and K.T. Thomson, *Linear algebra and linear operators in engineering with applications in Mathematica*: Academic Press, 2000.
- [61] P. Dirac, *Principles of quantum mechanics*, 4th ed.: Oxford at the Clarendon Press.
- [62] S. Elias and W. Guido, *Introduction to Fourier Analysis on Euclidean Spaces*: Princeton University Press, 1971.

- [63] L. Henri, *Leçons sur l'intégration et la recherche des fonctions primitives*. Paris: Gauthier-Villars, 1904.
- [64] S.R. Deans, *The Radon Transform and Some of Its Applications*. New York: John Wiley & Sons, 1983.
- [65] Y.C. Wei, G. Wang and J. Hsieh "An intuitive discussion on the ideal ramp filter in computed tomography (I)," in *Computers & mathematics with applications*, vol. 49, pp. 731-740, 2005.
- [66] P. Munshi, "Error analysis of tomographic filters. I: Theory," in *NDT & E international*, vol. 25, pp. 191-194, 1992.
- [67] I.A. Hazou and D.C. Solmon, "Filtered-backprojection and the exponential Radon," in *Journal of Mathematical Analysis and Applications*, vol. 141, pp. 109-119, 1989.
- [68] C. Nguyen and T.S. Huang, "Image blurring effects due to the depth discontinuities: blurring that creates emergent image details," in *Image and Vision Computing*, vol. 10, pp. 689-698, 1992.
- [69] R. Hartley, "A Gaussian- weighted multiresolution edge detector," *Computer Vision, in Graphics and image Processing*, vol. 30, pp. 70-83, 1985.
- [70] R.N. Bracewell, *The Fourier transform and its applications*, 2 ed.: McGraw-Hill Press, 1986.
- [71] B.V. Khvedelidze, *Hilbert transform*. Hazewinkel: Springer Press, 2001.
- [72] F.W. King, *Hilbert transforms*. Cambridge: Cambridge University Press, 2009.
- [73] G.L. Zeng, *Medical Image Reconstruction*: Higher Education Press, 2010.
- [74] A.M. MATHAI, "Jacobians of Matrix Transformation and functions of Matrix Argument," in *World Scientific Pub Co Inc Press*, 1997.
- [75] A.C. Kak and M. Slaney, *Principles of Computerized Tomographic Image*: IEEE Press, 1988.

- [76] A.C. Kak and M. Slaney, *Principles of Computerized Tomographic Imaging chapter 3*: Society of Industrial and Applied Mathematics Press, 2001.
- [77] Beer, "Determination of the absorption of red light in coloured liquids," in *Annalen der Physik und Chemie*, vol. 86, pp. 78-88, 1852.
- [78] J.R. Brock, "A note on the Beer-Lambert Law," in *Analytica Chimica Acta*, pp. 95-97, 1962.
- [79] H. Inomata, Y. Yagi, M. Saito and S. Saito, "Density dependence of the molar absorption coefficient-Application of the beer-lambert law to supercritical CO<sub>2</sub>-Naphthalene mixture," in *The journal of supercritical fluids*, vol. 6, pp. 237-240, 1993.
- [80] G. Tomasi and R. Bro, "Multilinear Models: Iterative Methods," in *Comprehensive chemometrics*, pp. 411-451, 2009.
- [81] B.D. Ripley and M.D. Kirkland, "Iterative simulation methods," in *Journal of Computational and applied Mathematics*, vol. 31, pp. 165-172, 1990.
- [82] O. Axelsson, "A class of iterative methods for finite element equations," in *Computer methods in Applied Mechanics and Engineering*, vol. 9, pp. 123-137, 1976.
- [83] G.T. Herman and A. Lent, "Iterative reconstruction algorithms," in *Computers in Biology and medicine*, vol. 6, pp. 273-294, 1976.
- [84] P.P.B. Eggefont, G.T. Herman and A. Lent, "Iterative algorithms for large partitioned linear systems, with applications to image reconstruction," in *Linear Algebra and its Applications*, vol. 40, pp. 37-67, 1981.
- [85] J.G. Colsher, "Iterative three-dimensional image reconstruction from tomographic projections," in *Computer Graphics and Image Processing*, vol. 6, pp. 513-537, 1977.
- [86] E.A. Korany, "Implementation and performance study of a generalized iterative algorithm for image reconstruction from the Hartley transform intensity," in *Pattern Recognition Letters*, vol. 14, pp. 771-780, 1993.

- [87] R. Gordon, R. Bender and G.T. Herman, "Algebraic reconstruction techniques (ART) for threedimensional electron microscopy and x- ray photography," in *Journal of Theoretical Biology*, vol. 29, pp. 471-481, 1970.
- [88] G.D. Colquhoun and R. Gordon, "The Use of Control Angles with MART (Multiplicative Algebraic Reconstruction Technique)," in *Technology in Cancer Research & Treatment*, vol. 4, pp. 183-192, 2004.
- [89] S.Sivakumar, M.C. Krishna and R. Murugesan, "Evaluation of Algebraic Iterative Algorithms for Reconstruction of Electron Magnetic Resonance Images," in *ICVGIP*, p. 353, 2004.
- [90] D.R. Neal, "Shack-Hartmann Wavefront Sensor testing of Aero-optic Phenomena," in *American Institute of Aeronautics and Astronautics*, 1998.
- [91] R. Navarroa, R. Riveraa and J. Aportab, "Representation of wavefronts in free-form transmission pupils with Complex ZernikePolynomials," in *Journal of Optometry*, vol. 4, pp. 41-48, 2011.
- [92] D. Malacara and V.N. Mahajan, "*chapter 13 ZernikePolynomial and Wavefront Fitting*," in *Optical Shop Testing*. New York: John Wiley & Sons, 2007.
- [93] Y. Huang and V. Yang, "Effect of swirl on combustion dynamics in a lean-premixed swirl-stabilized combustor," in *Proceedings of the combustion institute*, vol. 30, pp. 1775-1782, 2005.
- [94] D.M. Kang, F.E.C. Culick and A. Ratner, "Combustion dynamics of a low-swirl combustor," in *Combustion and flame*, vol. 151, pp. 412-425, 2007.
- [95] E.M., I.T.Fok, D.T.Gilks, J.Murray, D.Greenshields, G.P.Thomas, S.J.Horton, "MEng Report," 2002.

# Appendix Figure List

Figure App. 1 Comparison between laminar flame front and turbulent flame front .....	253
Figure App. 2 Different Surfaces of Benson Burner Flame .....	255
Figure App. 3 Particles Tracks of Methane-Air Flame [11].....	257
Figure App. 4 Large eddy simulation of a turbulent diffusion flame [12] .....	258
Figure App. 5 A Piece of Cone Flame Front .....	260
Figure App. 6 Detonation Process of explosive cartridge [30] .....	263
Figure App. 7 Rankine - Hugoniot Curve [31] .....	265
Figure App. 8 A Direct Photograph of Detonation Wave [35] .....	266
Figure App. 9 Spinning Detonation [36].....	267
Figure App. 10 A sinuous signal transmission representation in different domains. .....	269
Figure App. 11 Different frequency signals behaviour in spatial and frequency domains. Where (a) is a signal decomposed into three different frequencies; (b) is the composed signal from (a) and (c) is the frequencies distribution of a different signal.....	271
Figure App. 12 Fourier Slice theorem diagram.....	273
Figure App. 13 Image transform by FFT function in Matlab.....	274
Figure App. 14 FS-105 module (a) and WFS150C (b) module .....	277
Figure App. 15 The setup for measuring the flame wavefront.....	278

Figure App. 16 Turbulence flow generators.....	279
Figure App. 17 Single shot of spot field .....	280
Figure App. 18 Three orders of incoming beam .....	281
Figure App. 19 Beamview in pupil function .....	281
Figure App. 20 Comparison between reference spot intensity and flame intensity. .....	282
Figure App. 21 Diffraction illustration diagram.....	283
Figure App. 22 Spots diffractions on varying orders. ....	283
Figure App. 23 Candle flame .....	284
Figure App. 24 Premixed Burner flame .....	284
Figure App. 25 Methane Air premixed Gas flow (not burning).....	285
Figure App. 26 Special element Helium gas flow detecting. ....	285
Figure App. 27 Heat release turbulence measurement using Heatgun.....	286
Figure App. 28 Turbulence difference at different times .....	287
Figure App. 29 3D mesh of wavefronts of varying objects. ....	288
Figure App. 30 Biggs and Stratton OHV 206 pro engine .....	290
Figure App. 31 Briggs and Stratton Engine schematic diagram .....	293
Figure App. 32 Engine power specification .....	293
Figure App. 33 Safe guild operations.....	294
Figure App. 34 Schematic diagram of OAG base .....	295
Figure App. 35 Schematic diagram of OAG cover .....	296

Figure App. 36 3D models of OAG .....	297
Figure App. 37 Modified Engine Assembly.....	298
Figure App. 38 Compacted PC module.....	299
Figure App. 39 40 channels of sensitivity adjusting .....	300
Figure App. 40 External analogs input.....	300
Figure App. 41 Tomographic PMT acquisition interface.....	301
Figure App. 42 Scan Interval .....	303
Figure App. 43 PMTs tomography computer system hardware components .....	308
Figure App. 44 Spectrum meter for system calibrations.....	309
Figure App. 45 Intensity plots comparison between 2 voltages and 5 voltages..	310
Figure App. 46 Comparison between unfiltered and filtered signals.....	312
Figure App. 47 System configuration panel.....	313
Figure App. 48 Array fibre Settings .....	314
Figure App. 49 Array Parameters Settings .....	315
Figure App. 50 Sensitivity graph .....	315
Figure App. 51 Reconstruction Setting .....	316
Figure App. 52 Convergence of system in 1000 iterations .....	316
Figure App. 53 Image reconstruction graph.....	317
Figure App. 54 Testing mode panel .....	318
Figure App. 55 Certainty test panel.....	319
Figure App. 56 Certainty test of the sample model.....	319

Figure App. 57 Noise testing panel .....	320
Figure App. 58 Varying noises testing on a sample signal.....	320
Figure App. 59 B440 Blue Filter Specification Diagram.....	323
Figure App. 60 U340 UV Filter Specification Diagram .....	324
Figure App. 61 Generator.....	325



# Appendix A: Relevant Background Reviews

Flame velocity as a second significant marker of flame can be defined as the velocity of combustion propagation in the direction of explosion kernel to wavefront surface. Whereas combustion wave propagation is present the behaviors of flame front to understand the performance of combustion in burning ratio, explosion location, density distribution. During normal combustion of the engine, the flame starts burning at the ignition point and spreads from the burned region to the unburned region. Thus, a combustion wave front moves from the burned to the unburned medium. This flame is known as a 'deflagration' flame. It contains laminar and turbulent flames. It is a subsonic laminar flame that propagates smoothly layer by layer (Fig App1 a). Under abnormal combustion conditions unburned gas is left beyond the boundary of flame front due to heat and pressure transitions. The explosion beyond the flame front is known as 'detonation' flame and is a supersonic wave. This super turbulent flame is more random and dependent on the density distribution of the gas flow and detonation occurring. Measurements of flame velocity are commonly based on laminar flame and normal turbulence flame analysis. Since the adverse detonation flame is a supersonic combustion wave which caused damage to the internal engine but with great energies, some researchers are interested in the high burning efficiency of detonation. Thus a pulse detonation engine (PDE) is being developed to utilize detonation flame power [1]. In this section, the combustion wave velocity measurements will be reviewed for

(a)

(b)

## Laminar flame velocity

$$R_e = \frac{\rho v L}{\mu} = \frac{v L}{V}$$

253

- $v$  is the mean velocity of the object relative to the fluid (m/s);
- $L$  is a characteristic linear dimension. (m);
- $\mu$  is the dynamic viscosity of the fluid ( Pa \* s or N \* s/m<sup>2</sup> or kg/(m \* s);
- $\nu$  is the kinematic viscosity (m<sup>2</sup>/s) ;
- $\rho$  is the density of the fluid ( kg/m<sup>3</sup>) ;

In analyzing fluid flow dynamics, there are many techniques available to measure the speed and structure of laminar premixed flames [4-8]. Five typical methods for experimental measurement of laminar flame were considered.

#### 1. Bunsen burner methods

Bunsen burner flame is a typical diffusion flame. The flame is relatively clean and high temperature. The formula for measurement of flame velocity is:

$$S_L = V_t \frac{A_t}{A_f}$$

(App.1-2)

Where  $S_L$  is laminar flame velocity;  $V_t$  is the average flow velocity in burner tube;  $A_t$  is the tube area;  $A_f$  is surface area of inner cone. Burner methods are easy to experiment with at various temperatures. Disadvantages are that the interface between the flame and surrounding atmosphere changes the fuel-air ratio; velocity measurement in a vessel is difficult and the low accuracy of the velocity measurements in the experiment.

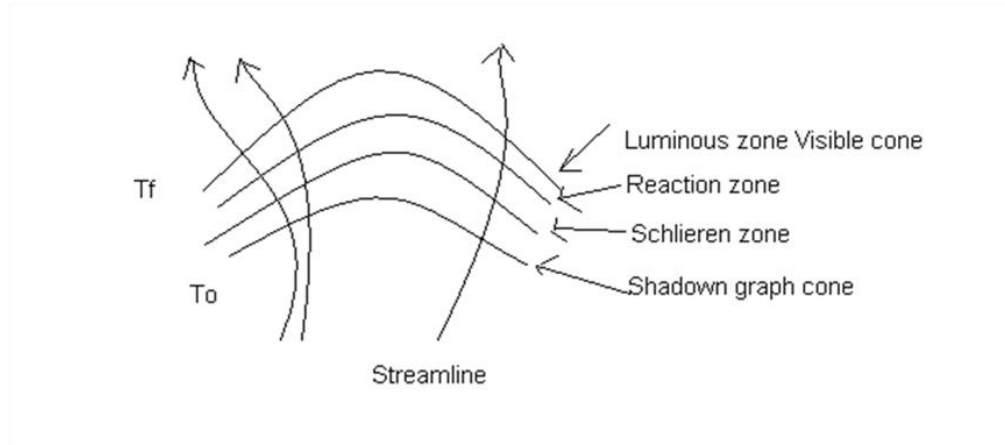


Figure App. 2 Different Surfaces of Benson Burner Flame

## 2. Transparent-tube method

A transparent tube is filled with a homogenous gas and ignited from one side of the tube. The burning flame spreads from one side of the tube to the other. To measure the mass flow rate a soap bubble is applied to the output surface of the tube. The velocity formula is:

$$S_L = (V_0 - V_g) \frac{A_t}{A_f}$$

(App.1-3)

Where  $V_0$  is the linear uniform velocity of flame;  $V_g$  is the velocity of unburned gas beyond the flame front.  $A_t$  is the tube area;  $A_f$  is bubble surface area. Generally, the result using the transparent tube is similar to that for the Benson Burner.

## 3. Closed Spherical Bomb method

A rigid spherical vessel filled with premixed gas is ignited from the center of the vessel. The burning gas spreads from the center to the edge of the vessel increasing the pressure and temperature. The velocity of flame is:

$$S_L = \left(1 - \frac{R^3 - r^3}{3p\gamma_\mu r^2}\right) \frac{dp}{dr} \frac{dr}{dt}$$

(App.1-4)

Where

- $\gamma_\mu \equiv \frac{c_p}{c_v}$  (unburned gas)
- $p$  = pressure at time  $t$
- $R$  = sphere radius
- $r$  = instantaneous radius of spherical flame

This method assumes absolute equilibrium behind the flame front and no heat losses in the combustion process. Normally the calculated value is less than the actual value.

#### 4. Particle tracking method

The particle method was developed to overcome the difficulty of measuring a curved flame front. The combustible gas is premixed with small solid particles. The particles in the gas stream will be illuminated with the flow of the flame front. Photographs of the particles show the direction of the flame front and the velocity can be calculated. However, the induced particles may affect flame front behavior and their large size gives rise to errors in measuring velocity. The photograph (Fig App.3) shows a laminar premixed methane-air flame using the particle track method. The flame streamline is shown by the green light particle tracks from MgO particles scattered in the flow.

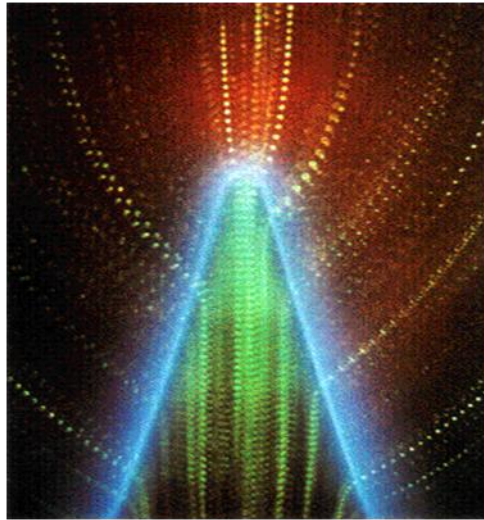


Figure App. 3 Particles Tracks of Methane-Air Flame [11]

Since the laminar flame is uniform without turbulences, the flame front velocities are easy to measure. However, most flames are turbulent, especially inside an engine. Thus, to find a solution of turbulent speed measurement is important. By comparison, the particles tracing method is present more accuracy results of laminar flame propagations. Furthermore, it also has been applied in turbulent flame measurements, for instant PIV [9, 10]. But It has been abandoned in this project due to the particles may damage the engine and alter the performance of engine.

## **Turbulence flame velocity**

Compared to laminar flames, turbulence flames are more complicated. In turbulent flow, the flame is unstable with random wrinkles. The varying wavefront surfaces are difficult to locate. The reaction region of the turbulent flame wavefront is much thicker than that for laminar flame. Many researchers are interested in the theoretical study of the relationship between turbulence and flame velocity. Theoretical

research is continuing into the random character of turbulence flame. Figure App.4 is a simulated image based on the understanding of turbulence flame structure. Many researchers have found that the speed of turbulent flame is far greater than laminar speed and that the velocity increased with Roynolds number.

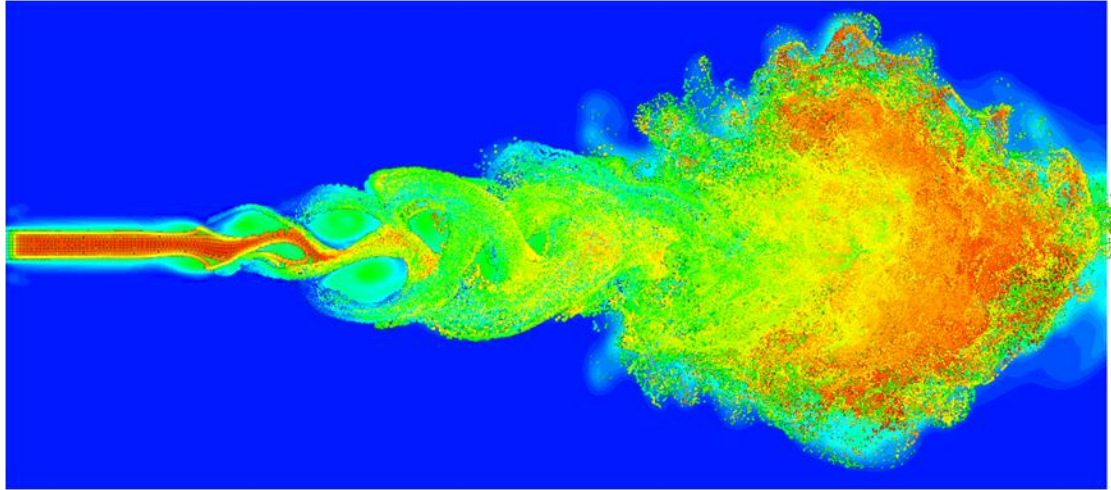


Figure App. 4 Large eddy simulation of a turbulent diffusion flame [12]

Damkohler [13] was the first researcher to attempt to measure the turbulence flame front velocity. He found that turbulence affected the velocity and measured the flame speed both theoretically and experimently in 1940. He used a Bunsen burner to measure the flame speed at various Reynolds numbers and suggested that:

- When  $Re \lesssim 2300$ , the turbulence flame velocity is independent of Reynolds number;
- When  $2300 \lesssim Re \lesssim 6000$ , i.e. small scale turbulence, the speed is proportional to the square root of the Reynolds number;
- When  $Re \gtrsim 6000$ , i.e. large scale turbulence, the speed is proportional to the Reynolds number.

Analytic geometry can be used to analyze the turbulent flame propagation speed.

Damkohler stated that the small scale turbulence simply increases the transport properties. Hence, the turbulence flame speed  $S_T$  is:

$$\frac{S_T}{S_L} \approx \left(\frac{\nu_T}{\nu}\right)^{1/2} \quad (\text{App.1-5})$$

Where  $\frac{\nu_T}{\nu} \approx 0.01Re$  in a pipe flow. Therefore,

$$\frac{S_T}{S_L} \approx 0.1Re^{1/2} \quad (\text{App.1-6})$$

On a large scale, turbulence eddies are larger than the depth of the flame front. However large eddies do not increase the diffusivities compared to that found in small scale turbulence. But the flame front area of the tube is increased. The large scale speed is:

$$\frac{S_T}{S_L} \propto \text{area} \propto \nu_T \propto Re \quad (\text{App.1-7})$$

Since  $S_T$  is a constant speed, thus the equation can be written:

$$S_T = A Re + B \quad (\text{App.1-8})$$

In 1943 Schelkin [14] considered that the time element is also important to turbulence. He assumed that the turbulence surfaces are distorted into cones (Fig App.5) that are proportional to the square of the average eddy diameter  $l'$ .



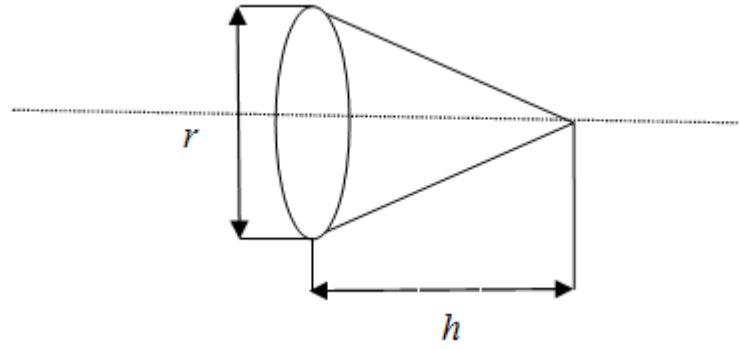


Figure App. 5 A Piece of Cone Flame Front

The volume of the cone is:

$$A_c = A_b \left( 1 + \frac{4h^2}{l^2} \right)^{1/2}$$

(App.1-9)

Where  $A_c$  is the area of cone and  $A_b$  is the area of the base and  $h$  is the cone height which can be represented by:

$$h = \mu_{rms} t = \mu_{rms} \frac{l_T}{S_L}$$

(App.1-10)

Where  $\mu_{rms}$  is unburned gas root mean square of fluctuation quantity in Reynolds averaging. Thus,

$$S_T = S_L \left[ 1 + \left( \frac{2\mu_{rms}}{S_L} \right)^2 \right]^{1/2}$$

(App.1-11)

Damkohler and Schelkin both based the theoretical measurement of turbulence speed on the turbulence flame consisting of a series of continuous laminar flames. Experimental results show that laminar flames do not exist under small scale high intensity turbulence flame conditions. Therefore, more precise experiments on the

turbulence effects from flame radiation are proposed. John and Mayer [15] suggest that the chemical time  $\tau_c$  and aerodynamic time  $\tau_a$  are related to the turbulence flame speed. The formula is called the Kovaszny number [16]:

$$Kz \equiv \frac{\tau_c}{\tau_a}$$

(App.1-12)

Where

$$\tau_c = \frac{\delta_L}{S_L}, \tau_a = \frac{M_T}{\mu_{rms}}$$

(App.1-13)

Where  $\delta_L$  is the thickness of the laminar flame front;  $M_T$  is the Taylor microscale of turbulence flame.

Developing new approaches to turbulent flame research have been proposed. Williams [17] considered the flame stretch and the ratio of the thickness of the combustion wave to the scale of turbulence. Bray, Libby and Moss [18-21] described a Bray-Moss-Libby modeled turbulence flame to consider of the effects of molecular transport and finite chemical reaction rates. Abdel-Gayed and Bradley [22] developed a ‘Two-Eddy’ conception theory to describe fine scale turbulence. Further, Spalding [23] proposed an ‘Eddy Break-up’ theory that considered the structure of small eddies. Andrew, Bradley and Lwakabama [24, 25] summarized recent efforts in research to identify the structure of the fine scale energy absorbing eddies of turbulence flame.

After the theoretical reviews, it is found that the turbulent flame is hard to simulate and measure due to its complex and fast varying. In the experiments, despite

the turbulent flame speed can be measured by PIV and high speed photographic methods [9, 10], it is still inaccuracy to measure the small turbulences. Therefore, in the POET project, only big turbulent flame front propagations have been considered. The flame speeds are evaluated by time and spatial differences of emissions using PMT projections data.

## **Detonation flame**

The detonation wave also known as shock wave was first identified by Berthelot and Vieille [26]. It is a turbulence wave that is sustained by chemical reaction and shock impression. The detonation flame unlike a deflagration flame is a supersonic flame with flame velocities from 1000 to 3000 m/sec depending on gas mixture, temperature and pressure. When flames are propagated in a tube under high pressure condition, a shock wave will appear. It will occur beyond the flame front and locate in unburned gas region. The detonation flames affect the engine performance and cause pre-ignition. Chapman, Jouguet, and Becker [27-29] developed theories about the character of shock and detonation waves. A detonation wave described by Chapman and Jouguet theory is displayed in Figure App.6. Three zones were identified, a zone of unburned fuels; a reaction zone and a zone of small high explosive fuels. The x axis is the CJ plane and is used in detonation wave velocity theory.

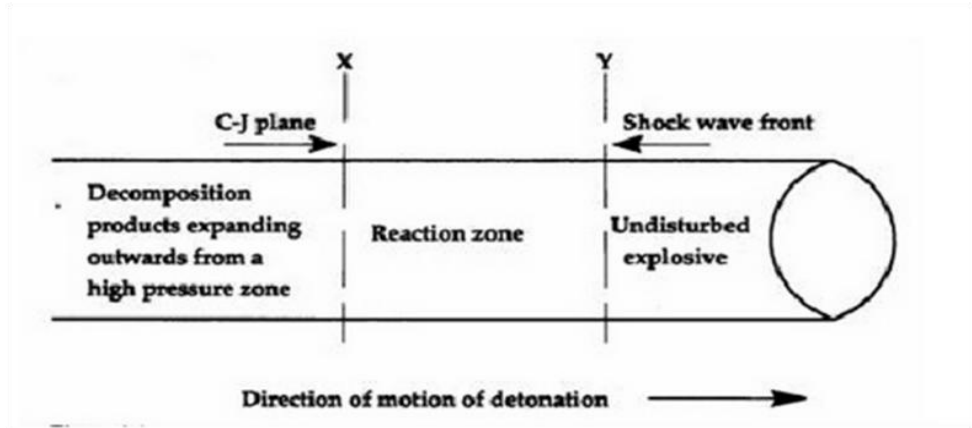


Figure App. 6 Detonation Process of explosive cartridge [30]

Chapman and Jouguet (CJ) plane theory and Zel'dovitch and von Neumann and Doring (ZND) model are both based on gasdynamic and thermodynamic arguments of fast chemical reactions. A simply detonation wave velocity can be described as:

$$D = \frac{v_1}{v_2} \sqrt{\gamma_2 n_2 R T_2} = \frac{v_1}{v_2} \sqrt{\gamma_2 n_2 v_2}$$

(App.1-14)

Where:  $D$  is the detonation speed;  $\gamma = C_p/C_v$ ,  $C$  is the molar heat capacity;  $n$  is the number of moles;  $p$  is the pressure; 1 means unburned gas, 2 means burned gas.  $v_1/v_2$  is times of sounds.

Zel'dovitch (1940), von Neumann (1942) and Doring (1943) separately proposed the ZND model structure of detonation wave propagation. Zel stated that the detonation wave is preceded by an infinitely thin shock that could compress reactions and generate high pressure and temperature. Unlike CJ propagation which terminates on reaching sonic velocity, the ZND model is a structure of various velocity conditions. The ZND model structure from the initial state to CJ plane is illustrated by the

Rankine-Hugoniot curve (Fig App.7). The parameters characterizing the Neumann state for a perfect gas with constant  $\gamma$  are given by the normal shock jump relations (Liepmann & Roshko 1957).

$$M_N^2 = \frac{2 + (\gamma - 1)M_u^2}{2\gamma M_u^2 - (\gamma - 1)} \quad (\text{App.1-15})$$

$$\frac{\rho_N}{\rho_u} = \frac{(\gamma - 1)M_u^2}{(\gamma - 1)M_u^2 + 2} \quad (\text{App.1-16})$$

$$\frac{\rho_N}{\rho_u} = 1 + \frac{2\gamma}{(\gamma + 1)}(M_u^2 - 1) \quad (\text{App.1-17})$$

$$\frac{T_N}{T_u} = \frac{\rho_N}{\rho_u} = 1 + \frac{2(\gamma - 1)}{(\gamma + 1)^2} \frac{(\gamma M_u^2 + 1)}{M_u^2} (M_u^2 - 1) \quad (\text{App.1-18})$$

These relations assume simple expressions for strong shocks, where  $M_u \gg 1$ ,

$$\rho_N \approx \frac{\gamma + 1}{\gamma - 1} \rho_u, \quad \rho_N \approx \frac{2}{\gamma + 1} \rho_u u_u^2 \quad (\text{App.1-19})$$

$$u_N = \frac{\rho_N}{\rho_u} u_u \approx \frac{\gamma - 1}{\gamma + 1} u_u, \quad u_N = u_u - u_N \approx \frac{2}{\gamma + 1} u_u \quad (\text{App.1-20})$$

Where the detonation velocity is  $u_u$  as given by the CJ equilibrium plane theory;  $M$  is the mass of the gas,  $\rho$  is the pressure of the gas.

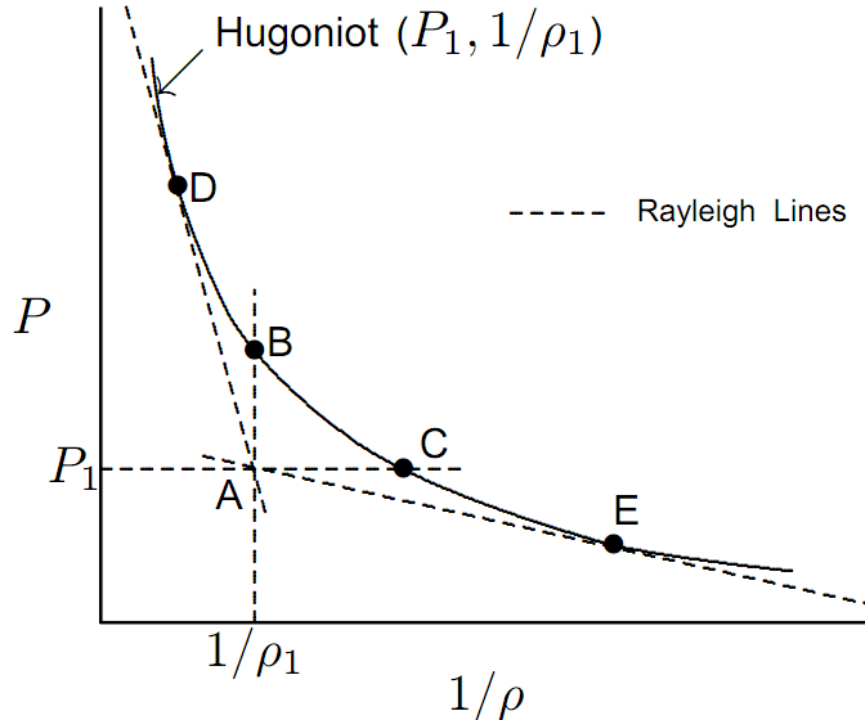


Figure App. 7 Rankine - Hugoniot Curve [31]

However, the CJ plane and ZND only fits a one dimension detonation wave, and cannot be used in multi-detonation velocity measurement. In Figure App.7, *D* is the upper Chapman-Jouguet point and *E* is the lower Chapman-Jouguet point. Strong detonations occur in the upper *D* point zone, strong deflagration occurs in the *E* point zone and wave detonation occurs in the zone between *D* and *E* [31].

Berthelot and Vielle [32] developed a chrono-electric method to experimentally measure the speed of the denotation flame. The principle is still used today with refinements afforded by modern electronic techniques for determining velocities in high explosive cartridges. In this experiment, probes are placed at a measured distance in the tube. The arrival of the detonation wave ruptures a wire passing a break signal to the electric circuit board. If the shock wave is not strong enough to break the wire, the

increased pressure is recognized by sensors in the tube wall [33]. Subsequently Mallard and Le Chatelier [34] developed a more accurate photographic method to measure the detonation wave using moving photographic plates. In the Schlieren photography method, powerful microsecond flashes are used to capture the high velocity flames. The composition of the detonation wave mixture is  $5\text{H}_2 + \text{O}_2$ .

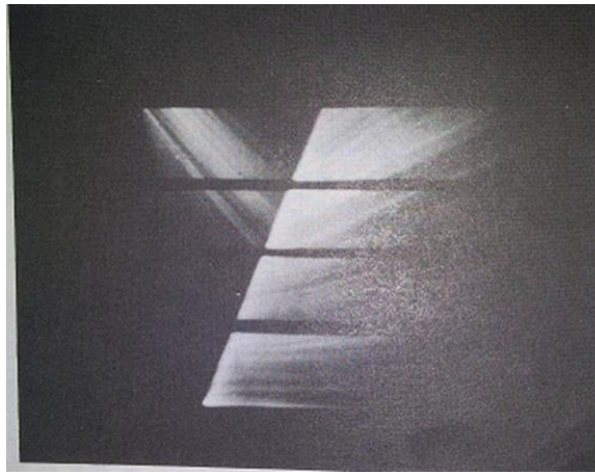


Figure App. 8 A Direct Photograph of Detonation Wave [35]

Reports of the extensive use of the photographic method using various fuel mixtures were published later. The stability of the detonation limits were determined from numerous investigations, Table App.1 gives the limits of mixture fuels and indicates the ranges of detonation wave stability.

Table App. 1 Limits of Detonability ( Laffitte. [36] )

Mixture	Lower limit fuel %	Upper limit fuel %
$H_2 - O_2$	15	90
$H_2 - \text{air}$	18.3	59
$CO - O_2, \text{moist}$	38	90
$CO - O_2, \text{well dried}$	---	83
$(CO + H_2) - O_2$	17.2	91
$(CO + H_2) - \text{air}$	19	59
$NH_3 - O_2$	25.4	75
$C_3H_8 - O_2$	3.2	37
$C_4H_{10} - O_2$	2.8	31
$C_2H_2 - O_2$	3.5	92
$C_2H_2 - \text{air}$	4.2	50
$C_4H_{10}O(\text{ether}) - O_2$	2.6	>40
$C_4H_{10}O - \text{air}$	2.8	4.5

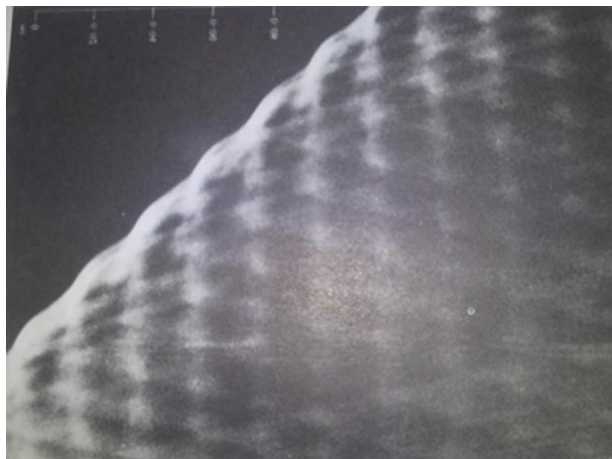


Figure App. 9 Spinning Detonation [36]



Campbell and Woodhead [36] indentified the ‘spinning’ detonation wave. In moist  $2\text{CO} + \text{O}_2$  mixture fuels, a glass tube consisting of a part of tube inner covered by a film of gray lead, a helical path are recorded by tracing the detonation. Bone and Fraser photographed the spiral track front of the detonation wave and observed a spinning detonation. Figure App.9 shows a spinning detonation in a moist mixture of  $2\text{CO} + \text{O}_2$  fuel. Furthermore, researches have used circular, triangular, square, and oblong tubes. The research found that in a  $2\text{CO} + \text{O}_2$  mixture medium, a persistent ‘spin’ with a single rotating head is established in a circular tube. The velocity along its helical path is practically constant than other mixture mediums.

After the reviews of flame velocity measurements, it has been found the laminar velocity is easier to be measured using classic methods. In comparison, the turbulent flame is difficult to be precisely evaluated in the experiment due to its random features, especially in small turbulences. Therefore, in the POET project, the only big turbulences have been considered. To consider the random features of flame, the flame velocity has been evaluated using amounts of data by statistics method to improve the measurement accuracy. In special, the flame speed may have some great errors due to the detonated flame.

# Fourier transform and Fourier slice transform theorem

## Fourier transform

The Fourier transformation is based on the ‘Fourier series’ deduced by Joseph Fourier (1768-1830) and is used in many disciplines [37-40]. In Fourier transform a sinuous signal at a constant frequency is propagated in a time domain. If the signal is transformed by the Fourier algorithm equation, it moves in a circular orbit around the polar coordinate system. One rotation of 360 degree represents one period of signal transmission in the time domain (Fig App 10).

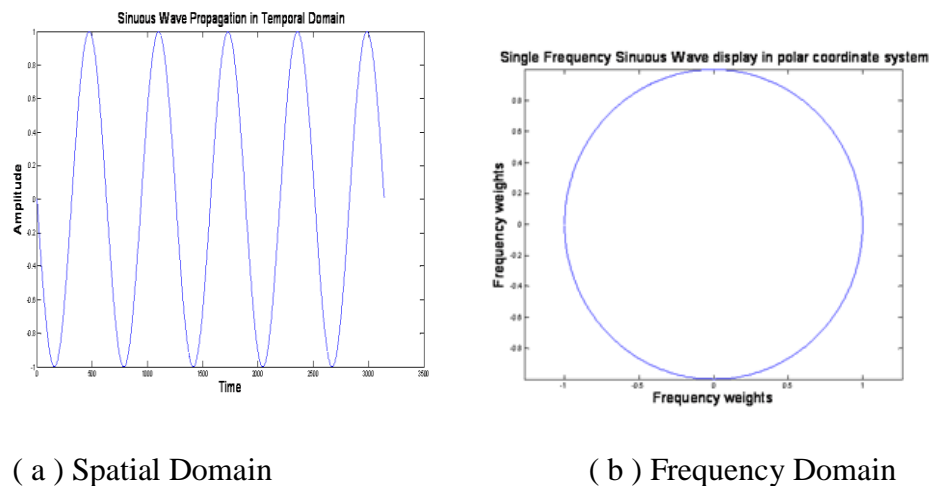


Figure App. 10 A sinuous signal transmission representation in different domains.

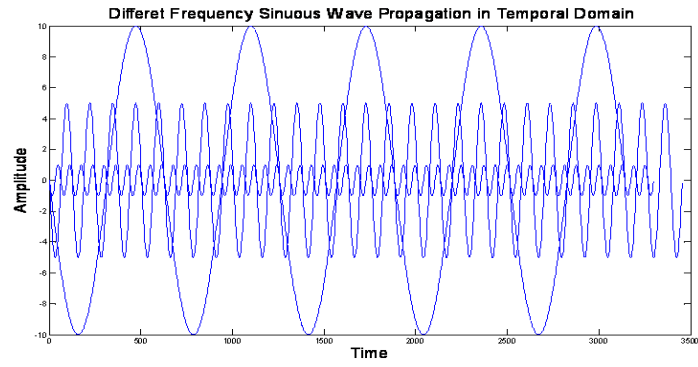
A waveform with a sinuous signal at constant frequency transmitted in a time coordinate system is represented by a constant circular orbit in a polar coordinate system. The Fourier transform algorithm uses the polar coordinate system to present the signals in a different weighted mean frequency. Only frequency behaviors of the

signals are present in this frequency domain. The equation of a typical Fourier transform is expressed by:

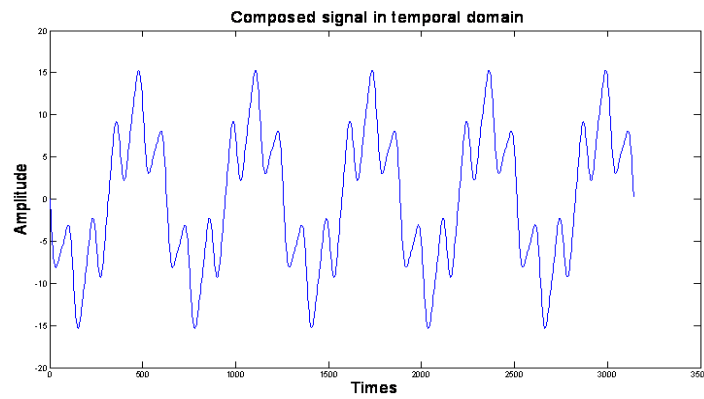
$$F(\xi) = \int_{-\infty}^{\infty} f(x) e^{-2\pi i x \xi} dx$$

(App.1-21)

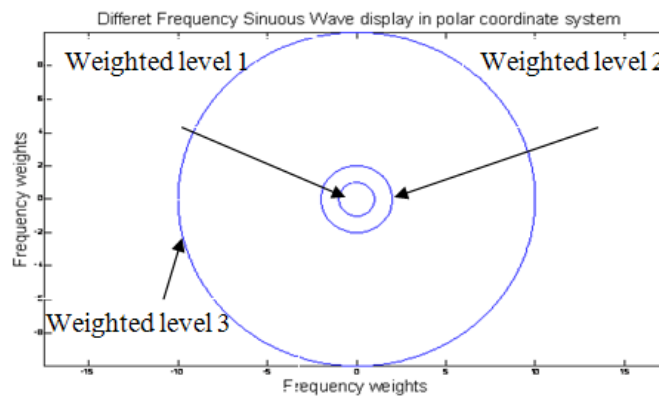
A composed signal consists of different frequency signals (fig. 4.13 (a)). When a white light (composed signal) beam is passed through the prism, the beam is split into different colour light (in different refractive index) beams at different frequencies. The white light is propagated complexly in a spatial domain but uniformly in a polar coordinate system (Fourier frequency domain). Figure App.11 (b) shows a complex periodic signal composed of three periodic signals at different frequencies. The irregular signals and induced noise prevent analysis of the signal.



( a )



( b )



( c )

Figure App. 11 Different frequency signals behaviour in spatial and frequency domains. Where (a) is a signal decomposed into three different frequencies; (b) is the composed signal from (a) and (c) is the frequencies distribution of a different signal.

By comparison, figure App.10 (c) shows a uniform frequency signals after transforming. If noise is added to the original signals, the analysis of the signal becomes more complex. In frequency, signals still carry coherent information in different weightings. In the image reconstruction process, the projections from detectors are commonly noisy linear integrated information due to the gray gradient [41-43] of the images. The projection data for the object is transformed into frequency by Fourier transform theorem. Then using backprojection the image can be transformed back from frequency to spatial domain greatly reducing errors.

## **Fourier slice transform**

The Fourier transform application is the basis for ‘tomography’ reconstruction. The target information is carried by the passing light beam and received by the surrounding ‘tomo’ detector array. Although the information captured by the detector is not uniform in the spatial domain after Fourier transformation it is uniform in the frequency domain. A normal image contains large amounts of information. After it is transformed into the frequency domain it exhibits a scattering of frequencies at angles from  $-\pi$  to  $\pi$ . Figure App.12 (b) and (c) is 2D Fast Fourier Transform (FFT) from a Greek Church photo. To overcome the scatter noise, a Fourier slice theorem was developed from the Fourier transform theorem. A linear integrated signal is transformed by FFT in 1D, the frequency behavior of signal is present as a ‘slice’ in the frequency domain (Fig App.12). The plot in App.12 (a) is a transform from

projection to the Fourier frequency domain by a 1D FFT function. Different frequencies are only present in a linear line; low frequencies are found near the origin point and high frequencies at a distance. The CT function makes use of the Fourier slice theorem.

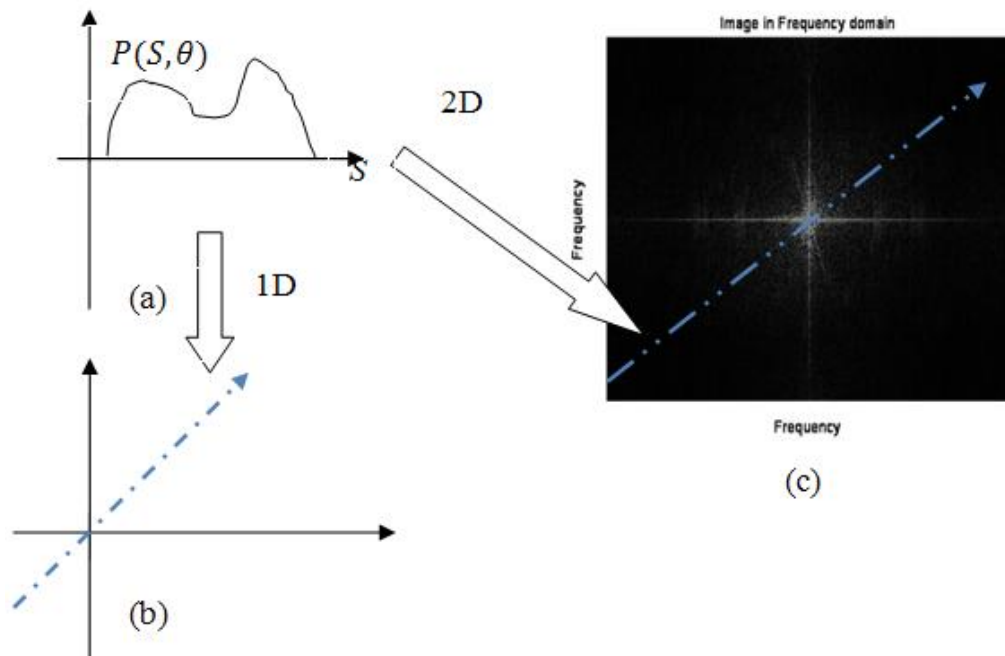


Figure App. 12 Fourier Slice theorem diagram.

In the Fourier slice theorem, various projections of the object are taken from  $-\pi$  to  $\pi$  angles. The signal is transformed to a polar coordinated signal by the FFT function. By summing the frequencies of the images at different angles, the frequencies image of the object can be reproduced. The spatial image can be obtained through the inverse Fourier transform fundamental.

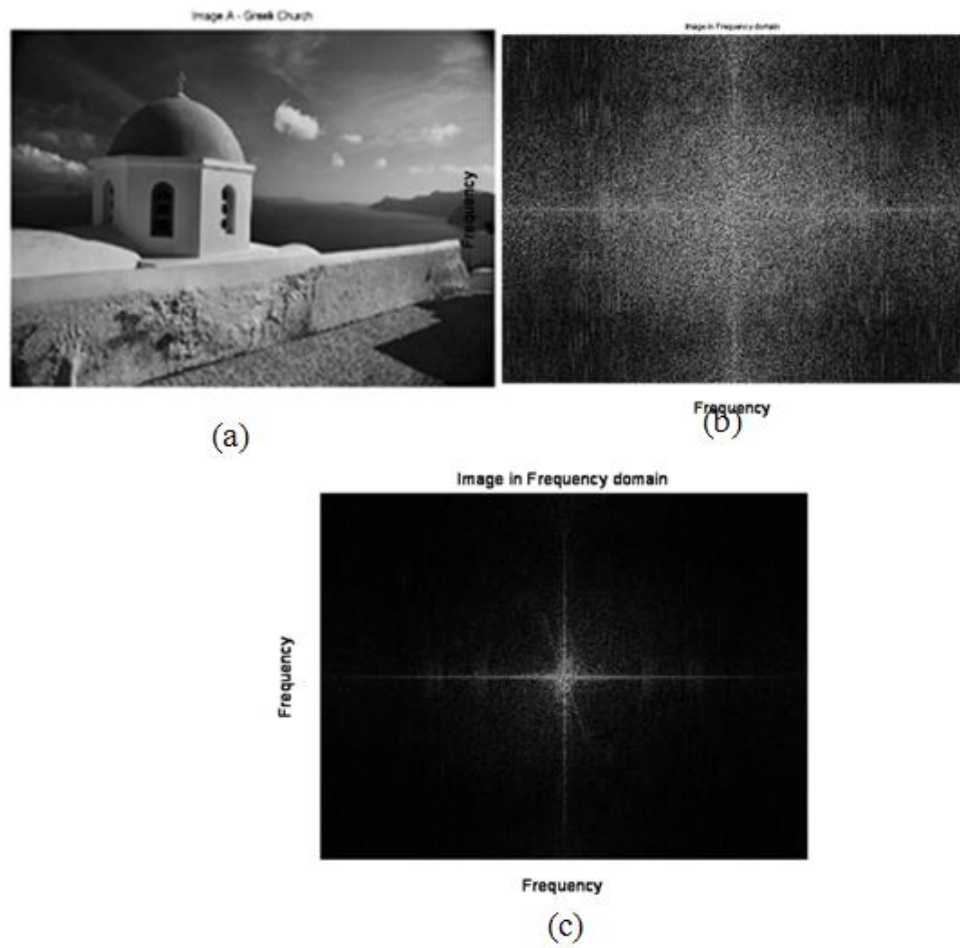


Figure App. 13 Image transform by FFT function in Matlab

## **Appendix B: Shack Hartmann**

The appendix consists of parts of Shack-Hartmann specifications, the schematic diagrams of the mounts for the naked lenslet array and some experimental results.

### **Shack-Hartmann sensor applications**

The SHWF sensors were used in the study of the flame wavefront. In the experiment, two types of lenslet array were employed: one was the naked lens array OPT-MLA-FS-105. It is a naked lens without a mounting. A house was designed to site the lenses. The other lenslet was the packaged SHWF sensor WFS 150 C. The specifications of two type lenses are below:



Table App. 2 Lenslet array specifications

	FS-105	WFS 150C
Wavelength Range	400-900 nm	300-1100 nm
Lenslet Grid Type	Square Grid	Square Grid
Lenslet Pitch	105 $\mu\text{m}$	150 $\mu\text{m}$
Lens Shape	Round,Plano Convex Spherical	Round,PlanoConvex Spherical
Lens Diameter	108 $\mu\text{m}$	146 $\mu\text{m}$
Chrome Apertures	Yes	Yes
Focal length	4.607 mm	5.2 mm
Effective focal length (Mounted in house)	4 mm	3.7 mm
Array size	9mm $\times$ 11m $\times$ 1.2mm	10mm $\times$ 10m $\times$ 1.2mm
Materials	Fused Silica	Fused Silica

The FS-105 lenslet array is mounted with a USB 2.0 colour 1.3 MP CCD Camera with Frame Buffers. The maximum resolution is  $1280 \times 1024$ . The WFS 150 C micro lens was fitted to a 1.3 MP CCD Camera in a globe shutter. At maximum resolution the FS-105 has  $41 \times 29$  spots and the WFS has  $37 \times 29$  spots in total (fig. App.14).



( a )



( b )

Figure App. 14 FS-105 module (a) and WFS150C (b) module

The experiment is to measure the aberration when a parallel laser beam is passed over an object. A reference coherent beam was generated by a 638.5 Helium-neon laser. Then a collimated parallel light is passed through several lenses and past the turbulent target (Fig App.15). The refractive indexes differ throughout the object due to the density gradients. The aberration wavefront was detected by the sensor through the lenslet array.

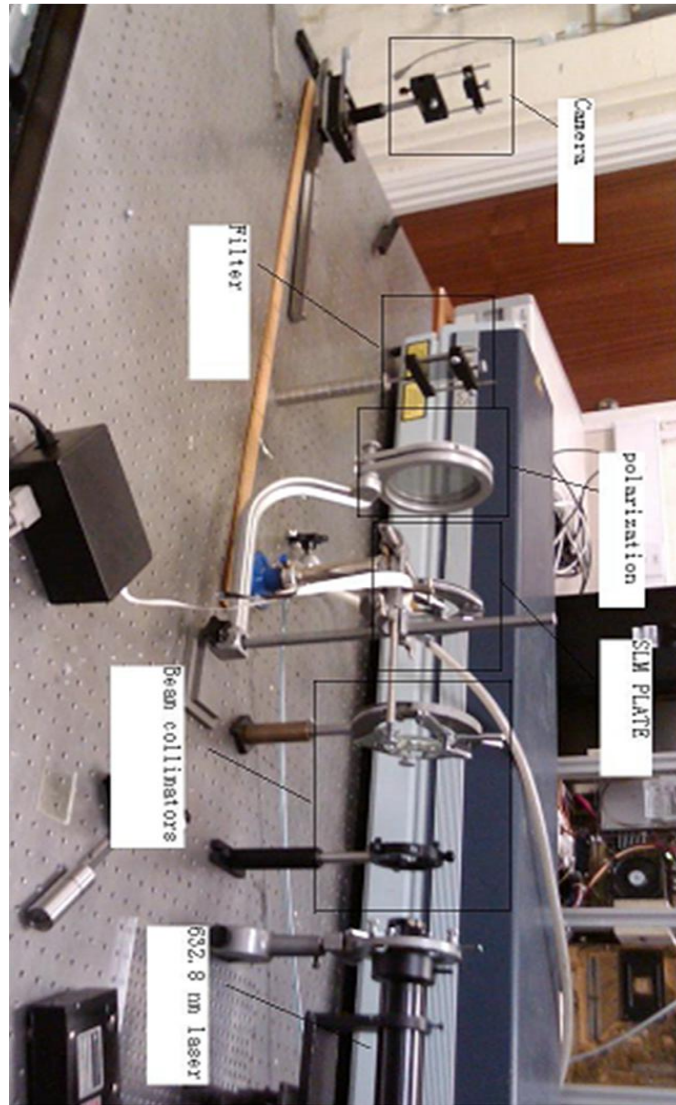


Figure App. 15 The setup for measuring the flame wavefront

In the experiment, several luminous sources were employed: a candle, a premixed flame, a burning gas flow, a heat gun flow and a Helium gas flow (fig. App.16). The candle flame as a sooty luminous target created a strong background projection on the screen. The others made little background noise for the detector. The turbulence information was carried by diffraction spots. This is discussed further in the results.



Figure App. 16 Turbulence flow generators

## **Thorlabs      Shack-Hartmann      software application**

The WFS 150C compact SHWF camera is packaged with thorlabs wavefront software to measure the tilts of the lenslet array. This software calibrates the incoming beam and displays the intensity on the screen (fig. App.17).

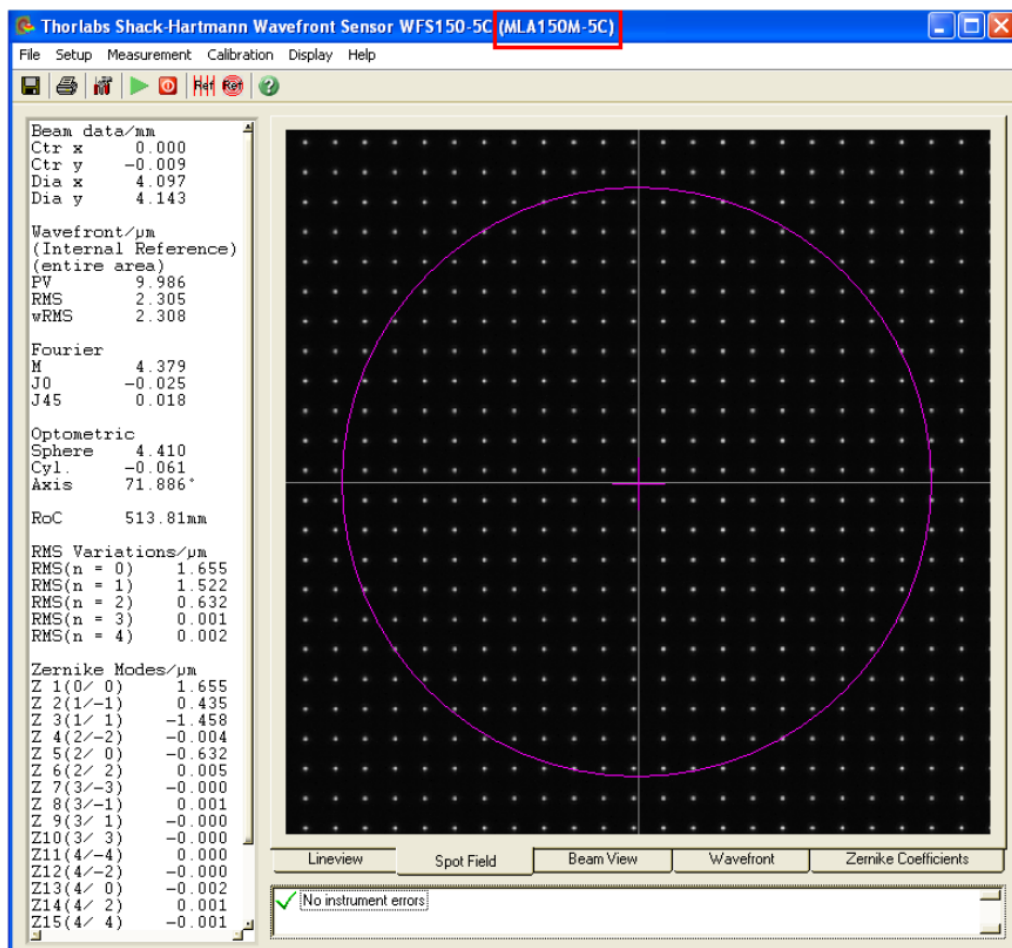


Figure App. 17 Single shot of spot field

During calibration, the software is applied to collimate the parallel beam. The defocus information is present in a pupil border function (fig. App.18). The software can simulate the 3D wavefront and graph it in a pupil function. The results help to understand the tendency of aberrations when the wavefront is distorted (fig. App.19).

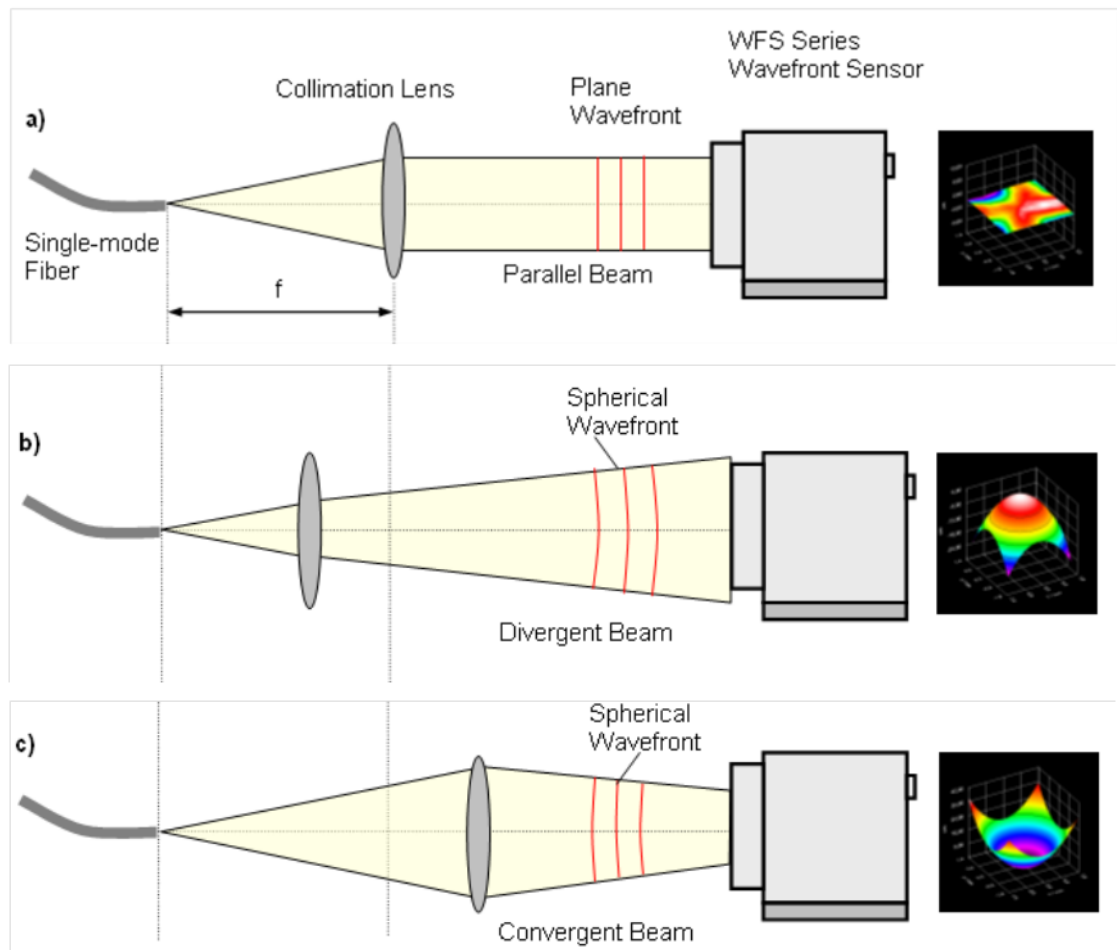


Figure App. 18 Three orders of incoming beam

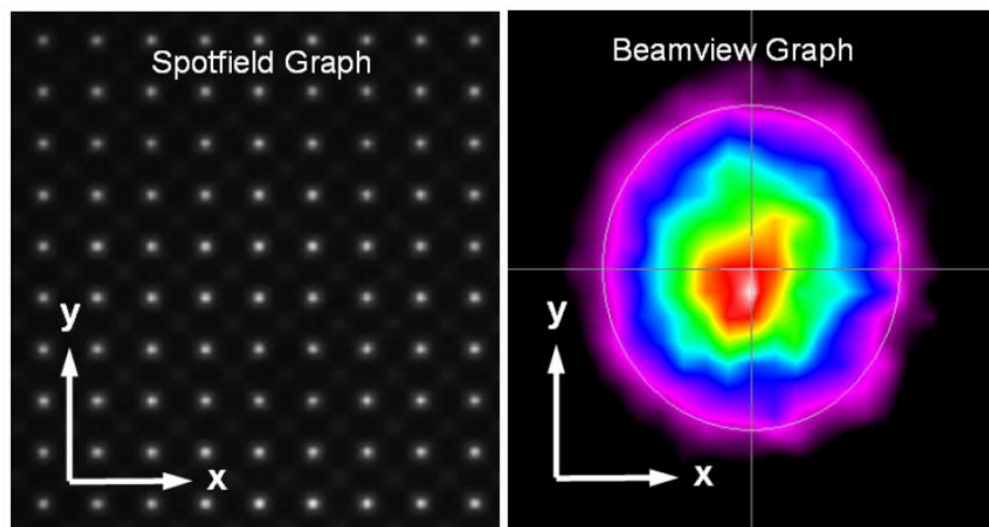


Figure App. 19 Beamview in pupil function



# House schematic diagrams for FS-105 lenslet array

A housing to hold the 105 microlens for testing was designed. Since the small size of lens, the design is restricted in 0.1 mm level. The housing was made by micro technicians of WMG department. In the design, solidworks are utilized due to its powerful function of micro design.

## Results

The measurements of density gradients are to multi large amounts deviations of lens spots to analyze the distortion of object. Then using the deviations reconstructs the aberration wavefront. In the experiment, the intensity of a single spot is distributed as a Gaussian function. There are differences between a reference single spot and a flame spot intensity in location and intensity.

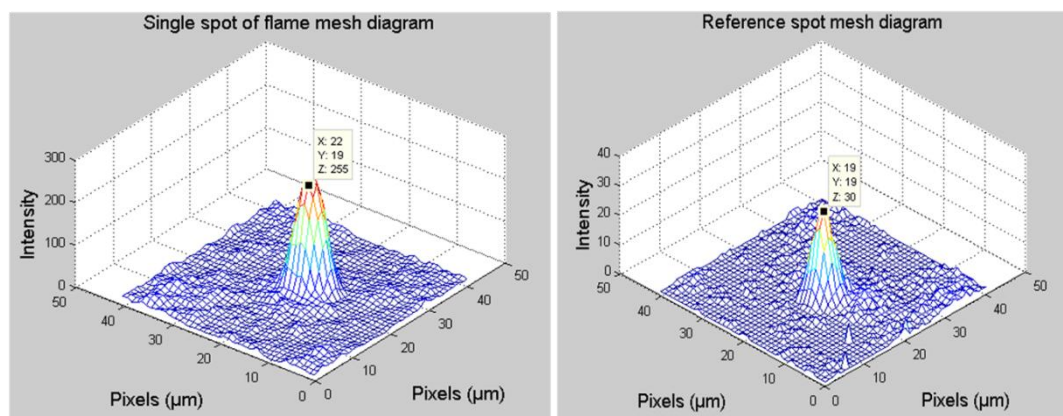


Figure App. 20 Comparison between reference spot intensity and flame intensity.

The coherence of a laser beam, the diffractions are slight due to small varying of density refractive index. Non-zero orders of diffractions are adopted to measure the

refractive index due to their sensitivity to transmission path differences (fig. App.21).

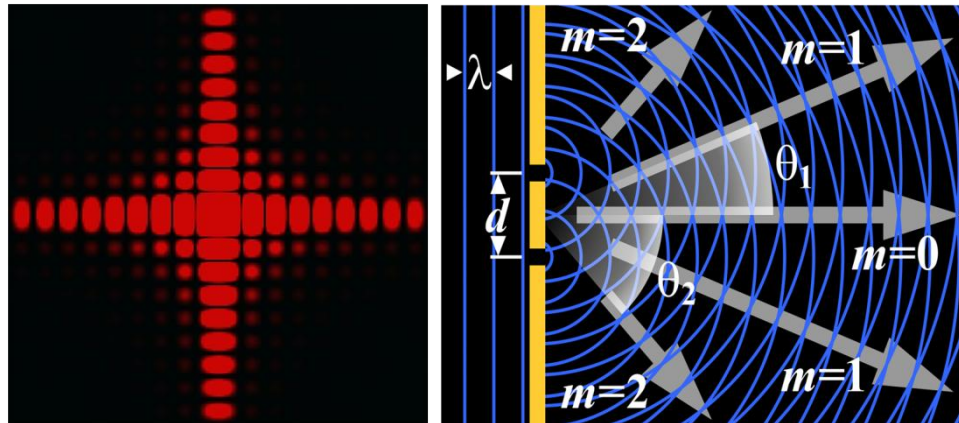


Figure App. 21 Diffraction illustration diagram

Thus, we have apparent aberrations of second orders. Figure App. 22 is a candle flame diffractions diagram which shows the strong intensity of the second order of diffraction spot. The varying of second order diffraction with the associated variation in wavefront intensity is recorded.

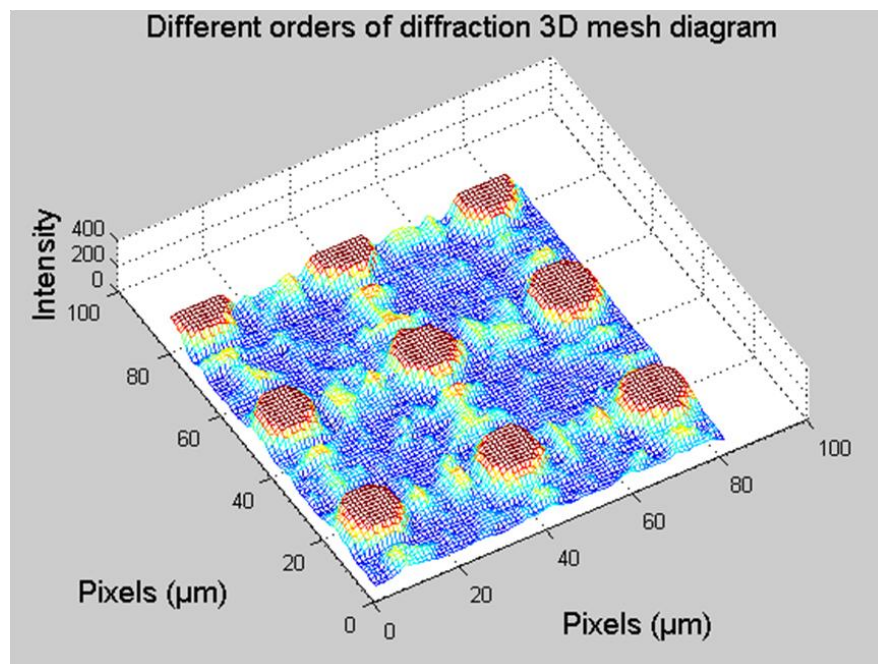


Figure App. 22 Spots diffractions on varying orders.

A series of turbulence in varying density object is tested in the experiment (fig. App



23-27).

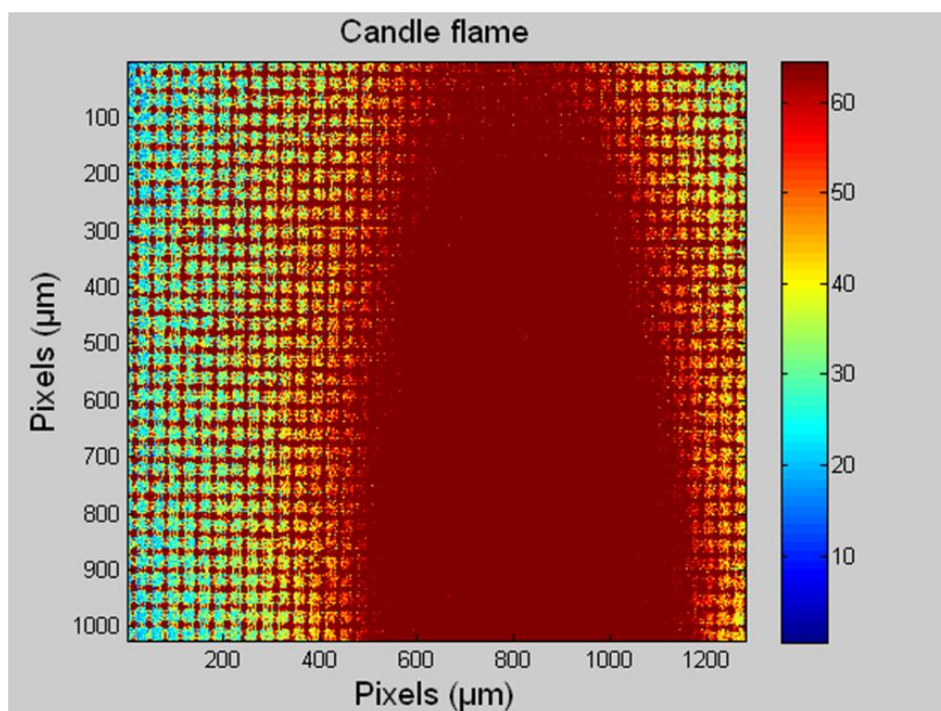


Figure App. 23 Candle flame

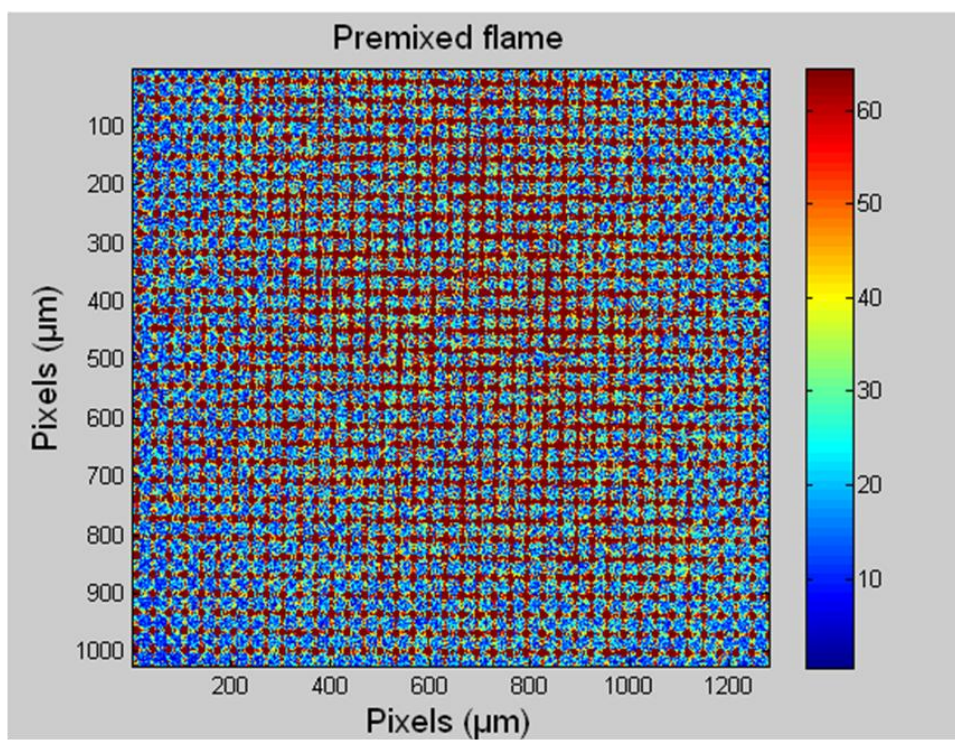


Figure App. 24 Premixed Burner flame

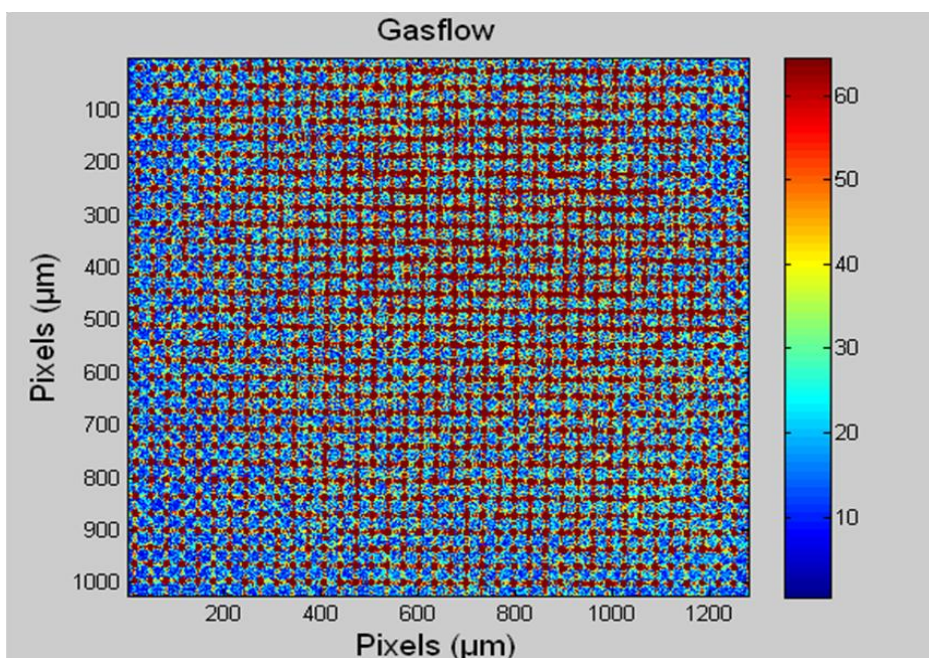


Figure App. 25 Methane Air premixed Gas flow (not burning)

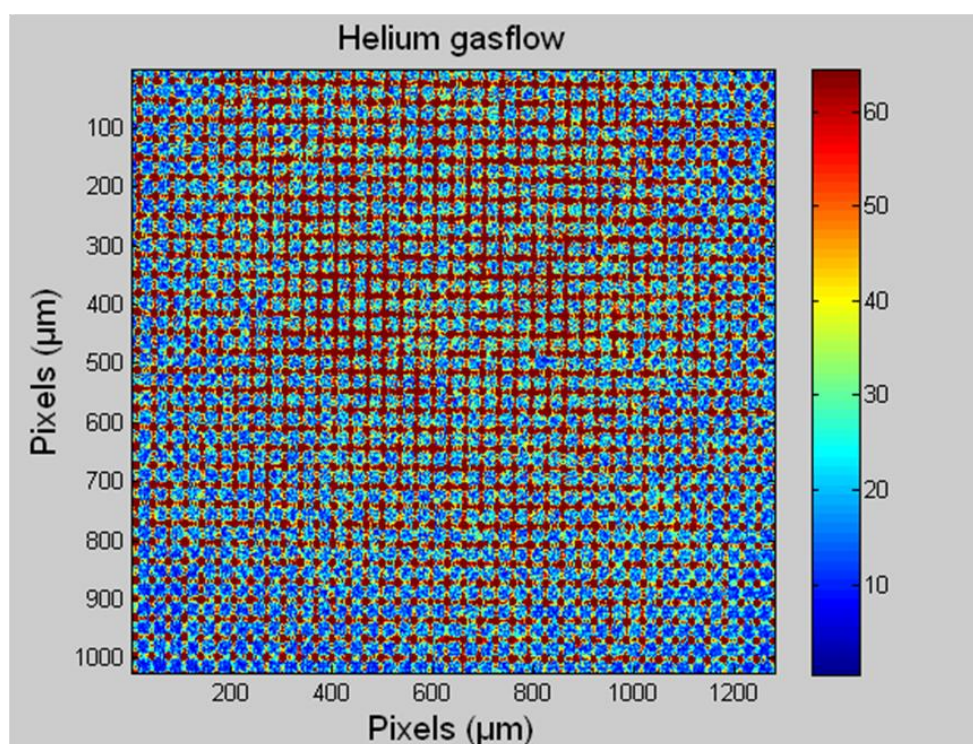


Figure App. 26 Special element Helium gas flow detecting.



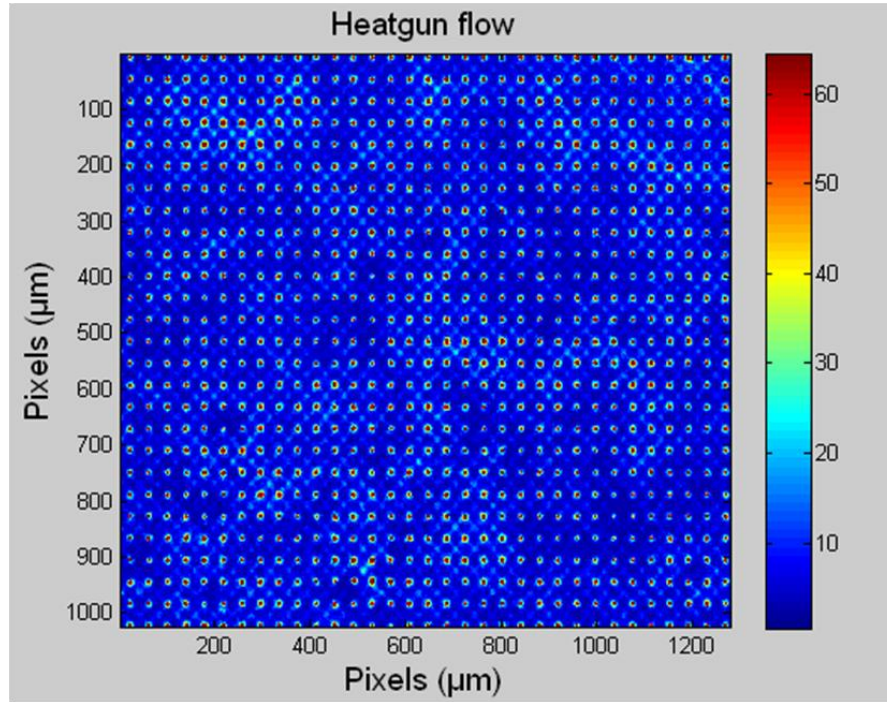
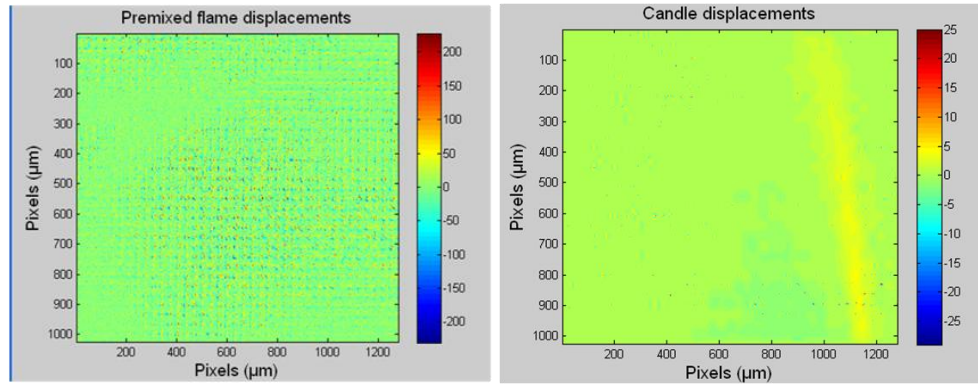


Figure App. 27 Heat release turbulence measurement using Heatgun

The above figures show the rough outline of wavefront turbulence with several objects. The candle flame generates a large sooty luminous noise and the contours of the candle are clearly recorded. The premixed burning flame and the non ignited gas flow (fig. App.24 and App.25) use methane and air mixture fuel. Fewer flame wavefront contours are present due to the greater turbulence and less background noise. A special gas is used to measure the turbulence (fig. App.26). To test the heat effect on turbulence, a heatgun is used to generate a heat flow (fig. App.27).

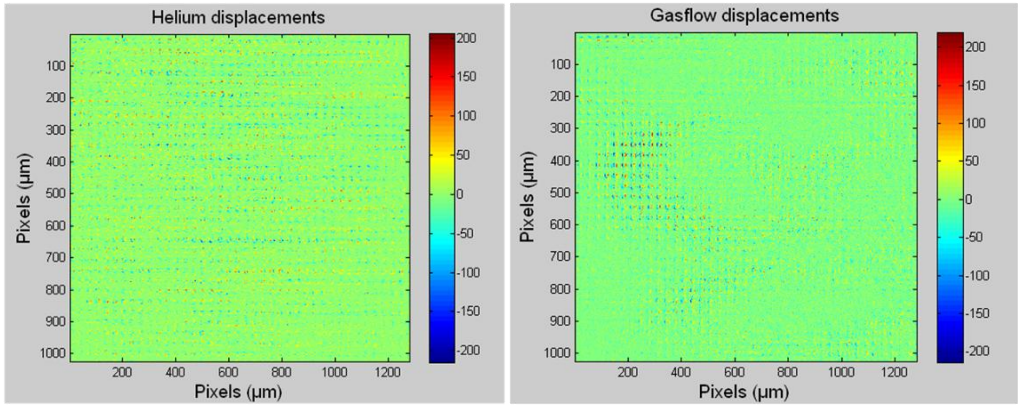
At a sampling frequency of 50 Hz, the camera captures a maximum resolution of  $1024 \times 1280$  displaying the displacement of  $10 \mu\text{m}$  per pixel. Figure App.28 shows the turbulences of different objects. The candle flame image shows a clear displacement due to its uniformity and less turbulence. Images for the other heat

sources display more complex turbulence and irregular displacement. Although the displacements are irregular, the particle deviations are clearly illustrated due to the lenslet array sensitivity of small tilts



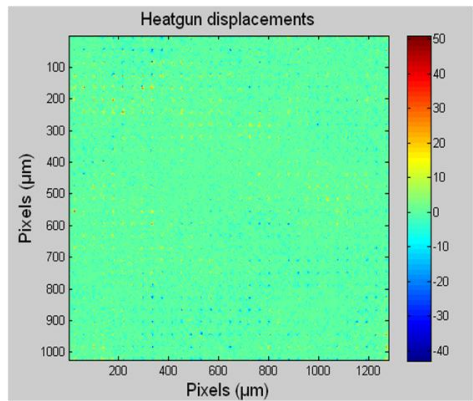
( a )

( b )



( c )

( d )



( e )

Figure App. 28 Turbulence difference at different times

It is difficult to display the turbulence outline because of the discrete singles. A matlab image compress technique is used to visualize the turbulence outline. The Global threshold of coefficients and Huffman encoding are used to program the image. The computer code is listed below.

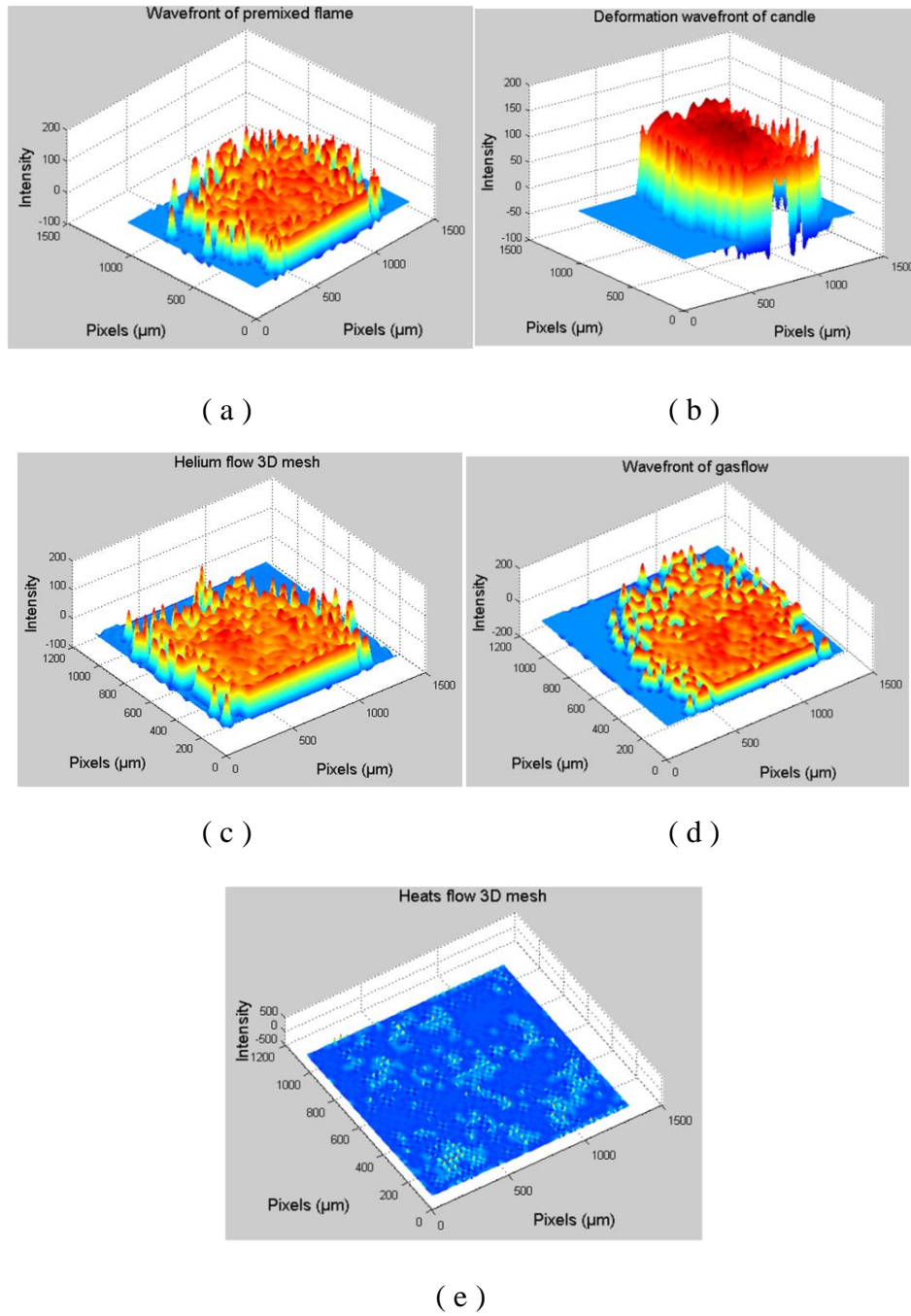


Figure App. 29 3D mesh of wavefronts of varying objects.

Figure App.29 illustrates the visualization of the target wavefronts. The laminar candle flame (a) is more uniform and less turbulent than the other flames. Images (b) to (d) show high turbulence flames. These similar images indicate that the SHWF gives good results in measuring the premixed flame. Image (e) displays filtered heat releasing turbulence. More accurate results are obtained using a Neutral Density (ND) filter to eliminate the noise. Thus, particular turbulences are distinctly revealed without noises in the image. The key code is below (discrete image conversion to continuous):

```
%%%%%%%%%%%%%%%%%%%%%%%%%%%%%%%%%%%%%%%%%%%%%%%%%%%%%%%%%%%%%%%%%%%%%%%%
Discrete convert to Continuous
Map compression
%%%%%%%%%%%%%%%%%%%%%%%%%%%%%%%%%%%%%%%%%%%%%%%%%%%%%%%%%%%%%%%%%%%%%%%%

meth    = 'gbl_mmc_h'; % Method name
option = 'c';          % 'c' stands for compression
[CR,BPP] = wcompress(option,a,'a.wtc',meth,'maxloop',2);
option = 'u'; % 'u' stands for uncompression
```

## Appendix C: POET system

Appendix B consists of mechanical, compacted PC and software application three parts. In mechanical design, the schematic diagrams of engine and OAG are described. In compacted PC section, the operation manual of PC is explained. In the software applications, the software is implemented in varying tests.

### Mechanical

In the experiment, a Briggs and Stratton OHV pro 206 engine is employed and modified to measure the combustion. It is a small commercial engine with 6.5 HP power. It is good for laboratory due to its small sizes and special 30 degree overhead design.

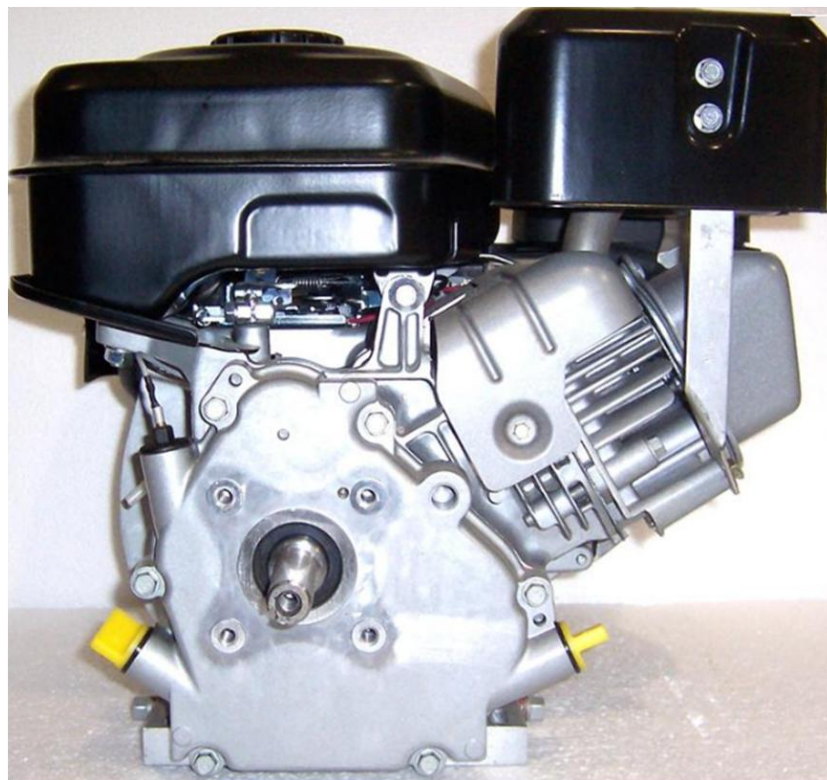


Figure App. 30 Biggs and Stratton OHV 206 pro engine



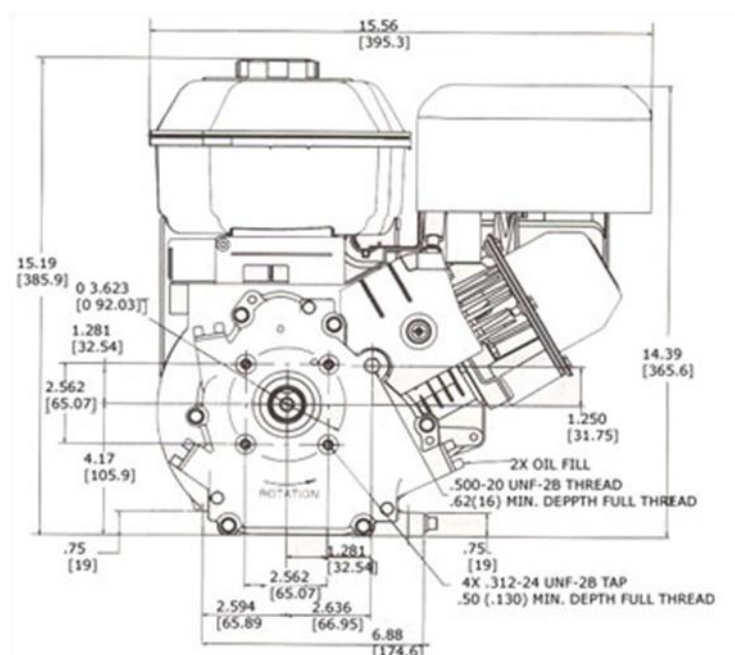
The specification of engine and schematic diagrams are in the table below.

Table App. 3 Briggs and Stratton engine specification

<b>Features</b>	<b>Benefits</b>
TransportGuard System	Simultaneous fuel/ignition shut-off protects the engine from oil/fuel dilution during transport
Overhead Valve Design	Runs cooler and cleaner delivering more power, longer engine life and improved fuel economy
Commercial-style Carburetor	Additional fuel passages ensure reliable starting and smooth running operation at a wide range loads
Large, Efficient Sediment Filter	Sediment is collected in a large, clear bowl and is drained using a convenient tool-free valve
All-metal Fuel Tank	Reduces emissions and is mounted directly to the engine block to enhance durability
<b>Lubrication</b>	
Motorsports Rod/Dipper Design	Efficiently improves oil flow throughout the engine; assures maximum protection of internal components
Oil	Automatically shuts down the engine in low oil situations to safeguard investment
Splash Lubrications system	Delivers superior lubrication to the engine to ensure long life and reliability
<b>Mechanical</b>	
High-mounted Canister-style Air Cleaner	22% more filter area than the competition; water-repellent filter with innovative triple seal design dramatically decreases dirt, dust and debris intake



Magnetron Ignition	Electronic	Quick dependable starts with no maintenance required
Larger Ignition Coil		Assures fast, easy starts
Innovative Chamber	Combustion	Improves air and fuel flow, resulting in a cleaner burn, reduced emissions and increased horsepower
Cylinder Head and Head Gasket Forged Crankshaft		Incorporates heat-treated ball bearings to minimize friction and heat build-up
<b>Engine Dimensions</b>		
Dimensions(LxWxH)		10.83 in (275 mm) x 15.28 in (388) x 14.29 in (363mm)
Weight		41.2 lbs (18.7 kg)
Fuel Tank Capacity		4.1 L
Oil Capacity		20oz (0.6L)
Engine Displacement		205 cc (12.51 cu in)



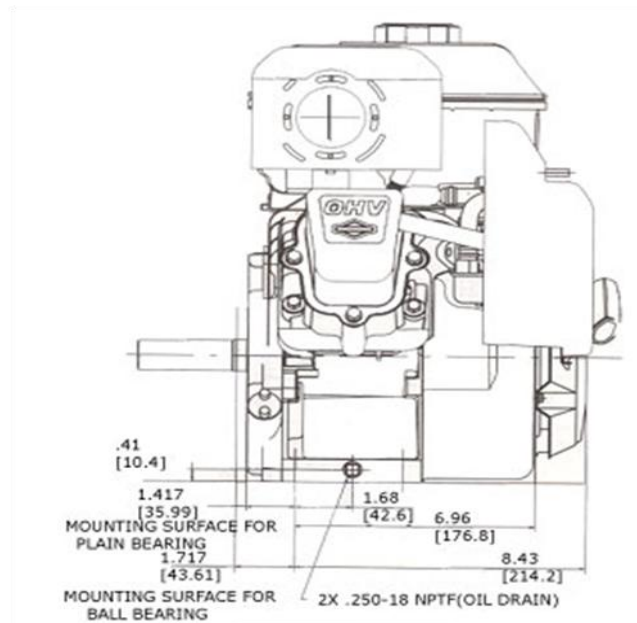


Figure App. 31 Briggs and Stratton Engine schematic diagram

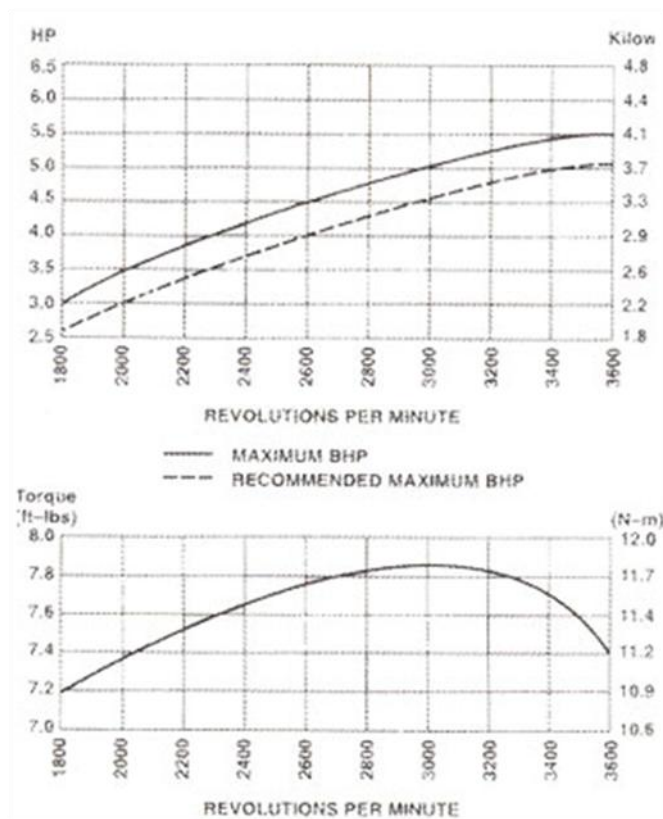


Figure App. 32 Engine power specification

In the experiment, the engine has been modified to implement. Several operations are in practice.

1. Remove the start motor and clutch
2. Remove the flywheel
3. Exchanging the gas intake between engines
4. Draining the engine Oil
5. Remove the cylinder head
6. Replace the cylinder head using modified parts.
7. Reverse procedure above to complete the engine system with modified parts.

In starting of engine, following the guideline below (fig App.33): Firstly, turn on extractor; then open gas valve; at last press ignition button.

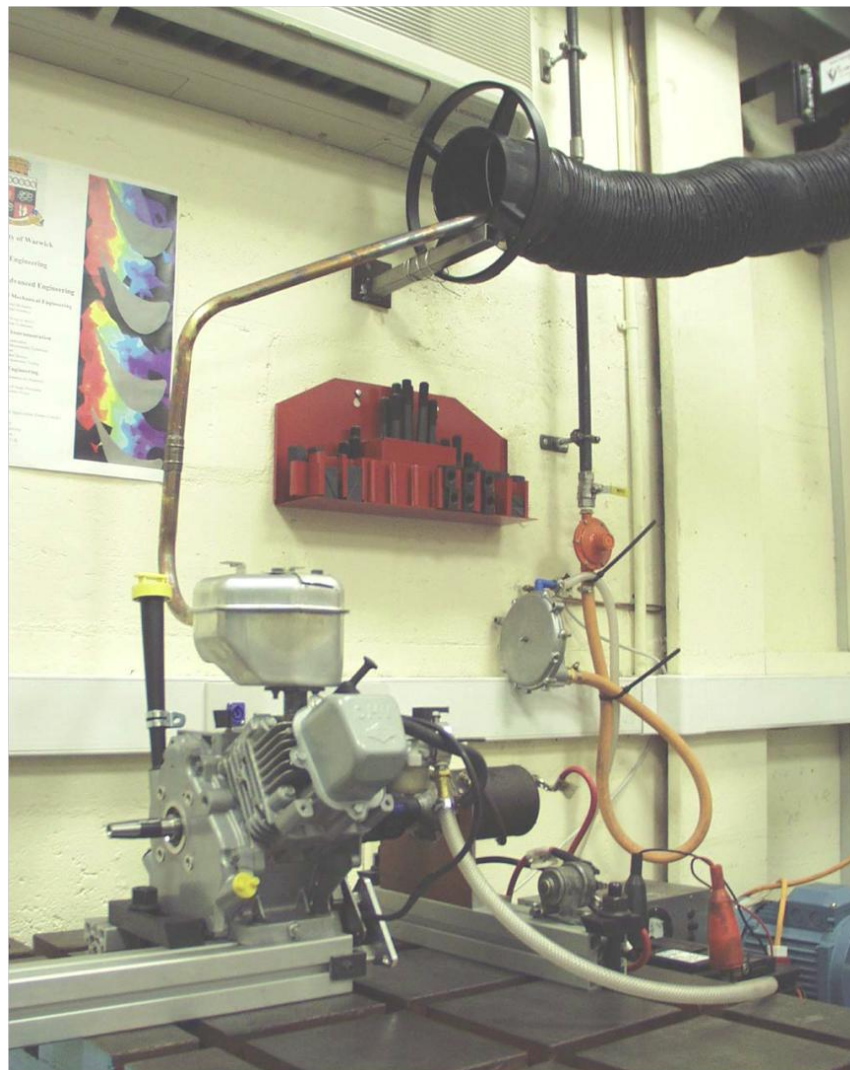


Figure App. 33 Safe guild operations

**SECTION A-A**  
SCALE 2:1

**DETAIL B**  
SCALE 2:1

**DETAIL C**  
SCALE 2:1

**SECTION D-D**  
SCALE 2:1

**DETAILS:**  
 - 0.25 X 45 DEG  
 - R0.2 TYP  
 - 0.05 A  
 - C 0.002  
 - 1.6  
 - 2.31  
 - 2.30  
 - 1.45  
 - 1.55  
 - 15.5  
 - 15.5  
 - 7  
 - 45°  
 - 7 X 5 SLOT ARRAY  
 - SLOT PITCH 4 PLACES  
 - 55.4  
 - 90  
 - 10  
 - X 2 POSN

**SECTION A-A**  
SCALE 2:1

**DETAIL B**  
SCALE 2:1

**DETAIL C**  
SCALE 2:1

**SECTION D-D**  
SCALE 2:1

**DETAILS:**  
 - 0.25 X 45 DEG  
 - R0.2 TYP  
 - 0.05 A  
 - C 0.002  
 - 1.6  
 - 2.31  
 - 2.30  
 - 1.45  
 - 1.55  
 - 15.5  
 - 15.5  
 - 7  
 - 45°  
 - 7 X 5 SLOT ARRAY  
 - SLOT PITCH 4 PLACES  
 - 55.4  
 - 90  
 - 10  
 - X 2 POSN

295

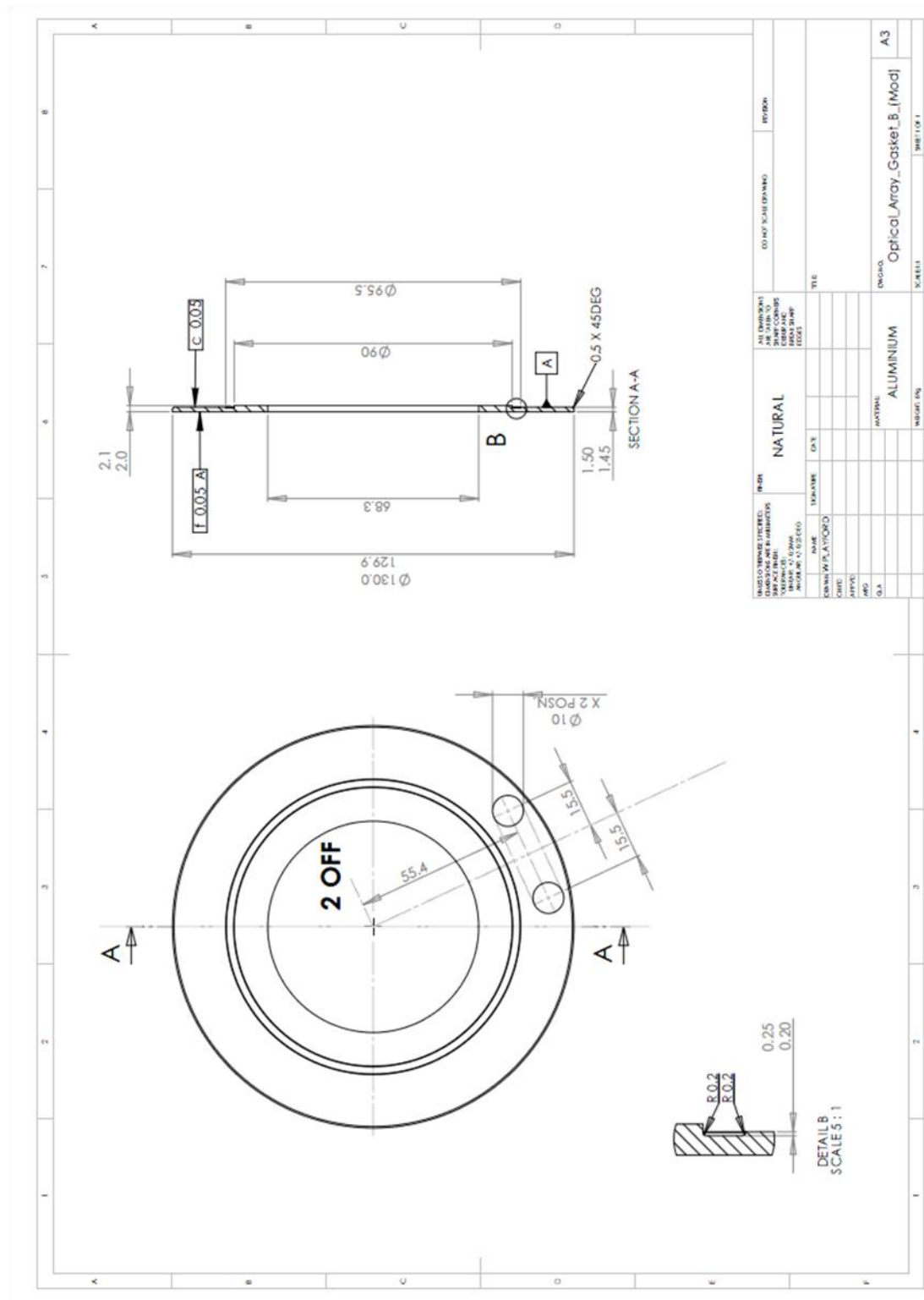


Figure App. 35 Schematic diagram of OAG cover

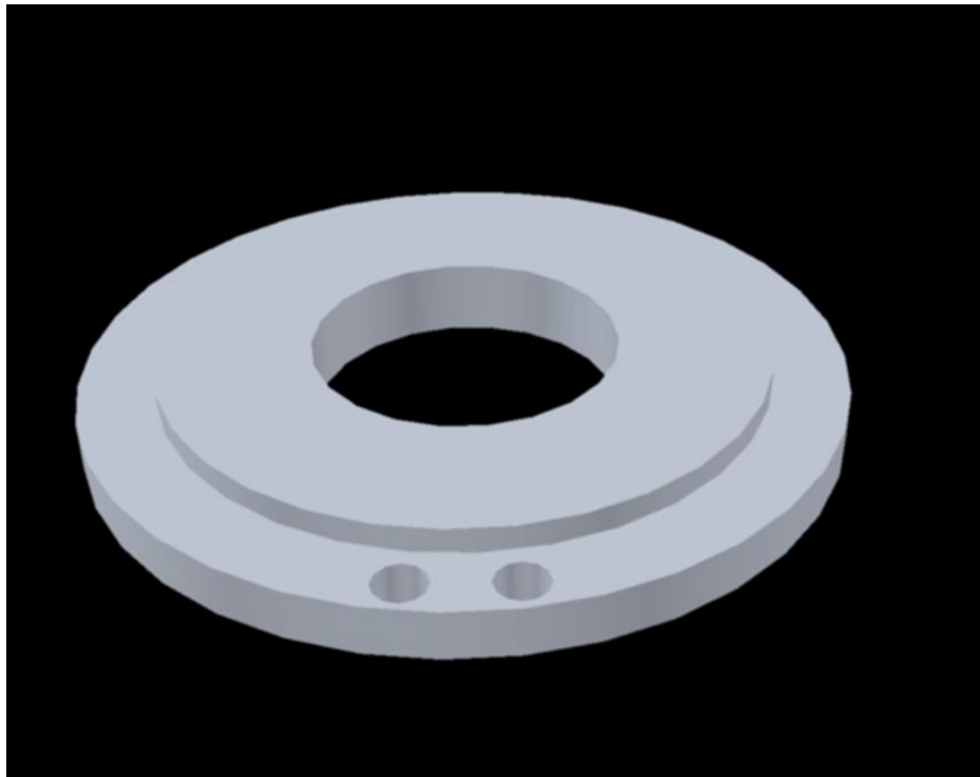
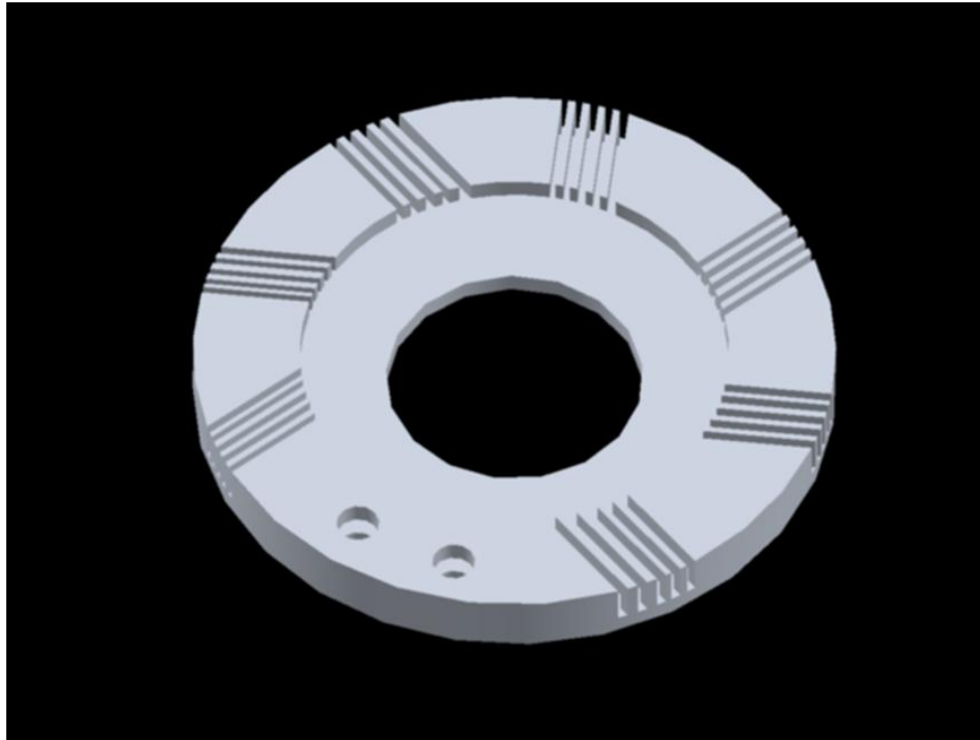


Figure App. 36 3D models of OAG

The assembly of engine schematic diagram is below.



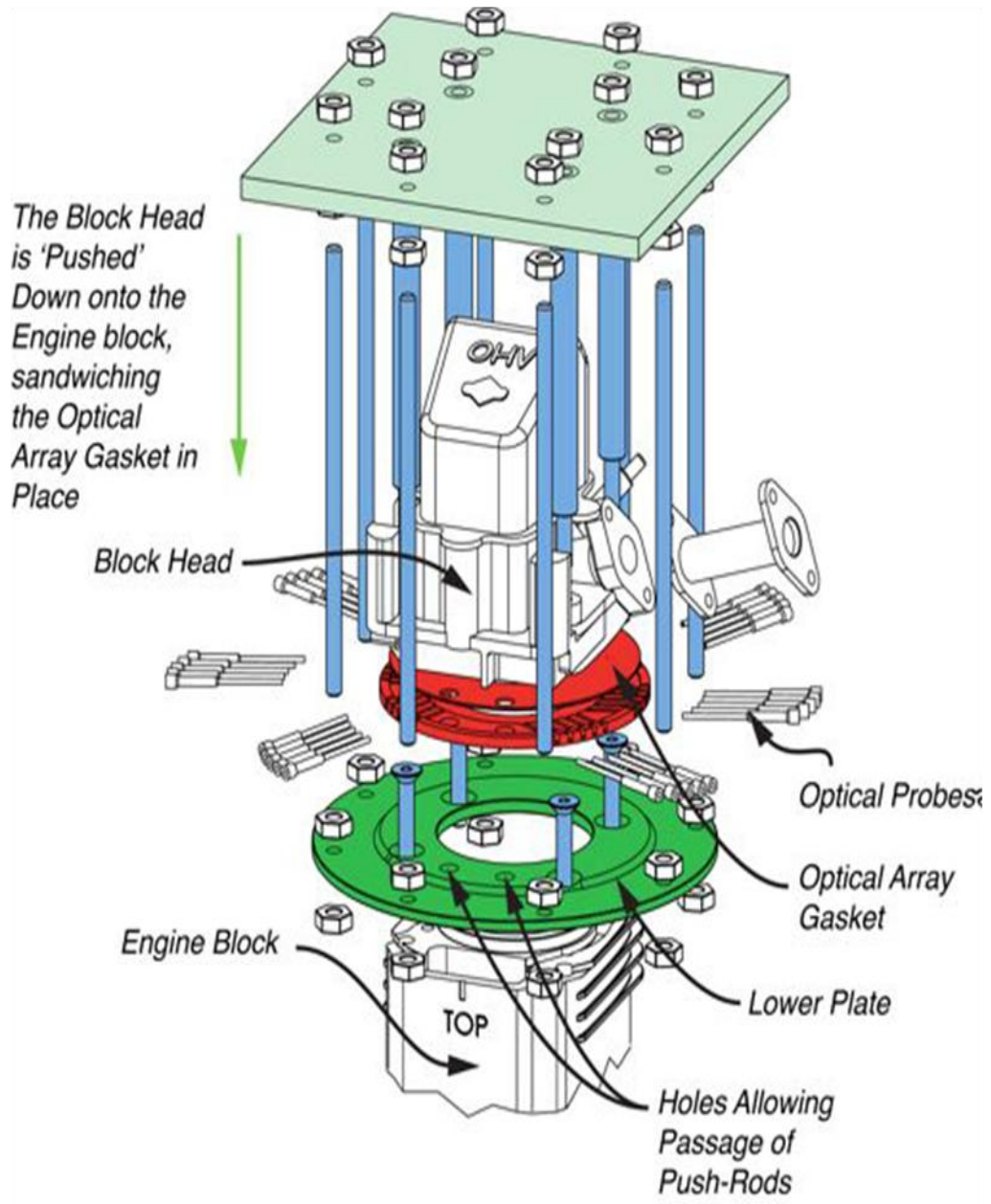


Figure App. 37 Modified Engine Assembly

## Compacted PC module

### Overviews

To measure the combustion, an intelligent POET system has been designed.

The compacted PC consists of 40 PMTs, DAQ card and other PC components (fig.

App. 38).

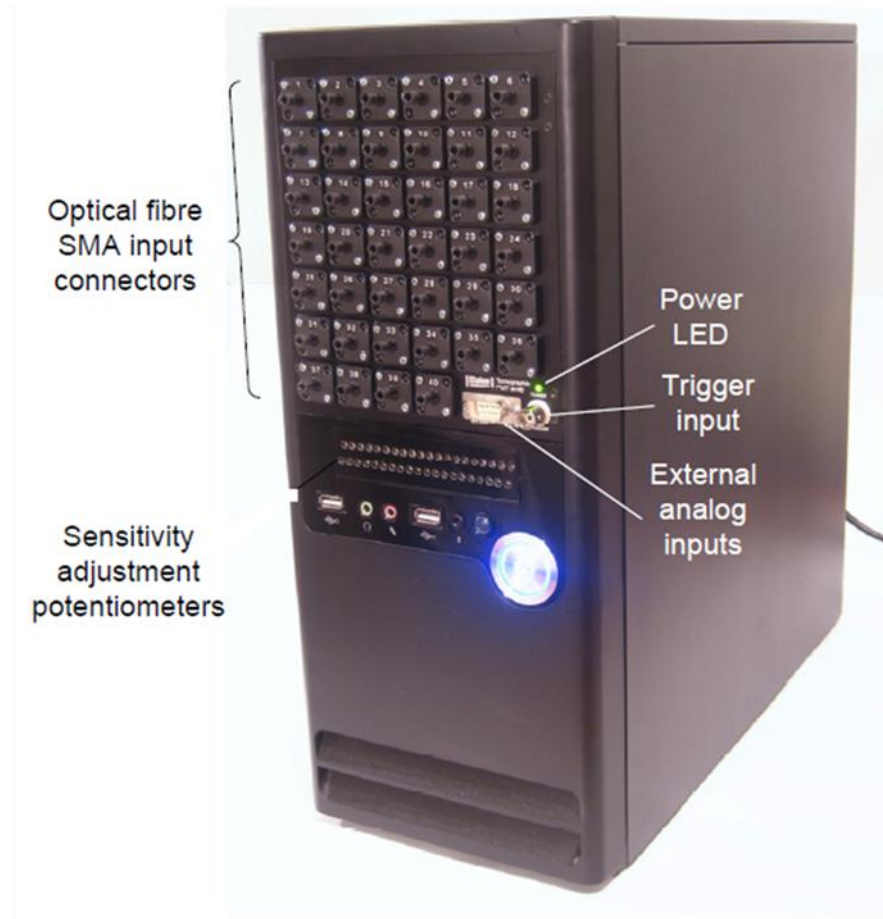


Figure App. 38 Compacted PC module

The overviews of PC (fig. App.38) consists of a power button, 40 PMTs connector interface, sensitivity adjustment potentiometers, trigger input and external analog inputs interface.

In Adjusting PMT sensitivity part, each PMT module can have its sensitivity individually set, using one of the 40 potentiometers embedded in the smaller panel on the front of the PC. The channel numbering for this panel is shown below. To increase a channel's sensitivity, turn the potentiometer screw clockwise. Each control rotates through a maximum of 5 turns.



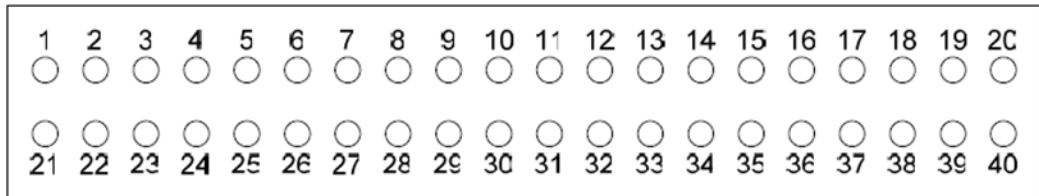


Figure App. 39 40 channels of sensitivity adjusting

In external analog input, the DAQ is connected to 8 “extra” analog inputs, which can be sampled alongside the 40 PMT signals. The pin-out for the inputs’ 9-pin D-type connector is shown right. Note: Input voltages must not exceed the range -10 to +10V. Also be aware that there are no pull-up or pull-down resistors connected to these inputs. The inputs will therefore “float” if not connected to anything, and this will result in spurious values appearing for the 8 inputs. If you are not using the inputs, you can either deselect the channels from software interface, or attach the supplied “grounding connector” (in which all 9 pins are linked).

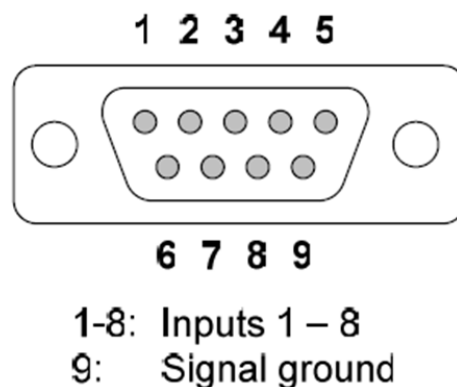


Figure App. 40 External analogs input

## Tomographic acquisition (TOMACK) software

The Tomack (tomographic acquisition) software provides a simple interface to the

DAQ hardware, and allows users to record data from the PMTs in a variety of formats.

The software consists of a single window, which comprises 5 distinct areas (App.41):

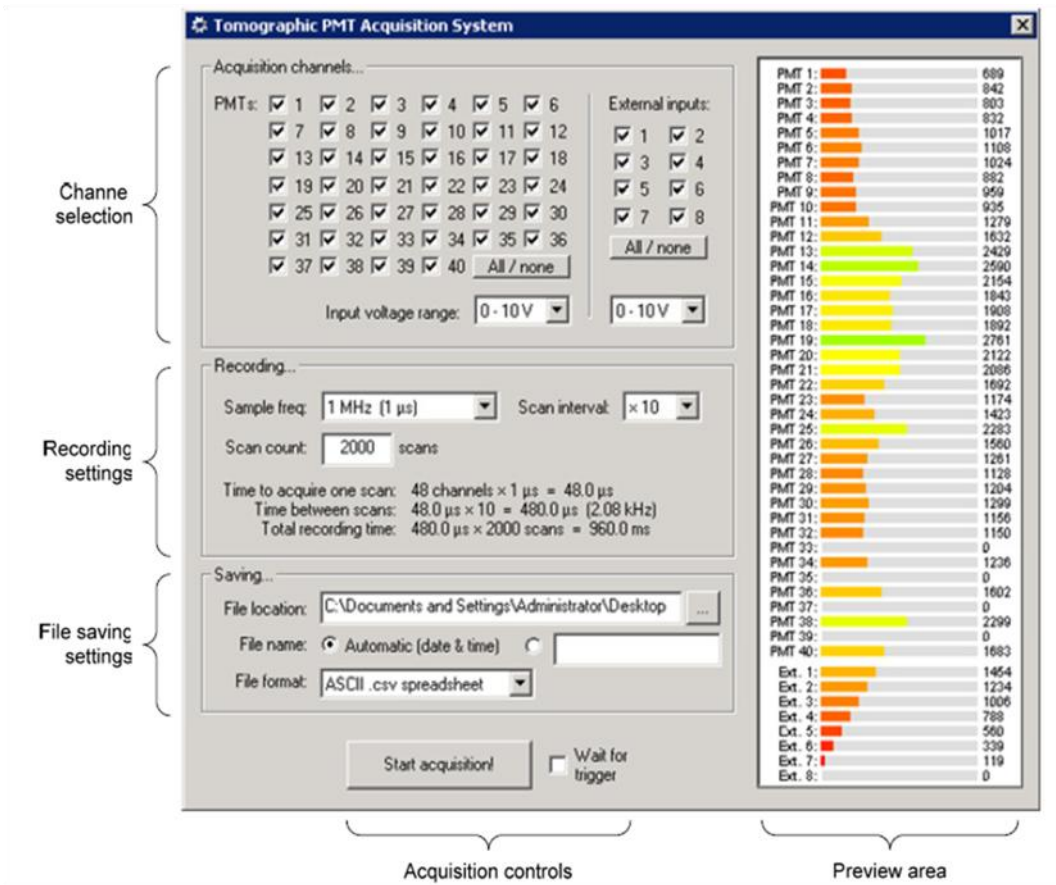


Figure App. 41 Tomographic PMT acquisition interface

As soon as the software loads, you will see live data (from as many channels are selected) within the preview area. During acquisition, this area will instead display status messages. Upon closing the application, all of your settings will be saved to the registry, and these are loaded when the Tomack is next started. The following sections provide further information about each set of controls.

- Channel selection

Use the checkboxes to select which of the 40 PMT channels and 8 external input channels you wish to record from. You can click the “All/none” button to cycle

between all, none, or some of the channels, and you can also select from a variety of different input voltage ranges (0 – 1, 2, 5 or 10 V). Reducing the PMT channels' input voltage effectively increases the gain of the system, however, if you instead use the physical sensitivity controls (detailed on page 4), you will avoid introducing any extra measurement noise from the DAQ's electronics. All channel data is displayed and saved as "raw" integer values. Due to the DAQ's 12-bit resolution, this equates to values of between 0 – 4095. Note that the external channels may be configured to have a bipolar (e.g.  $\pm 5$  V) instead of unipolar (e.g. 0 – 5 V) input voltage range. If bipolar inputs are selected, then an external signal of 0 V will be displayed and saved as value 2048.

- Recording settings:

The Recording controls allow you to set both the frequency and number of samples to record. Please note the following terminology: a single recording from one input channel is called a "sample", while a set of samples (from each of the channels) is referred to as a "scan". Tomack provides 2 controls to determine the speed at which data is acquired. These are shown in the diagram below, which represents a scenario in which just 7 PMT channels are sampled:

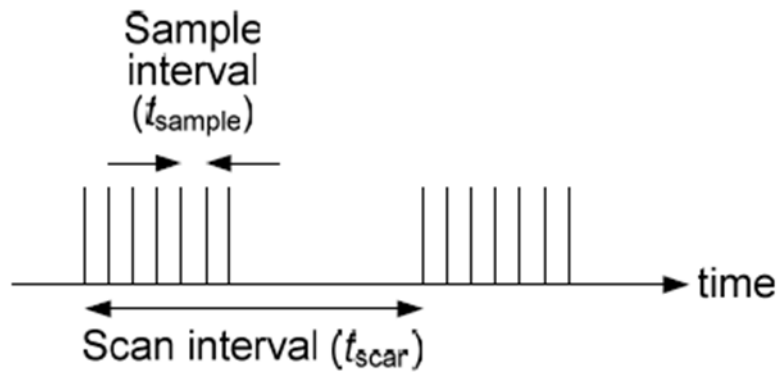


Figure App. 42 Scan Interval

The sample interval is set directly (with possible values ranging from 350 ns – 100  $\mu$ s). Usually, there will be little reason to set  $t$  greater than 350 ns, as this will only decrease the simultaneous-ness with which adjacent PMTs are sampled. If you are recording a slowly evolving phenomenon however, you may wish to increase the scan-interval. This is defined below:

$$t = \text{sampling frequencies} \times \text{numbers of channels} \times K$$

where scan interval  $K$  is an integer of value 1, 2, 5, 10 or 100. If it is set to 1, there will be no additional delays and the channels will be sampled continuously. Setting  $K > 1$  will result in the card “pausing” between scans, as represented in the diagram above. Please note that you cannot set  $K = 100$  while  $t = 100 \mu$ s, as this may result in pauses that are longer than the DAQ card can support. You will be warned with a prompt should you try and select these conditions. The number of scans to record is entered directly, and the text below this control updates to let you know how long (in milliseconds) it will take to record that number. Should you enter too large a number,

you will prompt to either reduce the number of scans, or refer to the following section in order to learn how to increase the DAQ driver's sample count limit.

- The DAQ driver's sample count limit

The DAQ card is allocated an amount of RAM upon start-up, but the D2K Configuration Utility (available from the ADLINK section of the Start menu) allows you to alter this amount. Beware that setting the value too high will affect the performance of your PC. With the utility loaded, select Card Type: Daq2208, then enter the desired buffer size in the AI: field. Note that the number of samples that Tomack can save is equal to the number you enter, multiplied by 2048.

- Triggered Operation

Under normal operation, acquisition will begin as soon as you press the "Start Acquisition" button. While acquisition is underway, this button will turn into a "Stop!" button, which you can use to stop acquisition at any time. Note that an aborted acquisition will not result in any data being saved. If you select the "Wait for trigger" checkbox, then the system will wait for a rising edge trigger to be applied to the BNC connector on the front of the device. As soon as the applied voltage rises from zero, acquisition will start. Note: The trigger accepts TTL level (i.e. 0 or +5V) signals. Do not apply larger voltages.

## **File formats**

Tomack supports 3 different file formats: ArrayMART.txt file, Matlab.mat archive and ASCII .csv spreadsheet.

The first format is designed specifically for use with the ArrayMART tomographic reconstruction software package. Please be aware that only the 40 PMT values will be saved to disk when using this format (i.e. external input data will be discarded). Furthermore, the ArrayMART format requires that exactly 40 values are saved; therefore, any unselected PMT channels will be saved as having value zero.

The CSV format can be loaded into any spreadsheet software (e.g. Excel), and it contains as many columns as the number of channels that you chose to save. There is 1 header row (detailing the channel represented by each column) and then as many rows as there are scans.

The MAT archive is arguably the best format to save data into, as it is not only binary (i.e. the file size is kept to a minimum) but it also contains acquisition information in addition to the raw data. The archive contains the following 3 variables:

Name	Size	Type	Description
acqSettings	1 × 1	Struct	The acquisition settings used
Channels	Channel count	Uint16	The channels from which data was sampled.
Data	Channel counts x Scan counts	Uint 16	The raw data

The acqSettings structure contains the following 7 fields, which should be self-explanatory:

Name	Type	Example value
PMT_Voltage_Range	Char	0-10 V
Ext_Input_Voltage_Range	Char	$\pm 5$ V
Time_Between_Samples	Char	10 $\mu$ s
Samples_Per_Scan	Double	48
Time_Per_Scan	Char	480.00 $\mu$ s
Time_Between_Scans	Char	960.00 $\mu$ s
Number_Of_Scans	Double	10000

Files can be named automatically, or according to a filename that you supply. In the latter case, you do not need to add the file extension to the name, but you do need to change the name between recordings (you will receive an error if the supplied filename already exists). Automatically named files take the form:

PMTdata\_168.00\_U10-B5\_2009-01-01\_24.59.59.ext

which can be seen to comprise several elements, separated by underscores. These elements are described below:

Element	Value in example above	Description
1	168.00	This is the scan interval in microseconds
2	U10-B5	This is the input voltage ranges for the PMT and external channels, with U & B standing for unipolar and bipolar.
3	2009-01-01	This is the date.
4	24.59.59	This is the time.
5	ext	The file's extension will be either .txt, .mat, or csv.

## Hardware components

The embedded PMTs module comprises an independent power supply of PMTs, PMTs, PCB board power control, a sensitivity potentiometer with a ADlink connection to the DAQ card (Fig App.43). In the embedded system there is a 15 voltages PMT bipolar power supply and a PCI-2208 ADlinkCPCI board is for supporting the DQA card.



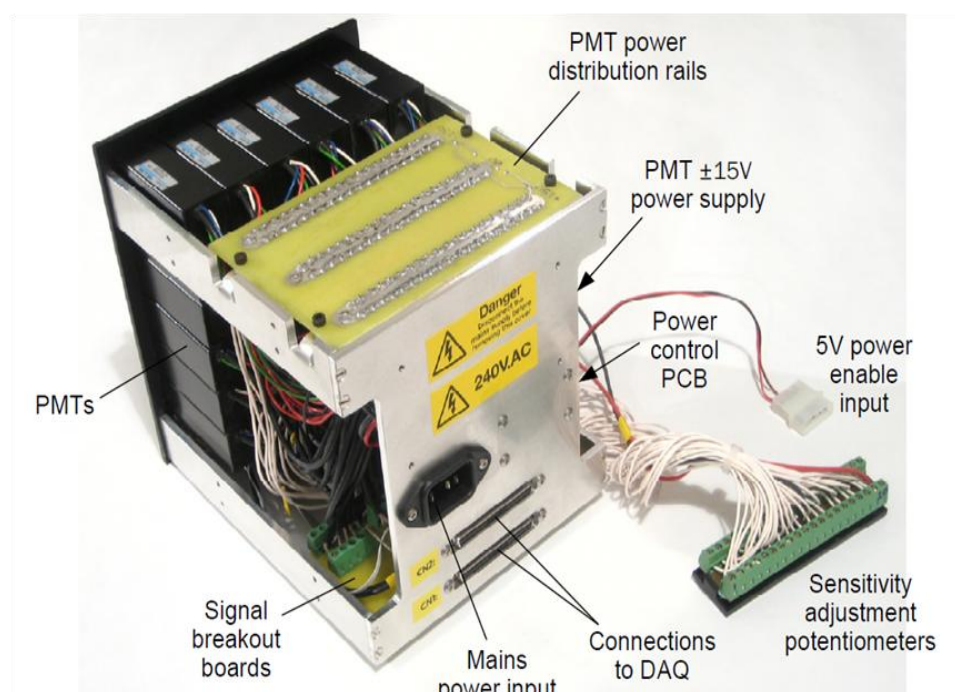


Figure App. 43 PMTs tomography computer system hardware components

36 PMTs modules are employed and the Hamamatsu H5784-04 consists of 40 modules. Channels 33, 35, 37 and 39 are empty. Channels 1 to 6 have different sensitivities to the others. Prior calibration is therefore necessary.

PMT channels	Serial number
1 to 6	58690025 to 58690030
7 to 32	60690002 to 60690027
34	60690028
36	60690029
38	60690030
40	60690031

# Software applications

## System calibration

The MART software has been applied to display the turbulence combustion. During operation, some errors and noises occurred in the experiment. Then, calibrations of system are implemented to improve the system accuracy.



Figure App. 44 Spectrum meter for system calibrations

The calibration system is using a manual spectrum meter to measure the individual intensities of each PMT. The light emissions are passed the spectrum meter from one side and received by sensors from another side. Through observing of intensity panel of software, intensities of PMTs are initialized at constant intensity within acceptable errors by adjusting the potentiometers. The display of intensity is maximum 4095; the signals have been collected in different input power levels: 10 Voltages, 5 Voltages, 2 Voltages and 1 Voltage. At 1 Voltage, signals are up to 4095 in

maximum and signals are too weak to present combustion. Since that, combine with the practice, the signals have been collected at 5 Voltages and 2 Voltages. In comparisons, the plot of 5 voltages is in low intensity with little noise; the plot of 2 voltages is in high intensity with more noises (fig App.45). Thus, the noise has to be considered.

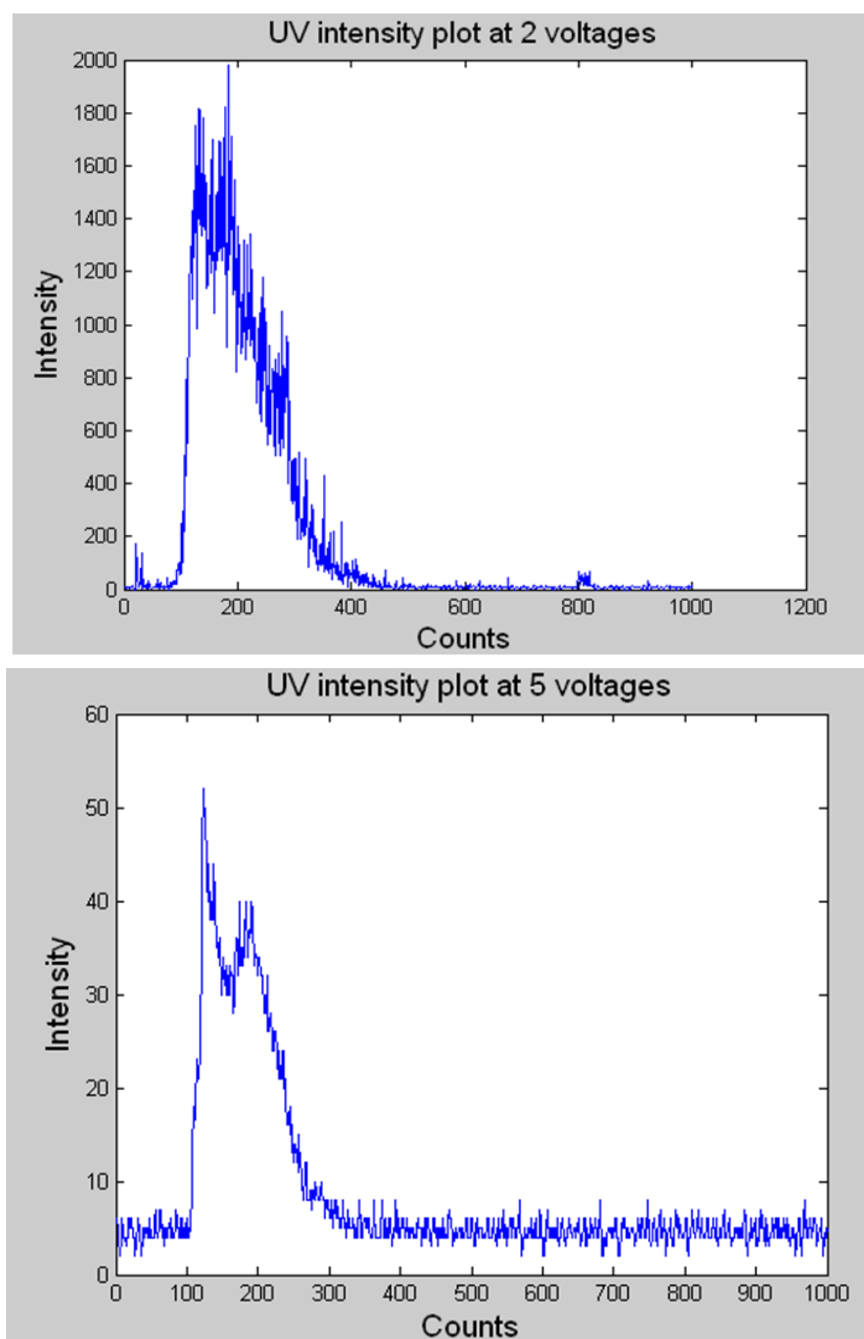


Figure App. 45 Intensity plots comparison between 2 voltages and 5 voltages

In the practice, some noises occurred from system and operation of system setup. By comparison of plots of 5 voltages and 2 voltages, the SNR of 5 voltages is 21.76 dB and SNR of 2 voltages decreases to 13 dB. The noise has an effect on displaying of combustion and it serious affect the data of combustion. However, the reconstructed images are reduced to low resolutions in  $10 \times 10$  pixels. Thus, noise affects the visualization in less. In testing, the signals are discrete samples. Thus, to improve results accuracy, the windows filter method is employed to reduce the noise in matlab. In different data, varying sizes of windows are employed to increase the SNR over 20 dB. A sample of windows filter is below:

```
%%%%%%%%%%%%%%%%%%%%%%%%%%%%%%%%%%%%%%%%%%%%%%%%%%%%%%%%%%%%%%%%%%%%%%%%
Filter sample
%%%%%%%%%%%%%%%%%%%%%%%%%%%%%%%%%%%%%%%%%%%%%%%%%%%%%%%%%%%%%%%%%%%%%%%%
data = [1:0.2:4]';
windowSize = 5;
filter(ones(1,windowSize)/windowSize,1,data)
%%%%%%%%%%%%%%%%%%%%%%%%%%%%%%%%%%%%%%%%%%%%%%%%%%%%%%%%%%%%%%%%%%%%%%%%
```

After filtering, the singles have not been altered and it performs well for filtering noise using windows filter method.

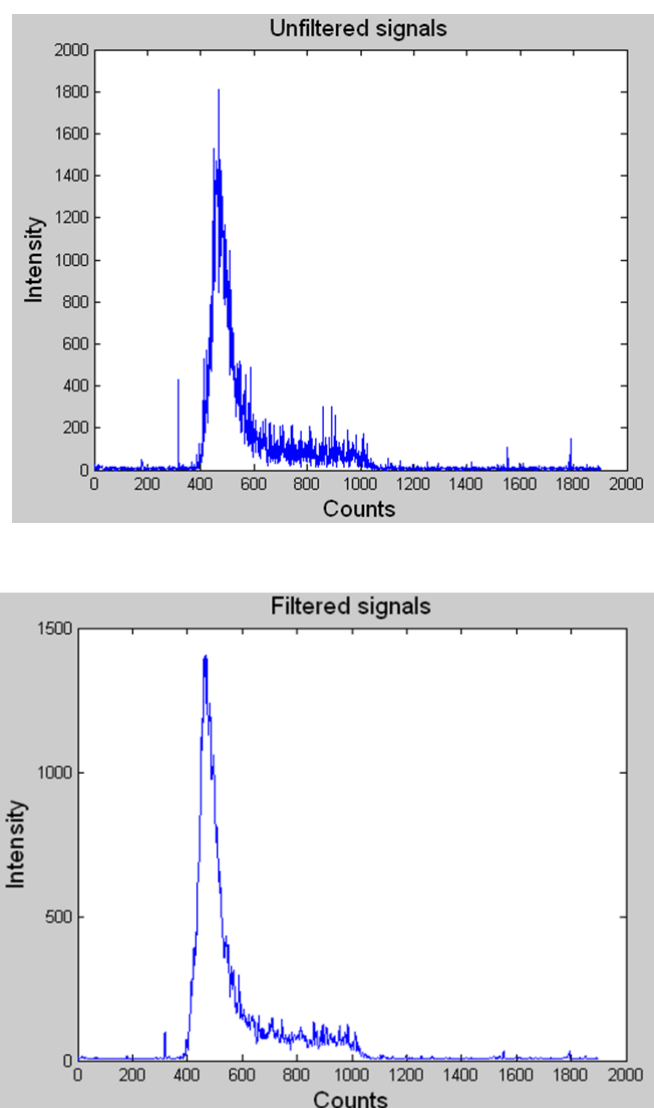


Figure App. 46 Comparison between unfiltered and filtered signals.

## Software user manual

After calibrations of system, the MART software is applied to collect signals. This program is based on the previous version of Array Reconstruction version which was developed by previous OEL group. The system applies the principle of tomography and incorporates an algorithm implementing the Multiplicative Algebraic Reconstruction Technique (MART) for generating a solution that can be visualized.

# System initialization

The configuration window of software is to initialize the tomography system and assistant the settings of detecting parameters (fig. App.47). The panel window consists of array fibres settings, array parameters setting and reconstruction setting. In addition, an function of algorithm testing mode to test the performance of system initializations in varying parameters.

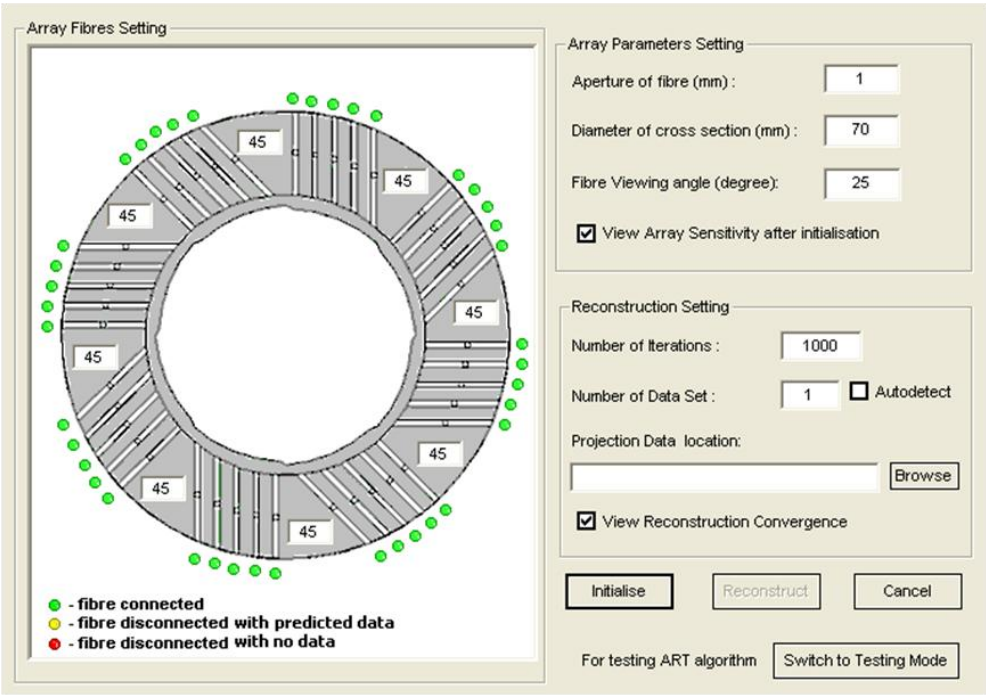


Figure App. 47 System configuration panel

## 1. Array Fibre Setting

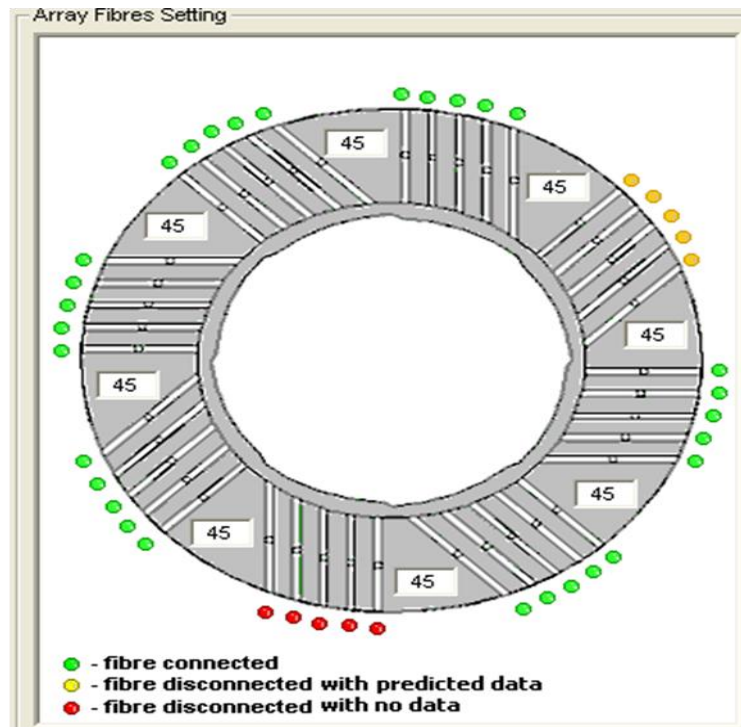


Figure App. 48 Array fibre Settings

In this panel, 40 fibres are able to connect with system to detect signals. The angles between each group can be altered. However, it has to be 360 degrees in total. In the test, some fibres are possible to be disconnected depending on the system requirements. For example, in the testing, only 35 fibres are connected due to the structure of modified engine. clicking the round buttons to change the status of individual fibre. Green is active; Yellow is disconnected and it is substituted by predicted data (Note: the predicted data must follow the rules of MART simulation, otherwise the software may not work.); Red is present total disconnected (Note: more disconnects of fibre, more distortion of combustion. The certainty ratio of system is in test mode.).

## 2. Array Parameters Setting

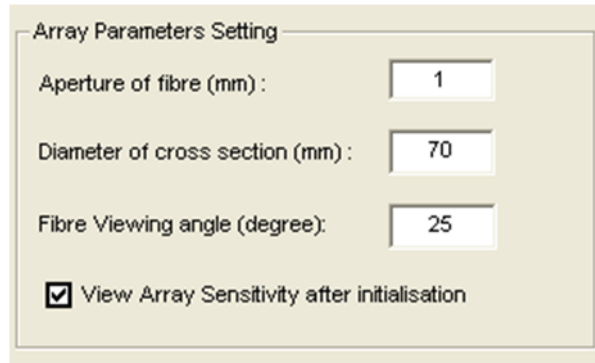


Figure App. 49 Array Parameters Settings

In this panel, three parameters can be set to adjust the detection regions of combustion. Aperture is corresponding to the fibre starting view angles. The fibre viewing angle is to adjust the sensitivity of detection region. The diameter of cross section is relative to the size of chamber (Figure App.49). In addition, the view array sensitivity clicks is to display the sensitivity graph of system according to the visualization spatial resolutions (fig. App. 50).

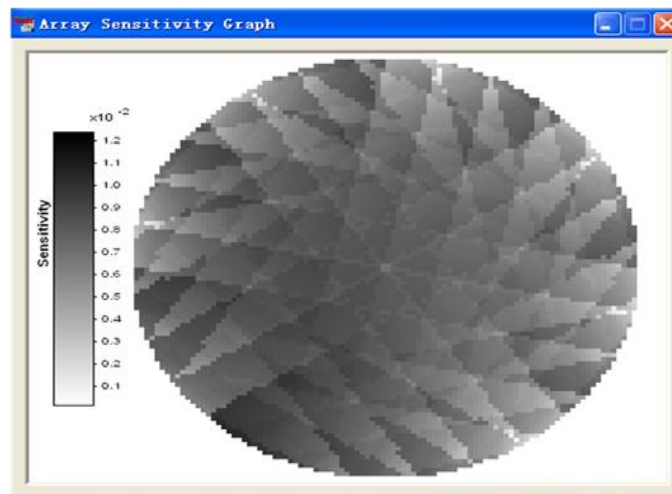
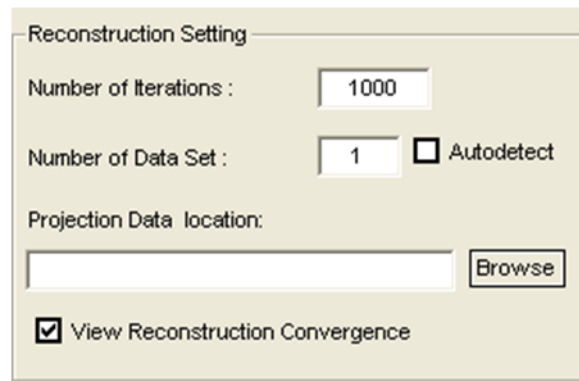


Figure App. 50 Sensitivity graph

### 3. Reconstruction Setting





Reconstruction Setting

Number of Iterations :

Number of Data Set :  ☐ Autodetect

Projection Data location:

☒ View Reconstruction Convergence

Figure App. 51 Reconstruction Setting

Number of iterations is to control iteration times. The visualizations of combustion are unstable with the increasing of number iterations. Thus, the system stable has been tested in the experiment (referred to chapter 4.3.3). The most stable is regularly 1000. The software takes data groups by groups; thus the load of data can be auto detected or selected. The data can be loaded from locations and it has to be note pad format. The convergence of simulations can be displayed in curves according to the varying of iteration numbers (fig. App.52).

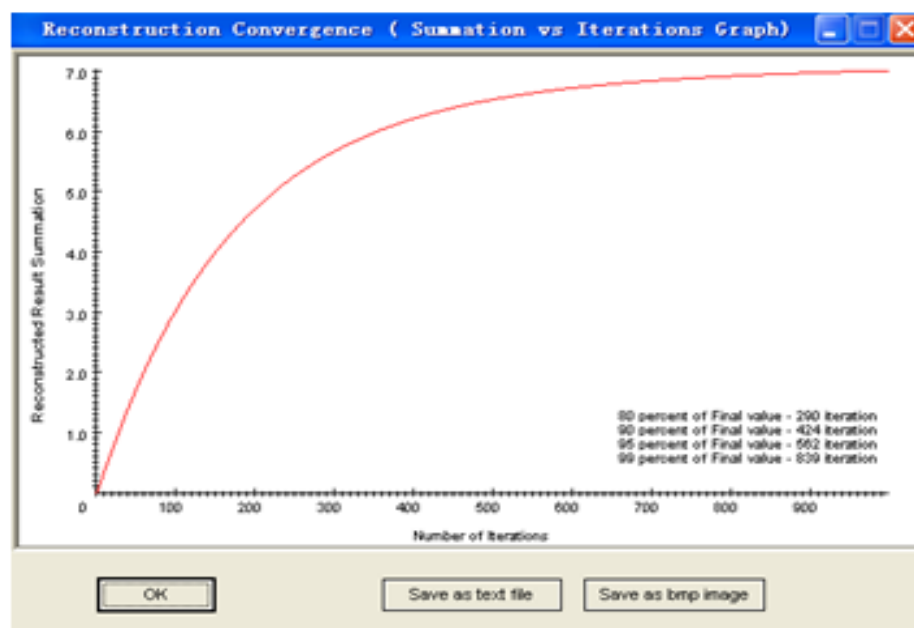


Figure App. 52 Convergence of system in 1000 iterations

# Image reconstruction

In the image reconstruction graph, there are several functions. The data set navigation is to control the presentation of each individual reconstructed image. It can choose interval times to play a sequence of images in different seconds. The reconstructed data can be saved as numerical data or bmp image. (fig. App. 53)

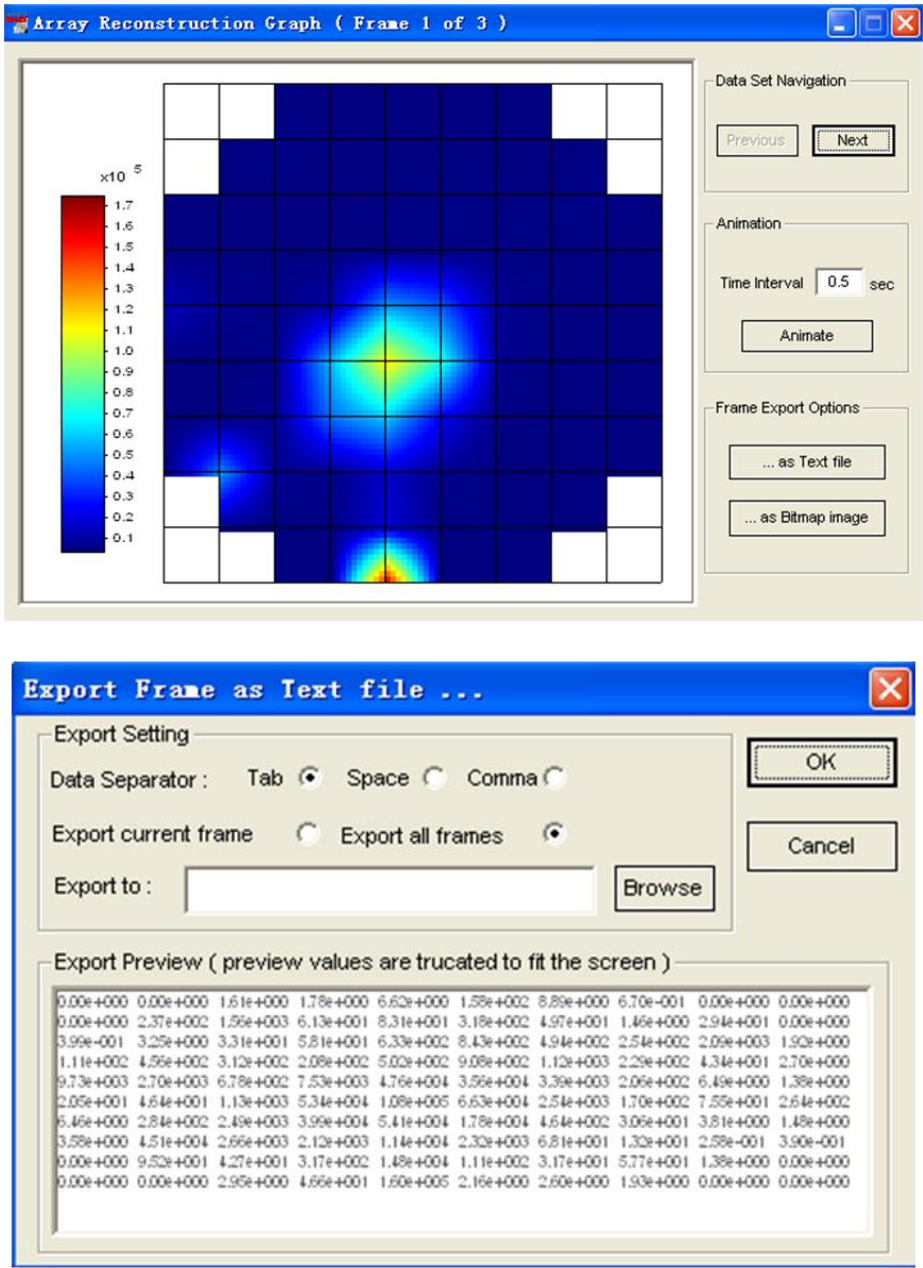


Figure App. 53 Image reconstruction graph

If the reconstructed image are saved as numerical data, the set data will be separated by selections of table, space or comma. Each of data is including 100 floating point numbers corresponding to the image resolution.

### Testing mode

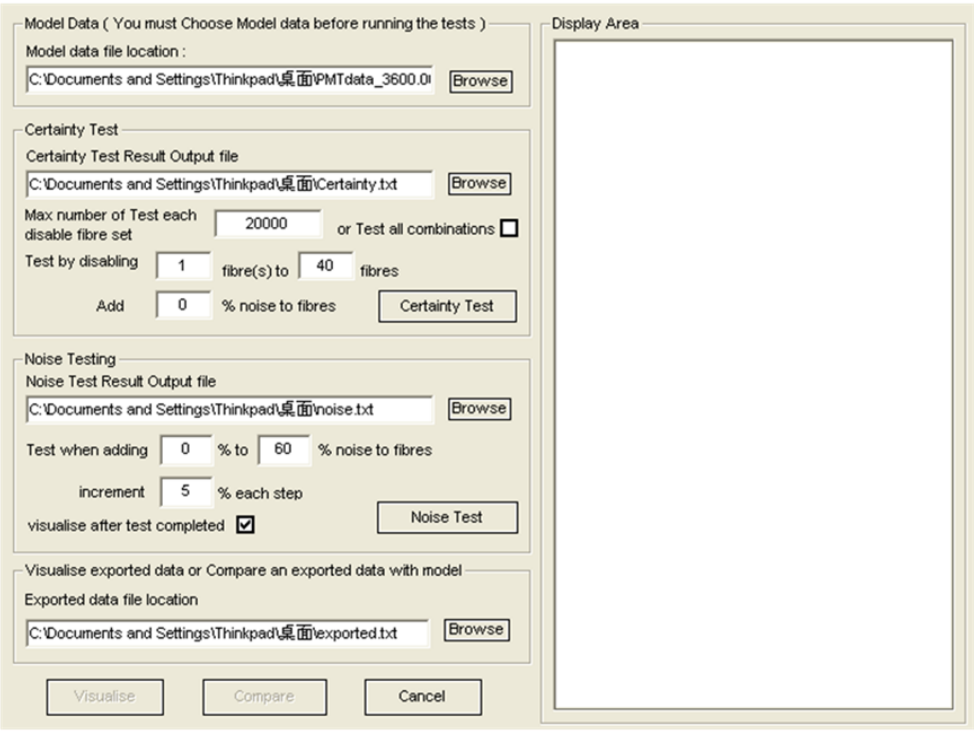


Figure App. 54 Testing mode panel

The test mode is designed to test the certainty ratios of system depending on how many are disabled. The noise testing is to add percentages background noises to initial signals for observing the reconstructed images in varying noises.

While several fibres are disabled in system, the tomography system missed some projections. Too much missing values reduces the system sensitivity and may cause the reconstructed images in distortion. To testing the stability of system, the certainty test is applied (fig. App. 41). In the panel, numbers of projections data set can

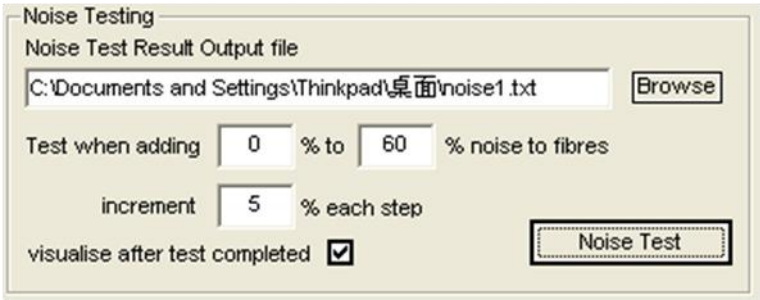
be valued; however, two large numbers may take several hours to calculate. For testing varying disabled fibres, numbers of disabled fibres are selected from 1 to 40. In addition, the noise can be considered to add into system (fig App.55). It is present if disabled fibres are over 11, the certainty of system decreases lower than 50 percents.

Figure App. 55 Certainty test panel

Disable (# of fibres)	Avg Errors	Certainty(%)
0	26057.97	96.30
1	30621.56	95.65
2	37536.20	94.67
3	38493.06	94.53
4	43043.90	93.89
5	141867.83	79.85
6	173207.09	75.40
7	273138.64	61.21
8	307818.69	56.29
9	294198.69	56.22
10	328349.39	53.37
11	336475.17	52.22
12	392681.95	44.24
13	417902.20	40.66
14	419786.91	40.39
15	448140.34	36.36
16	462708.88	34.30
17	514787.69	26.90
18	542898.47	22.91
19	543406.98	22.84
20	568964.85	19.21
21	563092.06	20.04
22	635012.66	9.83
23	654508.24	7.06
24	669309.57	6.38
25	674549.93	4.21
26	681191.91	3.27
27	702216.95	0.28
28	697658.98	0.93
29	697257.14	0.99
30	706958.95	0.00
31	711158.25	0.00
32	711985.36	0.00
33	703171.39	0.15
34	703171.39	0.15
35	703594.87	0.09
36	703594.87	0.09
37	704222.93	0.00
38	704222.93	0.00
39	704222.93	0.00
40	704222.93	0.00

Figure App. 56 Certainty test of the sample model

In the noise test, a background noise can be added into system to test the certainty of image reconstruction in different noises. The noises are selectable from 0 to 100 percents by 5 percent (selectable) increment each step (fig. App.57). With the increasing of noise, the reconstructed images are more distorting (fig. App.43). A sequence of images display the reconstructed photos of sampling signals when they are added noises from 0% to 60% with 5% each step on increment.



Noise Testing

Noise Test Result Output file  
 C:\Documents and Settings\Thinkpad\桌面\noise1.txt Browse

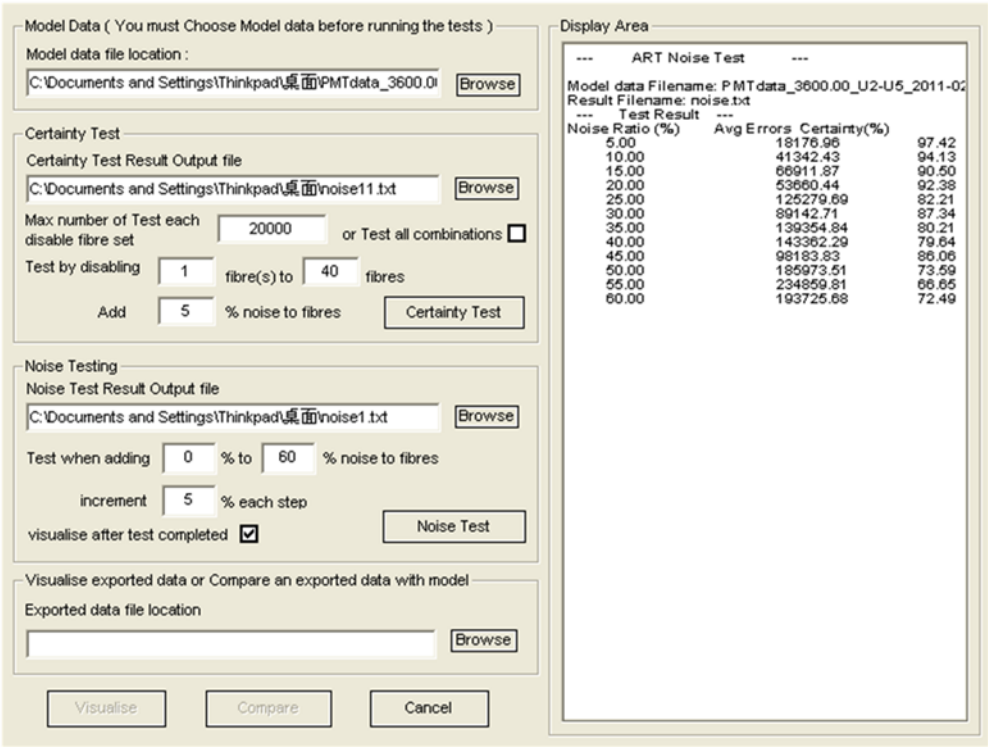
Test when adding  % to  % noise to fibres

increment  % each step

visualise after test completed ☒

Noise Test

Figure App. 57 Noise testing panel



Model Data ( You must Choose Model data before running the tests )

Model data file location :  
 C:\Documents and Settings\Thinkpad\桌面\PMTdata\_3600.0 Browse

Certainty Test

Certainty Test Result Output file  
 C:\Documents and Settings\Thinkpad\桌面\noise11.txt Browse

Max number of Test each disable fibre set  or Test all combinations ☐

Test by disabling  fibre(s) to  fibres

Add  % noise to fibres Certainty Test

Noise Testing

Noise Test Result Output file  
 C:\Documents and Settings\Thinkpad\桌面\noise1.txt Browse

Test when adding  % to  % noise to fibres

increment  % each step

visualise after test completed ☒ Noise Test

Visualise exported data or Compare an exported data with model

Exported data file location  
 Browse

Visualise Compare Cancel

Display Area

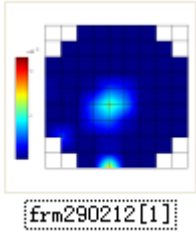
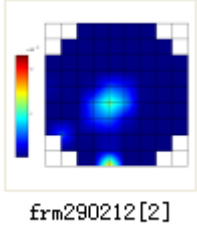
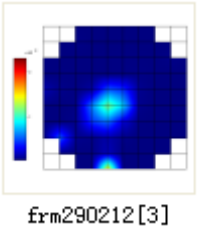
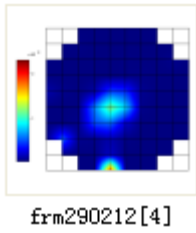
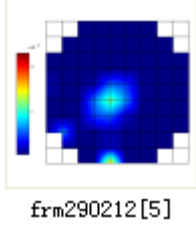
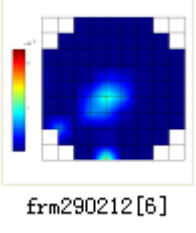
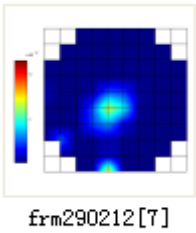
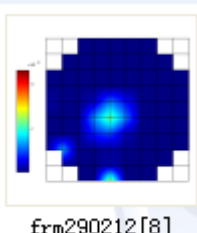
--- ART Noise Test ---

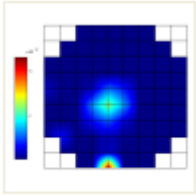
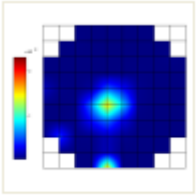
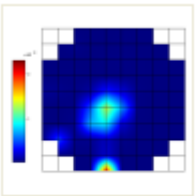
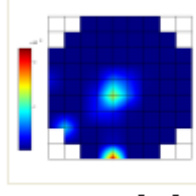
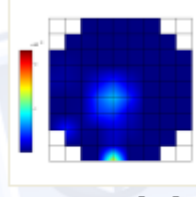
Model data Filename: PMTdata\_3600.00\_U2-U5\_2011-02  
 Result Filename: noise.txt

Noise Ratio (%)	Avg Errors	Certainty(%)
5.00	18176.96	97.42
10.00	41342.43	94.13
15.00	66911.87	90.50
20.00	53660.44	92.38
25.00	125279.69	82.21
30.00	89142.71	87.34
35.00	139354.84	80.21
40.00	143362.29	79.64
45.00	98183.83	86.06
50.00	185973.51	73.59
55.00	234859.81	66.65
60.00	193725.68	72.49

Figure App. 58 Varying noises testing on a sample signal

Table App. 4 Varying noises testing on a sample signal

 <p>frm290212[1]</p>	 <p>frm290212[2]</p>
5% background noise	10% background noise
 <p>frm290212[3]</p>	 <p>frm290212[4]</p>
15% background noise	20% background noise
 <p>frm290212[5]</p>	 <p>frm290212[6]</p>
25% background noise	30% background noise
 <p>frm290212[7]</p>	 <p>frm290212[8]</p>
35% background noise	40% background noise

 <p>frm290212[9]</p>	 <p>frm290212[10]</p>
45% background noise	50% background noise
 <p>frm290212[11]</p>	 <p>frm290212[12]</p>
55% background noise	60% background noise
 <p>frm290212[13]</p>	
65% background noise	



## Appendix D: Generals

In the system, blue and UV filters are applied in system. The specifications of these filters are below.

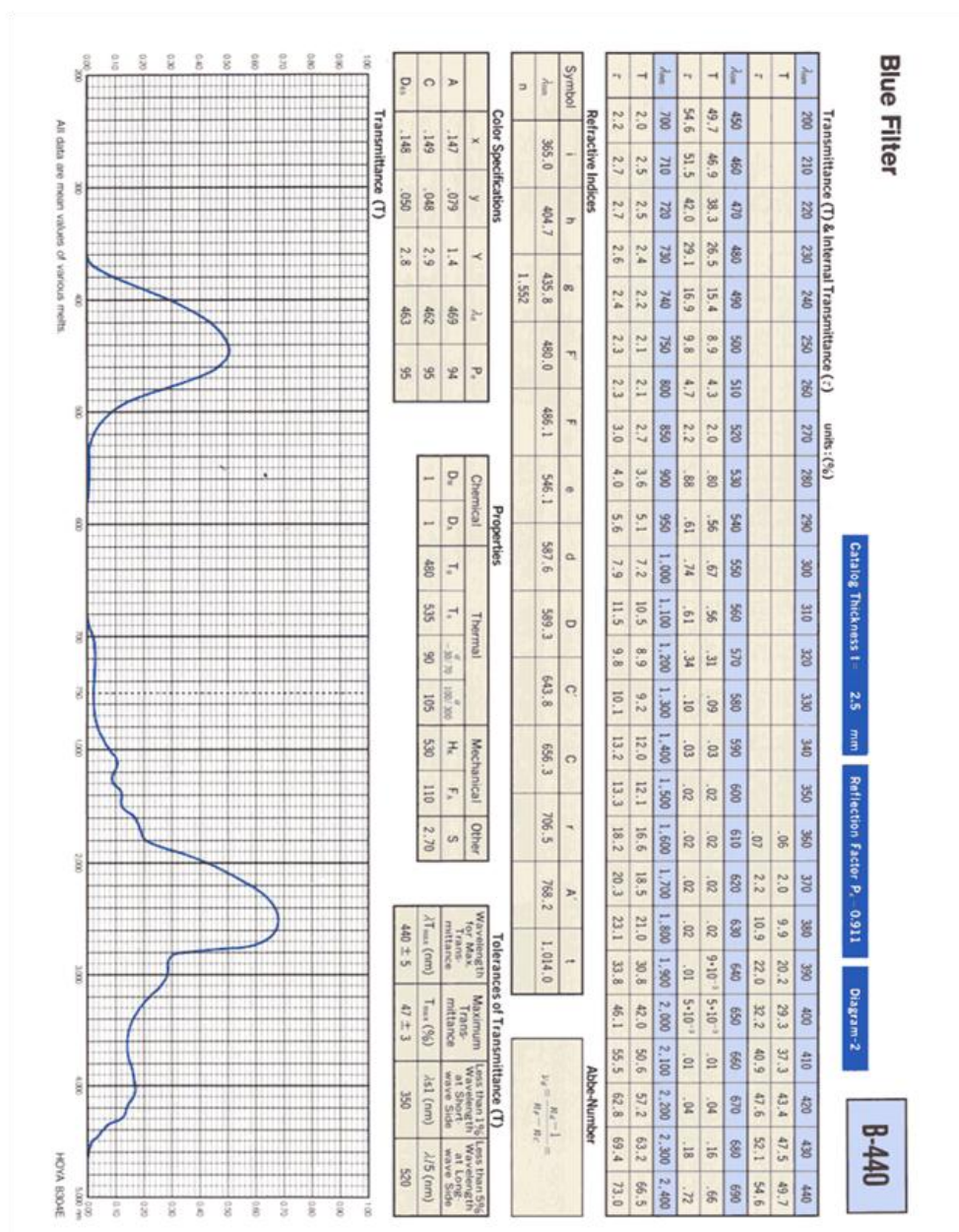


Figure App. 59 B440 Blue Filter Specification Diagram



# Ultraviolet Transmitting, Visible Absorbing Filter

Catalog Thickness t = 2.5 mm    Reflection Factor P<sub>r</sub> = 0.907    Diagram-7

U-340

Transmittance (T) & Internal Transmittance (τ)																									
units: (%)																									
λ <sub>nm</sub>	200	210	220	230	240	250	260	270	280	290	300	310	320	330	340	350	360	370	380	390	400	410	420	430	440
T						2·10 <sup>-3</sup>	.55	11.7	38.9	61.3	72.7	77.2	79.0	79.8	79.9	75.5	65.8	46.6	13.1	.22					
τ						2·10 <sup>-3</sup>	.61	12.9	42.9	67.6	80.2	85.1	87.1	88.0	88.1	83.2	72.5	51.4	14.4	.24					
λ <sub>nm</sub>	450	460	470	480	490	500	510	520	530	540	550	560	570	580	590	600	610	620	630	640	650	660	670	680	690
T																							2·10 <sup>-3</sup>	.04	.40
τ																							2·10 <sup>-3</sup>	.04	.44
λ <sub>nm</sub>	700	710	720	730	740	750	800	850	900	950	1,000	1,100	1,200	1,300	1,400	1,500	1,600	1,700	1,800	1,900	2,000	2,100	2,200	2,300	2,400
T	1.4	2.2	2.2	1.9	1.0	.48	.02					.03	.03	.04	.05	.05	.06	.07	.07	.08	.09	.09	.1	.3	.5
τ	1.5	2.4	2.4	2.1	1.1	.53	.02					.03	.03	.04	.06	.06	.07	.08	.08	.09	.1	.1	.3	.6	

## Refractive Indices

Symbol	i	h	g	F	F	e	d	D	C	C	r	A'	t
λ <sub>nm</sub>	365.0	404.7	435.8	480.0	486.1	546.1	587.6	589.3	643.8	656.3	706.5	768.2	1,014.0
n						(1.568)							

## Abbe-Number

$$V_d = \frac{n_d - 1}{n_F - n_C} =$$

## Color Specifications

	x	y	Y	λ <sub>u</sub>	P <sub>e</sub>
A	—	—	—	—	—
C	—	—	—	—	—
D <sub>11</sub>	—	—	—	—	—

## Properties

Chemical		Thermal				Mechanical		Other	
D <sub>v</sub>	D <sub>1</sub>	T <sub>g</sub>	T <sub>h</sub>	T <sub>h</sub> <sup>2</sup>	T <sub>h</sub> <sup>3</sup>	H <sub>k</sub>	F <sub>A</sub>	S	
4	4	530	565	85	96	430	250	2.92	

## Tolerances of Transmittance (T)

Wavelength for Max. Transmittance	Maximum Transmittance	Transmittance at 254 nm	Transmittance at 405 nm
λT <sub>max</sub> (nm)	T <sub>max</sub> (%)	T <sub>254</sub> (%)	T <sub>405</sub> (%)
340 ± 5	75 ± 5	< 1.0	< 0.1

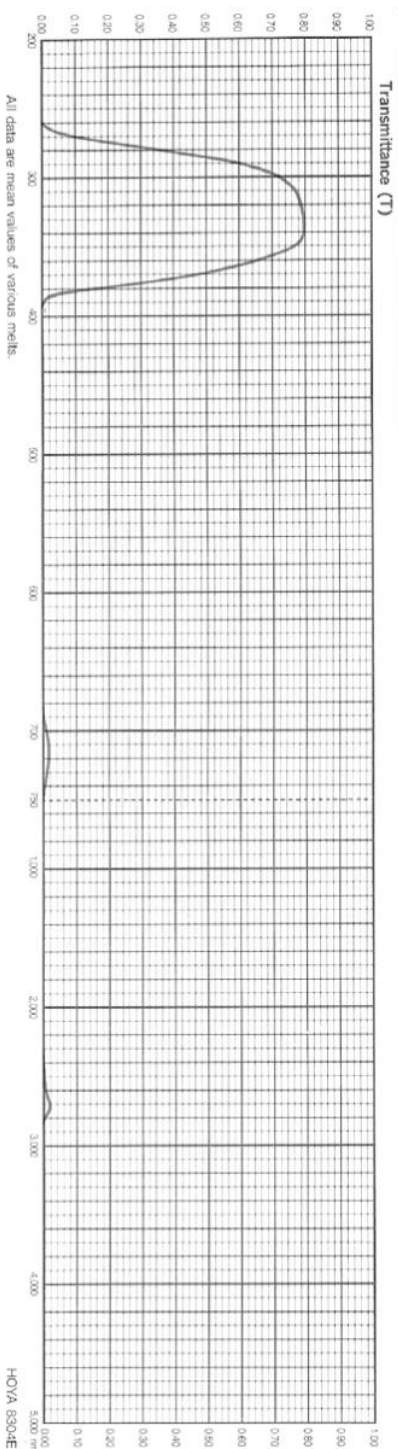


Figure App. 60 U340 UV Filter Specification Diagram

In the experiment, a generator is to make system test on different loads. However, due to the connector design problems, it has not been achieved. The specification of generator is below.



Figure App. 61 Generator

In experiment, R8900 PMTs are employed to setup POET system, the specifications of R8900 is below.

## GENERAL

Parameter		Description / Value	Unit
Spectral Response		300 to 650	nm
Wavelength of Maximum Response		420	nm
Photocathode	Material	Bialkali	—
	Minimum Effective Area	23.5 × 23.5	mm
Window	Material	Borosilicate glass	—
	Thickness	0.8	mm
Dynode	Structure	Metal channel dynode	—
	Number of Stages	11	—
Anode		6 (X) + 6 (Y) Cross plate anode	—
Weight		Approx. 28 (U Type: Approx. 38)	g
Suitable Socket		E678-32B (sold separately)	—
Operating Ambient Temperature		-80 to +50 (U Type: -30 to +50)	°C
Storage Temperature		-80 to +50 (U Type: -30 to +50)	°C

## MAXIMUM RATINGS (Absolute Maximum Values)

Parameter		Value	Unit
Supply Voltage	Between Anode and Cathode	1000	V
Average Anode Current in Total		0.1	mA

## CHARACTERISTICS (at 25 °C)

Parameter		Min.	Typ.	Max.	Unit
Cathode Sensitivity	Luminous (2856 K)	50	85	—	μA/lm
	Quantum Efficiency at 420 nm	—	25	—	%
	Blue Sensitivity Index (CS 5-58)	7.5	10	—	—
Anode Sensitivity	Luminous (2856 K)	15	60	—	A/lm
Gain		—	$0.7 \times 10^6$	—	—
Anode Dark Current in Total of Anodes (after 30 min storage in darkness)		—	2	10	nA
Time Response	Anode Pulse Rise Time	—	2.2	—	ns
	Electron Transit Time	—	11.9	—	ns
	Transit Time Spread (FWHM)	—	0.75	—	ns

**NOTE:** Anode characteristics are measured with the voltage distribution ratio shown below.

## VOLTAGE DISTRIBUTION RATIO AND SUPPLY VOLTAGE

Electrodes	K	G	Dy1	Dy2	Dy3	Dy4	Dy5	Dy6	Dy7	Dy8	Dy9	Dy10	Dy11	P
Ratio	0.5	1.5	2	1	1	1	1	1	1	1	1	1	1	0.5

Supply Voltage: 800 V, K: Cathode, G: Grid, Dy: Dynode, P: Anode

Figure 1: Typical Spectral Response

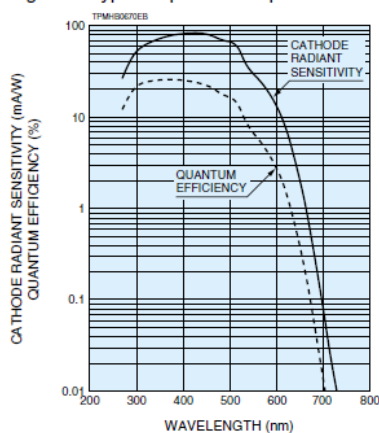


Figure 2: Typical Gain and Anode Dark Current

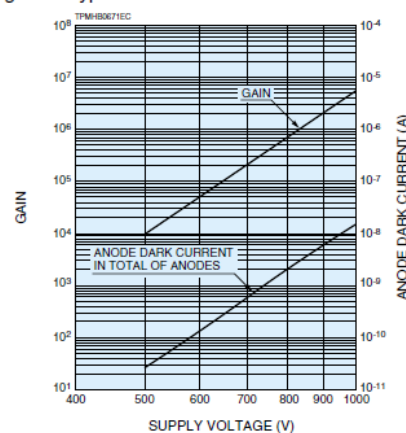


Figure 3: Spatial Resolution

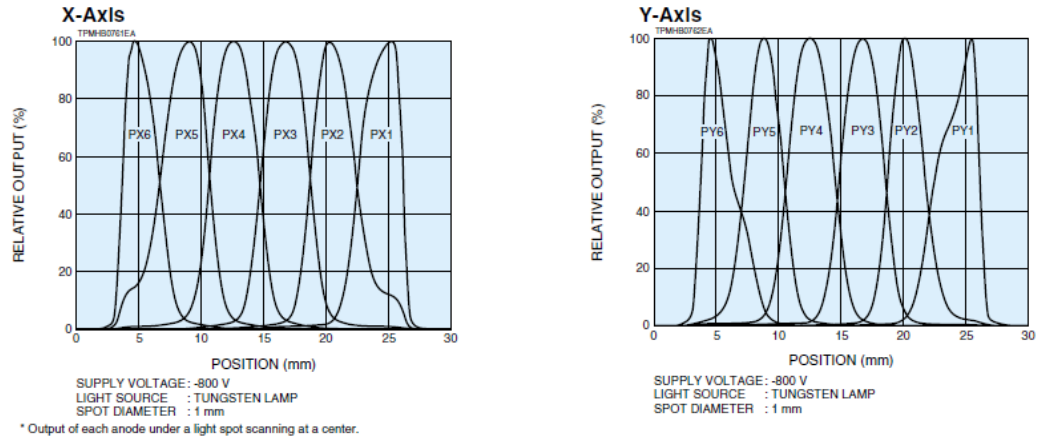


Figure 4: Position Response Using PX/PY Anodes

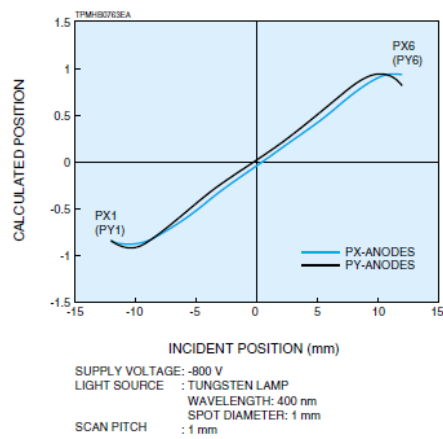


Figure 5: Positioning Histogram Example

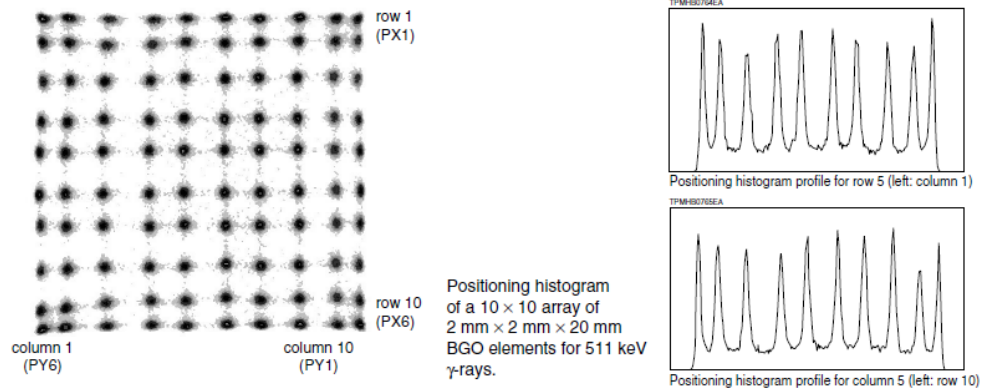
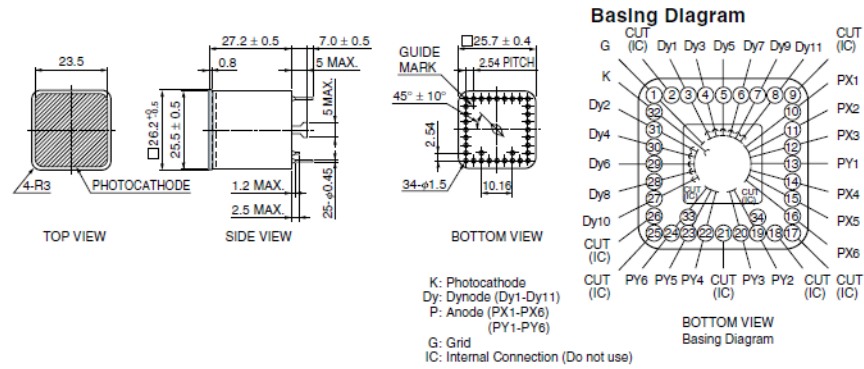


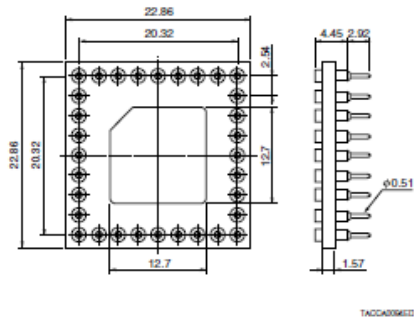
Figure 6: R8900-00-C12 Dimensional Outline and Basing Diagram (Unit: mm)



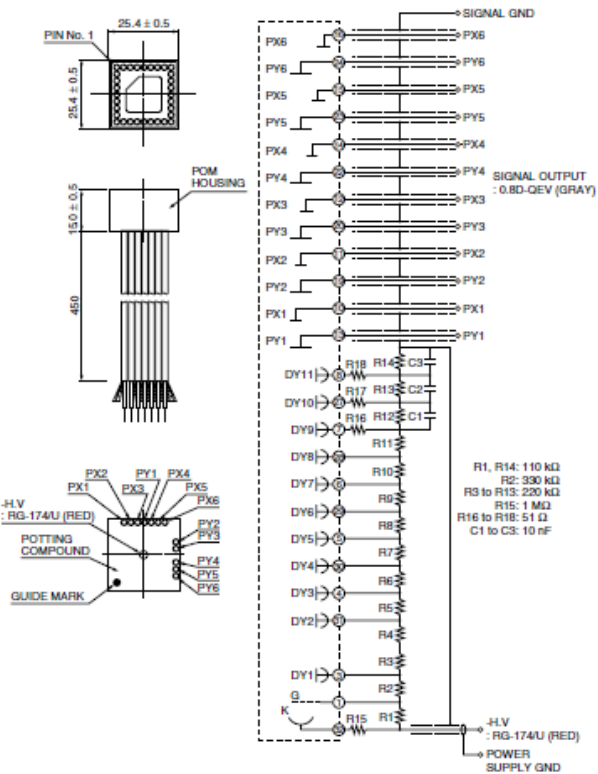
TPM-H0523EA

[ACCESSORIES] (Unit: mm)

● Socket E678-32B **SOLD SEPARATELY**



● D Type Socket Assembly E7514 **SOLD SEPARATELY**

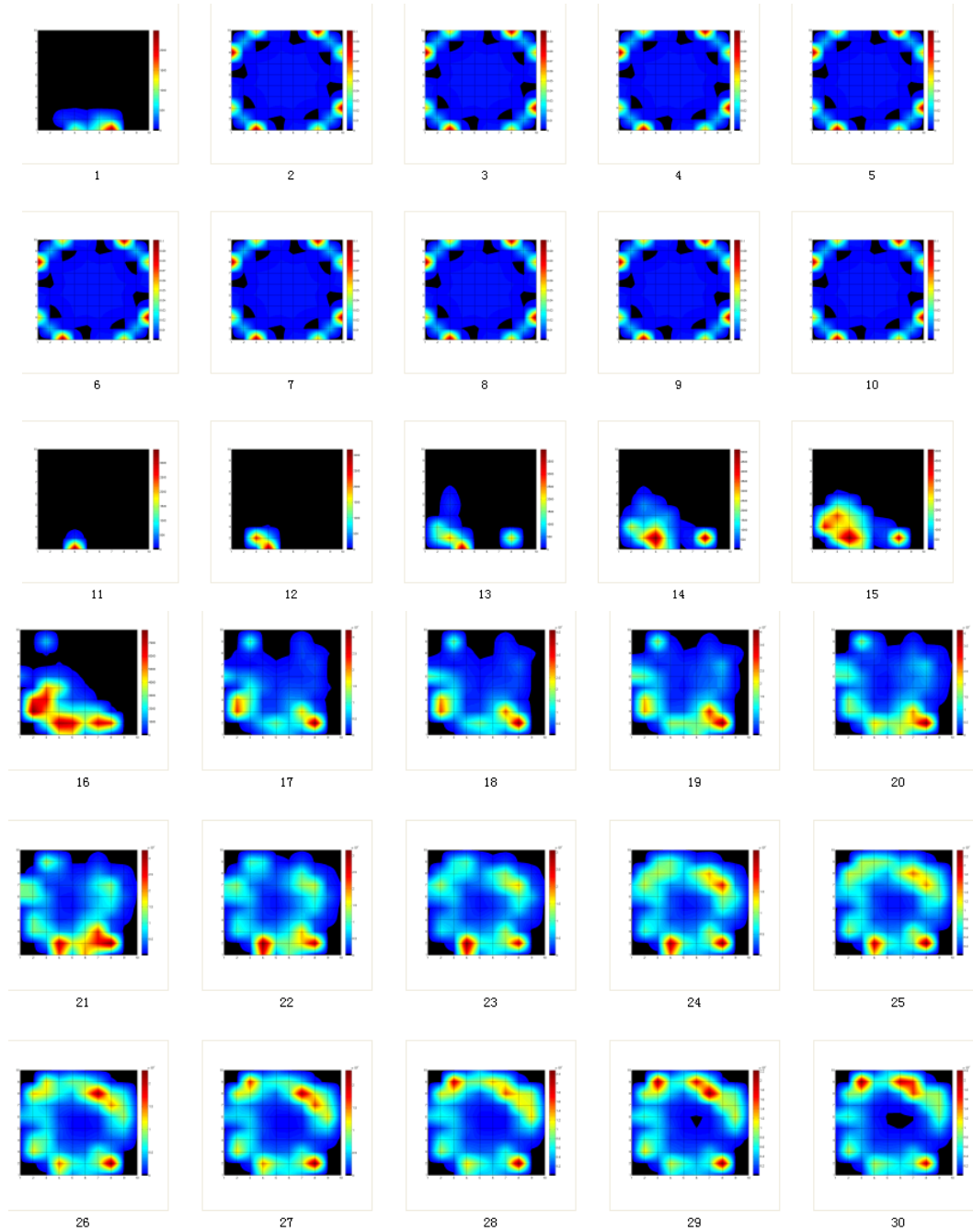


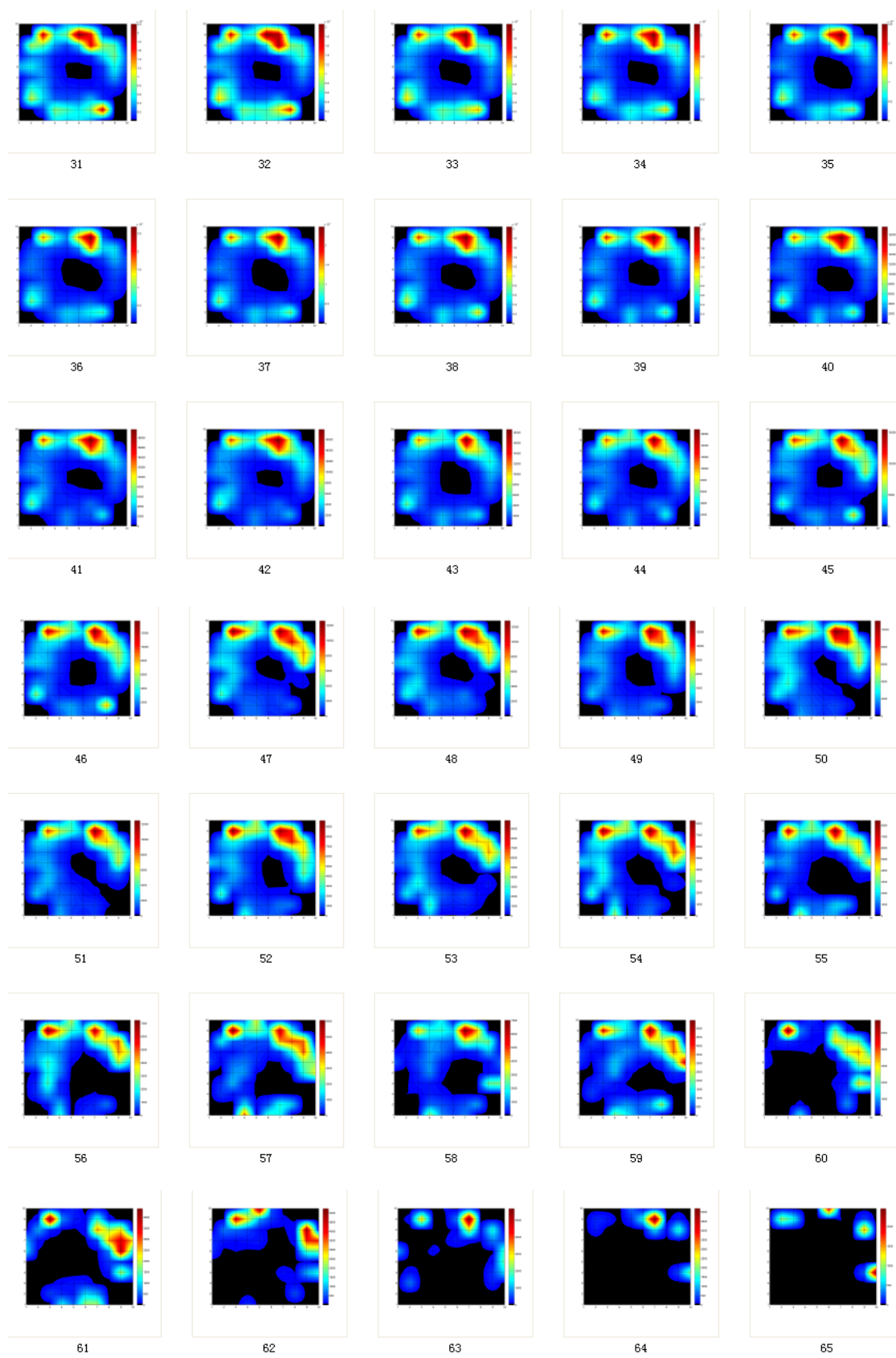
In case of using PMT with E7514, PMT must be operated within 0 °C to 50 °C  
(Storage temperature for E7514 only: -15 °C to +60 °C)

# Appendix E: POET Reconstruction Results

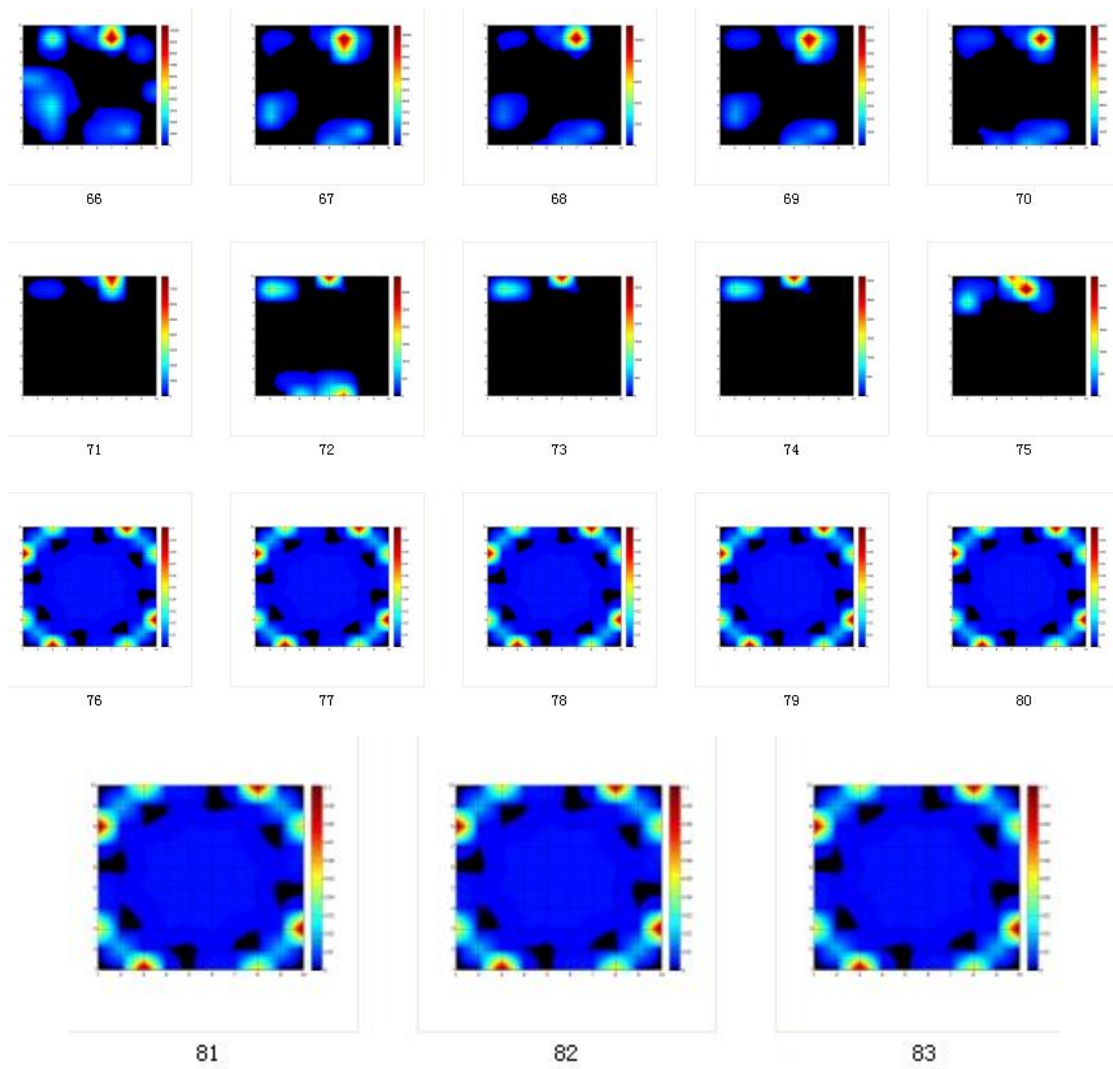
## UV Filtered Combustion

- Parameters: 83 Frames; Sampling rate is 2.5 Degrees of Crank Angle; Start from -27 degrees and end with 180 degrees. Free scale colourbar.





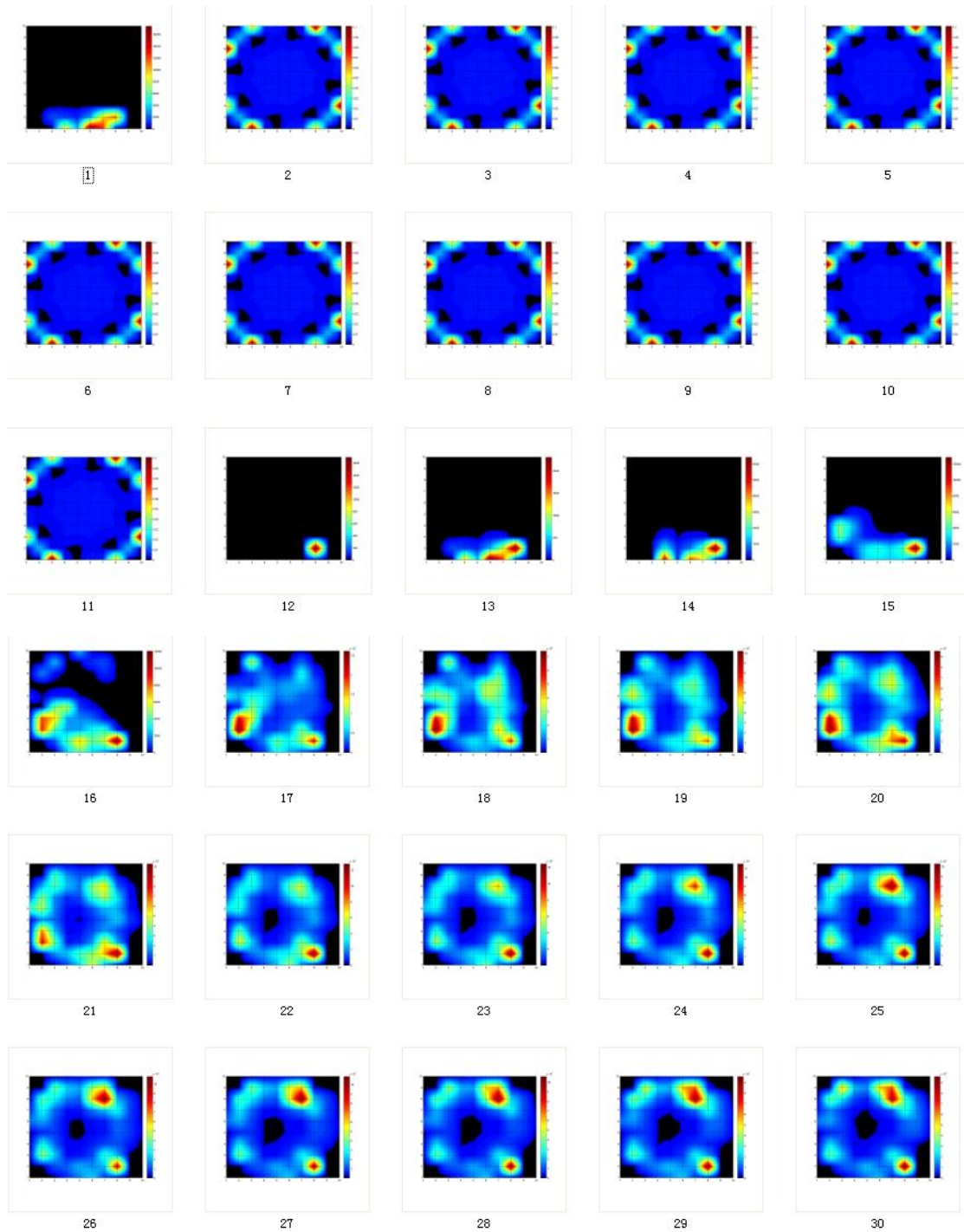


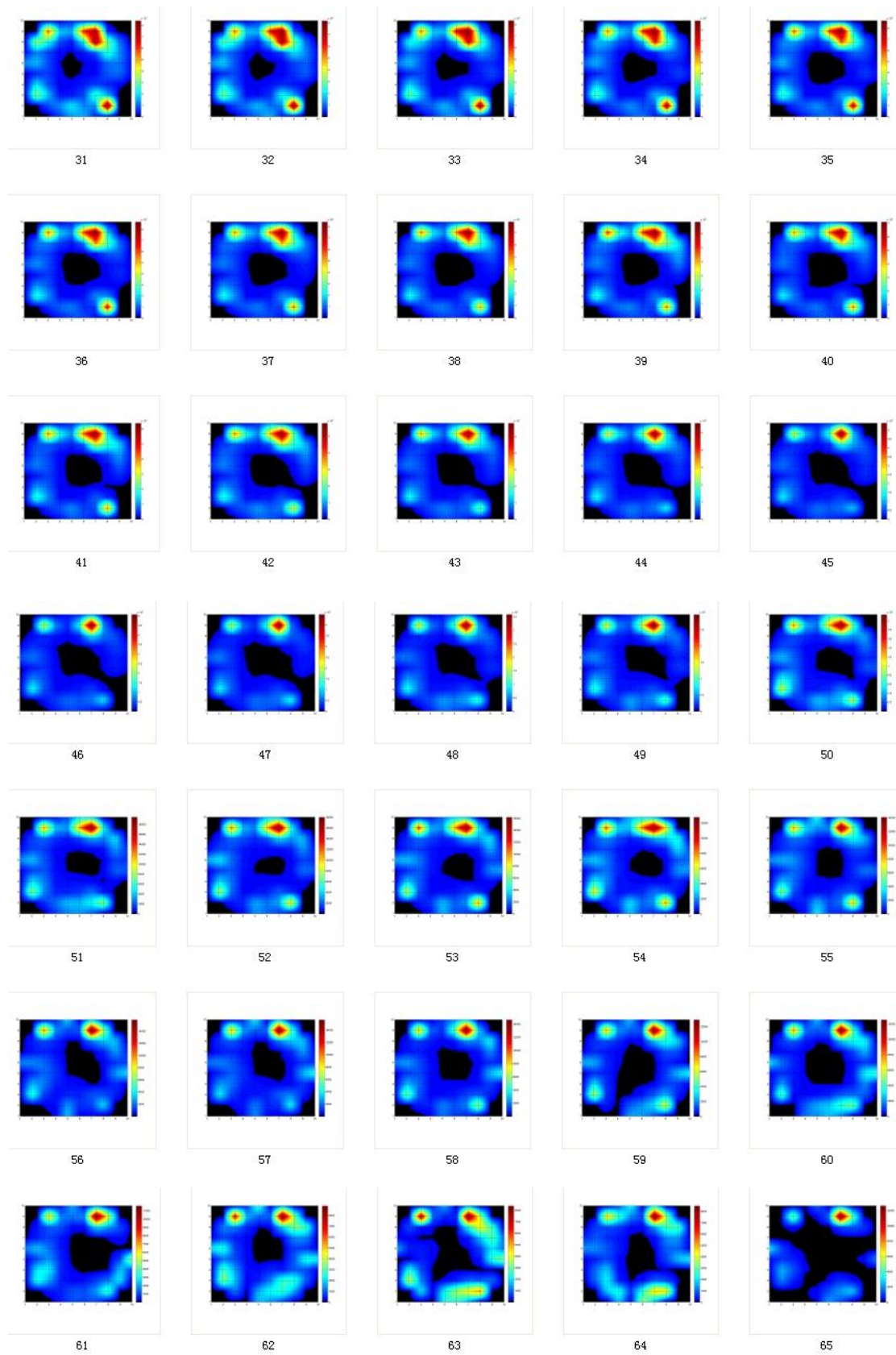


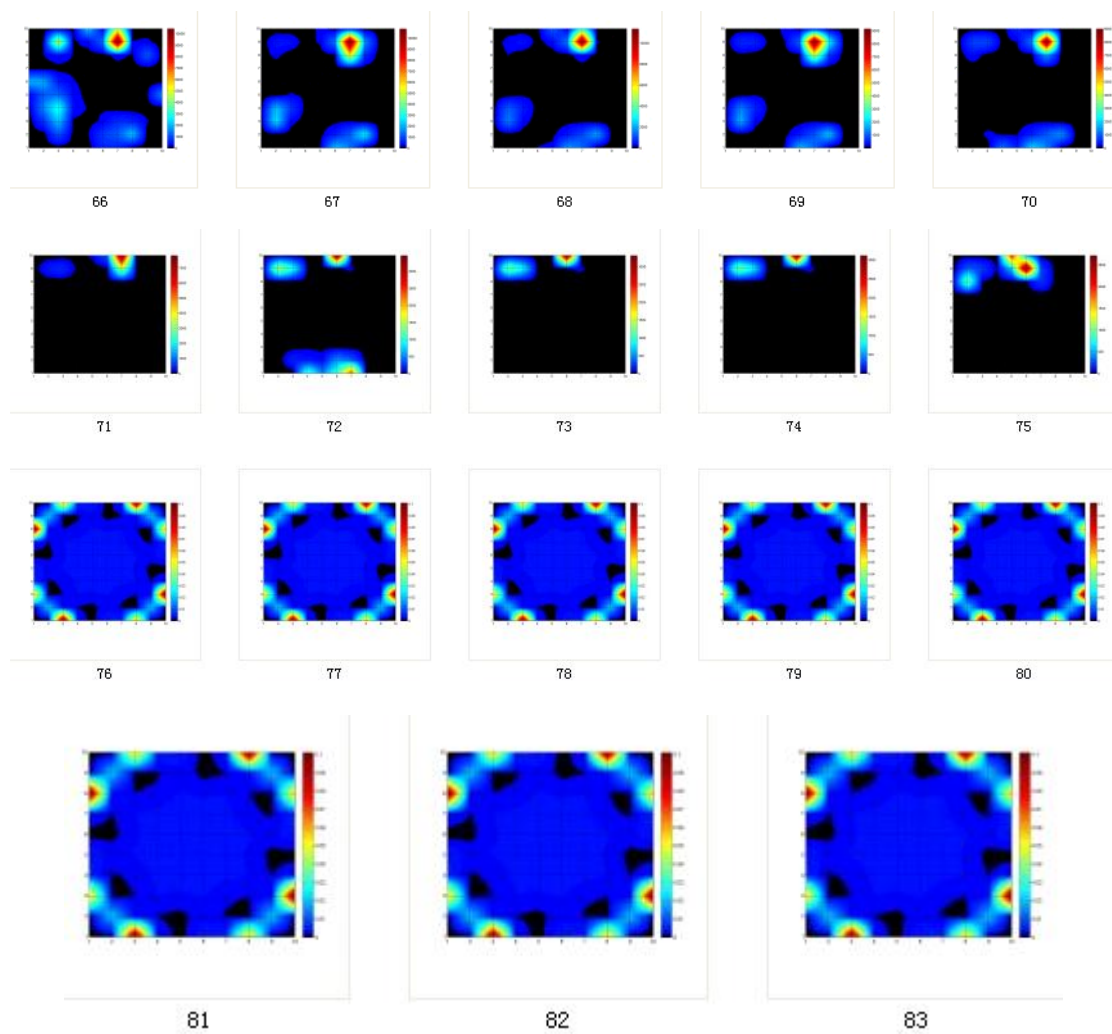


# Blue Filtered Combustion

- Parameters: 83 Frames; Sampling rate is 2.5 Degrees of Crank Angle; Start from -27 degrees and end with 180 degrees. Set colourbar 60000.







## Appendix Reference

- [1] G. Norris, "Pulse Power: Pulse Detonation Engine-powered Flight Demonstration Marks Milestone in Mojave," in *Aviation Week & Space Technology*, vol. 168, p. 60, 2008.
- [2] G. Stokes, "On the Effect of the Internal Friction of Fluids on the Motion of Pendulums," in *Transactions of the Cambridge Philosophical Society*, vol. 9, p. 106, 1851.
- [3] O. Reynolds, "An experimental investigation of the circumstances which determine whether the motion of water shall be direct or sinuous, and of the law of resistance in parallel channels," in *Philosophical Transactions of the Royal Society*, vol. 174, pp. 935–982, 1883.
- [4] I. Glassman, *Combustion*. New York: Academic Press, 1977.
- [5] A.G. Gaydon and H.G. Wolfhard, *Flames: Their Structure, Radiation and Temperature*, 2nd ed. London: Chapman and Hall, 1960.
- [6] F. J. Weinberg, *Optics of flames*. London: Butterworths, 1963.
- [7] A.M. Kanury, *Introduction to Combustion Phenomena*. New York: Gordon and Breach, 1975.
- [8] J.M. Beer and N.A. Chigier, *Combustion Aerodynamics*. London: Applied Science Publishers, 1974.
- [9] M. Tanahashia, S. Murakamia, G. Choib, Y. Fukuchia and T. Miyauchia, "Simultaneous CH–OH PLIF and stereoscopic PIV measurements of turbulent premixed flames," in *Proceedings of the Combustion Institute*, vol. 30, pp. 1665-1672, 2005.
- [10] C.H. Brücker, "3D scanning PIV applied to an air flow in a motored engine using digital high-speed video," in *Meas. Sci. Technol.*, vol. 8, pp. 1480-1492, 1997.
- [11] T. Echehki, and M.G. Mungal, "Particle Tracking in a Laminar Premixed Flame," in *Gallery of Fluid Motion, Physics of Fluids*, 1990.
- [12] L. Anton, N. Li and K.H. Luo, "A study of scalability performance for

hybrid mode computation and asynchronous MPI transpose operation in DSTAR," in *Cray User Group 2011 conference*, 2011.

- [13] G. Damkohler and Z. E. Angew, "physik," in *Chem*, vol. 46, p. 601, 1940.
- [14] K.I. Schelkin, "NACA Tech," *Memo*, p. 1110, 1947.
- [15] R.R. John and E. Mayer, *Arde Assoc. Tech*, pp. 4555-5, 1957.
- [16] L.S.G. Kovasznay, *Jet Propul*, vol. 26, p. 485, 1956.
- [17] F.A. Williams, *Combustion Theory*, 2 ed. Menlo Park, CA: Benjamin/Cummings, 1984.
- [18] K.N.C. Bray and J.B. Moss, "AASU Report," vol. 335, 1974.
- [19] K.N.C. Bray and J.B. Moss, "Acta. Astronaut," vol. 4, p. 291, 1977.
- [20] K.N.C. Bray and P.A. Libby, *Phys.*, vol. Fluids 19, 1977.
- [21] P.A. Libby and K.N.C. Bray, "Turbulence production in premixed turbulent flames," in *Combust. Sci. Technol*, vol. 25, pp. 127–140, 1981.
- [22] O.O. Akindele, D. Bradley, P.W. Mak and M. McMahon, "Spark-Ignition of Turbulent Gases," in *Combustion and Flame*, vol. 47, pp. 129-155, 1982.
- [23] D.B. Spalding, *Sixteenth Symposium on Combustion*. Pittsburgh: The combustion Institute.
- [24] G.E. Andrews, D. Bradley and S.B. Lwakabamba, "Measurement of turbulent burning velocity for large turbulent Reynolds numbers," in *Symposium (International) on Combustion*, vol. 15, pp. 655 - 664, 1975.
- [25] G.C. Andrews, D. Bradley and S.B. Lwakabamba, "Turbulence and turbulent flame propagation—A critical appraisal," in *Combustion and Flame*, vol. 24, pp. 285-304, 1975.
- [26] M. Berthelot and P. Vieille, *Comp. Rend*, vol. 93, 1881.
- [27] D.L.Phil. Chapman, *Mag.*, vol. 25, p. 475, (1913)

- [28] J.E. Jouguet, *Mathematique*, p. 347 1905.
- [29] Z.R. Becker, *Physik* vol. 8, p. 321, 1922.
- [30] S. Dessureault, "Rock Excavation," in *University of Arizona Mining and Geological Engineering*, vol. MnE pp. 415-515, 2006.
- [31] C.K. Law, *Combustion Physics*: Cambridge University Press, 2006.
- [32] M. Berthelot and P. Vielle, *Compt, Rend, Acad. Sci*, pp. 94, 101, 149, 822, 1882.
- [33] W.E. Gordon, *Third Symposium on Combustion and Flame and Explosion Phenomena*. Baltimore: Williams & Wikins, 1949.
- [34] E. Mallard and H.L. Chatelier, *Ann. Mines* vol. 4, pp. 274,335, 1883.
- [35] B. Lewis and J.B. Friauf, *J. Am. Chem. Soc*, vol. 52, p. 3905, 1930.
- [36] P. Laffitte, *Science of Petroleum*, vol. 4, p. 2995.
- [37] S.R. Deans, *The Radon Transform and Some of Its Applications*. New York: John Wiley & Sons, 1983.
- [38] Y.C. Wei, G. Wang and J. Hsieh, "An intuitive discussion on the ideal ramp filter in computed tomography (I)," in *Computers & mathematics with applications*, vol. 49, pp. 731-740, 2005.
- [39] P. Munshi, "Error analysis of tomographic filters. I: Theory," in *NDT & E international*, vol. 25, pp. 191-194, 1992.
- [40] I.A. Hazou and D.C. Solmon, "Filtered-backprojection and the exponential Radon," in *Journal of Mathematical Analysis and Applications*, vol. 141, pp. 109-119, 1989.
- [41] C. Nguyen and T.S. Huang, "Image blurring effects due to the depth discontinuities: blurring that creates emergent image details," in *Image and Vision Computing*, vol. 10, pp. 689-698, 1992.
- [42] R. Hartley, "A Gaussian- weighted multiresolution edge detector," in *Computer Vision, Graphics and image Processing*, vol. 30, pp. 70-83, 1985.

- [43] R. Bracewell, *The Fourier transform and its applications*, 2 ed.: McGraw-Hill Press, 1986.